Synthesis of High-Entropy Alloy Nanoparticles and Compounds Using Germanium-Based Nanostructures

by

Chuyi Ni

A thesis submitted in partial fulfillment of the requirements for the degree of

Doctor of Philosophy

Department of Chemistry
University of Alberta

Abstract

High-entropy alloy nanoparticles and compounds exhibit significant potential in various emerging energy storage and conversion fields due to their compositional flexibility for precise tuning of desired functionalities. The research described in this thesis aims to explore germanium-based nanostructures for the synthesis of high-entropy alloy nanoparticles and compounds.

In Chapter 1, the principles of high-entropy alloys, nanoparticles, and compounds are introduced. The most common synthetic methods that provide high-entropy alloy nanoparticles are discussed, highlighting the importance of rapid heating and cooling. Additionally, a compilation of high-entropy compounds is presented. The chapter concludes with a detailed discussion of germanium nanostructures, including nanoparticles and nanosheets, and the synthetic methodologies used to prepare them.

Chapter 2 outlines a method for introducing a suite of metal nanoparticles (i.e., Au, Ag, Cu, Pd, Pt) onto the surfaces of germanium nanosheets (GeNSs). Characterization confirming the integrity of the GeNS structure and the formation of metal nanoparticles is then discussed. The resulting materials are investigated as photocatalysts for the selective oxidation of benzyl alcohol, demonstrating higher efficiency compared to freestanding metal nanoparticles and GeNSs. The direct linking of metal nanoparticles to GeNSs showcases a synergistic effect, and thin films of the decorated GeNSs offer convenient catalyst recovery and recyclability.

Chapter 3 details the deposition of high-entropy alloy nanoparticles onto various germanium surfaces through surface-mediated reduction. Techniques including XRD, FTIR, XPS, and TEM confirm the structure, composition, and morphology of the resulting

nanoparticles. Freestanding high-entropy alloy nanoparticles can be liberated from GeNSs via UV light irradiation while maintaining their single-phase solid solution structure. This methodology is extended to different germanium substrates.

Chapter 4 introduces a method for preparing high-entropy germanides through rapid thermal annealing, presenting two types of high-entropy germanides (i.e., AuAgCuPdPtGe and FeCoNiCrVGe). XRD, XPS, and TEM analyses confirm the synthesis and composition of the high-entropy germanides. The formation and growth mechanisms are studied using in situ heating experiments, revealing a multi-stage process involving the initial decomposition of germanane, followed by gradual grain growth and rapid grain growth at elevated temperatures. A summary of the experimental chapters is provided in Chapter 5, along with future research directions.

Preface

Chapter 2 of this thesis has been published as Ni, C.; Chevalier, M.; Veinot, J. G. C., Metal Nanoparticle-decorated Germanane for Selective Photocatalytic Aerobic Oxidation of Benzyl Alcohol. *Nanoscale Adv.* **2022**, *5* (1), 228-236. I was responsible for concept formation, data collection and analysis, and manuscript preparation. Madison Chevalier assisted with data collection, data analysis, and manuscript editing. Prof. Jonathan Veinot was the supervisory author and assisted with concept formation, data analysis, and manuscript preparation.

Chapter 3 of this thesis has been published as Ni, C.; O'Connor, K. M.; Trach, J.; Butler, C.; Rieger, B.; Veinot, J. G. C. Facile synthesis of high-entropy alloy nanoparticles on germanane, Ge nanoparticles and wafers. *Nanoscale Horiz.* **2023**, *8* (9), 1217-1225. I was responsible for concept formation, data collection and analysis, and manuscript preparation. Kevin O'Connor assisted with data collection, data analysis, and manuscript editing. Jonathan Trach performed the scanning electron microscopy and energy dispersive X-ray spectroscopy. Cole Butler collected the X-ray photoelectron spectra. Prof. Bernard Rieger and Prof. Jonathan Veinot was the supervisory author and assisted with concept formation, data analysis, and manuscript preparation.

Chapter 4 of this thesis has been published as Ni, C.; O'Connor, K. M.; Butler, C.; Veinot, J. G. C. Synthesis of high-entropy germanides and investigation of their formation process. *Nanoscale Horiz.* **2024**, *9* (4), 580-588. I was responsible for concept formation, data collection and analysis, and manuscript preparation. Kevin O'Connor assisted with data collection, data analysis, and manuscript editing. Cole Butler collected the X-ray

photoelectron spectra. Prof. Jonathan Veinot was the supervisory author and assisted with concept formation, data analysis, and manuscript preparation.

Acknowledgments

It is hard to believe that it is almost five years since I started my Ph.D. study. In the past five years, I worked on challenging but exciting projects, operated multi-million-dollar instruments, collaborated with international colleagues, exchanged to TUM in Germany, and attended many international conferences. I feel like I have done a lot in the past five years and I would have done more if there is no COVID-19. All those things would not have happened without my family, supportive supervisor, and friends.

I want to thank my parents first and I love you. I know we have been separated by the Pacific Ocean most of the time since I started my studies in Canada, but you have never complained about it. You were always supportive of any decisions that I made. I am indebted to my parents for their unwavering support, love, and understanding. Your belief in me has been a constant source of motivation, and I am profoundly grateful for the sacrifices you have made to see me succeed.

I want to express my deepest gratitude to my supervisor, Prof. Jonathan Veinot, whose guidance, wisdom, and unwavering support have been invaluable throughout this journey. Your mentorship has shaped not only my research but also my growth as a scholar and an individual. Jon, your presence and unwavering faith in our abilities have created a unique and trusting mentor-student relationship. When I face any challenges, I do not hesitate to tell you my honest feeling, and we chat more like friends than a traditional mentor-student dynamic. Your keen ability to recognize my strengths, even when I may not see them, has been a constant source of encouragement. I am grateful for your generosity in supporting and guiding us, often encouraging us to step outside the confines of the lab for valuable learning experiences. Your positive "push" towards exploration has

proven immensely beneficial. Additionally, I deeply admire your rigorous approach to scientific inquiry, particularly your commitment to meticulous data analysis, which has significantly influenced my own perspectives in this regard.

A big thank to the previous and current group members, Dr. John Washington, Dr. Jonathan Hiltz, Dr. Nduka Ikpo, Dr. Haoyang Yu, Dr. Christopher Jay Robidillo, Dr. Alyxandra N. Thiessen, Dr. Sarah Milliken, Dr. Yingjie (Jay) He, Dr. I Teng (Emily) Cheong, Dr. Kevin M. O'Connor, Md Asjad Hossain, Riley Hooper, Ziqi (Amber) Li, Jonathan Trach, Leanne A. Milburn, Cole Butler, Cemre Mertoglu, Madison Chevalier, Brayden Glockzin, Abbie Rubletz, Mia Dolanjski, Suni Guo, Christina Zafeiridou, and many others. Thank you for your help through the most stressful times of my Ph.D. life, the 502 presentation and the candidacy.

I would like to thank the ATUMS family. First of all, Leah Veinot, you have been spent so much effort on us in the ATUMS program. I am so glad and honored to be a member of the ATUMS family, where all my research and collaborations started. This thesis would not exist without you! I also like to thank Dr. Sergei Vagin, Dr. Elisabeth Groß, Amelie Mühlbach and Kathrin Vosseler for the help when I was conducting research in Germany. I would like to thank Prof. Thomas Fässler, Prof. Tom Nilges, Prof. Rieger, and their teams, as well as my amazing friends in Germany for their great hospitality.

I have also recognized the generous continued support from my supervisory committee member, Prof. Arthur Mar, and faculty members in the Department of Chemistry, Prof. Jillian Buriak, Prof. Vladimir Michaelis, and Prof. Eric Rivard. I am also grateful to the useful instrumentation trainings and discussions from Peng Li, Dr. Shihong Xu, Dr. Anqiang He, Wayne Moffat, Jennifer Jones, Michael Ferguson, Randy Whittal, Dr.

Table of Contents

List of Tables

List of Figures

List of Symbols, Nomenclatures and Abbreviations

Abbreviation	Meaning
2D	Two-dimensional
a	Lattice parameter
ABF	Annular bright-field
AI	Artificial intelligence
AIBN	Azobisisobutyronitrile
AQE	Apparent quantum efficiency
BA	Benzyl alcohol
BAL	Benzaldehyde
BCC	Body-centered cubic
Bn	P-nitrobenzyl
C	Conversion
c_i	Mole fraction of component i
c_j	Mole fraction of component j
CTS	Carbothermal shock
DEED	Disordered enthalpy-entropy descriptor
DMF	Dimethylformamide
DNA	Deoxyribonucleic acid
DRA	Diffuse reflective absorption
EDX	Energy dispersive X-ray spectroscopy
E_{red}	Redox potential

F127	Poly(ethyleneglycol)-block-poly(propyleneglycol)-block-poly(ethylene glycol)
FBP	Fixed bed pyrolysis
FCC	Face-centered cubic
FFC-Cambridge	Fray-Farthing-Chen Cambridge
FFT	Fast Fourier transform
FMBP	Fast moving bed pyrolysis
FTIR	Fourier transform infrared spectroscopy
FWHM	Full-width-at-half-maximum
ΔG_{mix}	Change in Gibb's free energy of mixing
GeNP(s)	Germanium nanoparticle(s)
GeNS(s)	Germanium nanosheet(s)
KIT-6	Korea Advanced Institute of Science and Technology-6
ΔH_{mix}	Change in entropy of mixing
H_{ij}	Enthalpy of mixing between the ith and j^{th} components
HAADF	High-angle annular dark-field
HEA(s)	High-entropy alloy(s)
HEB(s)	High-entropy metal diboride(s)
HEC(s)	High-entropy carbide(s)
HEG(s)	High-entropy germanide(s)
HEM(s)	High-entropy material(s)
HEN(s)	High-entropy metal nitride(s)
HEO(s)	High-entropy oxide(s)

HEPF(s)	High-entropy perovskite fluoride(s)
HR	High resolution
HES(s)	High-entropy silicide(s)
H-SiQD(s)	Hydride-terminated Si quantum dot(s)
I	Number of incident photons
ICSD	Inorganic Crystal Structure Database
K	Degrees Kelvin
L-AA	L-ascorbic acid
LOD	Limit of detection
n	Number of moles
N	Number of molecules
M@GeNSs	Metal-decorated germanium nanosheets
MNP(s)	Metal nanoparticle(s)
Na/Naph	Sodium naphthalide
NS(s)	Nanosheet(s)
NP(s)	Nanoparticles
OER	Oxygen evolution reaction
OHEA-mNC	Ordered HEA NPs on a 2D nitrogen-rich mesoporous carbon
ORR	Oxygen reduction reaction
PEO_{10500}-b-$PMMA_{18000}$	Poly(ethylene oxide)-block-poly(methyl methacrylate) (The subscript numbers indicate the average molecular weight (g mol^{-1}) of the corresponding blocks)

R	Ideal gas constant
rGO	Reduced graphene oxide
S	Selectivity
ΔS_{mix}	Change in entropy associated with mixing
SAED	Selected area electron diffraction
SBA-15	Santa Barbara Amorphous-15
SE	Secondary electron
SEM	Scanning electron microscopy
SiNP(s)	Silicon nanoparticle(s)
SLS	Sodium lauryl sulphate
SMCR	Seed-mediated co-reduction
SPS	Spark plasma sintering
STEM	Scanning transmission electron microscopy
T	Temperature
TEM	Transmission electron microscopy
TF	Tannic acid/formaldehyde resin oligomers
TGA	Thermogravimetric analysis
THF	Tetrahydrofuran
UHTC	Ultra-high temperature ceramics
x	Mole fraction
XP	X-ray photoelectron
XPS	X-ray photoelectron spectroscopy
XRD	X-ray diffraction

Y   Yield

zT Figure of merit of thermoelectric materials

1. Chapter 1: Introduction

1.1 High-Entropy Alloys

Alloys, combination of multiple metals, have played a significant role in the development of human society throughout history, particularly since the Bronze Age.[1] The conventional practice for producing alloys involves introducing a secondary element (or elements) into a primary metal.[2] Recently, a class of alloys has emerged in which multiple principal elements are combined at high concentrations to produce what has come to be known as high-entropy alloys (HEAs). The concept of HEAs was initially introduced by Yeh *et al.*, who defined them as alloys comprising five or more metals, with each element constituting 5 to 35 atomic percent of the total composition (Figure 1.1).[3] Their study focused on FeNiZrM^i (M^i = $i \geq 2$ other metals) HEA ingots prepared via arc-melting and showed these materials exhibited high strength, thermal stability and excellent resistance to oxidation. In a previous work, Cantor *et al.* also reported the development of "multicomponent alloys" based on the FeCoNiCrMnM^i (M^i = $i \geq 0$ other metals) system (or Cantor alloy) that was prepared via induction heating and showed randomly mixed FCC structure.[4] Both sets of alloys exhibited high strength and ductility that the authors attributed to, in part, the high degree of entropic mixing resulting from the incorporation of multiple primary metals.[3, 4] Compared with the extensive study on the FCC HEA, there are only limited reports of BCC HEAs due to their brittleness and high melting points that lead to a inhomogeneous structure and composition.[5, 6] Senkov first synthesized a series of BCC alloys often referred to as refractory HEAs (i.e., VNbMoTaW, NbCrMo$_{0.5}$Ta$_{0.5}$TiZr and TiZrHfNbTa) by arc melting.[5-7] These alloys exhibit a high yield stress and tensile ductility at room temperature. Later, other BCC HEAs (e.g.,

TiZrNbMoV and TiVZrNbHf) have been studied as hydrogen storage material.[8, 9] These alloys could be hydrogenated with a H/M ratio of at least 2.5 in a body centered tetragonal hydride phase.
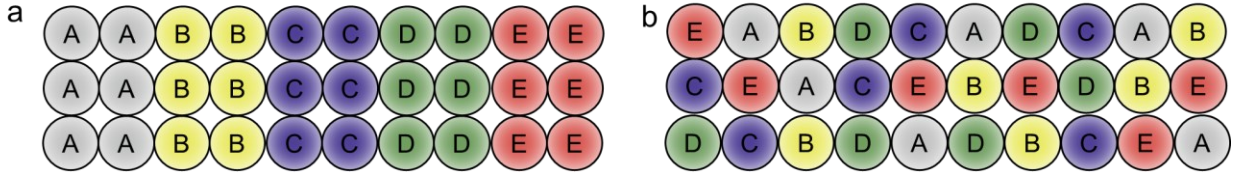
Figure 1.1. (a) Five components in equimolar ratios before mixing and (b) after mixing to form a random solid solution. (For convenience all atoms are presented as being the same size).

The term "high-entropy" suggests the energetic considerations underlying the formation of HEAs. The free energy of mixing in a substitutional alloy can be represented as follows:

$$\Delta G_{mix} = \Delta H_{mix} - T\Delta S_{mix} \qquad (1.1)$$

Where:

$$\Delta H_{mix} = -R \sum_{i}^{n} \sum_{j>1}^{n} 4H_{ij}c_i c_j \qquad (1.2)$$

and,

$$\Delta S_{mix} = -R \sum_{i=1}^{n} c_i \ln c_i \qquad (1.3)$$

where ΔG_{mix} is the change in Gibbs free energy of mixing, ΔH_{mix} is the change in enthalpy of mixing, T is temperature in Kelvin, ΔS_{mix} is the change in entropy of mixing, R is the ideal gas constant, H_{ij} is the enthalpy of mixing between the ith and j^{th} components, c_i and c_j are the mole fractions of the ith and j^{th} components, respectively.[10]
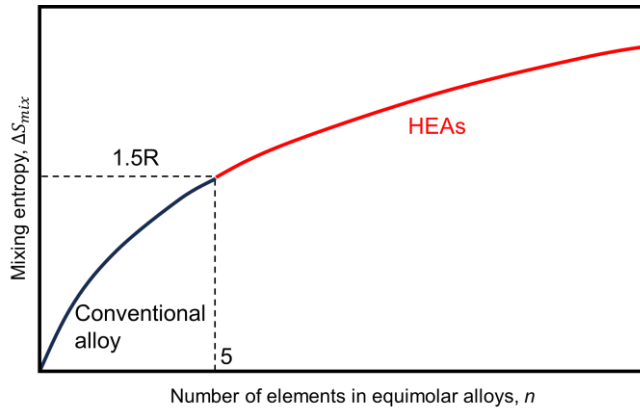
Figure 1.2. Entropy of mixing as a function of the number of elements for equimolar alloys in the random solution state.

The stabilities of HEAs are predominantly influenced by the entropy of mixing, which increases significantly with the number of components. This can be attributed to the logarithmic rise shown in Equation 1.3 coupled with the rapid decrease in enthalpy depicted in Equation 1.2. The crucial role played by entropy of mixing in determining the overall free energy of mixing is illustrated in Figure 1.2.[10]

Bulk HEAs exhibit attractive characteristics such as strength and ductility compared to conventional alloys. The Cantor alloy stands out among HEAs as it exhibits exceptional fracture toughness, excellent ductility, and high strength.[4, 5] Of late, making HEAs at the nanoscale has garnered attention and offers the promise of material properties that could exceed their bulk counterpart.[11, 12] Prior to 2018, most studies of multimetallic nanoparticles prepared via wet-chemistry reported limit element compositions (less than four elements) or phase separation within the particles (more than four elements). Synthesis methods that provide HEA NPs with controllable element composition, particle size and phase are required to facilitate the study of their inherent properties and explore their diverse applications.[13]

1.1.1 High-Entropy Alloy Nanoparticles

The development of synthesis methods that provide HEA NPs began with the emergence of carbothermal shock technique (CTS) in 2018.[14] Later, other methods were reported that afford HEA NPs including fast-moving bed pyrolysis,[15] vapor phase spark discharge,[16] rapid radiative heating or annealing,[17] low-temperature hydrogen spillover,[18] and microwave heating.[19] We will discuss each of these methods in following sections.

Carbothermal Shock. Yao and colleagues made a significant breakthrough by implementing a carbothermal shock (CTS) technique to prepare a diverse array of quinary to octonary HEAs (e.g., PtCoNiFeCu, PtPdCoNiFe, PtCoNiFeCuAu, PtPdCoNiFeCuAu and PtPdCoNiFeCuAuSn) as monodisperse nanoparticles (NPs) with diameters ranging from 5 to 25 nm (size distribution < 5%), supported on carbon microfibers (Figure 1.3).[14] This methodology first involves mixing of metal precursors onto a conductive carbon support, followed by subsequent rapid heating and cooling cycling. A controllable synthesis of HEA NPs with different particle sizes can be achieved by changing the peak temperature and shock duration time. One resulting quinary PtPdRhRuCe HEA NPs showed catalytic activity in ammonia oxidation at a comparatively low reaction temperature (i.e., 973 K) with 100% conversion and >99% product selectivity toward nitrogen oxide (i.e., NO) under continuous operation. This catalytic reactivity and stability contrasts what is observed for widely employed Pt-Rh or Pt-Rh-Pd alloys that require higher temperatures (i.e., 1073-1273 K) to achieve high yields of nitrogen oxide and tend to degrade under continuous operation.[20] Although a special external power source (a temporal resolution down to 1 ms and a current source up to 3.15 A) is required, the CTS technique achieved a tailorable synthesis of HEA

NPs with diverse element composition, well controlled particle size and monodisperse size distribution.
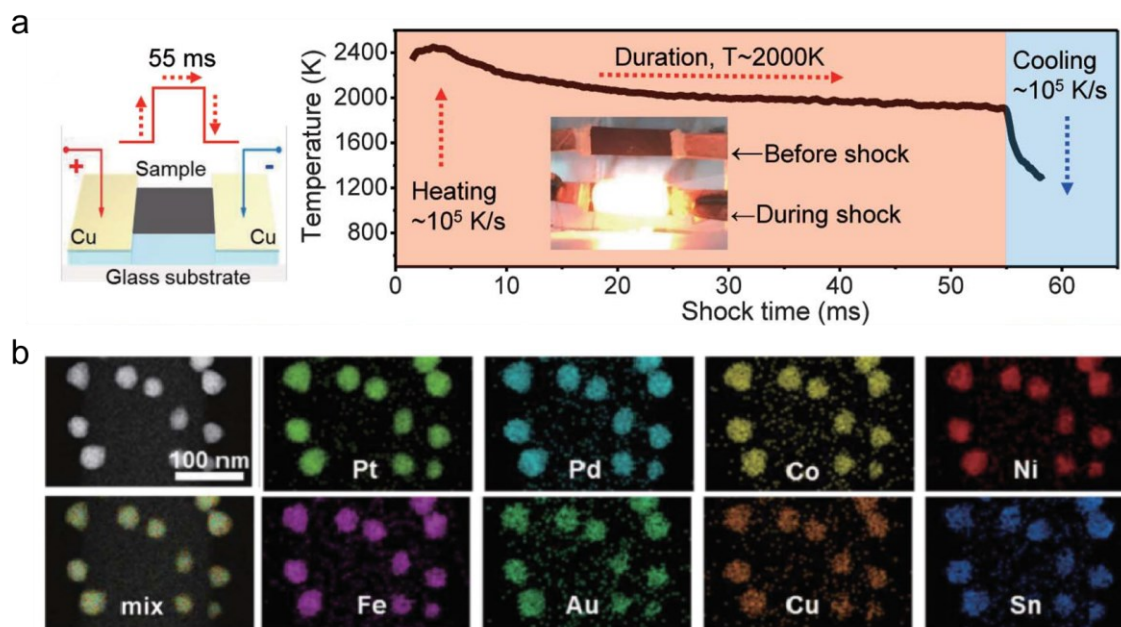
Figure 1.3. (a) A pictorial illustration of the carbothermal shock and the temperature profile during the 55-ms thermal shock. (b) HAADF-STEM image and EDX mappings of PtPdCoNiFeCuAuSn HEA NPs. Reprinted with permission from ref 14. Copyright 2018 American Association for the Advancement of Science.

Fast Moving Bed Pyrolysis. Gao and collaborators developed fast moving bed pyrolysis (FMBP) as a method to access various monodisperse quinary to octonary HEA NPs (e.g., CuSnPdPtAu, FeCoPdIrPt, CuCoNiSnPtPdAu, CuCoNiSnIrPtPdAu, MnCoNiCuRhPdSnIrPtAu) on granular supports with diameters from 2 to 50 nm (Figure 1.4).[15] Typically, the metal precursor-loaded support (e.g., graphene oxide, carbon black, zeolites, Al_2O_3) was evenly placed in a quartz boat, which was placed in a region outside of the furnace. The furnace was heated to 923 K and the quartz boat was then pushed into the center of the hot zone. After annealing for 2 h at 923 K, the quartz boat was pushed out and cooled rapidly to room temperature. Larger HEA NPs can be obtained by increasing the annealing time and temperature. The FMBP strategy ensures rapid and

simultaneous pyrolysis of mixed metal precursors and leads to the formation of nuclei with reduced size.[15] While a specialized furnace is needed, the FMBP method yields a variety of HEA NPs with controlled size and narrow size distribution on diverse supports.
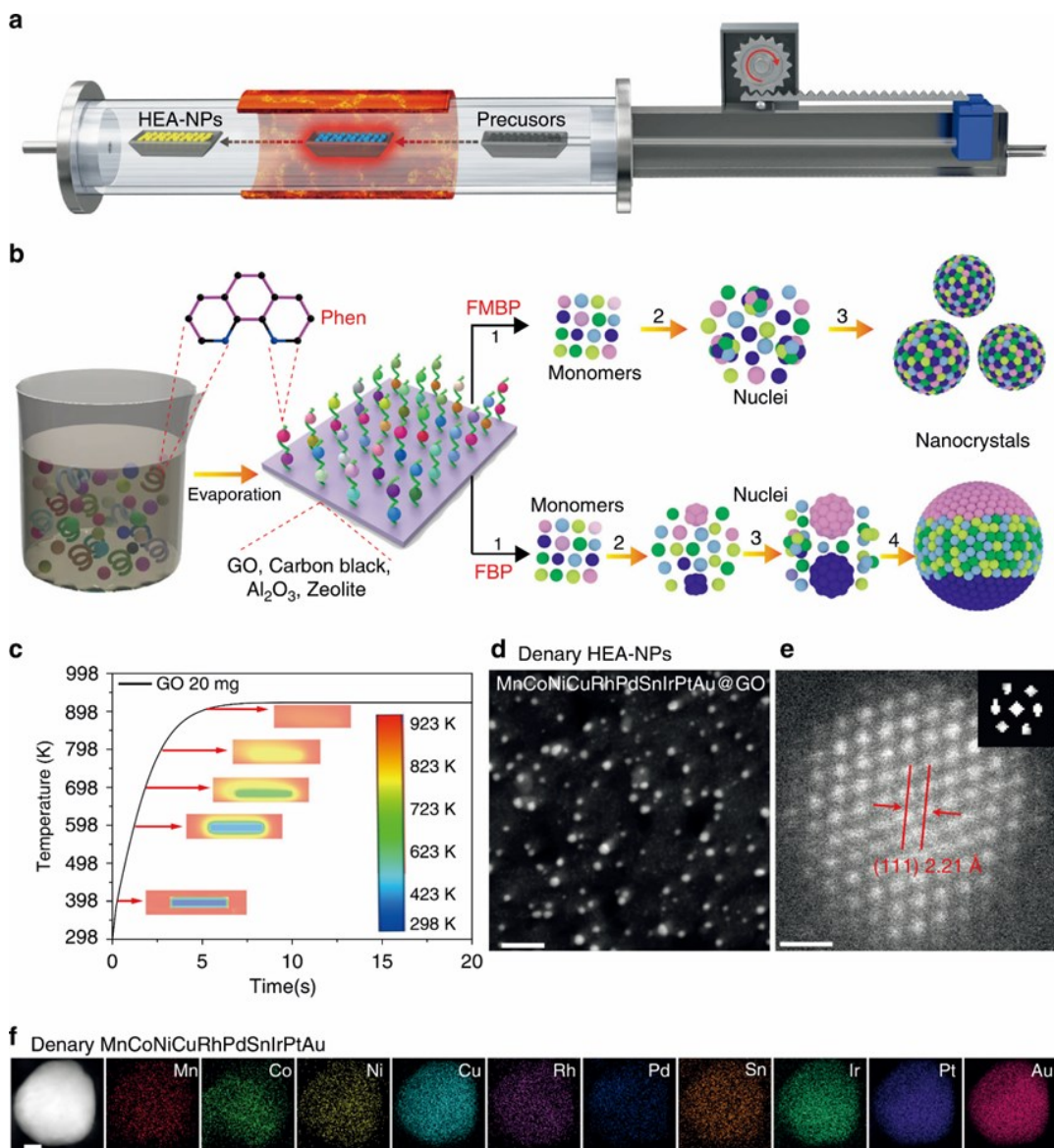
Figure 1.4. (a) A pictorial illustration of the FMBP experiment. (b) A pictorial representation for the synthesis of homogeneous and phase-separated HEA NPs by FMBP and FBP strategies, respectively. (c) The temperature profile in the FMBP process. (d) HAADF-STEM images for the MnCoNiCuRhPdSnIrPtAu HEA NPs. (e) HR-STEM image for the MnCoNiCuRhPdSnIrPtAu HEA NPs with the FFT analysis indicating an FCC structure. (f) EDX mappings for MnCoNiCuRhPdSnIrPtAu HEA NPs. Scale bar d: 10 nm, e: 0.5 nm, and f: 10 nm. Reprinted with permission from ref 15. Copyright 2020 Springer Nature.

Vapor Phase Spark Discharge. Feng and coworkers utilized a vapor-source (i.e., vapor phase spark discharge) that provided an unrestricted mixing environment for manufacturing quinary and senary HEA NPs (e.g., NiCrCoCuPd, NiCrCoAuAg, NiCrCoMoAuAg, NiCrCoMoCuPd) with diameters of approximately 5 nm. In a typical synthesis, five or more constituent materials are vaporized by an oscillatory spark, followed by ballistic transport and intermixing to form HEA NPs (Figure 1.5A).[16] The sparking mashup can facilitate the deposition of the resulting HEA NPs into a certain form and shape at the highest nanoscale resolution to achieve 3D-printed nanostructure (Figure 1.5b).[16] Though the technique can be used in the additive manufacturing of 3D nanostructural arrays, the method requires a special instrument and lacks a broad applicability across other elements and control in the size.
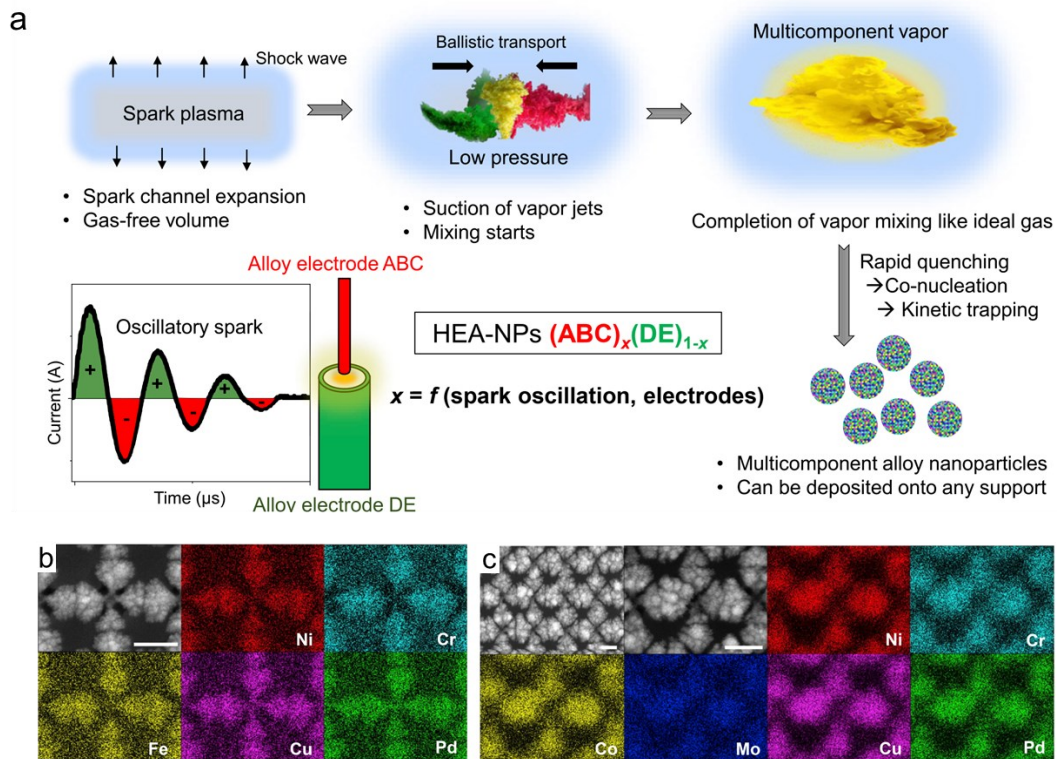
Figure 1.5. (a) Mechanism of the spark mixing. (b-c) SEM images and EDX mappings of 3D-printed HEA NPs (NiCrFeCuPd and NiCrCoMoCuPd). Reprinted with permission from ref 16. Crown Copyright 2020 published Elsevier B.V.

Aerosol Droplet Mediated Synthesis. Yang and colleagues devised an aerosol droplet mediated approach that afforded scalable synthesis of FeCoNiCuPt, FeCoNiPdPt, and FeCoNiCuPd HEA NPs with atomic-level mixing of immiscible metal elements.[17] This procedure involved an aqueous precursor solution containing five types of metal salts in equimolar ratios being nebulized to create aerosol droplets. The nebulized aerosol droplets, transported by 10% H_2/90% Ar reducing gas mixture, were first passed through a silica dryer for water solvent removal. The resulting dried aerosol particles traveled through a high-temperature reaction zone (1100 °C). In this zone, a rapid temperature increase, induced by thermal shock, triggered the thermal decomposition and hydrogen reduction of the metal ions, ultimately leading to the formation of HEA nanoparticles with a diameter of 60 nm. (Figure 1.6).[17] This method demonstrates a scalable synthesis of HEA NPs but lacks control over elemental composition and size distribution.
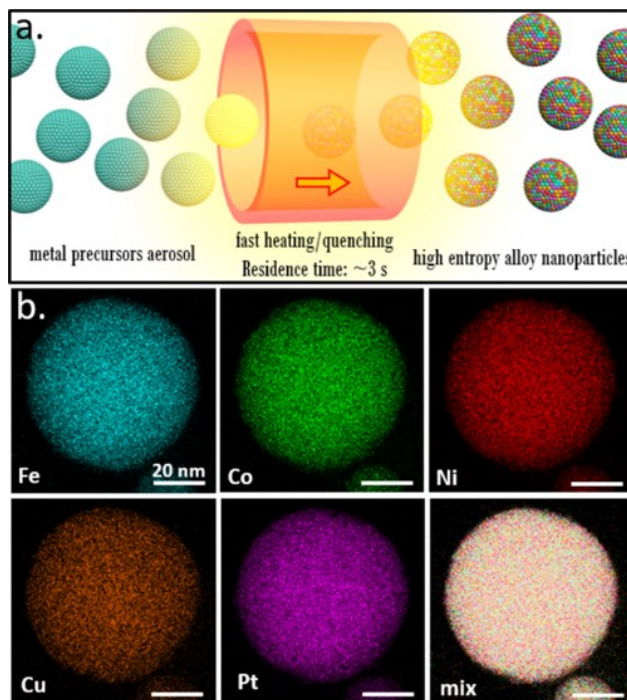
Figure 1.6. Scalable synthesis of HEA NPs by aerosol droplet-mediated technique: (a) A pictorial illustration of the synthesis and (b) EDX mappings for a single HEA NP. Reprinted with permission from ref 17. Copyright 2020 American Chemical Society.

Low Temperature H₂ spill over on TiO₂. In contrast to previously mentioned high-temperature synthesis methods that yield HEA NPs, Mori *et al.* introduced a comparatively low-temperature synthesis (400 °C) of CoNiCuRuPd HEA NPs on TiO_2.[18] This process (Figure 1.7) is driven by a pronounced hydrogen spillover effect on TiO_2 coupled with concurrent proton/electron transfer mechanisms. In the presence of a H_2 atmosphere, Pd^{2+} precursors are first partially reduced to generate nuclei. Dissociative adsorption of H_2 on the surfaces of these Pd nuclei forms Pd−H species (Step 1). The reduction of Ti^{4+} to Ti^{3+} occurs concurrently with the transfer of H atoms from Pd nuclei at the metal-support interfaces (Step 2). The migration of electrons from Ti^{3+} ions to adjacent Ti^{4+} ions facilitate the transfer of protons to O^{2-} anions attached to these neighboring Ti^{4+} ions (Step 3). The rapid movement of hydrogen atoms across the TiO_2 surface is essential to reach all metal ions (Step 4). Finally, these ions are collectively reduced to form the HEA NPs, with Ti^{4+} being regenerated in the process (Step 5).[14] Specifically, CoNiCuRuPd HEA NPs on TiO_2 exhibited high activity and exceptional stability during the CO_2 hydrogenation reaction.[18] The author presented a relatively low-temperature synthesis of HEA NPs and the formation mechanism behind the process but the choice of the metal elements is limited to the noble metal due to the hydrogen spillover effect.
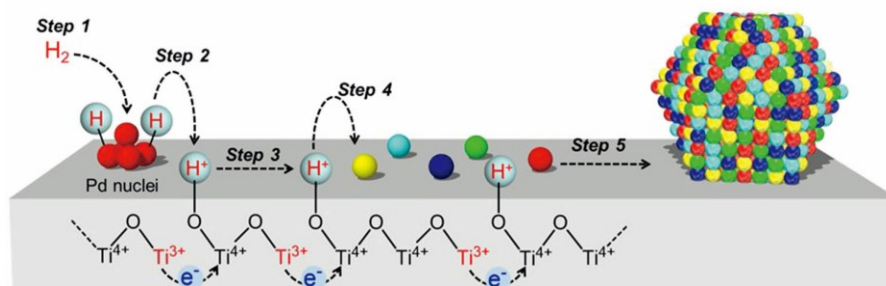
Figure 1.7. Schematic illustration of the formation mechanism of HEA NPs on a TiO_2 support assisted by hydrogen spillover. Reprinted with permission from ref 18. Copyright 2021 Springer Nature.

Microwave Heating. Microwave heating has proven to be a highly effective method and has been extensively employed in the synthesis of various nanomaterials.[21-23] Qiao *et al.* demonstrated that microwave heating can afford rapid and facile synthesis of PtPdFeCoNi HEA NPs (12.8 ± 5.1 nm).[19] Under argon, a reduced graphene oxide (rGO) film loaded with metal salt precursors acts as a microwave because of the dipoles of the surface functional group defects. The induced localized heating (1850 K) at the defects distributes throughout the entire sample leading to uniform heating of the metal salt precursors. Consequently, these precursors decompose into liquid metals, simultaneously oxidizing the rGO to a highly oxidation state. The highly reduced rGO preferentially reflects, rather than absorb, microwaves leading to a spontaneous cessation of the heating. The resulting abrupt quenching of the rGO, following its reduction at high temperatures,[24] facilitates the direct solidification of the liquid metal into PtPdFeCoNi HEA NPs. (Figure 1.8).[19] The microwave heating method achieves a rapid and facile synthetic route to HEA NPs. However, it is only a proof-of-concept demonstration and fails to show its applicability to other elements.
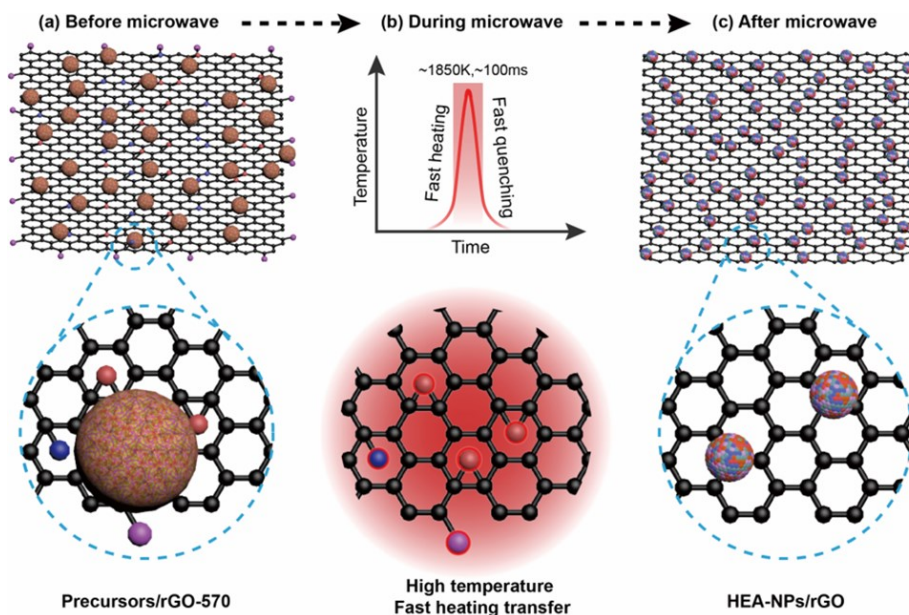
Figure 1.8. A pictorial illustration of the formation of HEA NPs on rGO by microwave heating. Reprinted with permission from ref 19. Copyright 2021 American Chemical Society.

Solvothermal Colloidal Synthesis. The Iversen group aimed to address the limitations imposed by specialized and costly infrastructure and focused on the application of colloidal synthesis methods to prepared HEA NPs.[25] Their general approach involved combining metal salts in a suitable solvent mixture (e.g., acetone-ethanol) and then transferred to Teflon lined steel autoclave, which was sealed and placed in an oven preheated to 200 °C. Despite the success in composition control, the method did not provide the desired level of structural uniformity, and illustrates the ongoing challenges in developing colloidal synthesis techniques for HEA NPs (Figure 1.9).[25]
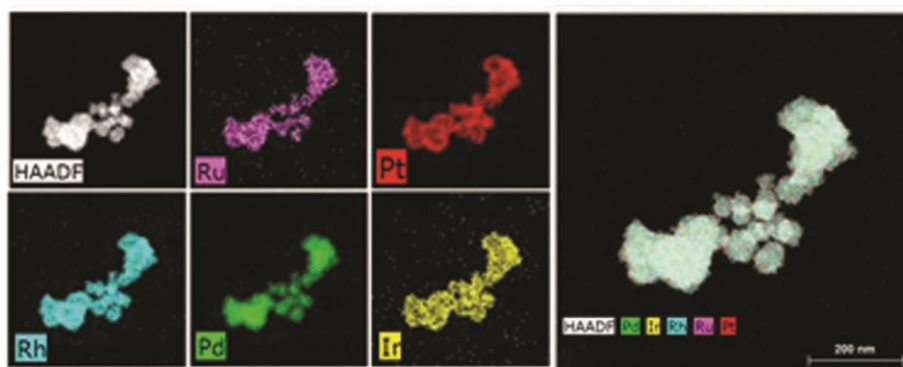
Figure 1.9. STEM-EDX for $Pt_{0.20}Pd_{0.20}Ir_{0.20}Rh_{0.20}Ru_{0.20}$. Reprinted with permission from ref 25. Copyright 2019 Wiley-VCH Verlag GmbH & Co.

Subsequent to the pioneering work of Iverson *et al.*, numerous "wet chemical" methods for HEA NP syntheses have been reported. Wu *et al.* successfully synthesized HEA NP incorporating all six platinum-group metals (i.e., Ru, Rh, Pd, Os, Ir, Pt) for the first-time using solution method.[26] The procedure involved introducing an equimolar aqueous solution of six metal precursors into a preheated triethylene glycol solution with poly(*N*-vinyl-2-pyrrolidone) as a capping agent at 230 ˚C. This method resulted in a single-phase face-centered cubic (FCC) structure of HEA NPs with a homogenous composition and a narrow size distribution (3.1 ± 0.6 nm, Figure 1.10).[26] The HEA NPs shows record-high activity for the ethanol oxidation reaction and stable for over 50 cycles.

However, the synthesis involves only noble metals and provide no transferable applicability to other metal elements such as earth-abundant metals.
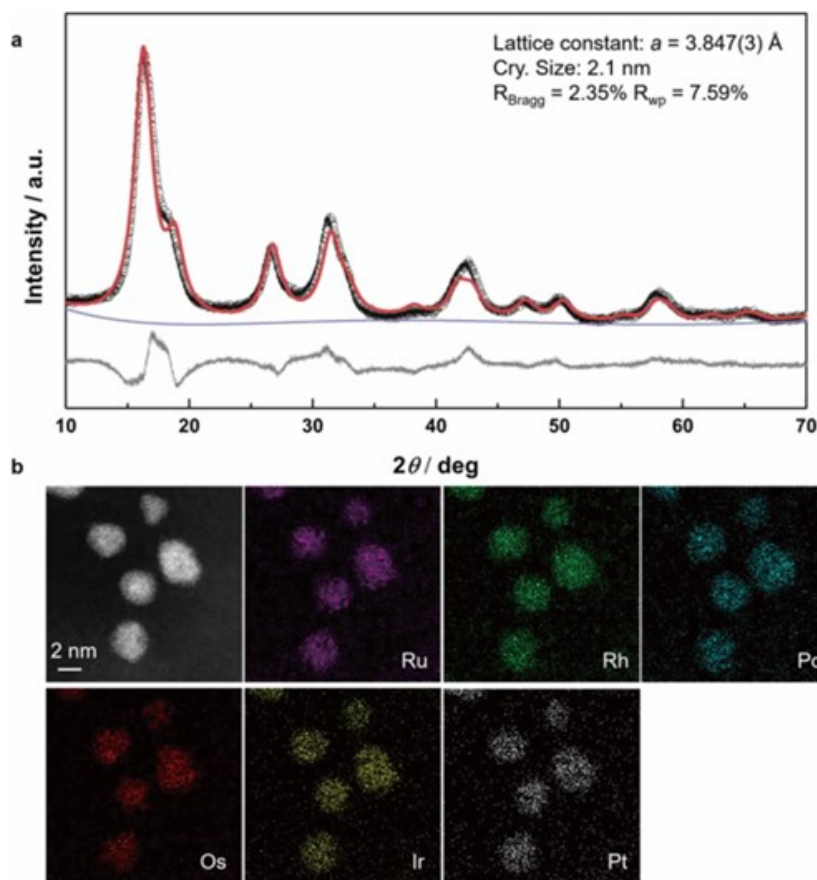
Figure 1.10. (a) Synchrotron XRD pattern of HEA NPs with Rietveld refinement. Wavelength: λ = 0.62938(6) Å. (b) HAADF-STEM image and EDX mappings of HEA NPs. Reprinted with permission from ref 26. Copyright 2020 American Chemical Society.

The Skrabalak group has introduced an alternative solution-based method to synthesize HEA NPs that begins with the initial colloidal synthesis core@shell NPs consisting of five metals (PdCu@PtNiCo).[27] Subsequent annealing of these precursor particles provided monodisperse PdCuPtNiCo HEA NPs with diameters of 10.6 ± 0.2 nm (Figure 1.11).[27] The PdCuPtNiCo HEA NPs showed high catalytic performance and stability in the oxygen reduction reaction (ORR) in alkaline media, where the enhanced ORR activity can be attributed to the highly dispersed Pt/Pd content in HEAs.[27]
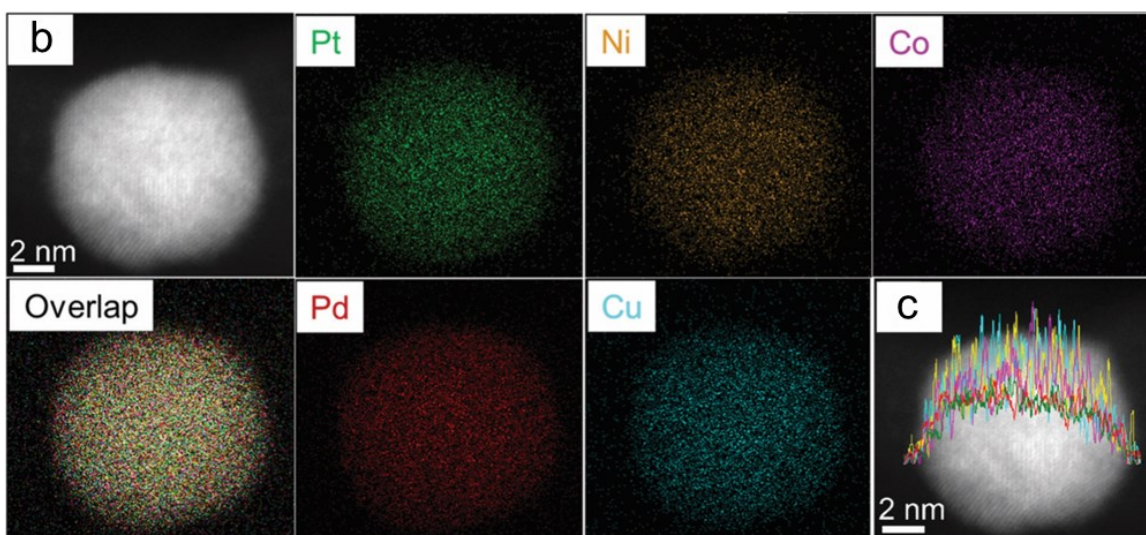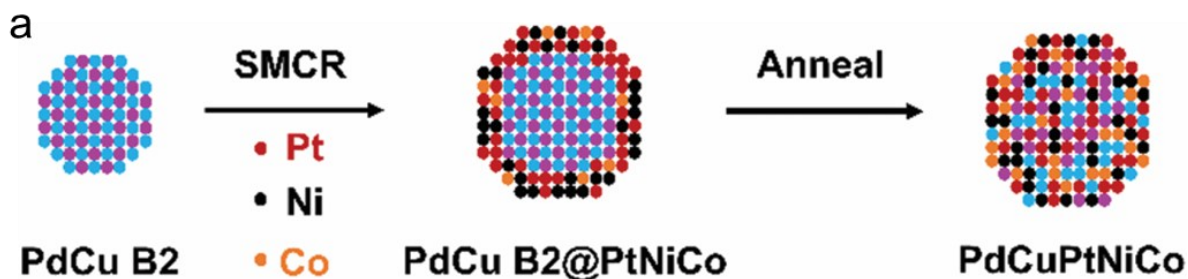
Figure 1.11. (a) Synthetic process of PdCuPtNiCo HEA NPs (b) HAADF-STEM image and EDX mappings of PdCuPtNiCo HEA NPs (c) Line scan profile of the PdCuPtNiCo HEA NPs. Reprinted with permission from ref 27. Copyright 2021 Royal Society of Chemistry.

Using this general approach, the Skrabalak group successfully synthesized five different quinary alloy phases (i.e., PdCuPtNiCo, PdCuPtNiIr, PdCuPtNiRh, PdCuPtNiFe, and PdCuPtNiRu), as well as senary (PdCuPtNiCoRh) and septenary (PdCuPtNiCoRhRu and PdCuPtNiCoRhIr) phases (Figure 1.12).[28] This modular and versatile methodology enables the retrosynthetic design of precursor core@shell NPs with the stoichiometry of the HEA NPs determined by the compositions and relative volumes of the core and shell.[28] The principles for selecting which metals are incorporated into the core versus the shell regions of the nanoparticles are crucial in extending this methodology beyond the prototype system.

13
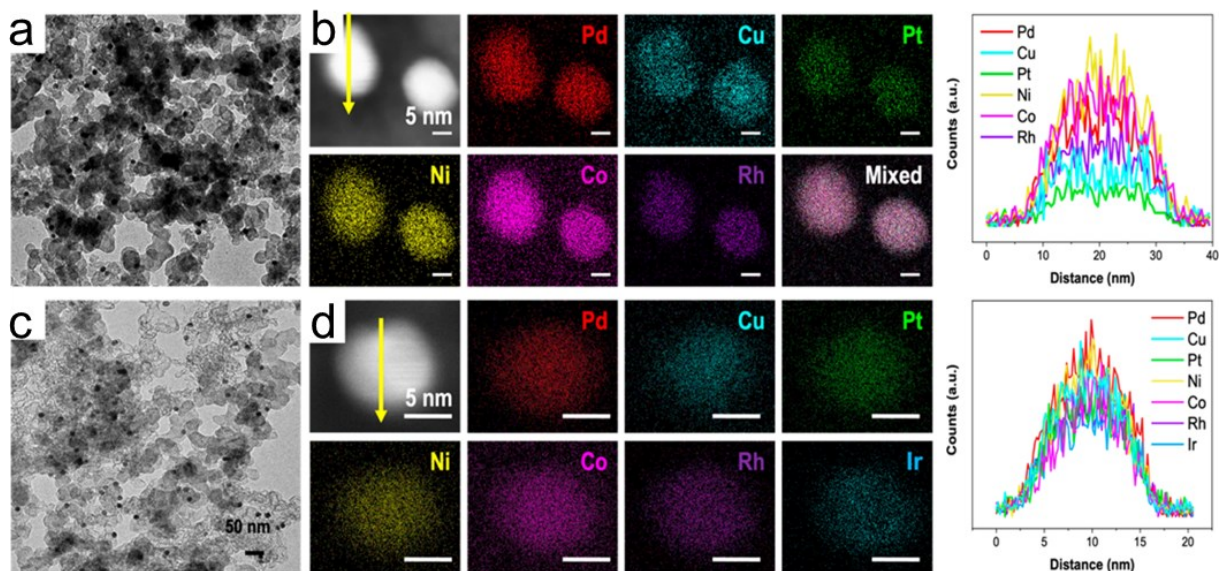
Figure 1.12. (a) TEM, (b) HAADF-STEM image, EDX mappings and line scan analysis of senary PdCuPtNiCoRh HEA NPs. (c) TEM, (d) HAADF-STEM image, EDX mappings and line scan analysis of septenary PdCuPtNiCoRhIr HEA NPs. Yellow arrow in (b) and (d) indicates the directions of line scans. Reprinted with permission from ref 28. Copyright 2022 American Chemistry Society.

Retrosynthetic design principles for synthesizing monodisperse HEA NPs were established while considering the relative redox potential (E_{red}) of the metal or metal precursors used in SMCR.[29] This property is important as galvanic replacement may occur when metal precursors with high E_{red} replace metals with low E_{red} in the seeds.[30] Design principles include: (1) metal precursors with a high E_{red} relative to other metals should be incorporated into the core of the core@shell NPs, (2) metal precursors with a substantially lower E_{red} relative to the other metals should be in the shell, (3) metals that hinder alloy phase formation or possess poor wettability should be in the core.[29] These principles provide a systematic framework for selecting the arrangement of metals in core@shell NPs during the SMCR process. The subsequent annealing process demonstrates the broad applicability of these principles across various HEA NPs (e.g. AuCuPtPdNi, PdSnPtNiCu, PdAgPtNiCu and PdCuPtNiCo) (Figure 1.13).[29] This specific method

14

and the associated studies reached beyond what had been previously reported by providing design principles that allow its generalization across materials.
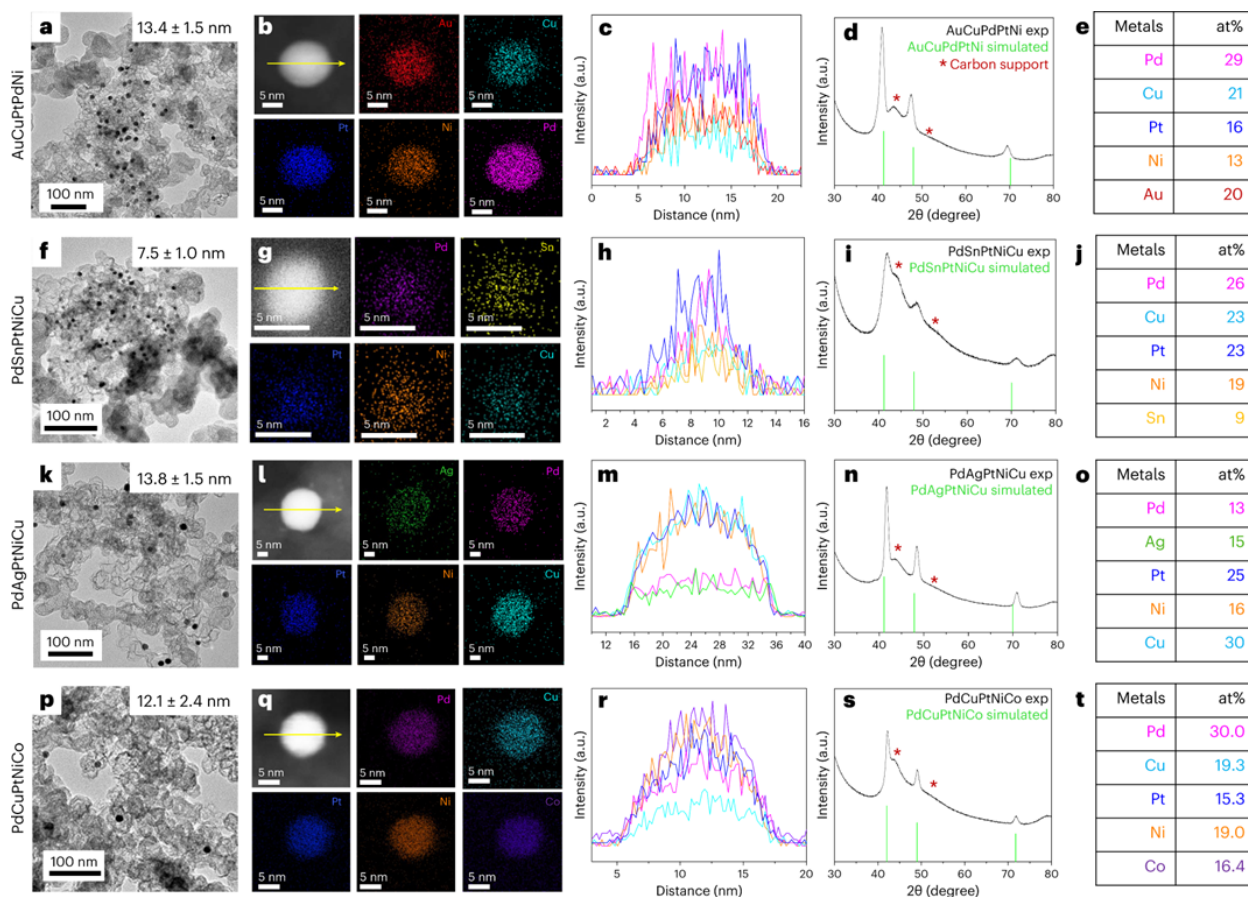
Figure 1.13. (a, f, k and p) TEM images, (b, g, l and q) HAADF-STEM images, EDX mappings, (c, h, m and r) line scan analysis according to yellow lines in HAADF-STEM image, (d, i, n and s) experiment and simulated XRD pattern and (e, j, o and t) table showing the atomic percentages from XPS of the (a–e) AuCuPtPdNi, (f–j) PdSnPtNiCu, (k–o) PdAgPtNiCu and (p–t) PdCuPtNiCo. Red asterisks show the pattern from the carbon support. Reprinted with permission from ref 29. Copyright 2023 Springer Nature.

Porous Metallic HEAs. Porous metallic materials with high surface areas, tunable pore structures, and efficient mass/electron transportation processes constitute an important class of nanomaterials.[31] Classic mesoporous metallic alloys prepared through wet-chemical reduction methods predominantly comprise two or three metal elements.[31] Expanding the metal elements to five or more in mesoporous NPs presents a significant challenge presumably because of the diverse

15

physicochemical properties and differences in E_{red} of the metal.[32] The Faustini group introduced a straightforward route to synthesize ordered macro- and mesoporous PtPdRuRdIr HEA NPs with uniform pore size and high surface area that relies on spray-drying aqueous solutions comprising five different noble metal precursors onto polymer latex beads.[33] During annealing at 350 °C, the polymer facilitates the formation of HEA NPs-based porous networks by serving a dual role as both a templating and reducing agent (Figure 1.14).[33] The resultant porous HEA NPs exhibited notable thermal stability and catalytic activity toward CO oxidation. *In situ* TEM heating investigations revealed the HEA NP porous structure remained stable up to 800°C.[33] Despite these impressive advancements, reports involving the synthesis of mesoporous HEA NPs under comparatively mild conditions, such as wet-chemical reduction in the solution phase, remain rare.
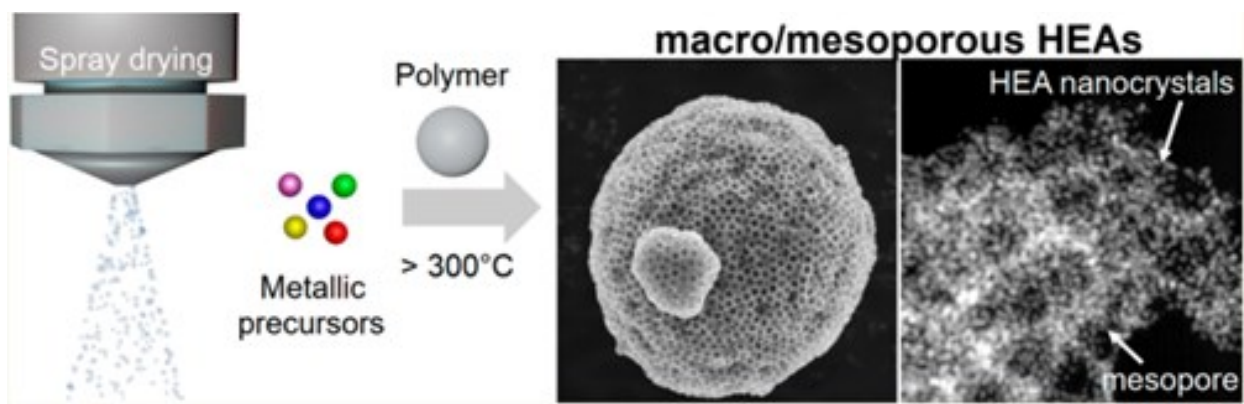
Figure 1.14. A pictorial representation of the fabrication process of porous HEA-based particles by aerosol synthesis followed by thermal annealing. SEM and HAADF-STEM images show the mesoporous morphology of the HEA NPs. Reprinted with permission from ref 33. Copyright 2022 American Chemistry Society.

An alternative approach reported by the Yamauchi group used one-pot wet-chemical reduction to synthesize mesoporous PtPdRhRuCu HEA NPs using a deblock polymer as the soft template.[34] Poly(ethylene oxide)-b-poly(methyl methacrylate) (PEO$_{10500}$-b-PMMA$_{18000}$) micelles and *L*-ascorbic acid (L-AA) were used as the pore-directing and reducing agents, respectively. The reaction solution was maintained at 80 °C for 4 h in an oil bath after which, PtPdRhRuCu HEA

NPs were collected by centrifugation. The resultant PtPdRhRuCu HEA NPs exhibit well-distributed large exposed mesopores (d = 23 nm), with tunable pore sizes (Figure 1.15).[34] However, the HEA exhibited a core@shell structure with a Pd-rich core and Rh/Ru-rich shell due to the different reduction properties of each metal element during the chemical reduction process.
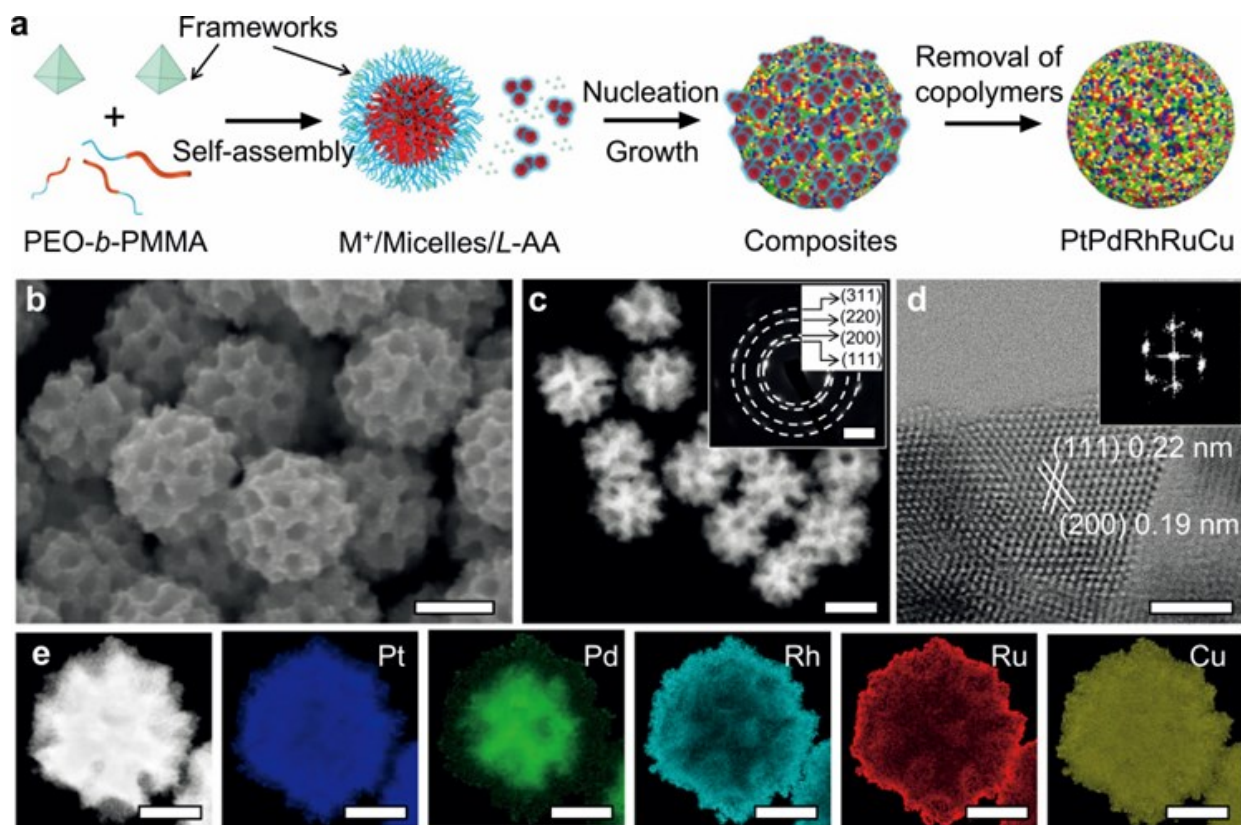
Figure 1.15. (a) A pictorial illustration of the synthesis of PtPdRhRuCu. (b) SEM, (c) HAADF–STEM with the corresponding SAED pattern (scale bar: 5 nm^{-1}), (d) HRTEM with FFT pattern, (e) EDX mapping images. Scale bar was (b) 100 nm, (c) 100 nm, (d) 2 nm and (e) 50 nm, respectively. Reprinted with permission from ref 34. Copyright 2023 Springer Nature.

To date, a variety of substrates have exhibited promise as supports for HEA NPs, as indicated in enhanced stability and catalytic performance.[35-37] For example, Rekha *et al.* reported a two-step synthesis of HEA NPs decorated graphene.[35] First, high-purity graphite powder was mechanically milled with metal powders (Ni, Cr, Co, Cu, Fe) to produce multimetal-graphite composite. Sonication of this composite with sodium lauryl sulphate (SLS) for 2 hours gave a

dispersion of graphene decorated with NiCrCoCuFe HEA NPs with a large distribution in nanoparticle sizes (Figure 1.16).[35] The HEA NPs-graphene composite can be further spray painted over surfaces and exhibited high corrosion resistance performance.
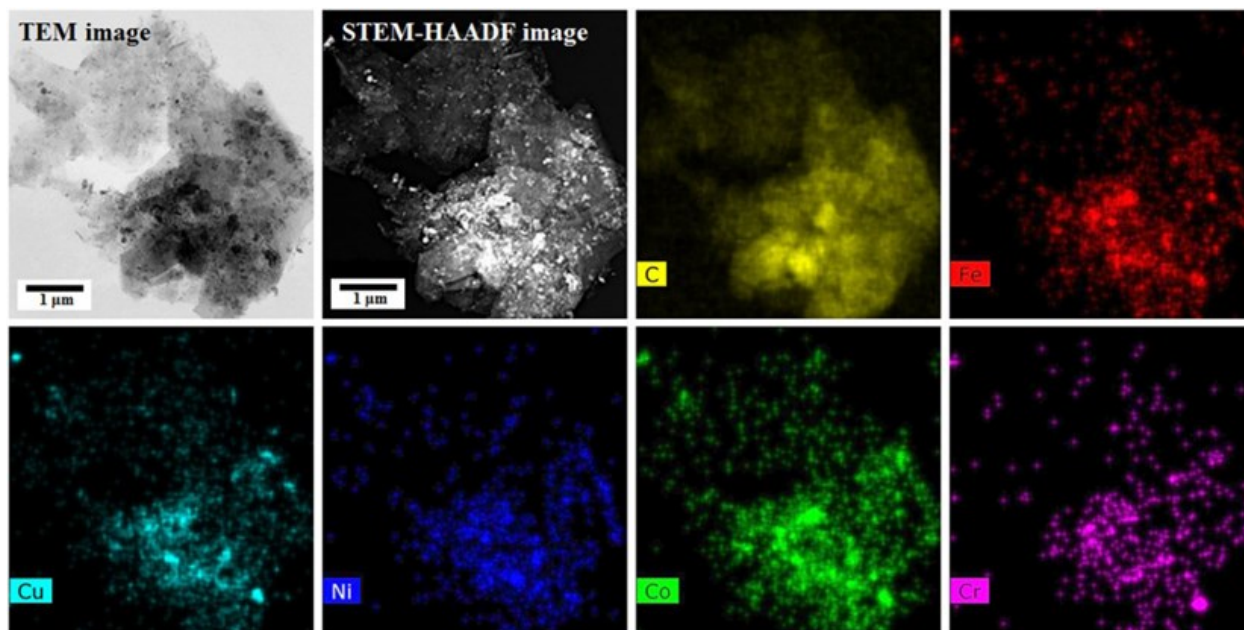
Figure 1.16. Representative TEM, HAADF-STEM image and EDX mappings of NiCrCoCuFe NPs on a graphene sheet. Reprinted with permission from ref 35. Copyright 2018 Springer Nature.

Urs and coworkers also presented a two-step approach but for the fabrication of exfoliated and decorated MoS_2 flakes with single-phase AgAuCuPdPt HEA NPs.[36] The synthesis of the AgAuCuPdPt HEA NPs involved arc melting and casting, followed by cryomilling. The MoS_2 powder was independently subjected to cryomilling for a duration of 7 hours. The cryomilled MoS_2 powder was sonicated with AgAuCuPdPt HEA NPs in a water/dimethylformamide (DMF) solution for a period of 30 hours in order to facilitate the decoration with HEA NPs (Figure 1.17). The resulting nanoscale junction formed between HEA and MoS_2 exhibited a tenfold increase in the response towards hydrogen gas (5000 ppm) at 80 °C.[36]
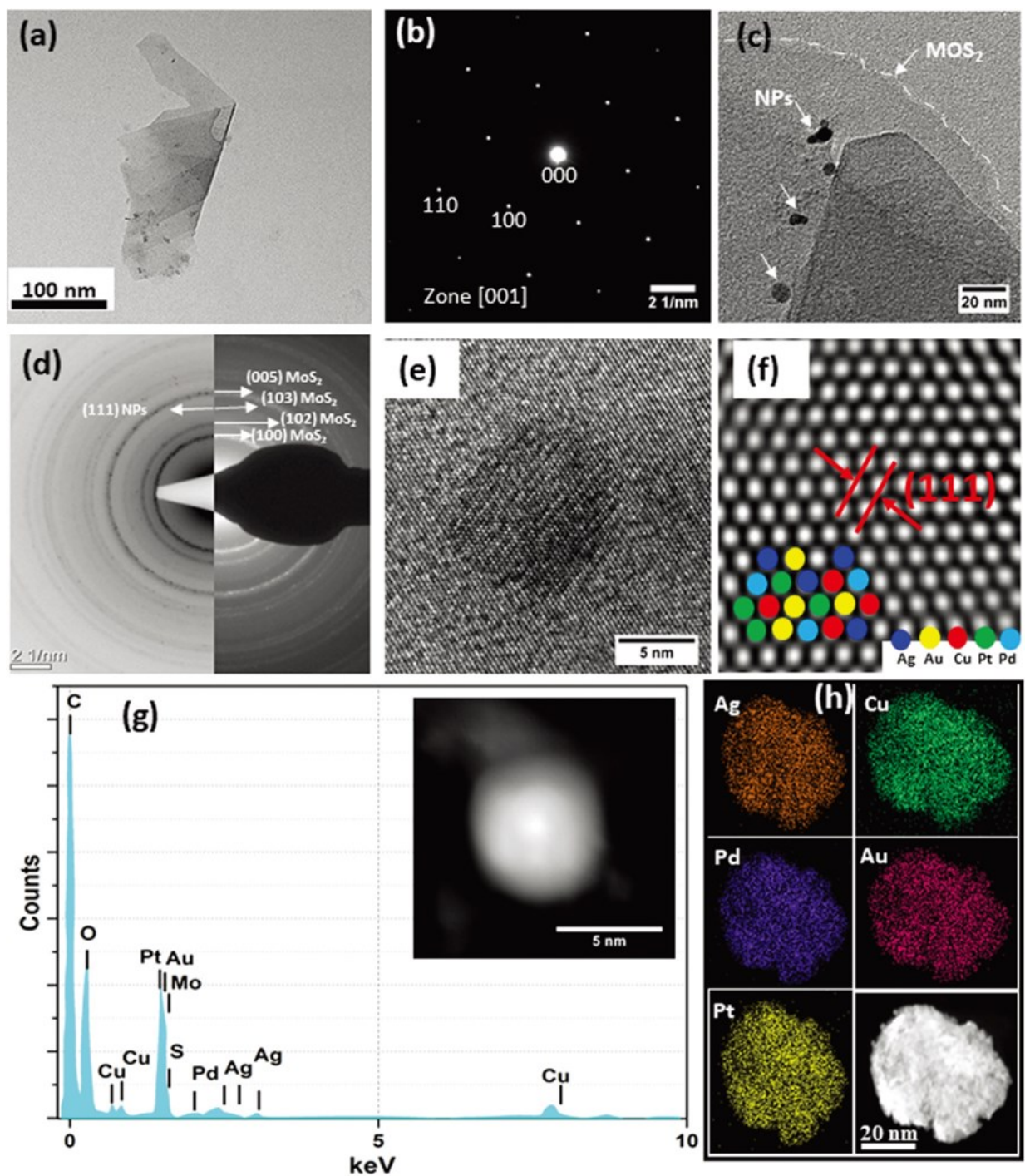
Figure 1.17. (a) TEM image and (b) SAED pattern of a MoS$_2$ nanosheet (c) TEM image of HEA NPs decorated MoS$_2$ nanosheet; (d) the corresponding SAED pattern. (e) HRTEM image of AuAgCuPdPt NPs on the MoS$_2$ sheet; (f) FFT filtered HRTEM image of AuAgCuPdPt NPs. (g) EDX spectrum and HAADF-STEM image of a single nanoparticle. (h) EDX mapping of AuAgCuPdPt NPs. Reprinted with permission from ref 36. Copyright 2020 Royal Society of Chemistry.

19

Zhu *et al.* constructed structurally ordered HEA NPs on a 2D nitrogen-rich mesoporous carbon sandwich framework (OHEA-mNC) by employing ligand-assisted interfacial assembly coupled with NH_3 annealing (Figure 1.18).[37] The OHEA-mNC NPs show significantly enhanced catalytic performance. This includes a large half-wave potential (0.90 eV) and a high durability (0.01 V decay after 10000 cycles); surpassing the performance of disordered HEA and commercial Pt/C catalysts. This remarkable performance is attributed to an improved mass transfer rate and enhanced electron conductivity due to the presence of stable chemically ordered HEA phase.[37]
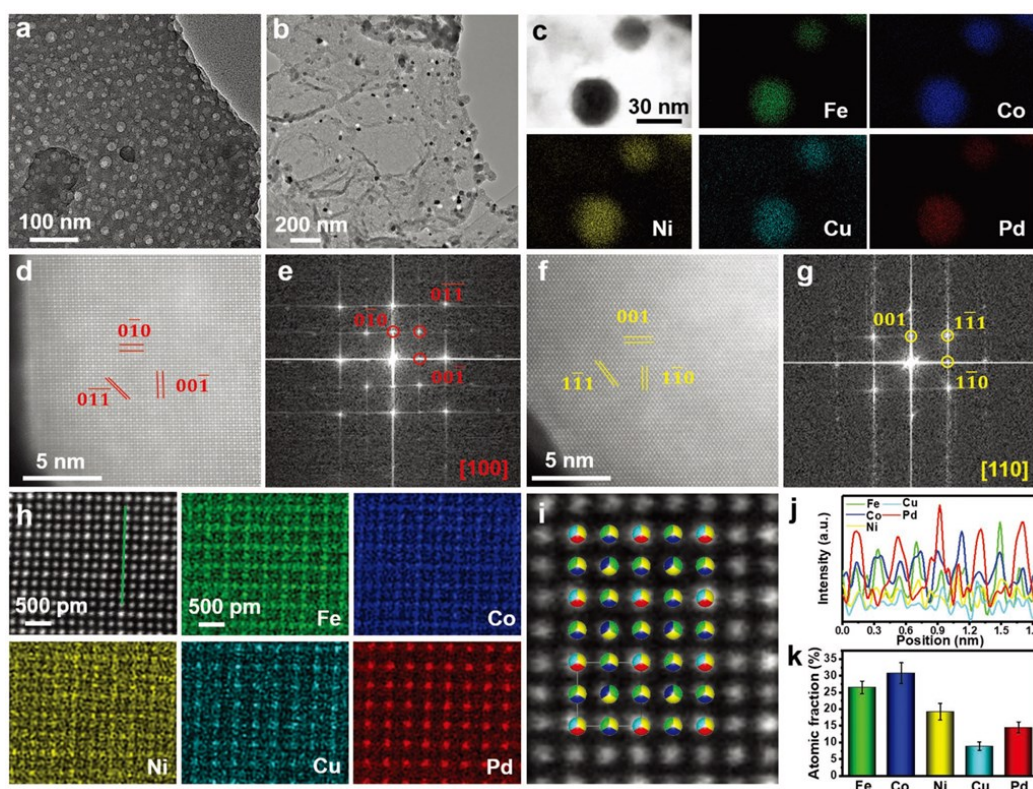
Figure 1.18. (a) TEM image of the synthesized organic-inorganic hybrid material. (b) TEM image of the OHEA-mNC catalyst. (c) ABF-STEM image and corresponding elemental mappings for the FeCoNiCuPd NPs. (d) Atomic-resolution HAADF-STEM image and (e) corresponding FFT pattern along [100] zone axis. (f) Atomic-resolution HAADF-STEM image and (g) corresponding FFT pattern along [110] zone axis. (h) Atomic-resolution HAADF-STEM image and corresponding EDX mappings. (i) A pictorial illustration of the elements on each site, superimposed on the HAADF image along the [100] zone axis. (j) Line scan profile along the line in (h). (k) Quantitative analysis for each element. Reprinted with permission from ref 37. Copyright 2022 Wiley-VCH Verlag GmbH & Co.

Germanium-based materials have attracted much attention due to their narrow band gap (0.67 eV), high ion intercalation capacity, high electron mobility and low toxicity.[38] They have been explored as metal-semiconductor heterostructure in energy storage and electronic devices.[38, 39] Notably, germanium-based materials (e.g., germanane) have yet to be reported as a potential support for HEA NPs to form heterostructure. The synthesis of HEA NPs on germanane, germanium nanoparticles, and wafers will be discussed in Chapter 3.

1.1.2 High-Entropy Compounds

With the constantly increasing number of reports related to HEAs, it is reasonable that the concept of multicomponent high entropy systems is expanding beyond alloys to other material classes and as a result various high-entropy compounds have appeared. Among the first of such reports was one describing (MgCoNiCuZn)O, an entropy-stabilized oxide.[40] The synthesis begins with the mixing of MgO, NiO, CuO, CoO, and ZnO powders. Mixtures were subjected to varying temperatures ranging from 700 to 1100 ˚C (2 h in an air furnace), followed by air quenching (Figure 1.19). Specifically, the precursors of this high-entropy oxide possessed rocksalt (MgO, NiO, and CoO), tenorite (CuO), and wurtzite (ZnO) crystal structures. At 700 ˚C, XRD analysis revealed the presence of rocksalt and tenorite phases in the mixture consistent with insufficient entropic contribution to free energy. However, as the temperature increased, the concentration of tenorite phase diminished, ultimately resulting in the formation of a single rocksalt structure (Figure 1.19b). The utilization of starting materials with diverse crystal structures increased the mixing enthalpy, rendering the formation of a single rocksalt lattice more challenging. Consequently, a substantial entropic contribution of free energy, achievable through higher temperatures or increased entropy, is required to form single-phase high-entropy oxide (HEO).[40] As the first report on HEOs, their properties and applications were underexplored.
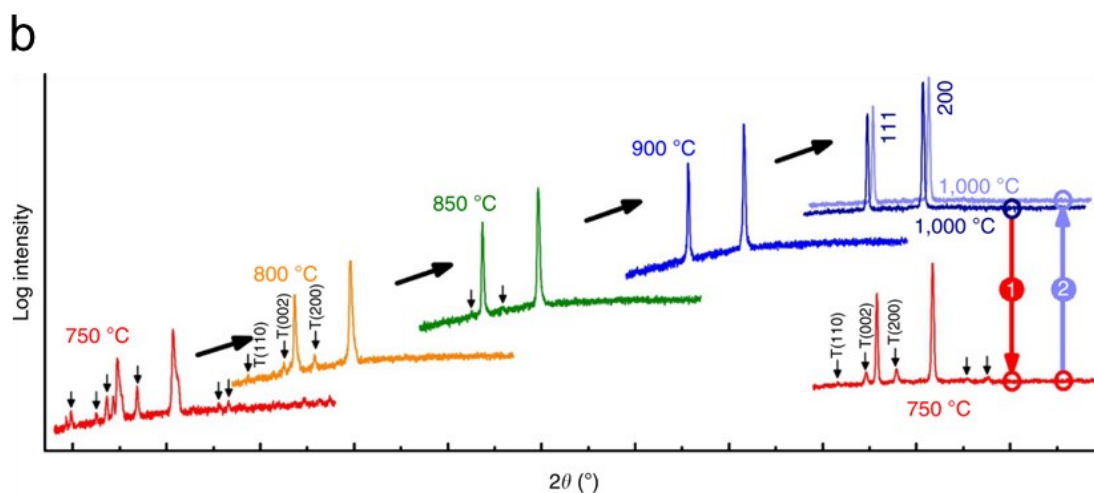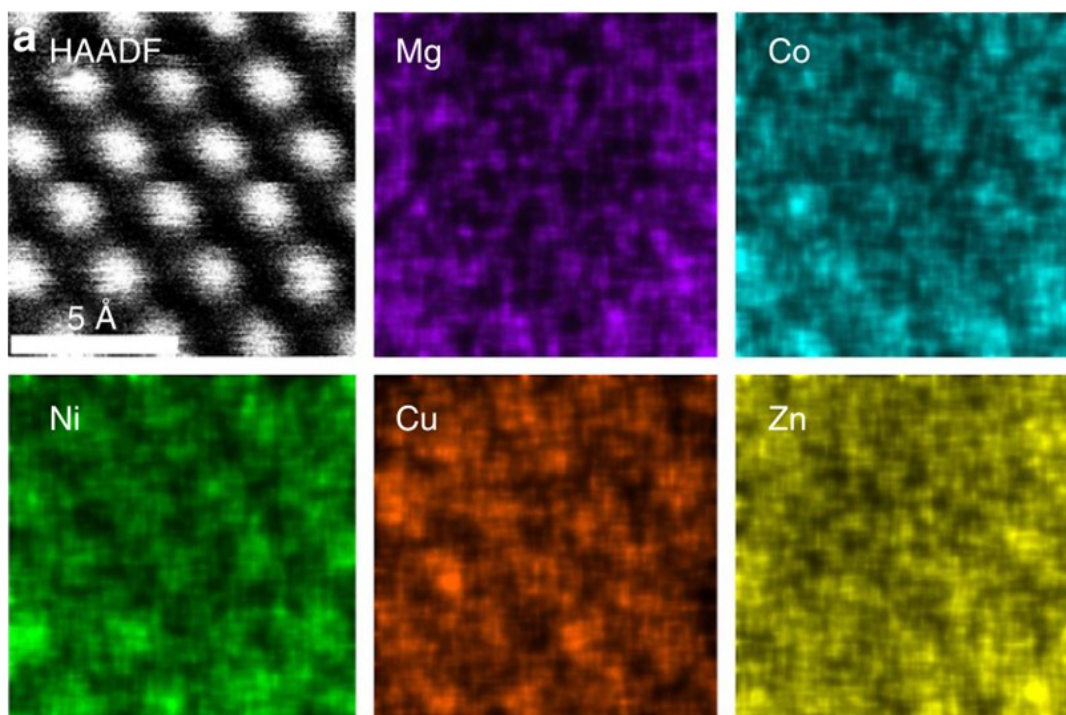
Figure 1.19. (a) HAADF-STEM image and EDX mappings of (MgCoNiCuZn)O. (b) XRD patterns for (MgCoNiCuZn)O. The patterns were measured from one pellet which was equilibrated for 2 h at each temperature in air, then air quenched to room temperature by direct removing from the furnace. X-ray intensity is plotted on a logarithmic scale and arrows indicate reflections associated with non-rocksalt phases and reflections indexed with (T) correspond to tenorite phase. Reprinted with permission from ref 40. Copyright 2015 Springer Nature.
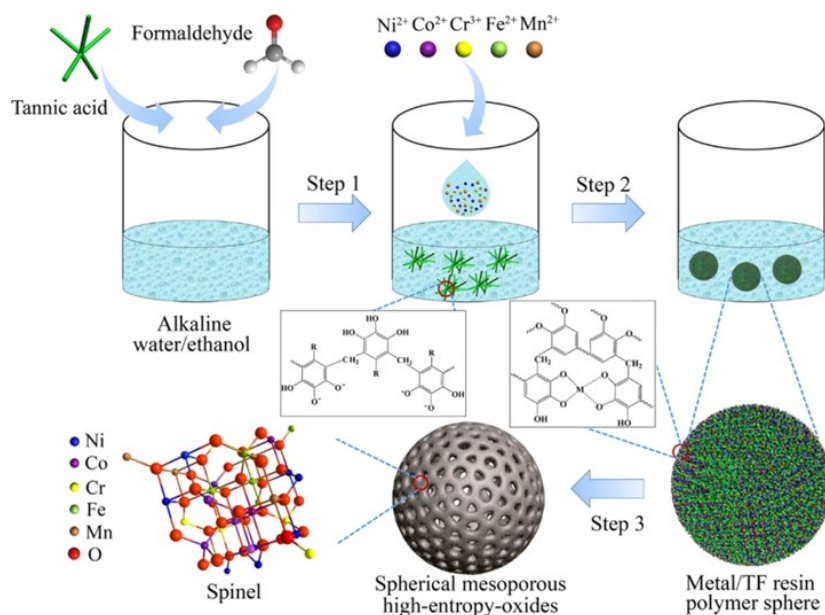
Figure 1.20. A pictorial illustration of the sol−gel synthesis of mesoporous HEO spheres. Reprinted with permission from ref 43. Copyright 2020 American Chemistry Society.

HEOs have conventionally been synthesized by solid-state reactions using solid metal oxide particles as precursors.[41] Alternatively, wet-chemistry synthesis, such as the general sol-gel strategy with the inclusion of organic templates can offer a straightforward approach to precisely control the compositions and structure/morphology of mesoporous materials.[42] Wang *et al.* developed a controllable wet-chemistry sol-gel strategy for crafting spherical mesoporous HEOs (NiCoCrFeMn oxide) exhibiting a general spinel structure that possess high specific surface areas, large pore sizes and volumes, and uniform particle diameters.[43] Spherical metal/polyphenol-formaldehyde resins were first synthesized via a sol-gel process using plant polyphenol formaldehyde, and metal salts as a precursor (Figure 1.20). Following calcination, the metal species aggregated to form HEOs, with the organic resin undergoing decomposition to generate mesopores (Figure 1.21).[43] The mesoporous HEOs can adsorb single-stranded nucleic acid labelled with dye to fabricate a DNA sensor, which showed high sensitivity with an LOD of 0.16−0.20 nM.
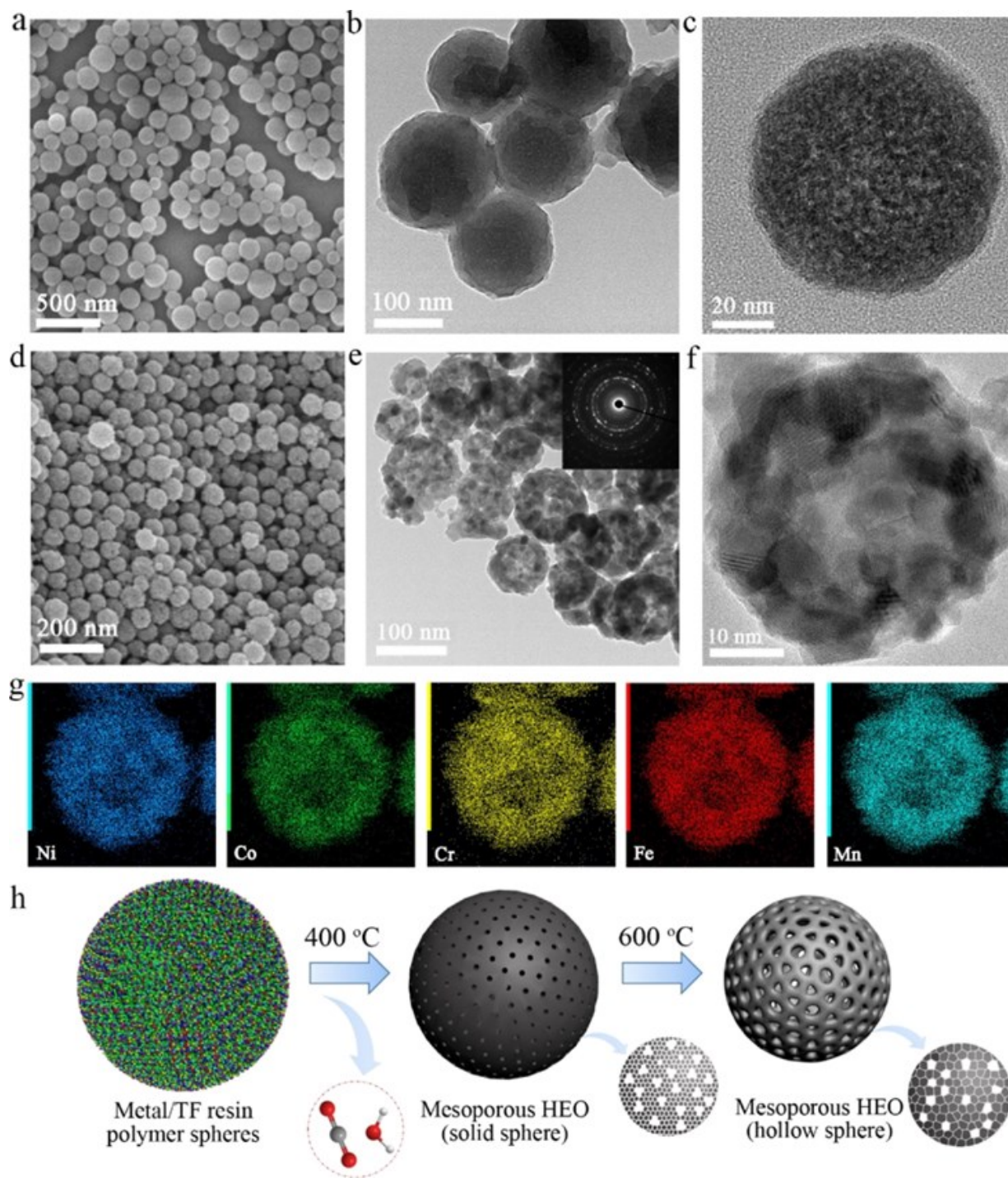
Figure 1.21. Representative (a) SEM and (b) TEM images of NiCoCrFeMn−TF polymer spheres. (c) TEM image for NiCoCrFeMn−TF-400 solid HEO sphere. (d) SEM image, (e,f) TEM images, and (g) EDXX mappings for NiCoCrFeMn−TF-600 hollow HEO sphere. Corresponding SAED pattern were shown in inset of (e). (h) A pictorial representation of the formation of solid and hollow mesoporous HEO spheres. Reprinted with permission from ref 43. Copyright 2020 American Chemistry Society.

24

A variety of high-entropy compounds, including carbides, nitrides, borides, silicides, sulfides and halides have now been synthesized and extensively analyzed.[44-53] Wang *et al.* used five different metal oxides and carbon black to fabricate an equimolar (TiZrNbTaMo)C high-entropy carbide (HEC). Carbothermal reduction was performed at 1500 ˚C in vacuum for 1 h resulting (TiZrNbTaMo)C HEC, which possessed an FCC structure (Figure 1.22). The measured hardness values of (TiZrNbTaMo)C are 25.3 GPa at 9.8 N which is comparable to or even higher than those (15 GPa or 18.8 GPa) obtained in other related high-entropy (TiZrNbTaHf)C.[44]
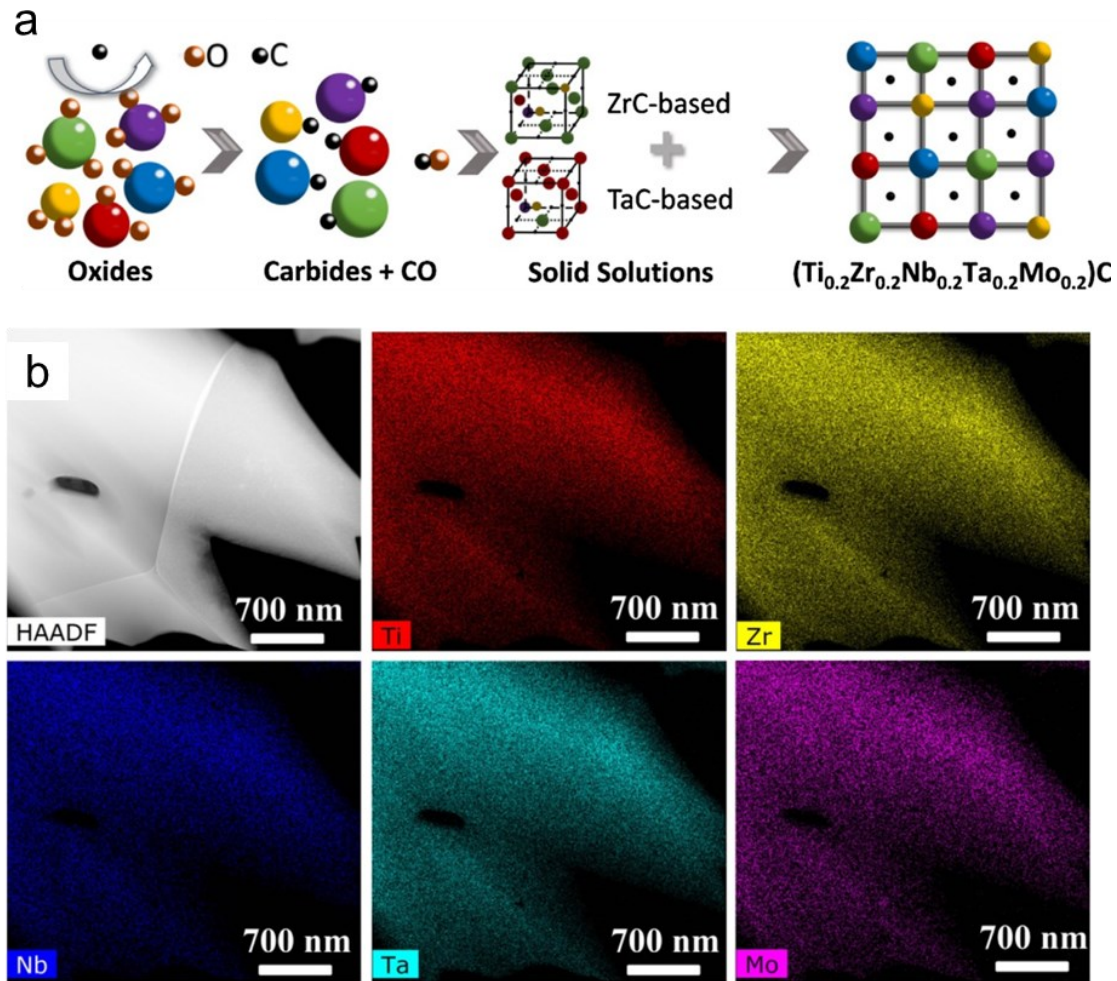
Figure 1.22. (a) A pictorial illustration of the formation process of $(Ti_{0.2}Zr_{0.2}Nb_{0.2}Ta_{0.2}Mo_{0.2})C$ (different colors represent different metallic atoms). (b) HAADF image and EDX mappings of HEC. Reprinted with permission from ref 44. Crown Copyright 2019 published Elsevier B.V.

Sure *et al.* reported a facile and single-step method to prepare HECs using the FFC-Cambridge electro-deoxidation process.[45] This method involves designating the metal oxide as the cathode in molten $CaCl_2$ electrolyte and polarizing it against a carbon anode; this causes expulsion of oxide ions from the cathode into the electrolyte.[54] A mixture of individual metal oxides and graphite is reduced in a melt of $CaCl_2$ at a temperature as low as 900 ˚C. The resulting (TiNbTaZrHf)C is characterized by a single-phase FCC structure and exhibits a powdery morphology with particle sizes from 15 to 80 nm (Figure 1.23). The HEC exhibit a long-term stability as supercapacitor electrodes with 87% capacity retention after 2000 cycles.[45]
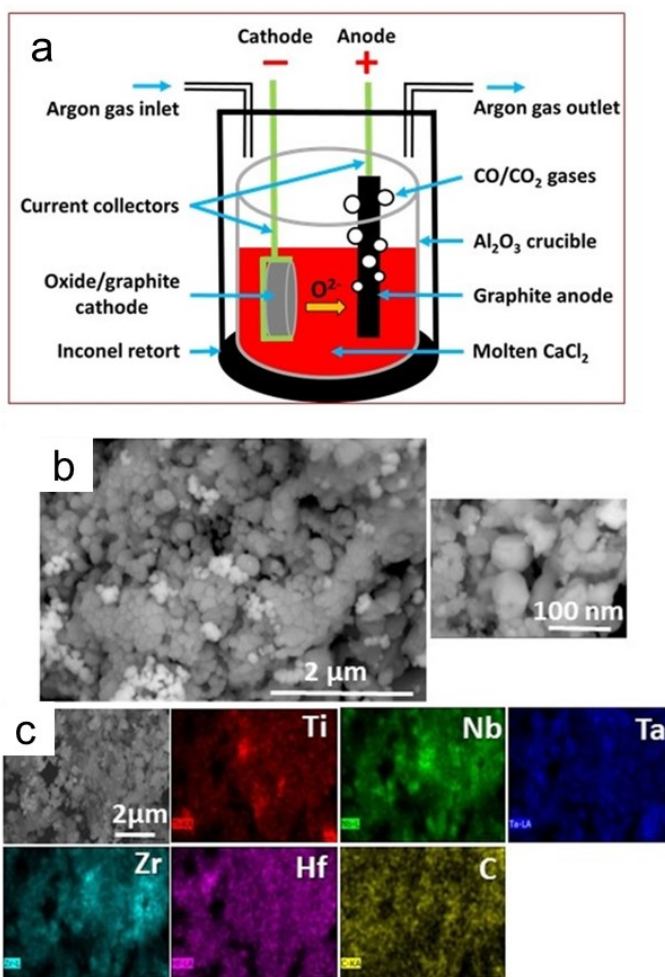
Figure 1.23. (a) A pictorial illustration of the electro-deoxidation experiment. (b) SEM images of (TiNbTaZrHf)C. (c) SEM and EDX mapping of (TiNbTaZrHf)C. Reprinted with permission from ref 45. Copyright 2020 Wiley-VCH Verlag GmbH & Co.

High-entropy metal nitrides (HEN) were first achieved by Jin *et al.* via a urea-based mechanochemical synthesis.[46] The process involved the ball milling of five transition-metal chlorides with urea, yielding a gel-like product uniformly dispersed and stabilized through metal-urea complexation. The resulting gel-like composite was heated in a N_2 atmosphere (800 °C for 3 h) leading to the formation of HEN as a black powder without additional post-treatment (Figure 1.24). The HEN was used as supercapacitor electrodes and showed a specific capacitance of 78 F g^{-1} at a scan rate of 100 mV s^{-1} in 1 m KOH.[46]
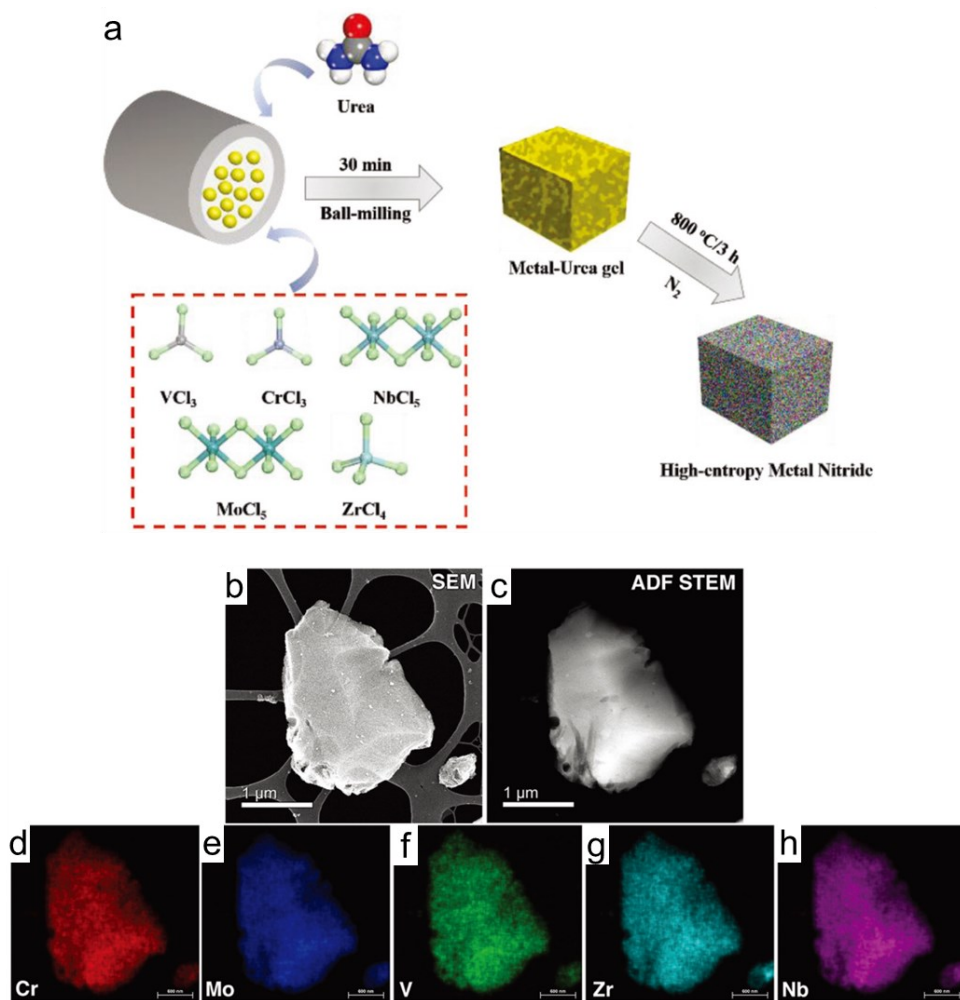
Figure 1.24. (a) A pictorial illustration of two-step synthetic strategy for HEN. (b) Representative SEM image and (c) ADF STEM image. (d-h) EDX mappings of HEN. Reprinted with permission from ref 46. Copyright 2018 Wiley-VCH Verlag GmbH & Co.

High-entropy metal diborides (HEBs) are crystalline high-entropy AlB_2-type ceramics.[41] Gild *et al.* used mechanical alloying and spark plasma sintering (SPS) methods to synthesize six different diborides with five equimolar components (selected from Zr, Hf, Ti, Ta, Nb, W, and Mo).[47] As confirmed by HAADF and ABF imaging, these high-entropy diborides exhibited a distinctive layered hexagonal AlB_2 structure separated by the rigid 2D boron nets and high-entropy 2D metal cation layers (Figure 1.25).[47] As a novel category of ultra-high temperature ceramics (UHTCs) and high-entropy materials, these HEBs not only stand out as the first high-entropy non-oxide ceramics (borides) but also show a unique non-cubic (hexagonal) and layered (quasi-2D) high-entropy crystal structure. These HEBs exhibit greater hardness and better oxidation resistance than other UHTC and have the potential for oxidation protective coating.[47]
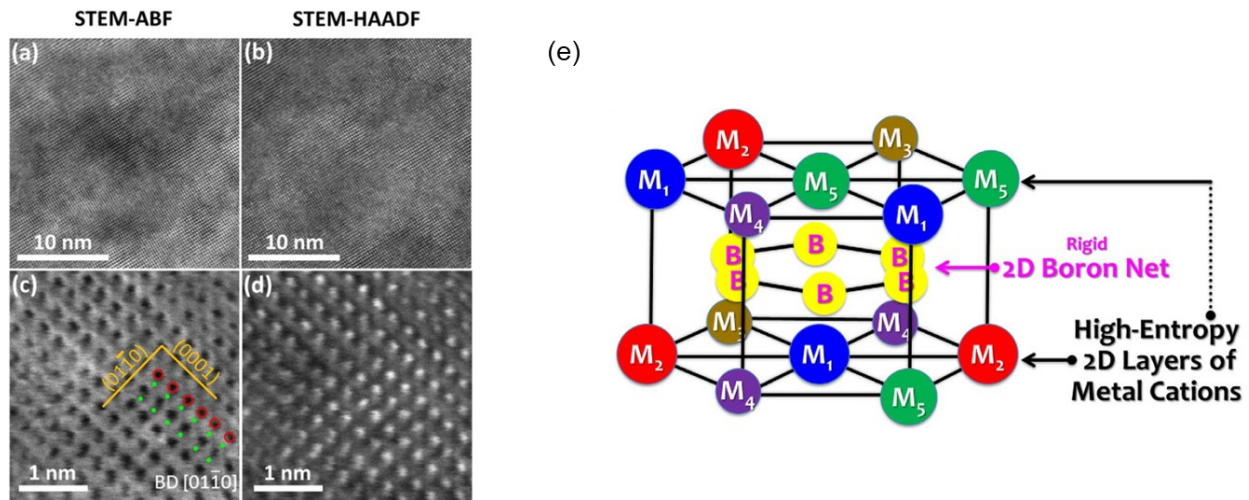
Figure 1.25. (a) ABF-STEM and (b) HAADF-STEM images of HEB at a low magnification. High-resolution (c) ABF-STEM and (d) HAADF-STEM images showing atomic configuration of the HEB. The electron beam is parallel to the [0110] zone axis of hexagonal structure. (0001) and (0110) planes are showed in (c). The red circles correspond to the columns of transition metal atoms. The green dots represent the boron atoms. (e) A pictorial illustration of the crystal structure of the high-entropy metal diborides. Reprinted with permission from ref 47. Copyright 2016 Springer Nature.

Dong and coworkers reported a molten salt-assisted boron thermal reduction method for the synthesis of HEBs.[48] In this approach, raw materials including WO_3, MoO_3, V_2O_5, Nb_2O_5,

CeO_2, and boron powder were combined with KCl and NaCl, followed by grinding for 30 min. The presence of K^+ and Na^+ in the molten salt state enhances the ion transmission capacity and reduces the temperature required for reduction. The resulting mixture was subjected to high-temperature sintering (1000 °C) in a vacuum tube furnace for 30 minutes to synthesize the WMoVNbCeB HEB (Figure 1.26). It effectively improved the HER activity and long-term stability in an alkaline medium (increased 15 mA after 5000 cycles). [48]
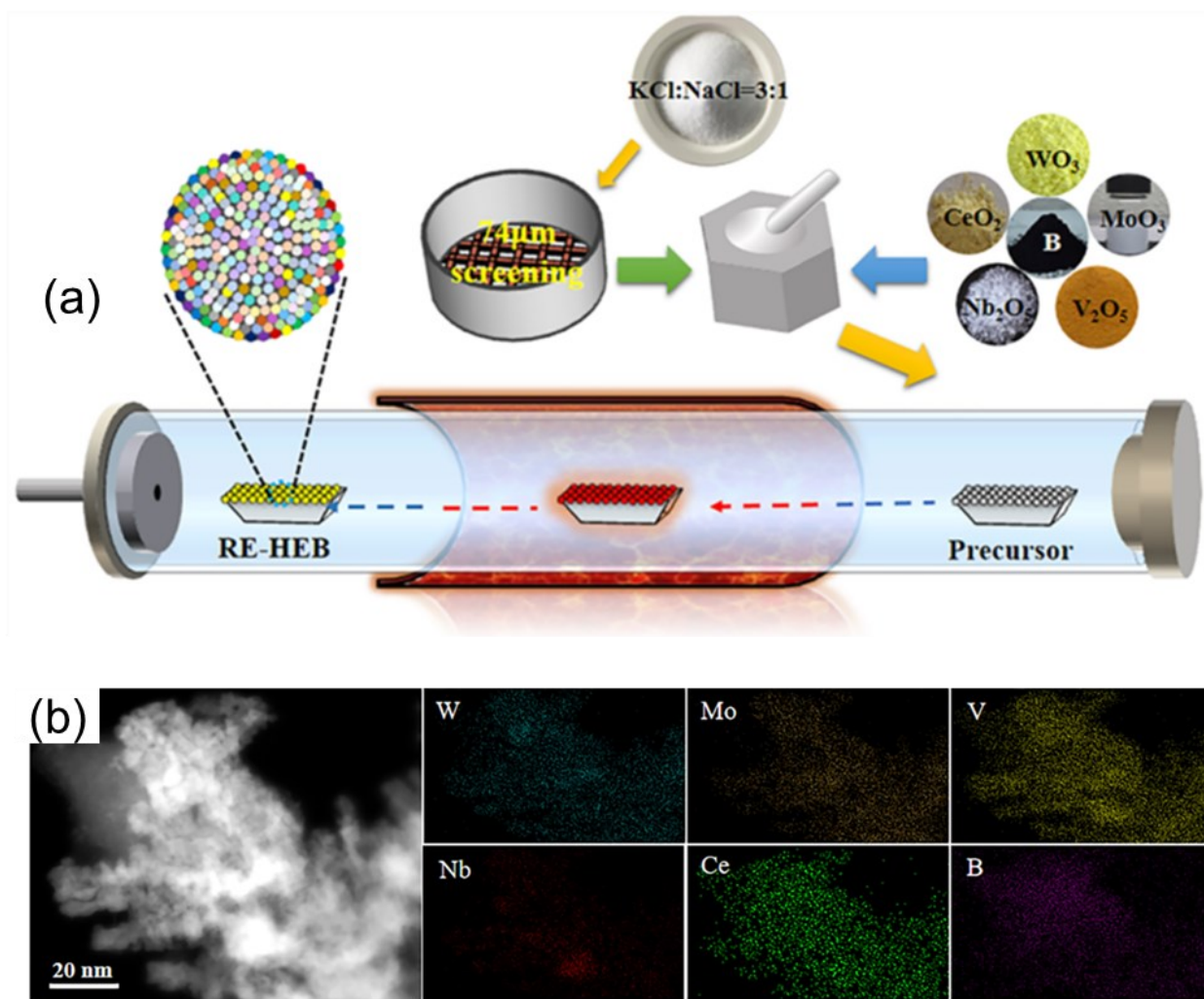
Figure 1.26. (a) A pictorial representation of the synthesis process of WMoVNbCeB HEB. (b) HAADF-STEM image and EDX mapping of WMoVNbCeB HEB. Reprinted with permission from ref 48. Crown Copyright 2023 published Elsevier B.V.

Qin and colleagues have synthesized a high-entropy silicide (HES) ceramic with enhanced hardness via reactive spark plasma sintering (SPS).[49] In this methodology, metallic powders and silicon were employed to create a HES, $(Ti_{0.2}Zr_{0.2}Nb_{0.2}Mo_{0.2}W_{0.2})Si_2$, with a close-packed hexagonal structure. EDX analysis confirmed the uniform, excluding zirconium, distribution of elements, and showed oxygen incorporated in impurity particles (Figure 1.27). The hardness of the HES was measured to be 12.09 GPa which is in the upper range of silicides (10 - 13 GPa).[49]
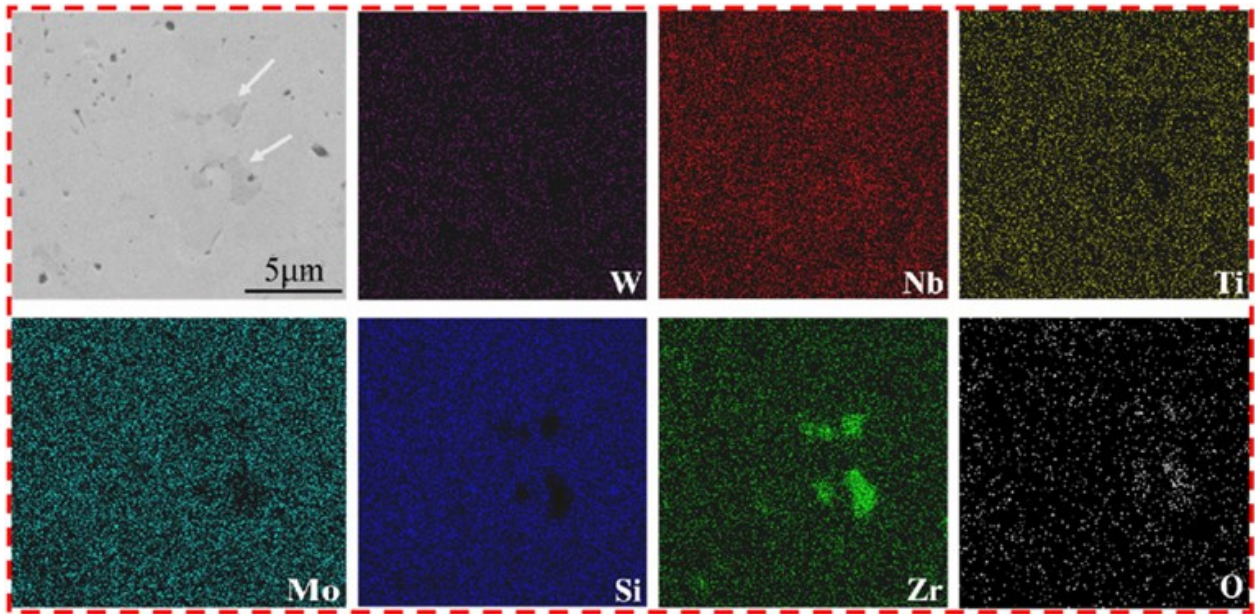
Figure 1.27. SEM images of the polished surface of $(Ti_{0.2}Zr_{0.2}Nb_{0.2}Mo_{0.2}W_{0.2})Si_2$ SPSed at 1300 °C for 15 min, with the corresponding EDS mapping of Ti, Zr, Nb, Mo, W, and Si elements. Reprinted with permission from ref 49. Copyright 2019 Springer Nature.

Wang and colleagues made the discovery of high-entropy perovskite fluorides (HEPFs) along with demonstrating their efficacy in effective oxygen evolution reaction (OER) catalysis.[50] The synthesis begins with the ball milling of metal sulfates/acetates to ensure thorough mixing of the metal sources. The mixed metal sulfate/acetate powder was then directly introduced into a boiling KF solution, leading to the rapid precipitation of HEPFs (Figure 1.28).[50]
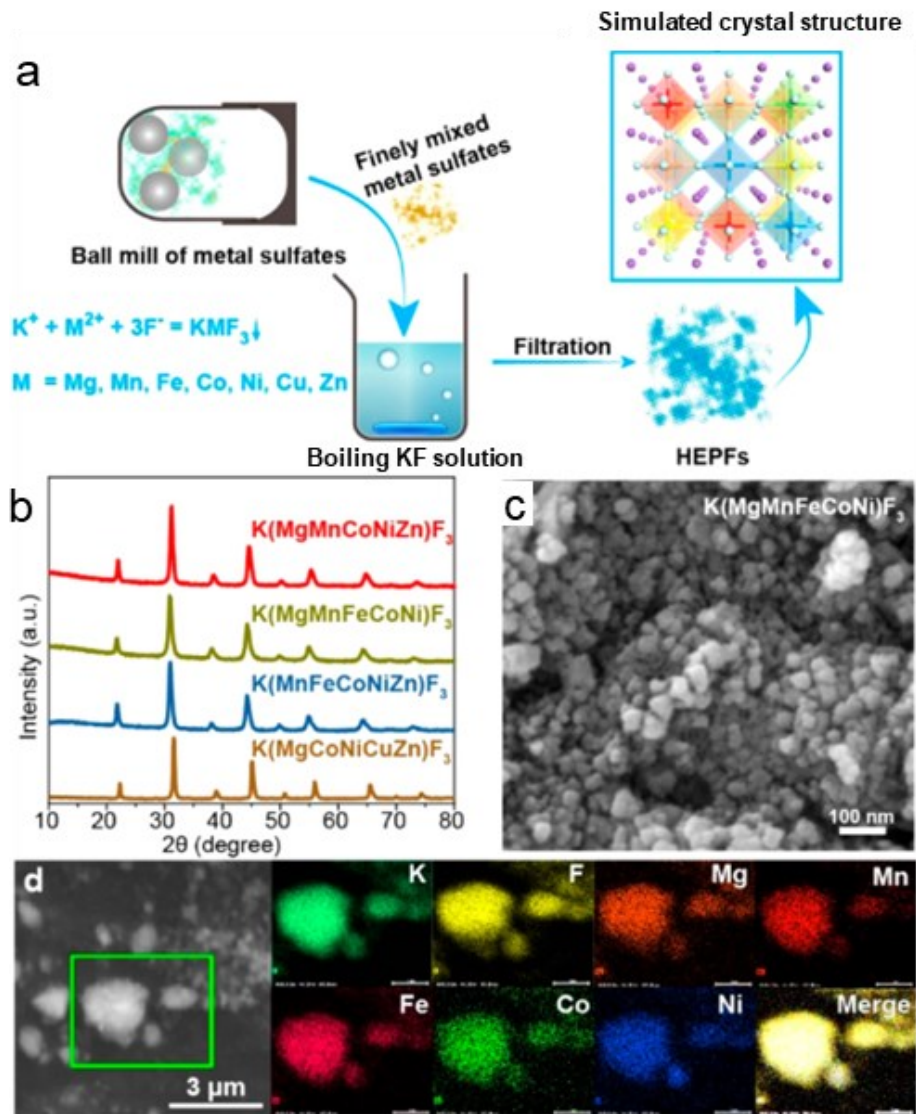
Figure 1.28. (a) A pictorial illustration of HEPF synthesis; (b) XRD patterns of HEPFs; (c) Secondary electron SEM image of K(MgMnFeCoNi)F$_3$; (d) SEM image and EDX mappings of K(MgMnFeCoNi)F$_3$ in the green region. Reprinted with permission from ref 50. Copyright 2020 American Chemistry Society.

Using the vacancy-ordered double perovskite Cs$_2$MCl$_6$ crystal structure as a platform, the Yang group extended the exploration of high-entropy halide perovskite single crystals to the Cs$_2${ZrSnTeHfRePt}$_1$Cl$_6$ and Cs$_2${SnTeReOsIrPt}$_1$Cl$_6$ families.[51] Building on their prior work involving the formation of mixed from Cs$_2$TeX$_6$ (X=Cl$^-$, Br$^-$, I$^-$) powders,[55] they dissolved the appropriate one-element Cs$_2$MCl$_6$, (M = Zr, Sn, Te, Hf, Re, Os, Ir, Pt) starting powders in 12 M

hydrochloric acid (HCl). This generated multi-element solution containing free Cs^+ cations and isolated $[MCl_6]^{2-}$ ($M=Zr^{4+}$, Sn^{4+}, Te^{4+}, Hf^{4+}, Re^{4+}, Os^{4+}, Ir^{4+}, or Pt^{4+}) octahedral anions examined by Raman spectroscopy, multiwavelength anomalous diffraction and electron backscatter diffraction (Figure 1.29a). The (re)crystallization process from these multi-element solutions was used to achieve single crystals of $Cs_2\{SnTeReIrPt\}_1Cl_6$, $Cs_2\{ZrSnTeHfPt\}_1Cl_6$, $Cs_2\{SnTeReOsIrPt\}_1Cl_6$, and $Cs_2\{ZrSnTeHfRePt\}_1Cl_6$ (Figure 1.29b).[51] The adsorption and emission properties of these single crystals were studied. Their adsorption spectra exhibited the superposition of features from electronic transitions of all constituent octahedra, while the photoluminescence excitation spectra demonstrated energy transfer behaviour among the octahedra. These high-entropy halide perovskite single crystals have a great potential for the optoelectronic applications.[51]
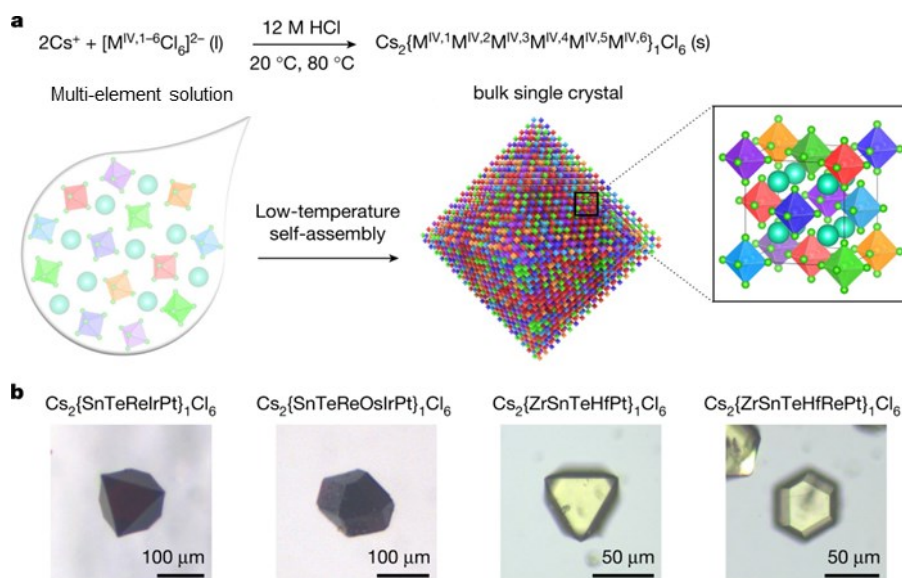
Figure 1.29. (a) A pictorial illustration of the solution phase self-assembly processes from multi-element solution to high-entropy perovskite single crystals. 12 M HCl was used as the solvent for an excess chloride environment, facilitating the formation of six coordinated $[MCl_6]^{2-}$ octahedral molecules in solution. (b) Optical microscopy images of high-entropy quinary ($Cs_2\{ZrSnTeHfPt\}_1Cl_6$ and $Cs_2\{SnTeReIrPt\}_1Cl_6$) and senary ($Cs_2\{SnTeReOsIrPt\}_1Cl_6$, and $Cs_2\{ZrSnTeHfRePt\}_1Cl_6$) single crystals. Reprinted with permission from ref 51. Copyright 2023 Springer Nature.

Zhang and coworkers designed two high-entropy sulfides (metallic $Cu_5SnMgGeZnS_9$ and semiconducting $Cu_3SnMgInZnS_7$) based on a data-driven model which selected suitable elements to minimize the enthalpy of formation and maximize the chance of single-phase formation. They calculated the cations-sulfur bond lengths of the 47 compounds from Inorganic Crystal Structure Database (ICSD) and used it as the chemical descriptor for the high-entropy sulfide design since the bond lengths of cations are a decent indicator of local strain (Figure 1.30).[52] Two possible compositions ($Cu_5SnMgGeZnS_9$ and $Cu_3SnMgInZnS_7$) were synthesized using SPS based on the criterion. The metallic $Cu_5SnMgGeZnS_9$ was tested for their thermoelectric properties showing a comparable zT value of 0.58 at 723 K to those of typical Cu-S based thermoelectric materials. This approach advances later data-driven discovery of high-entropy materials.[52]
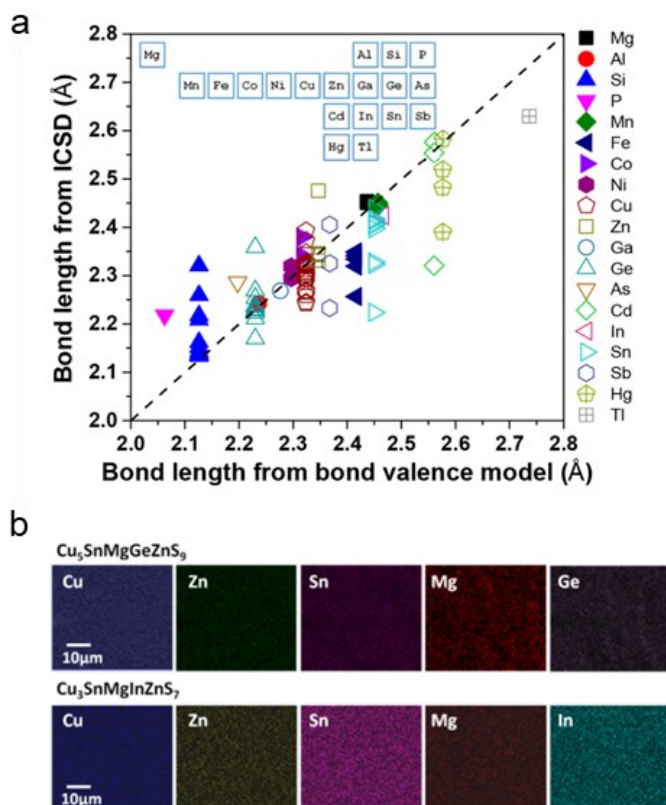
Figure 1.30. (a) Bond length from ICSD and bond valence model. (b) EDX of high-entropy sulfides. Reprinted with permission from ref 52. Copyright 2018 American Chemistry Society.

The Schaak group reported low temperature synthesis of a high-entropy copper sulfide NPs by using a significantly different pathway as compared to previous methods for the bulk high-entropy sulfides.[52] Initially, roxbyite copper sulfide ($Cu_{1.8}S$) nanoparticles undergo simultaneous multication exchange with substoichiometric amounts of Zn^{2+}, Co^{2+}, In^{3+}, and Ga^{3+}. This results in the formation of a crystalline, wurtzite-type Zn-Co-In-Ga-Cu sulfide product. Nanoparticle cation exchange reactions, involving the replacement of cations in the nanoparticle by cations from the solution, harness both enthalpic and entropic driving forces. Coupled with configurational entropy, this synergistically facilitates the formation of a high-entropy material at low temperatures (Figure 1.31).[53] This method provides a new approach to design and synthesize high entropy materials that can be extend to other systems including metal halides, metal selenides and metal tellurides. The prepared high-entropy metal sulfide NPs are promise candidates in catalysis, energy storage, and thermoelectric.
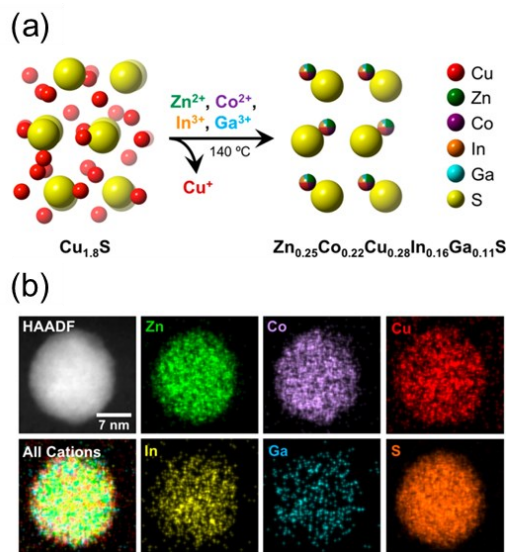
Figure 1.31. (a) A pictorial illustration showing the transformation of roxbyite $Cu_{1.8}S$ to the high-entropy wurtzite-type metal sulfide $Zn_{0.25}Co_{0.22}Cu_{0.28}In_{0.16}Ga_{0.11}S$ via a simultaneous ion exchange of the Cu^+ cations. (b) HAADF-STEM image and EDX mappings of the $Zn_{0.25}Co_{0.22}Cu_{0.28}In_{0.16}Ga_{0.11}S$. Reprinted with permission from ref 53. Copyright 2021 American Chemistry Society.

Currently, most studies have focused on various developing methods to prepare high-entropy alloys and compounds along with the characterization of the high-entropy structure. Novel properties are also investigated. Germanides are a class of compounds that have garnered significant interest in recent years due to their potential applications in the fields of thermoelectricity and electronics.[56, 57] These compounds are formed through the combination of germanium with diverse metallic elements such as iron, nickel, cobalt, and palladium.[58-61] The distinctive physical properties exhibited by germanides, including high electrical conductivity, low thermal conductivity, and favorable thermoelectric characteristics, make them highly attractive for various applications. However, high-entropy germanide materials has been relatively limited up to now except some of intermetallics.[62] We will discuss the synthesis of high-entropy germanides and the formation processes using advanced *in situ* heating characterization techniques in Chapter 4.

1.2 Ge Nanostructures

Germanium is a heavier congener of silicon in Group 14. While similarities exist between these two congeners (e.g., both are indirect band gap semiconductors, chemical reactivity, crystal structure), key differences make germanium and derived materials attractive functional systems for numerous applications. With a small band gap (0.67 eV at 300 K),[63] large Bohr-exciton radius (24.3 nm),[64, 65] high electron and hole mobility (~3900 $cm^2/V \cdot s$),[66] as well as large capacity for and diffusivity of ions (e.g., Li^+), Ge has the potential to impact applications such as photodetectors,[67] field-effect transistors,[68] and lithium-ion batteries.[69] Nanoscale Ge allows for additional tailoring because of the impacts of surface area and quantum confinement.[70, 71]

1.2.1 Ge Nanoparticles

Germanium nanoparticles (GeNPs) have received significant attention in light of their potential use in various applications including, solar cells, field-effect transistors, memory devices, photodetectors, and biological imaging.[72] GeNPs present a compelling and less toxic alternative to traditional narrow band gap semiconductor nanoparticles containing heavy metals such as Pd, Cd, and Hg.[73] Controlled synthesis methods are required to ensure GeNPs with well-defined sizes and morphologies are realized to facilitate investigation of the inherent properties of GeNPs and their diverse applications.[72]

The synthesis of GeNPs has been extensively reported throughout the literature and primarily focus on four main techniques: mechanochemical ball milling of bulk crystals,[74] metathesis reactions involving Zintl salts such as NaGe,[75] solution phase hydride reduction of Ge halides,[76-79] and the thermal disproportionation of Ge-rich precursors.[80, 81]   In the Veinot Laboratory, germanium hydroxide, $Ge(OH)_2$, was employed as a precursor to prepare GeNPs.[80] Thermal processing of $Ge(OH)_2$ at 400°C under an Ar atmosphere results in GeNPs embedded in a GeO_2 matrix.[80] Subsequent dissolution of the GeO_2 matrix using ethanolic hydrofluoric acid produces hydride-terminated GeNPs (Figure 1.32). Further details on this process will be discussed in Chapter 3.
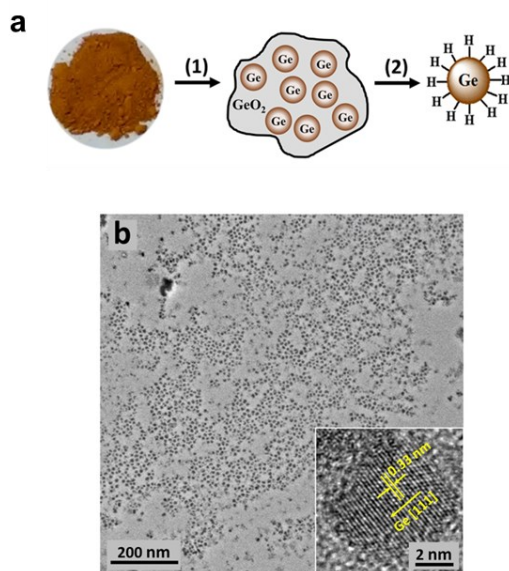
Figure 1.32. (a) A pictorial representation of the synthesis of hydride-terminated GeNPs. (b) TEM and HRTEM images of hydride-terminated GeNPs showing (111) lattice plane. Reprinted with permission from reference 80. Copyright 2017 American Chemical Society.

1.2.2 Ge Nanosheets (Germanane)

Two-dimensional (2D) materials represent an exciting material class poised to revolutionize many sectors including electronics, sensing, multifunctional coatings and a host of other applications.[82] Materials including graphene, transition metal dichalcogenides, black phosphorus, boron nitride, and heterostructures of the same are being rapidly developed for use in low power electronics, wearable sensors and point-of-care diagnostics.[83]

Germanane (Ge nanosheets; GeNSs) has a 2D structure made up of germanium atoms in sheets with a buckled honeycomb arrangement to form nonplanar sheets.[84] Depending upon surface chemistry, GeNSs can possess an optical band gap in the range of 1.4 - 1.7 eV,[85] and several studies have reported its integration into prototype devices such as transistors and Li-ion batteries.[86, 87]

Vogg *et al.* reported the first preparation of hydride-terminated germanane through topotactically deintercalation of CaGe$_2$ in concentrated aqueous HCl.[88] In 2013, Goldberger and collaborators conducted a systematic study on the thermal stability of germanane (Figure 1.33) and found that the Ge framework is disrupted when annealing temperatures surpass 100 °C, as evidenced by the diminishing Ge–Ge vibration and the reduction in the optical band gap from 1.59 eV to 1.1 eV. A reduction in interlayer distance was then observed post-annealing at 150 °C, as manifested by an increased 2θ value in the XRD pattern. At elevated temperatures, the layered morphology completely disappears, and a dehydrogenative reaction was identified via thermogravimetric analysis (TGA).[89] This study provides a starting point for the synthesis of high-entropy germanides discussed in Chapter 4.
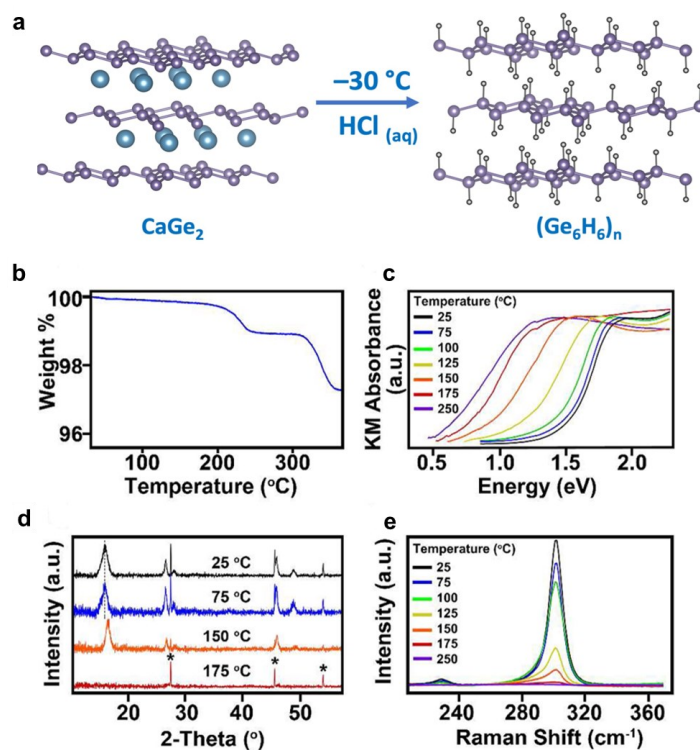
Figure 1.33. (a) A pictorial illustration of germanane (Ge$_6$H$_6$)$_n$ synthesis. (b) Analysis of (Ge$_6$H$_6$)$_n$ by TGA. (c) DRA spectra, (d) XRD patterns, and (e) Raman spectra of (Ge$_6$H$_6$)$_n$ after annealing at different temperature. (*) in (d) correspond to diffraction reflections of an internal Ge standard. (b-c) was reprinted with permission from ref 89. Copyright 2013 American Chemical Society.

The Goldberger group further advanced the topochemical deintercalation approach by substituting concentrated hydrochloric acid with alkylating agents such as methyl iodide. This substitution led to the synthesis of methyl-terminated germanane, accomplishing both chemical exfoliation and covalent functionalization in a single-step reaction (Figure 1.34).[90] The success of functionalizing germananes using this "top-down" approach provides for tunable properties by tailoring the ligand identity and coverage of the 2D germanane framework. It also allows for the preparation and subsequent investigation of additional covalently functionalized GeNSs.[91]
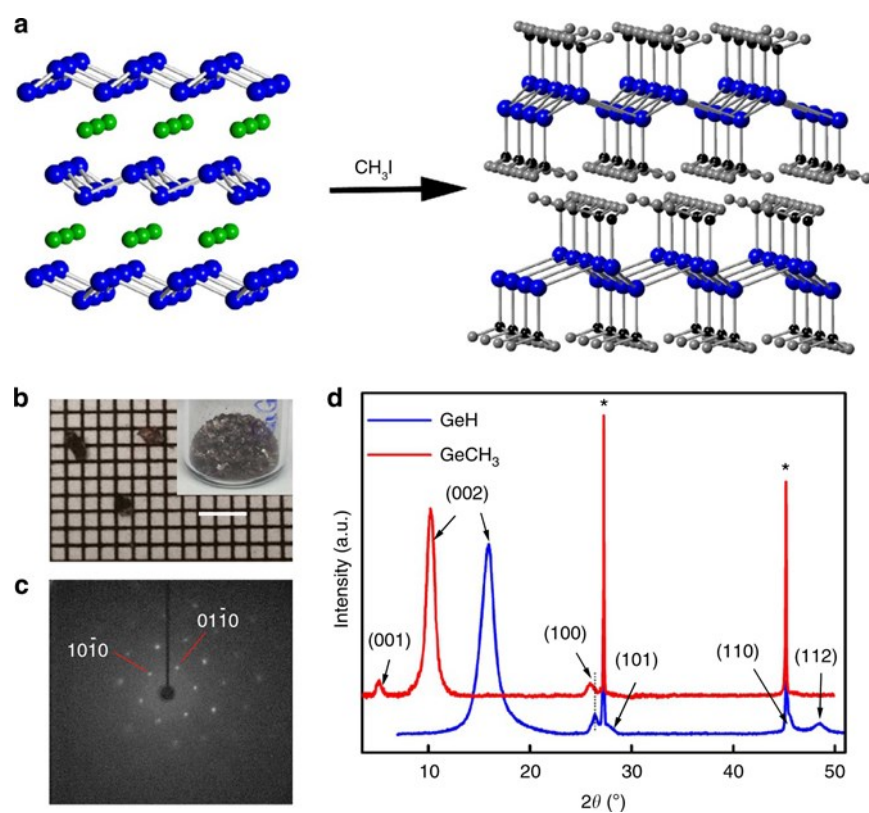
Figure 1.34. (a) A pictorial representation of conversion of $CaGe_2$ into $GeCH_3$ using CH_3I. (b) Optical image of $GeCH_3$ crystals on 1 mm grid paper with a 3 mm scale bar. (c) Single-crystal XRD pattern of $GeCH_3$ collected along the [001] zone axis. (d) Powder XRD patterns of GeH and $GeCH_3$. (*) correspond to diffraction reflections of an internal Ge standard. The dot line shows the difference in the (100) reflections between GeH and $GeCH_3$. Reprinted with permission from ref 90. Copyright 2014 Springer Nature.

Hartman *et al.* developed an alternative strategy involving a two-step reaction utilizes solid alkylating agents.[92] In the first step, in the THF solution alkali metal (M) arenides (MNp, Np = naphthalenide) serve as a strong base to deprotonate Ge-H (Ge-H → Ge⁻) and generate Ge⁻/M⁺ ion pairs. For instance, sodium naphthalide in THF forms Ge⁻/Na⁺. The subsequent step involves a nucleophilic SN_2 substitution with an appropriate alkylating reagent. (Figure 1.35).[92]
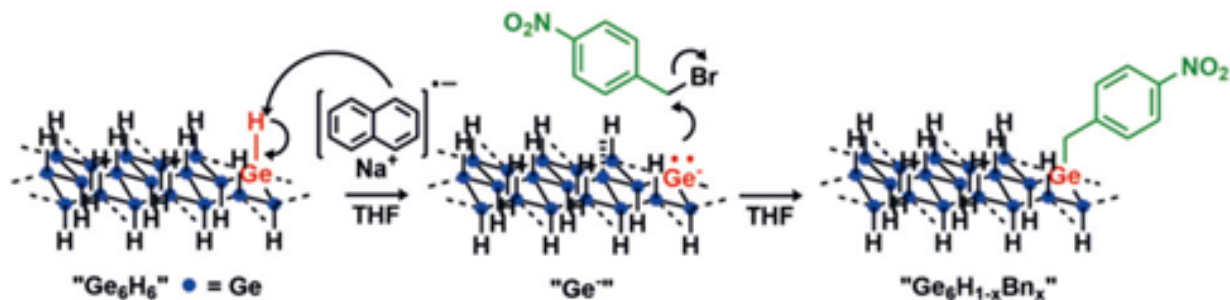
Figure 1.35. A pictorial illustration of two-step functionalization of GeH using solid alkylating agents. Reprinted with permission from ref 77. Copyright 2019 Wiley-VCH Verlag GmbH & Co.

Hydride-terminated Ge structures (e.g., GeNSs) can be modified with alkenes and alkynes via hydrogermylation.[93] In the Veinot laboratory, Yu *et al.* demonstrated the derivatization of GeNSs via two pathways: radical-initiated hydrogermylation with azobisisobutyronitrile (AIBN) as the radical initiator, and thermally-induced hydrogermylation with sonication in neat 1-dodecene (Figure 1.36).[94] The resulting dodecyl-functionalized GeNSs displayed slightly different properties depending on the functionalization method. Dodecyl-GeNSs prepared via reactions involving radical initiators provided monolayer coverage and showed a thickness of 4.5 nm, whereas those prepared thermally yielded higher density surface coverage with a film thickness of 5.5 nm – this difference was attributed to surface oligomerization.[94]
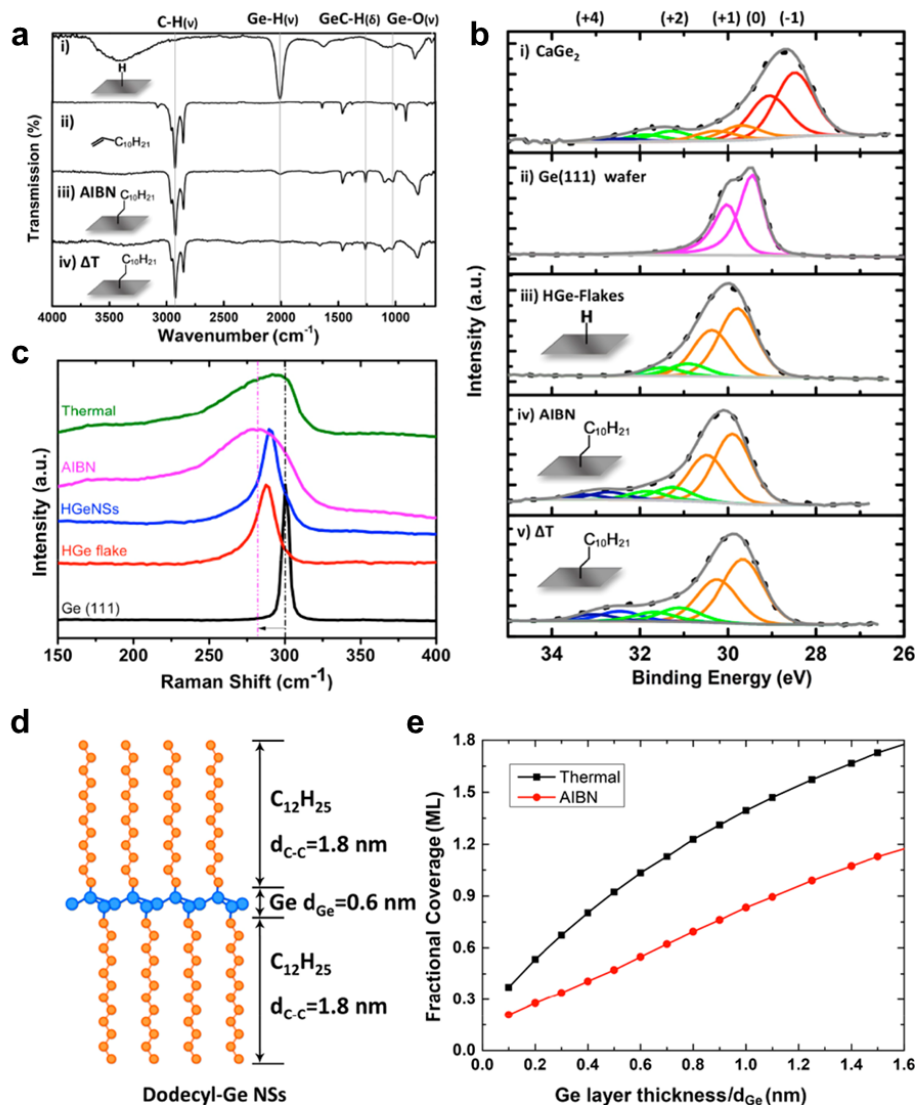
Figure 1.36. (a) FTIR spectra of GeNSs, 1-dodecene and dodecyl-terminated GeNSs prepared from thermal and AIBN radical hydrogermylation. (b) High-resolution XP spectra of the Ge 3d spectra region for CaGe$_2$, Ge (111) wafer, germanane flakes and dodecyl-terminated GeNSs prepared from thermal and AIBN radical hydrogermylation. (c) Raman spectra of Ge (111) wafer, germanane flakes, GeNSs and dodecyl-terminated GeNSs prepared from thermal and AIBN radical hydrogermylation. (d) A proposed ideal model for dodecyl-terminated GeNSs. (e) Calculation of fractional monolayer (ML) ligand coverage versus Ge layer thickness determined from XPS, for dodecyl-terminated GeNSs prepared from thermal and AIBN radical hydrogermylation. Reprinted with permission from ref 94. Copyright 2018 American Chemical Society.

Yu *et al.* further extended the chemistry of GeNSs by incorporating Ge-Si bonding through

the thermally-induced heteronuclear dehydrocoupling of organosilanes to hydride-terminated

germanane (Figure 1.37).[95] The resulting organosilane-functionalized GeNSs remained suspended in toluene for weeks and resisted oxidation in wet ethanol for days. Additionally, a 0D/2D hybrid material consisting of covalently linked SiNPs and GeNSs was prepared using a similar methdology.[95] The use of hydride-terminated GeNSs to create a 0D/2D hybrid material inspired the investigation of the preparation of metal nanoparticles on GeNSs, described in Chapter 2.
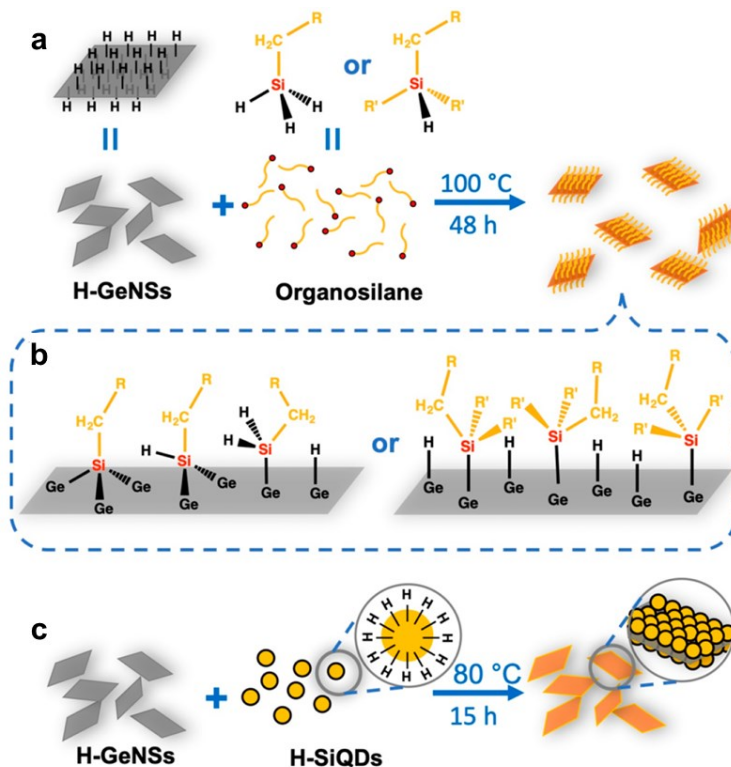
Figure 1.37. (a) A pictorial illustration of dehydrocoupling of organosilanes on the surfaces of GeNSs; (b) A pictorial representation of possible surface bonding models of primary (Left) and tertiary (Right) alkylsilanes on GeNSs; (c) A pictorial illustration of heteronuclear dehydrocoupling of H-SiQDs on the surfaces of GeNSs. Reprinted with permission from ref 95. Copyright 2018 American Chemical Society.

1.3 The Scope of This Thesis

This thesis is grounded in the hypothesis that hydride-terminated Ge (bulk and nano) materials can serve as convenient precursors for preparing metal nanoparticle/Ge hybrids.

Additionally, it explores the possibility of using solution methods for depositing HEA NPs onto germanane surfaces. Chapter 2 focuses on synthesizing metal-decorated GeNSs (M@GeNSs) and their prototype application as a catalyst in photocatalytic conversion of benzyl alcohol to benzaldehyde.

In Chapter 3, the deposition of HEA NPs onto germanane surfaces via surface-mediated reduction is explored. Freestanding HEA NPs can be liberated from the GeNSs through straightforward UV light irradiation while maintaining their single-phase solid solution structure after liberation. Similar investigations were extended to other Ge-based substrates, including hydrogen-terminated GeNPs and Ge (100) wafers.

Chapter 4 discusses the first reported synthesis of high-entropy germanides (HEG: AuAgCuPdPtGe and FeCoNiCrVGe) via a rapid thermal annealing. The formation and growth mechanisms of HEGs are elucidated through *in situ* heating XRD and TEM experiments. The observed process involves the initial decomposition of GeNSs during annealing, followed by a gradual grain growth via diffusion at temperatures below 600 °C, and ultimately, rapid grain growth at elevated temperatures.

Chapter 5 provides a summary of the findings from Chapters 2-4 and offers a brief and high-level outlook of the methodologies, materials synthesized in this Thesis and future work.

1.4 References

1.   Martinón-Torres, M.; Valcárcel Rojas, R.; Sáenz Samper, J.; Guerra, M. F. Metallic Encounters in Cuba: The technology, exchange and meaning of metals before and after Columbus. *J. Anthropol. Archaeol.* **2012**, *31* (4), 439-454.
2.   Nakaya, Y.; Furukawa, S. Catalysis of Alloys: Classification, Principles, and Design for a Variety of Materials and Reactions. *Chem. Rev.* **2023**, *123* (9), 5859-5947.
3.   Yeh, J. W.; Chen, S. K.; Lin, S. J.; Gan, J. Y.; Chin, T. S.; Shun, T. T.; Tsau, C. H.; Chang, S. Y. Nanostructured High-Entropy Alloys with Multiple Principal Elements: Novel Alloy Design Concepts and Outcomes. *Adv. Eng. Mater.* **2004**, *6* (5), 299-303.
4.   Cantor, B.; Chang, I. T. H.; Knight, P.; Vincent, A. J. B. Microstructural Development in Equiatomic Multicomponent Alloys. *Mater. Sci. Eng. A* **2004**, *375-377*, 213-218.
5.   Senkov, O. N.; Wilks, G. B.; Miracle, D. B.; Chuang, C. P.; Liaw, P. K. Refractory High-Entropy Alloys. *Intermetallics* **2010**, *18* (9), 1758-1765.
6.   Senkov, O. N.; Wilks, G. B.; Scott, J. M.; Miracle, D. B. Mechanical Properties of $Nb_{25}Mo_{25}Ta_{25}W_{25}$ and $V_{20}Nb_{20}Mo_{20}Ta_{20}W_{20}$ Refractory High Entropy Alloys. *Intermetallics* **2011**, *19* (5), 698-706.
7.   Senkov, O. N.; Scott, J. M.; Senkova, S. V.; Miracle, D. B.; Woodward, C. F. Microstructure and Room Temperature Properties of a High-Entropy TaNbHfZrTi Alloy. *J. Alloys Compd.* **2011**, *509* (20), 6043-6048.
8.   Sahlberg, M.; Karlsson, D.; Zlotea, C.; Jansson, U. Superior Hydrogen Storage in High Entropy Alloys. *Sci. Rep.* **2016**, *6*(1), 36770.
9.   Karlsson, D.; Ek, G.; Cedervall, J.; Zlotea, C.; Moller, K. T.; Hansen, T. C.; Bednarcik, J.; Paskevicius, M.; Sorby, M. H.; Jensen, T. R.; Jansson, U.; Sahlberg, M. Structure and Hydrogenation Properties of a HfNbTiVZr High-Entropy Alloy. *Inorg. Chem.* **2018**, *57* (4), 2103-2110.
10.   George, E. P.; Raabe, D.; Ritchie, R. O. High-entropy Alloys. *Nat. Rev. Mater.* **2019**, *4* (8), 515-534.
11.   Xin, Y.; Li, S.; Qian, Y.; Zhu, W.; Yuan, H.; Jiang, P.; Guo, R.; Wang, L. High-Entropy Alloys as a Platform for Catalysis: Progress, Challenges, and Opportunities. *ACS Catal.* **2020**, *10* (19), 11280-11306.
12.   Li, H.; Shin, K.; Henkelman, G. Effects of Ensembles, Ligand, and Strain on Adsorbate Binding to Alloy Surfaces. *J. Chem. Phys* **2018**, *149* (17), 174705.
13.   Yao, Y.; Dong, Q.; Brozena, A.; Luo, J.; Miao, J.; Chi, M.; Wang, C.; Kevrekidis, I. G.; Ren, Z. J.; Greeley, J.; Wang, G.; Anapolsky, A.; Hu, L. High-entropy nanoparticles: Synthesis-structure-property relationships and data-driven discovery. *Science* **2022**, *376* (6589), eabn3103.
14.   Yao, Y.; Huang, Z.; Xie, P.; Lacey, S. D.; Jacob, R. J.; Xie, H.; Chen, F.; Nie, A.; Pu, T.; Rehwoldt, M.; Yu, D.; Zachariah, M. R.; Wang, C.; Shahbazian-Yassar, R.; Li, J.; Hu, L. Carbothermal Shock Synthesis of High-entropy-alloy Nanoparticles. *Science* **2018**, *359* (6383), 1489-1494.
15.   Gao, S.; Hao, S.; Huang, Z.; Yuan, Y.; Han, S.; Lei, L.; Zhang, X.; Shahbazian-Yassar, R.; Lu, J. Synthesis of High-entropy Alloy Nanoparticles on Supports by the Fast Moving Bed Pyrolysis. *Nat. Commun.* **2020**, *11* (1), 2016.

16. Feng, J.; Chen, D.; Pikhitsa, P. V.; Jung, Y.-h.; Yang, J.; Choi, M. Unconventional Alloys Confined in Nanoparticles: Building Blocks for New Matter. *Matter* **2020**, *3* (5), 1646-1663.

17. Yang, Y.; Song, B.; Ke, X.; Xu, F.; Bozhilov, K. N.; Hu, L.; Shahbazian-Yassar, R.; Zachariah, M. R. Aerosol Synthesis of High Entropy Alloy Nanoparticles. *Langmuir* **2020**, *36* (8), 1985-1992.

18. Mori, K.; Hashimoto, N.; Kamiuchi, N.; Yoshida, H.; Kobayashi, H.; Yamashita, H. Hydrogen Spillover-driven Synthesis of High-entropy Alloy Nanoparticles as a Robust Catalyst for CO_2 Hydrogenation. *Nat. Commun.* **2021**, *12* (1), 3884.

19. Qiao, H.; Saray, M. T.; Wang, X.; Xu, S.; Chen, G.; Huang, Z.; Chen, C.; Zhong, G.; Dong, Q.; Hong, M.; Xie, H.; Shahbazian-Yassar, R.; Hu, L. Scalable Synthesis of High Entropy Alloy Nanoparticles by Microwave Heating. *ACS Nano* **2021**, *15* (9), 14928-14937.

20. Bagot, P. A. J.; Kruska, K.; Haley, D.; Carrier, X.; Marceau, E.; Moody, M. P.; Smith, G. D. W. Oxidation and Surface Segregation Behavior of a Pt–Pd–Rh Alloy Catalyst. *J. Phys. Chem. C* **2014**, *118* (45), 26130-26138.

21. Fei, H.; Dong, J.; Wan, C.; Zhao, Z.; Xu, X.; Lin, Z.; Wang, Y.; Liu, H.; Zang, K.; Luo, J.; Zhao, S.; Hu, W.; Yan, W.; Shakir, I.; Huang, Y.; Duan, X. Microwave-Assisted Rapid Synthesis of Graphene-Supported Single Atomic Metals. *Adv. Mater.* **2018**, *30* (35), e1802146.

22. Ju, Z.; Qi, X.; Sfadia, R.; Wang, M.; Tseng, E.; Panchul, E. C.; Carter, S. A.; Kauzlarich, S. M. Single-Crystalline Germanium Nanocrystals Via a Two-Step Microwave-Assisted Colloidal Synthesis from GeI_4. *ACS Mater. Au* **2022**, *2* (3), 330-342.

23. Zhong, G.; Xu, S.; Cui, M.; Dong, Q.; Wang, X.; Xia, Q.; Gao, J.; Pei, Y.; Qiao, Y.; Pastel, G.; Sunaoshi, T.; Yang, B.; Hu, L. Rapid, High-Temperature, in Situ Microwave Synthesis of Bulk Nanocatalysts. *Small* **2019**, *15* (47), e1904881.

24. Renteria, J. D.; Ramirez, S.; Malekpour, H.; Alonso, B.; Centeno, A.; Zurutuza, A.; Cocemasov, A. I.; Nika, D. L.; Balandin, A. A. Strongly Anisotropic Thermal Conductivity of Free-Standing Reduced Graphene Oxide Films Annealed at High Temperature. *Adv. Funct. Mater*. **2015**, *25* (29), 4664-4672.

25. Bondesgaard, M.; Broge, N. L. N.; Mamakhel, A.; Bremholm, M.; Iversen, B. B. General Solvothermal Synthesis Method for Complete Solubility Range Bimetallic and High-Entropy Alloy Nanocatalysts. *Adv. Funct. Mater.* **2019**, *29* (50), 1905933.

26. Wu, D.; Kusada, K.; Yamamoto, T.; Toriyama, T.; Matsumura, S.; Kawaguchi, S.; Kubota, Y.; Kitagawa, H. Platinum-Group-Metal High-Entropy-Alloy Nanoparticles. *J. Am. Chem. Soc.* **2020**, *142* (32), 13833-13838.

27. Chen, Y.; Zhan, X.; Bueno, S. L. A.; Shafei, I. H.; Ashberry, H. M.; Chatterjee, K.; Xu, L.; Tang, Y.; Skrabalak, S. E. Synthesis of Monodisperse High Entropy Alloy Nanocatalysts from Core@Shell Nanoparticles. *Nanoscale. Horiz.* **2021**, *6* (3), 231-237.

28. Bueno, S. L. A.; Leonardi, A.; Kar, N.; Chatterjee, K.; Zhan, X.; Chen, C.; Wang, Z.; Engel, M.; Fung, V.; Skrabalak, S. E. Quinary, Senary, and Septenary High Entropy Alloy Nanoparticle Catalysts from Core@Shell Nanoparticles and the Significance of Intraparticle Heterogeneity. *ACS Nano* **2022**, *16* (11), 18873-18885.

29. Kar, N.; McCoy, M.; Wolfe, J.; Bueno, S. L. A.; Shafei, I. H.; Skrabalak, S. E. Retrosynthetic Design of Core–Shell Nanoparticles for Thermal Conversion to Monodisperse High-entropy Alloy Nanoparticles. *Nat. Synth.* **2024**, *3*(2), 175-184.

30. Xia, X.; Wang, Y.; Ruditskiy, A.; Xia, Y. 25th Anniversary Article: Galvanic Replacement: A Simple and Versatile Route to Hollow Nanostructures with Tunable and Well-Controlled Properties. *Adv. Mater.* **2013**, *25* (44), 6313-6333.

31. Zou, Y.; Zhou, X.; Ma, J.; Yang, X.; Deng, Y. Recent Advances in Amphiphilic Block Copolymer Templated Mesoporous Metal-based Materials: Assembly Engineering and Applications. *Chem. Soc. Rev.* **2020**, *49* (4), 1173-1208.

32. Jiang, B.; Li, C.; Imura, M.; Tang, J.; Yamauchi, Y. Multimetallic Mesoporous Spheres Through Surfactant-Directed Synthesis. *Adv. Sci.* **2015**, *2* (8), 1500112.

33. De Marco, M. L.; Baaziz, W.; Sharna, S.; Devred, F.; Poleunis, C.; Chevillot-Biraud, A.; Nowak, S.; Haddad, R.; Odziomek, M.; Boissiere, C.; Debecker, D. P.; Ersen, O.; Peron, J.; Faustini, M. High-Entropy-Alloy Nanocrystal Based Macro- and Mesoporous Materials. *ACS Nano* **2022**, *16* (10), 15837-15849.

34. Kang, Y.; Cretu, O.; Kikkawa, J.; Kimoto, K.; Nara, H.; Nugraha, A. S.; Kawamoto, H.; Eguchi, M.; Liao, T.; Sun, Z.; Asahi, T.; Yamauchi, Y. Mesoporous Multimetallic Nanospheres with Exposed Highly Entropic Alloy Sites. *Nat. Commun.* **2023**, *14* (1), 4182.

35. Rekha, M. Y.; Mallik, N.; Srivastava, C. First Report on High Entropy Alloy Nanoparticle Decorated Graphene. *Sci Rep* **2018**, *8* (1), 8737.

36. Urs, K. M. B.; Katiyar, N. K.; Kumar, R.; Biswas, K.; Singh, A. K.; Tiwary, C. S.; Kamble, V. Multi-component (Ag-Au-Cu-Pd-Pt) Alloy Nanoparticle-Decorated P-Type 2D-Molybdenum Disulfide (MoS_2) for Enhanced Hydrogen Sensing. *Nanoscale* **2020**, *12* (22), 11830-11841.

37. Zhu, G.; Jiang, Y.; Yang, H.; Wang, H.; Fang, Y.; Wang, L.; Xie, M.; Qiu, P.; Luo, W. Constructing Structurally Ordered High-Entropy Alloy Nanoparticles on Nitrogen-Rich Mesoporous Carbon Nanosheets for High-Performance Oxygen Reduction. *Adv. Mater.* **2022**, *34* (15), e2110128.

38. Pescara, B.; Mazzio, K. A. Morphological and Surface-State Challenges in Ge Nanoparticle Applications. *Langmuir* **2020**, *36* (40), 11685-11701.

39. Wind, L.; Sistani, M.; Song, Z.; Maeder, X.; Pohl, D.; Michler, J.; Rellinghaus, B.; Weber, W. M.; Lugstein, A. Monolithic Metal-Semiconductor-Metal Heterostructures Enabling Next-Generation Germanium Nanodevices. *ACS Appl. Mater. Interfaces* **2021**, *13* (10), 12393-12399.

40. Rost, C. M.; Sachet, E.; Borman, T.; Moballegh, A.; Dickey, E. C.; Hou, D.; Jones, J. L.; Curtarolo, S.; Maria, J. P. Entropy-Stabilized Oxides. *Nat. Commun.* **2015**, *6* (1), 8485.

41. Zhang, R.Z.; Reece, M. J. Review of High Entropy Ceramics: Design, Synthesis, Structure and Properties. *J. Mater. Chem. A* **2019**, *7* (39), 22148-22162.

42. Boyjoo, Y.; Wang, M.; Pareek, V. K.; Liu, J.; Jaroniec, M. Synthesis and Applications of Porous Non-Silica Metal Oxide Submicrospheres. *Chem. Soc. Rev.* **2016**, *45* (21), 6013-6047.

43. Wang, G.; Qin, J.; Feng, Y.; Feng, B.; Yang, S.; Wang, Z.; Zhao, Y.; Wei, J. Sol-Gel Synthesis of Spherical Mesoporous High-Entropy Oxides. *ACS Appl. Mater. Interfaces* **2020**, *12* (40), 45155-45164.

44. Wang, K.; Chen, L.; Xu, C.; Zhang, W.; Liu, Z.; Wang, Y.; Ouyang, J.; Zhang, X.; Fu, Y.; Zhou, Y. Microstructure and Mechanical Properties of (TiZrNbTaMo)C High-Entropy Ceramic. *J. Mater. Sci. Technol.* **2020**, *39*, 99-105.

45. Sure, J.; Sri Maha Vishnu, D.; Kim, H. K.; Schwandt, C. Facile Electrochemical Synthesis of Nanoscale (TiNbTaZrHf)C High-Entropy Carbide Powder. *Angew. Chem., Int. Ed.* **2020**, *59* (29), 11830-11835.

46. Jin, T.; Sang, X.; Unocic, R. R.; Kinch, R. T.; Liu, X.; Hu, J.; Liu, H.; Dai, S. Mechanochemical-Assisted Synthesis of High-Entropy Metal Nitride via a Soft Urea Strategy. *Adv. Mater.* **2018**, *30* (23), e1707512.

47. Gild, J.; Zhang, Y.; Harrington, T.; Jiang, S.; Hu, T.; Quinn, M. C.; Mellor, W. M.; Zhou, N.; Vecchio, K.; Luo, J. High-Entropy Metal Diborides: A New Class of High-Entropy Materials and a New Type of Ultrahigh Temperature Ceramics. *Sci. Rep.* **2016**, *6*, 37946.

48. Dong, S.; Li, Q.; Hu, H.; Zhang, X.; Li, Y.; Ye, K.; Hou, W.; He, J.; Zhao, H. Application of Rare-Earth High Entropy Boride in Electrocatalytic Hydrogen Evolution Reaction. *Appl. Surf. Sci.* **2023**, *615*, 156413.

49. Qin, Y.; Liu, J.-X.; Li, F.; Wei, X.; Wu, H.; Zhang, G.-J. A High Entropy Silicide by Reactive Spark Plasma Sintering. *J. Adv. Ceram.* **2019**, *8* (1), 148-152.

50. Wang, T.; Chen, H.; Yang, Z.; Liang, J.; Dai, S. High-Entropy Perovskite Fluorides: A New Platform for Oxygen Evolution Catalysis. *J. Am. Chem. Soc.* **2020**, *142* (10), 4550-4554.

51. Folgueras, M. C.; Jiang, Y.; Jin, J.; Yang, P. High-Entropy Halide Perovskite Single Crystals Sabilized by Mild Chemistry. *Nature* **2023**, *621* (7978), 282-288.

52. Zhang, R. Z.; Gucci, F.; Zhu, H.; Chen, K.; Reece, M. J. Data-Driven Design of Ecofriendly Thermoelectric High-Entropy Sulfides. *Inorg. Chem.* **2018**, *57* (20), 13027-13033.

53. McCormick, C. R.; Schaak, R. E. Simultaneous Multication Exchange Pathway to High-Entropy Metal Sulfide Nanoparticles. *J. Am. Chem. Soc.* **2021**, *143* (2), 1017-1023.

54. Chen, G. Z.; Fray, D. J.; Farthing, T. W. Direct Electrochemical Reduction of Titanium Dioxide to Titanium in Molten Calcium Chloride. *Nature* **2000**, *407* (6802), 361-364.

55. Folgueras, M. C.; Louisia, S.; Jin, J.; Gao, M.; Du, A.; Fakra, S. C.; Zhang, R.; Seeler, F.; Schierle-Arndt, K.; Yang, P. Ligand-Free Processable Perovskite Semiconductor Ink. *Nano Lett.* **2021**, *21* (20), 8856-8862.

56. Shi, X. L.; Zou, J.; Chen, Z. G., Advanced Thermoelectric Design: From Materials and Structures to Devices. *Chem. Rev.* **2020,** *120* (15), 7399-7515.

57. Rabie, M. A.; Mirza, S.; Hu, Y.; Haddara, Y. M., Cobalt Germanide Contacts: Growth Reaction, Phase Formation Models, and Electrical Properties. *J. Mater. Sci. Mater. Electron.* **2019,** *30* (11), 10031-10063.

58. Götsch, T.; Stöger-Pollach, M.; Thalinger, R.; Penner, S., The Nanoscale Kirkendall Effect in Pd-Based Intermetallic Phases. *J. Phys. Chem. C* **2014,** *118* (31), 17810-17818.

59. Vaughn, D. D.; Sun, D.; Moyer, J. A.; Biacchi, A. J.; Misra, R.; Schiffer, P.; Schaak, R. E., Solution-Phase Synthesis and Magnetic Properties of Single-Crystal Iron Germanide Nanostructures. *Chem. Mater.* **2013,** *25* (21), 4396-4401.

60. Yan, C.; Higgins, J. M.; Faber, M. S.; Lee, P. S.; Jin, S., Spontaneous Growth and Phase Transformation of Highly Conductive Nickel Germanide Nanowires. *ACS Nano* **2011,** *5* (6), 5006-5014.

61. Yoon, H.; Seo, K.; Bagkar, N.; In, J.; Park, J.; Kim, J.; Kim, B., Vertical Epitaxial Co_5Ge_7 Nanowire and Nanobelt Arrays on A Thin Graphitic Layer for Flexible Field Emission Displays. *Adv. Mater.* **2009,** *21* (48), 4979-4982.

62. Nakaya, Y.; Hayashida, E.; Asakura, H.; Takakusagi, S.; Yasumura, S.; Shimizu, K. I.; Furukawa, S. High-Entropy Intermetallics Serve Ultrastable Single-Atom Pt for Propane Dehydrogenation. *J. Am. Chem. Soc.* **2022**, *144* (35), 15944-15953.

63. Collings, P. J. Simple Measurement of the Band Gap in Silicon and Germanium. *Am. J. Phys.* **1980**, *48* (3), 197-199.

64. Maeda, Y.; Tsukamoto, N.; Yazawa, Y.; Kanemitsu, Y.; Masumoto, Y. Visible Photoluminescence of Ge Microcrystals Embedded in SiO_2 Glassy Matrices. *Appl. Phys. Lett.* **1991**, *59* (24), 3168-3170.

65. Maeda, Y. Visible Photoluminescence of Ge Microcrystals Embedded in SiO_2 Glassy Matrix: Evidence in Support of the Quantum-Confinement Mechanism. *Phys. Rev. B Condens. Matter Mater. Phys.* **1995**, *51* (3), 1658-1670.

66. Cho, S.; Kang, I. M.; Kim, K. R.; Park, B.; Cho, J. S. H.; Kang, S.; Kim, I. M.; Park, B. K. R.; Kang, I. Man. Silicon-Compatible High-Hole-Mobility Transistor with an Undoped Germanium Channel for Low-Power Application. *Appl. Phys. Lett.* **2013**, *103* (22), 222102.

67. Michel, J.; Liu, J.; Kimerling, L. C. High-Performance Ge-on-Si Photodetectors. *Nat. Photon*. **2010**, *4* (8), 527-534.

68. Yongping, D.; Ying, D.; Bapat, A.; Nowak, J. D.; Carter, C. B.; Kortshagen, U. R.; Campbell, S. A. Single Nanoparticle Semiconductor Devices. *IEEE Trans. Electron Devices* **2006**, *53* (10), 2525-2531.

69. Serino, A. C.; Ko, J. S.; Yeung, M. T.; Schwartz, J. J.; Kang, C. B.; Tolbert, S. H.; Kaner, R. B.; Dunn, B. S.; Weiss, P. S. Lithium-Ion Insertion Properties of Solution-Exfoliated Germanane. *ACS Nano* **2017**, *11* (8), 7995-8001.

70. Lee, D. C.; Pietryga, J. M.; Robel, I.; Werder, D. J.; Schaller, R. D.; Klimov, V. I. Colloidal Synthesis of Infrared-Emitting Germanium Nanocrystals. *J. Am. Chem. Soc.,* **2009**, *131* (10). 3436-3437.

71. Prabakar, S.; Shiohara, A.; Hanada, S.; Fujioka, K.; Yamamoto, K.; Tilley, R. D. Size Controlled Synthesis of Germanium Nanocrystals by Hydride Reducing Agents and Their Biological Applications. *Chem. Mater.* **2010**, *22* (2). 482-486.

72. Vaughn II, D. D.; Schaak, R. E. Synthesis, Properties and Applications of Colloidal Germanium and Germanium-Based Nanomaterials. *Chem. Soc. Rev.* **2013**, *42* (7), 2861–2879.

73. McVey, B. F. P.; Prabakar, S.; Gooding, J. J.; Tilley, R. D. Solution Synthesis, Surface Passivation, Optical Properties, Biomedical Applications, and Cytotoxicity of Silicon and Germanium Nanocrystals. *Chempluschem* **2017**, *82* (1), 60–73.

74. Nogales, E.; Montone, A.; Cardellini, F.; ndez, B. M.; Piqueras, J. Visible Cathodoluminescence from Mechanically Milled Germanium. *Semicond. Sci. Technol.* **2002**, *17* (12), 1267–1271.

75. Taylor, B. R.; Kauzlarich, S. M.; Delgado, G. R.; Lee, H. W. H. Solution Synthesis and Characterization of Quantum Confined Ge Nanoparticles. *Chem. Mater.* **1999**, *11* (9), 2493–2500.

76. Chiu, H. W.; Kauzlarich, S. M. Investigation of Reaction Conditions for Optimal Germanium Nanoparticle Production by a Simple Reduction Route. *Chem. Mater.* **2006**, *18* (4), 1023–1028.

77. Prabakar, S.; Shiohara, A.; Hanada, S.; Fujioka, K.; Yamamoto, K.; Tilley, R. D. Size Controlled Synthesis of Germanium Nanocrystals by Hydride Reducing Agents and Their Biological Applications. *Chem. Mater.* **2010**, *22* (2), 482–486.

78. Vaughn II, D. D.; Bondi, J. F.; Schaak, R. E. Colloidal Synthesis of Air-Stable Crystalline Germanium Nanoparticles with Tunable Sizes and Shapes. *Chem. Mater.* **2010**, *22* (22), 6103–6108.

79. Wang, W.; Huang, J.; Ren, Z. Synthesis of Germanium Nanocubes by a Low-Temperature Inverse Micelle Solvothermal Technique. *Langmuir* **2005**, *21* (2), 751–754.

80. Javadi, M.; Picard, D.; Sinelnikov, R.; Narreto, M. A.; Hegmann, F. A.; Veinot, J. G. C. Synthesis and Surface Functionalization of Hydride-Terminated Ge Nanocrystals Obtained from the Thermal Treatment of $Ge(OH)_2$. *Langmuir* **2017**. *33* (35), 8757–8765.

81. Hossain, M. A.; Javadi, M.; Yu, H.; Thiessen, A. N.; Ikpo, N.;Oliynyk, A. O.; Veinot, J. G. C. Dehydrocoupling – an Alternative Approach to Functionalizing Germanium Nanoparticle Surfaces. *Nanoscale* **2020**, *12* (11), 6271–6278.

82. Li, M.; Su, S.; Wong, H.S.; Li, L.; How 2D Semiconductors Could Extend Moore's Law. *Nature* **2019**, *567* (7748), 169-170.

83. Novoselov, K. S.; Mishchenko, A.; Carvalho, A.; Castro Neto, A. H. 2D Materials and Van der Waals Heterostructures. *Science* **2016**, *353* (6298), aac9439.

84. Huey, W. L. B.; Goldberger, J. E. Covalent Functionalization of Two-Dimensional Group 14 Graphane Analogues. *Chem. Soc. Rev.* **2018**, *47* (16), 6201-6223.

85. Jiang, S.; Krymowski, K.; Asel, T.; Arguilla, M. Q.; Cultrara, N. D.; Yanchenko, E.; Yang, X.; Brillson, L. J.; Windl, W.; Goldberger, J. E. Tailoring the Electronic Structure of Covalently Functionalized Germanane via the Interplay of Ligand Strain and Electronegativity. *Chem. Mater.* **2016**, *28* (21), 8071-8077.

86. Serino, A. C.; Ko, J. S.; Yeung, M. T.; Schwartz, J. J.; Kang, C. B.; Tolbert, S. H.; Kaner, R. B.; Dunn, B. S.; Weiss, P. S. Lithium-Ion Insertion Properties of Solution-Exfoliated Germanane. *ACS Nano* **2017**, *11* (8), 7995-8001.

87. Madhushankar, B. N.; Kaverzin, A.; Giousis, T.; Potsi, G.; Gournis, D.; Rudolf, P.; Blake, G. R.; van der Wal, C. H.; van Wees, B. J. Electronic Properties of Germanane Field-Effect Transistors. *2D Mater.* **2017**, *4* (2), 021009.

88. Vogg, G.; Brandt, M. S.; Stutzmann, M. Polygermyne—A Prototype System for Layered Germanium Polymers. *Adv. Mater.* **2000**, *12* (17), 1278-1281.

89. Bianco, E.; Butler, S.; Jiang, S.; Restrepo, O. D.; Windl, W.; Goldberger, J. E. Stability and Exfoliation of Germanane: A Germanium Graphane Analogue. *ACS Nano* **2013**, *7* (5), 4414-4421.

90. Jiang, S.; Butler, S.; Bianco, E.; Restrepo, O. D.; Windl, W.; Goldberger, J. E. Improving the stability and optical properties of germanane via one-step covalent methyl-termination. *Nat. Commun.* **2014**, *5* (1), 3389.

91. Ng, S.; Pumera, M., 2D Functionalized Germananes: Synthesis and Applications. *Adv. Mater.* **2023,** *35* (7), e2207196.

92. Hartman, T.; Sturala, J.; Plutnar, J.; Sofer, Z., Alkali Metal Arenides as a Universal Synthetic Tool for Layered 2D Germanene Modification. *Angew. Chem., Int. Ed.* **2019,** *58* (46), 16517-16522.

93. Choi, K.; Buriak, J. M., Hydrogermylation of Alkenes and Alkynes on Hydride-Terminated Ge(100) Surfaces. *Langmuir* **2000,** *16* (20), 7737-7741.

94. Yu, H.; Helbich, T.; Scherf, L. M.; Chen, J.; Cui, K.; Fässler, T. F.; Rieger, B.; Veinot, J. G. C., Radical-Initiated and Thermally Induced Hydrogermylation of Alkenes on the Surfaces of Germanium Nanosheets. *Chem. Mater.* **2018,** *30* (7), 2274-2280.

95. Yu, H.; Thiessen, A. N.; Hossain, M. A.; Kloberg, M. J.; Rieger, B.; Veinot, J. G. C., Thermally Induced Dehydrogenative Coupling of Organosilanes and H-Terminated Silicon Quantum Dots onto Germanane Surfaces. *Chem. Mater.* **2020**, *32* (11), 4536-4543.

2. Chapter 2: Metal Nanoparticles-decorated Germanane for Selective Photocatalytic Aerobic Oxidation of Benzyl Alcohol[a]

Germanane and silicane are two-dimensional semiconductors comprised of atoms bonded in an arrangement approximating the (111) surfaces of hydrogen-terminated Ge and Si, respectively.[1] These materials possess surface chemistry dependant optical band gaps in the range of 1.4– 1.7 eV (germanane)[2] and 2.4–2.6 eV (silicane).[3] In line with a focus of this Chapter, studies have reported the use of both the Si and Ge materials as photocatalysts.[4] Visible light irradiation of hydrogen-terminated germanane provided Liu *et al.* with a source of hydrogen from aqueous methanol, as well as a means to photodegrade rhodamine B.[5] These authors later extended this same reactivity to methyl-terminated germanane.[6] Pumera and colleagues expanded upon Liu's studies and explored the reactivity of an array of germananes bearing various surface groups while evaluating the impact of surface chemistry on their photoelectrocatalytic activity in the hydrogen evolution reaction.[7] Taking a different approach, Ozin and coworkers modified silicanes by exploiting the reducing nature of Si–H surfaces and decorated said surfaces with Pd nanoparticles; these materials catalyzed photoreduction of carbon dioxide.[8] Most recently, Zhao *et al.* described yet another approach toward tailoring group 14 element nanosheets with the formation of

"siligenes" terminated with a mixture of –H/–OH surface groups. These mixed element 2D materials provided photocatalytic hydrogen evolution from water and carbon dioxide reduction to provide carbon monoxide.[9] All of these studies point to the tunability, intriguing reactivity, and practical potential of 2D nanomaterials based upon group 14 elements.

Drawing inspiration from metal decorated silicane as well as the established reactivity of bulk germanium,[10] we explored the reactivity of germanane (GeNS) and demonstrated the straightforward deposition of a variety of metal nanoparticles (MNPs) onto their surfaces (Figure 2.1).
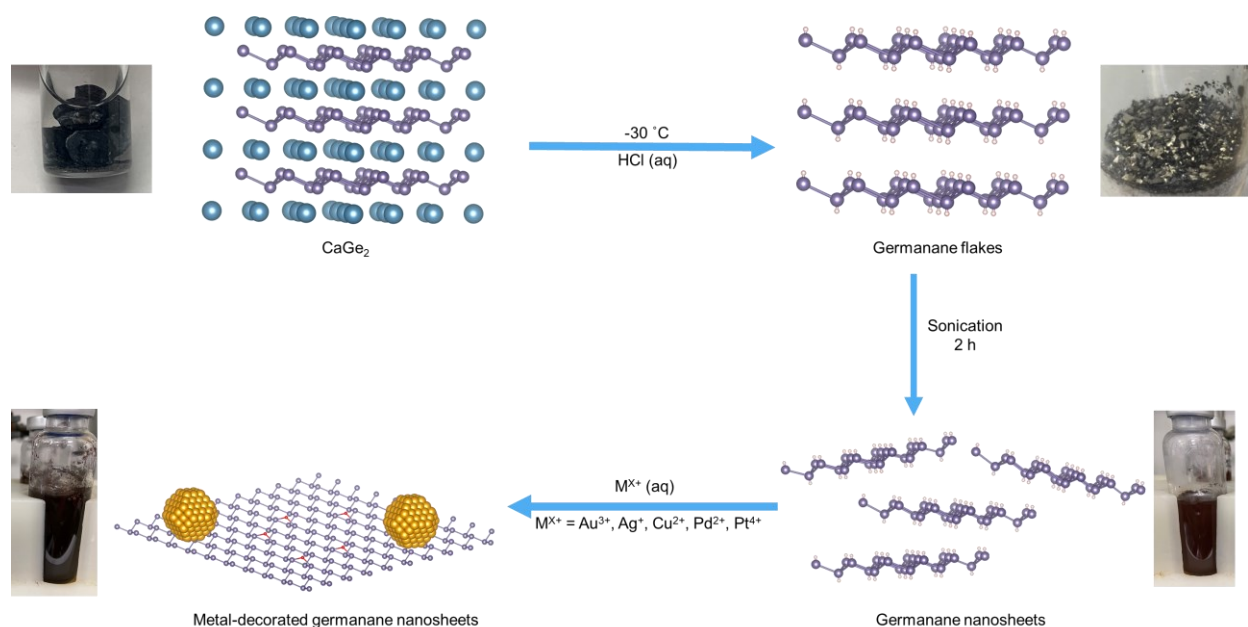
Figure 2.1. A pictorial illustration of the formation of metal nanoparticles germanane. Germanane flakes were prepared via topotactic deintercalation of calcium ions from CaGe$_2$. The flakes were subsequently sonicated in the Mill-Q water for 2 h to obtain the germanane nanosheets. Aqueous solutions of metal salts (i.e., AuCl$_3$, AgNO$_3$, CuCl$_2$, PdCl$_2$ and PtCl$_4$) were added into the aqueous suspension of germanane nanosheets. Metal ions are reduced to metal nanoparticles and deposited onto the germanane surfaces with the evolution of the bubbles.

2.1 Selective Oxidation of Alcohol

Selectively oxidizing alcohols to aldehydes so they can be utilized in aldol condensation reactions to form β-hydroxyaldehydes is essential to fine chemical and pharmaceutical syntheses (e.g., synthesis of cinnamaldehyde).[11] Traditionally, these transformations are achieved using stoichiometric quantities of homogenous chromate- or permanganate-based oxidants that bring with them concerns related to toxicity and responsible disposal.[12] Of late, much effort has been focused on developing alternative reaction schemes including those exploiting sustainable heterogeneous catalysts.[13-15] Many heterogeneous catalysts based upon active noble metals (e.g., Au, Pd, Pt, and their alloys) have been reported.[16,17] Among the new catalytic systems that have been explored for photocatalytic oxidation, metal-decorated semiconductor (e.g., TiO_2, CdS, Bi_2WO_6) substrates that can be light activated have garnered much attention in part because of the advent of efficient light sources that are driving a concerted push to decarbonize industrial chemical conversions.[16,18,19] In this Chapter, we first prepare metal-decorated germanane hybrid nanomaterials and then demonstrate that they can catalyze visible light-mediated, solvent-free oxidation of benzyl alcohol (BA) to benzaldehyde (BAL).

2.2 Materials and Methods

2.2.1 Materials

Germanium (Ge, 99.999%), calcium (Ca, 99.0%), gold chloride ($AuCl_3$, 99.99%), silver nitrate ($AgNO_3$, 99.9999%), copper chloride ($CuCl_2$, 99.999%), palladium chloride ($PdCl_2$, 99.9%) and platinum chloride ($PtCl_4$, 99.999%) were purchased from Sigma-Aldrich and hydrochloric acid (HCl, 37% w/w), ethanol (anhydrous) dichloromethane (HPLC grade) and toluene (HPLC grade) were purchased from Fisher Scientific. Milli-Q (18.2 MΩ·cm at 25 °C) water was used for

all experiments. All organic solvents were dried using an Innovative Technology, Inc. Grubbs-type solvent purification system.

2.2.2 Synthesis of CaGe$_2$

A stoichiometric mixture of calcium and germanium was pressed to a pellet and subsequently melted in an arc furnace. It is also noticed that an arc furnace in an ambient condition produces CaGe$_2$ in adequate quality after the chamber has been evacuated and backfilled with argon for three cycles (Figure 2.2). Since calcium has a high vapor pressure compared to germanium, the granulated calcium needs to be sandwiched between germanium powder during the pellet press. Direct exposure to a high temperature will result in the evaporation of calcium and leave elemental germanium in the sample. To ensure effective homogenization, the resulting silver metallic regulus was melted upon simultaneous heating from the top and bottom in the arc furnace, ground thoroughly in an agate mortar, pressed again to a pellet, melted from both sides in the arc furnace, and ground into a powder again.[20]
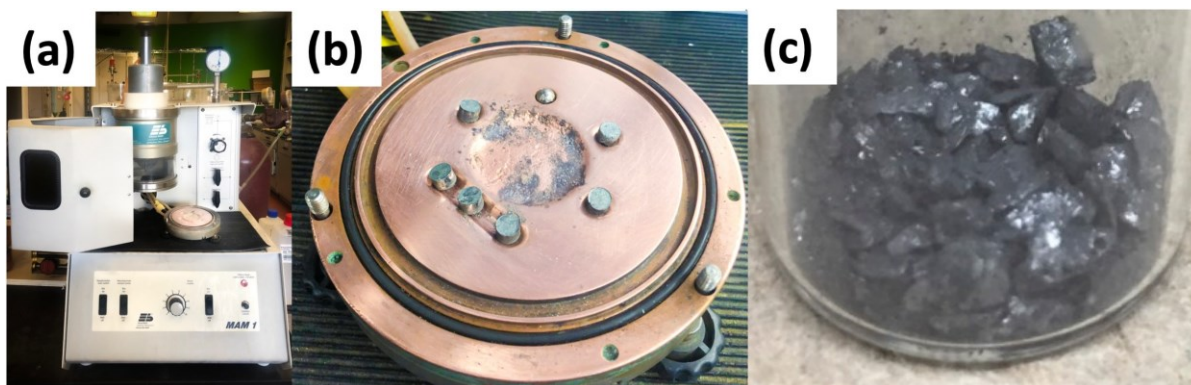
Figure 2.2. Photographs of (a) arc furnace, model Compact Arc Melter MAM-1, (b) calcium and germanium pressed into a pellet, and (c) the as prepared CaGe$_2$ granular.

2.2.3 Synthesis of Germanane (GeNSs)

Germanane was prepared via topotactic deintercalation of calcium ions from $CaGe_2$ using modified literature procedure.[21] Briefly, 0.3 g (2.7 mmol) of freshly prepared granular $CaGe_2$ was loaded into Schlenk flask that was charged with concentrated aqueous HCl (30 mL) that had been cooled to -30 ˚C. The reaction mixture was maintained at -30 °C for at least 7 days and agitated at regular intervals. Subsequently, the reaction mixture was filtered using a glass frit under nitrogen to provide grey flakes that exhibited a metallic sheen that were washed three times with ice-cold Milli-Q water and anhydrous ethanol (Figure 2.3). The resulting shiny grey solid was dried in vacuo on the Schlenk line and stored in a nitrogen-filled glovebox and subdued light until further use.
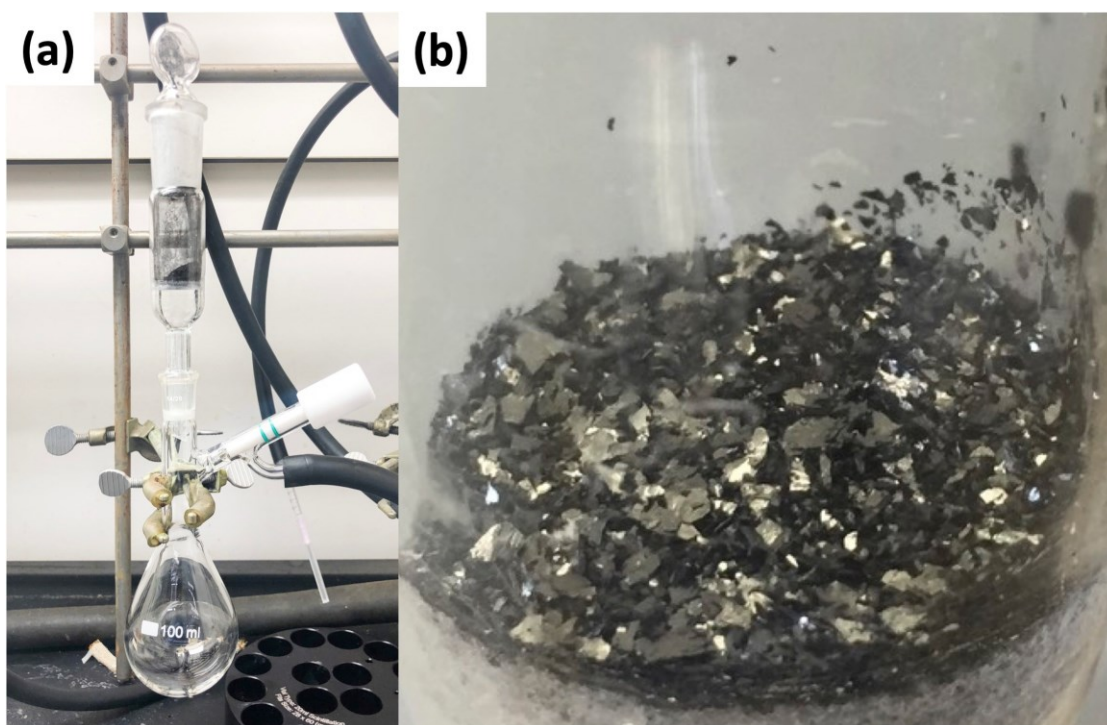
Figure 2.3. Photographs of (a) purification and drying apparatus and (b) dried germanane flakes in a glass frit.

2.2.4 Synthesis of Metal-decorated Germanium Nanosheets

To prepare Metal-decorated germanium nanosheets (M@GeNSs; M = Au, Ag, Cu, Pt, Pd), germanane powder (73 mg; 1 mmol) of was dispersed in 4 mL distilled water. The mixture was sonicated in a bath sonicator for 2 hours to yield a red suspension of exfoliated GeNSs. Subsequently, an appropriate mass (0.05 mmol) of the anhydrous metal salt in question ($AuCl_3$, $AgNO_3$, $CuCl_2$, $PdCl_2$ and $PtCl_4$) was dissolved in 1 mL of Milli-Q water. The metal salt solution (i.e., 0.1 ml) was then added into the GeNS dispersion at room temperature in subdued light and the original red suspensions turned black. The mixture was stirred for 10 min and the product was recovered by centrifugation and washed with Milli-Q water three times. The product was dried for 12 h in vacuo and subsequently stored in nitrogen filled glovebox and subdued light. Typical mass yields for this procedure were 55 mg.

2.2.5 Synthesis of Unsupported Metal Nanoparticles

Unsupported metal nanoparticles (MNPs) used for comparison with GeNS supported catalysts were synthesized by via $NaBH_4$ reduction.[22] Typically, 0.05 mol metal salts (i.e., $AuCl_3$, $AgNO_3$, $CuCl_2$, $PdCl_2$, $PtCl_4$) was dissolved in a 25 mL Milli-Q water and vigorously stirred at room temperature in air. Subsequently, aqueous sodium borohydride ($NaBH_4$, 100 mM, 1 mL) was rapidly injected into metal salt solution, immediately leading to a light-yellow solution. This process was also accompanied by the evolution of bubbles. After 5 min, the colloidal solution turned to a deep yellow due to the formation of small nanoparticles. Then the MNPs were isolated by centrifugation, resuspended with sonication in 5 mL ethanol, isolated via centrifugation (3 times). This suspension/centrifugation procedure was repeated three times with 5 mL of Milli-Q water. Finally, the resulting MNPs were stored Milli-Q water until further use.

2.2.6 Fabrication of Thin Films of GeNSs and Ag@GeNSs

Thin films of GeNSs were deposited onto glass substrates by first suspending GeNSs (73 mg, 1 mmol) in 1,3-dioxane (1 mL) with sonication for 30 min. Subsequently, a 100 μL aliquot of the suspension was drop-coated onto a glass substrate that had been precleaned by ethanol, acetone and Milli-Q water and dried in vacuum oven for 2h. The glass supported GeNS thin films were subsequently immersed in 10 mL of aqueous AgNO$_3$ (0.05 mmol) for 10 min. Upon removing the film from the AgNO$_3$ solution, the films were rinsed with 5 mL Milli-Q water three times and dried in a stream of flowing dry N$_2$ gas. The films were transferred to a nitrogen filled glovebox and maintained in subdued light.

2.3 Material Characterization

2.3.1 Fourier Transformed Infrared (FTIR) Spectroscopy

FTIR Analyses were performed using a Thermo Nicolet 8700 FTIR Spectrometer and Continuum FTIR Microscope. Samples were prepared by drop coating a toluene dispersion of the solid sample in question onto an electronics-grade Si-wafer (N-type, 100 surface, 100 μm thickness and 10 ohm·cm resistivity) and dried under flowing nitrogen.

2.3.2 Electron Microscopy

Transmission electron microscopy (TEM) bright and dark field images were acquired using a JEOL JEM-ARM200CF S/TEM electron microscope at an accelerating voltage of 200 kV. High resolution (HR) TEM images were processed using Gatan Digital Micrograph software (Version 3.4.1). TEM samples were prepared by depositing a drop of a dilute toluene suspension of the sample in question onto a holey or ultra-thin carbon coated copper grid (obtained from Electron Microscopy Inc.). The grid bearing the sample was kept in a vacuum chamber at a base pressure

of 0.2 bar for at least 24 h prior to data collection. The particles size distribution was assembled as an average shifted histogram as described by Buriak *et al.* for at least 300 particles in TEM. The average shifted histogram averaged the different histogram shapes formed by shifting the bin origin.[23]

Secondary electron scanning electron microscopy (SEM) images were acquired using a Hitachi S4800 FESEM electron microscope at an accelerating voltage of 10 kV. Samples were mounted on a stainless-steel stub by using a conductive tape.

2.3.3 X-ray Photoelectron Spectroscopy (XPS)

XPS analyses were performed using a Kratos Axis Ultra instrument operating in energy spectrum mode at 210 W. The base and operating chamber pressure were maintained at 10^{-7} Pa. A monochromatic Al Kα source ($\lambda = 8.34$ Å) was used to irradiate the samples, and the spectra were obtained with an electron take-off angle of 90°. CasaXPS software (VAMAS) was used to interpret high-resolution spectra. All spectra were internally calibrated to the C 1s emission (284.8 eV) of adventitious carbon. After calibration, a Shirley-type background was applied to remove most of the extrinsic loss structure. The Ge 3d region were deconvoluted into the Ge $3d_{5/2}$ and $3d_{3/2}$ spin-orbit couple for the element Ge and the energy separation of these doublets was fixed at 0.58 eV and the Ge $3d_{3/2}$ to $3d_{5/2}$ area was fixed at 0.67.[24] For the high-resolution XP spectra of metals, the spin-orbit couple energy separation and area were fixed and the spectral envelope was fit using a Lorentzian asymmetric line shape LA(a, b, n) where a and b define the asymmetry and n defines the Gaussian width. The various spectral regions were fit as follows: Au 4f was deconvoluted into the Au $4f_{7/2}$ and $4f_{5/2}$ spin-orbit couple and the energy separation of these doublets was fixed at 3.70 eV and the Au $4f_{5/2}$ to $4f_{7/2}$ area ratio was fixed at 0.75.[25] Ag 3d was deconvoluted into the Ag $3d_{5/2}$ and $3d_{3/2}$ spin-orbit couple and the energy separation of these doublets was fixed at 6.00

eV and the Ag $3d_{3/2}$ to $3d_{5/2}$ area ration was fixed at 0.67.[25] Cu 2p was deconvoluted into the Cu $2p_{3/2}$ and $2p_{1/2}$ spin-orbit couple and the energy separation of these doublets was fixed at 19.75 eV and the Cu $2p_{1/2}$ and $2p_{3/2}$ area ratio was fixed at 0.50.[25] Pd 3d was deconvoluted into the Pd $3d_{5/2}$ and $3d_{3/2}$ spin-orbit couple and the energy separation of these doublets was fixed at 5.26 eV and the Pd $3d_{3/2}$ to $3d_{5/2}$ area ratio was fixed at 0.67.[25] Pt 4f was deconvoluted into the Pt $4f_{7/2}$ and $4f_{5/2}$ spin-orbit couple and the energy separation of these doublets was fixed at 3.35 eV and the Pt $4f_{5/2}$ to $4f_{7/2}$ area ratio was fixed at 0.75.[25]

2.3.4 Powder X-ray Diffraction (XRD)

XRD was performed using on a Bruker D8 Advance diffractometer (Cu-K$_{\alpha 1}$ (λ = 1.5406 Å) and K$_{\alpha 2}$ (λ = 1.5444 Å) radiation). Samples were prepared by mounting the powder in question on a zero background Si crystal sample holder. XRD patterns were scanned between 2θ ranges of 10 - 80° with a scan step of 0.06 °/s.

2.3.5 Diffuse Reflective Spectroscopy (DRS)

Diffuse reflective analysis was performed using a Cary 5000 UV-Vis-NIR equipped with a diffuse reflectance integrating sphere attachment. Samples were prepared by mounting the powder sample of interest in the sample holder. The detector and grading filter were changed at 900 nm. The measured reflectance spectra were transformed to the corresponding absorption spectra by applying the Kubelka−Munk function.

2.4 Photocatalytic oxidation of benzyl alcohol

Photocatalytic oxidation of benzyl alcohol was performed using a modified literature procedure.[16] A typical reaction was performed using a Schlenk flask charged with benzyl alcohol (40 ml; 380 mmoles), catalyst of choice (Total mass: 22 mg; 0.02 mmoles of metal), and a new

Teflon coated stir bar. The reaction vessel was evacuated and backfilled 5 times with oxygen and finally maintained under a positive pressure of bubbling oxygen during the reaction. The reaction mixture was then stirred at 1500 rpm for 0.5 h after which it was exposed to the emission of a 140 W Hg lamp (Hanovia, wavelength >366 nm, photon flux 8×10^{17} s^{-1}). The reaction vessel was thermostated by immersing it in a water bath maintained at 25 ˚C. The reaction was carried out for 4 h and aliquots (4 mL) were extracted from the reaction mixture every 30 min and diluted to a total volume of 400 ml using dichloromethane and the diluted solution was evaluated using gas chromatography-mass spectrometry (Bruker SCION TQ with 456-GC). The molar concentrations of each component were determined using calibration curves prepared using standards of known concentrations. The conversion percentage (C) of benzyl alcohol (BA) and the selectivity (S) and the yield (Y) for benzaldehyde (BAL) are defined as:

$$C\ (\%) = \frac{n(\mathrm{BA_0}) - n(\mathrm{BA})}{n(\mathrm{BA_0})} \times 100\% \ (2.1)$$

$$S\ (\%) = \frac{n(\mathrm{BAL})}{n(\mathrm{BA_0}) - n(\mathrm{BA})} \times 100\% \ (2.2)$$

$$Y\ (\%) = \frac{n(\mathrm{BAL})}{n(\mathrm{BA_0})} \times 100\% \ (2.3)$$

where $n(\mathrm{BA_0})$ is the initial mole of BA and $n(\mathrm{BA})$ and $n(\mathrm{BAL})$ are the moles of the detected BA and BAL, respectively.

Generally, the apparent quantum efficiency (AQE) of the reaction is the ratio between the photons taking part in the reaction and the total number of incident photon:

$$AQE\ (\%) = \frac{N(\mathrm{BAL})}{I} \times 100\% \ (2.4)$$

where $N(\mathrm{BAL})$ represents the number of molecules of BAL produced, and I is the number of incident photons.[9]

2.5 Catalyst Recycling

The recyclability/reusability of the powder catalysts and thin films was evaluated by performing reactions under identical conditions as described above. A total of 5 cycles were performed for each sample. After each cycle, the powder catalyst was recovered by centrifugation, washed with 5 mL Mill-Q water three times and dried in vacuum and finally massed; thin films were rinsed with 5 mL Mill-Q water three times and dried with flowing N_2 gas and massed. The recovery percentage was determined based upon the difference between the weight before and after each cycle.

2.6 Results and Discussion

Germanane used in the present study was prepared by deintercalation of $CaGe_2$ (Figure 2.1).[3] The product of the deintercalation was sonicated for 2 h in water to maximize exfoliation of GeNSs that were immediately combined with aqueous solutions containing the metal salt of choice (i.e., $AuCl_3$, $AgNO_3$, $CuCl_2$, $PdCl_2$, $PtCl_4$). Upon adding the metal salt solution to the GeNS suspension, the Ge-H moieties on the GeNS surfaces immediately react, reduce the metal ions, and deposit size-polydisperse metal particles onto the GeNS surfaces. This process is accompanied by the evolution of bubbles (presumably hydrogen) and a colour change from red to grey/black independent of the metal employed.

Powder X-ray diffraction (XRD) was used to interrogate the nature of the metal deposits on the decorated GeNSs (i.e., M@GeNSs; Figure 2.4 and 2.5). In all cases, M@GeNSs showed broadened reflections characteristic of the target metals superimposed on the (006), (012), (110) and (116) reflections arising from GeNSs.[24] These observations are consistent with successful

deposition of metal nanoparticles and retention of the GeNS structure. The broadening of the characteristic reflections arising from the nanoparticles depends upon the metal in question. Analyses of these reflections provide approximate crystallite sizes (i.e., Au, 17.4 nm; Ag, 27.4 nm; Cu, 35.6 nm; Pd, 12.7 nm; Pt, 4.8 nm) by using the Scherrer equation.[26]
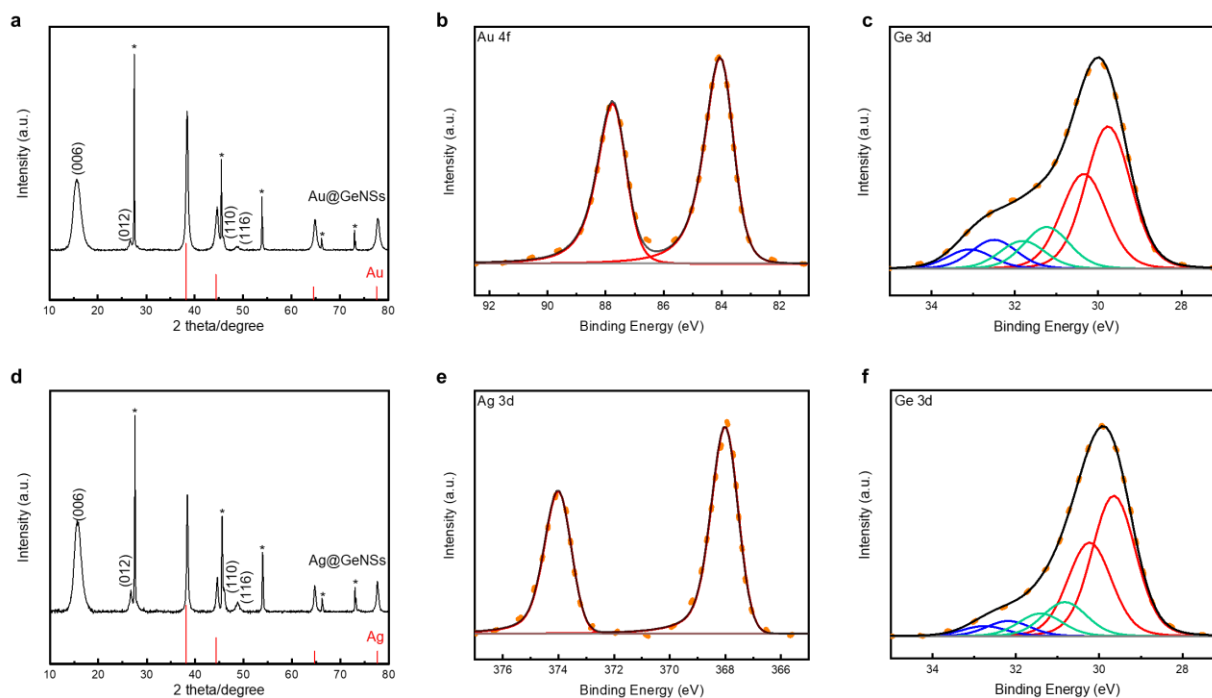
Figure 2.4. XRD (a and b) and high resolution XPS analyses (b, c, e and f) of Au@GeNSs (Top) and Ag@GeNSs (Bottom). Reflections marked with asterisks (*) correspond to crystalline Ge.[27] Au and Ag reflections (PDF#89-3697 and 89-3722, respectively) are provided for reference.
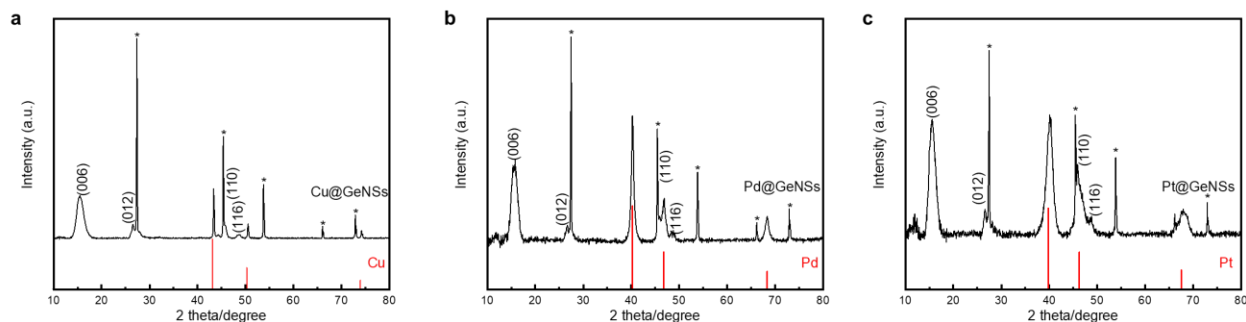
Figure 2.5. XRD patterns of (a) Cu@GeNSs, (b) Pd@GeNSs, and (c) Pt@GeNSs. Asterisks correspond to the Ge reflection; Cu, Pd and Pt reflections are from PDF#89-2838,88-2335 and 88-2343.
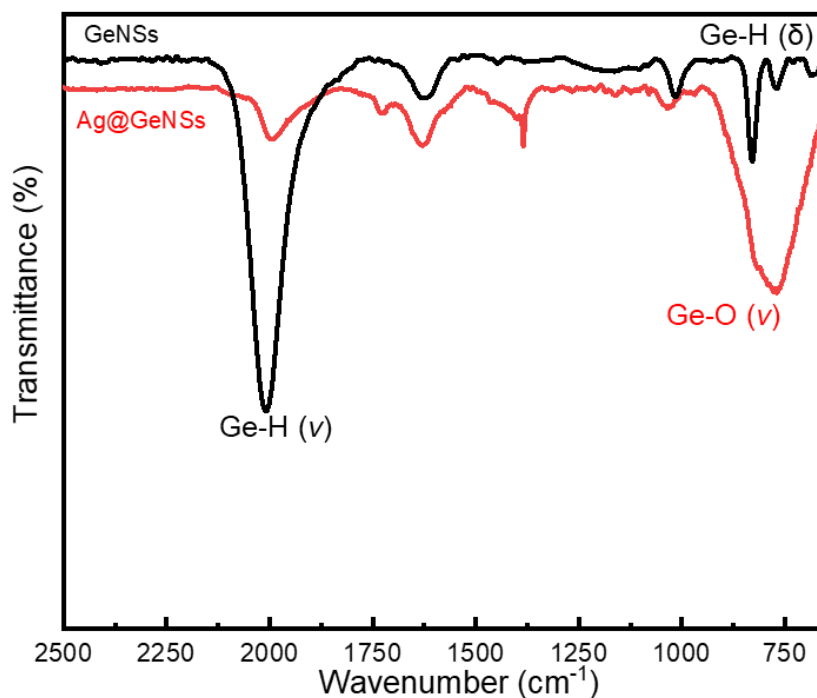
Figure 2.6. Representative FTIR spectra of Ge nanosheets before (black) and after (red) Ag deposition.

To further investigate the nature of the parent GeNSs and M@GeNSs, we interrogated the materials using Fourier-transform infrared (FTIR) and X-ray photoelectron (XPS) spectroscopies. The FTIR spectrum (Figure 2.6) of the parent GeNSs shows intense features associated with Ge-H stretching (2000 cm^{-1}) and bending modes (830 cm^{-1} and 770 cm^{-1}).[28] Following metal deposition, FTIR spectra of M@GeNSs displayed a prominent feature in the range of 700 to 890 cm^{-1} that we attribute to Ge-O vibrations. We also note that the intensities Ge-H associated features diminished, however they still remain obvious.[21] Our observations are similar to those reported for metal decorated silicane[8] and suggest the surface hydride functionalities have reduced metal ions leaving surface dangling bonds on the GeNSs that are subsequently oxidized to form Ge-O-Ge and Ge-O-H moieties.
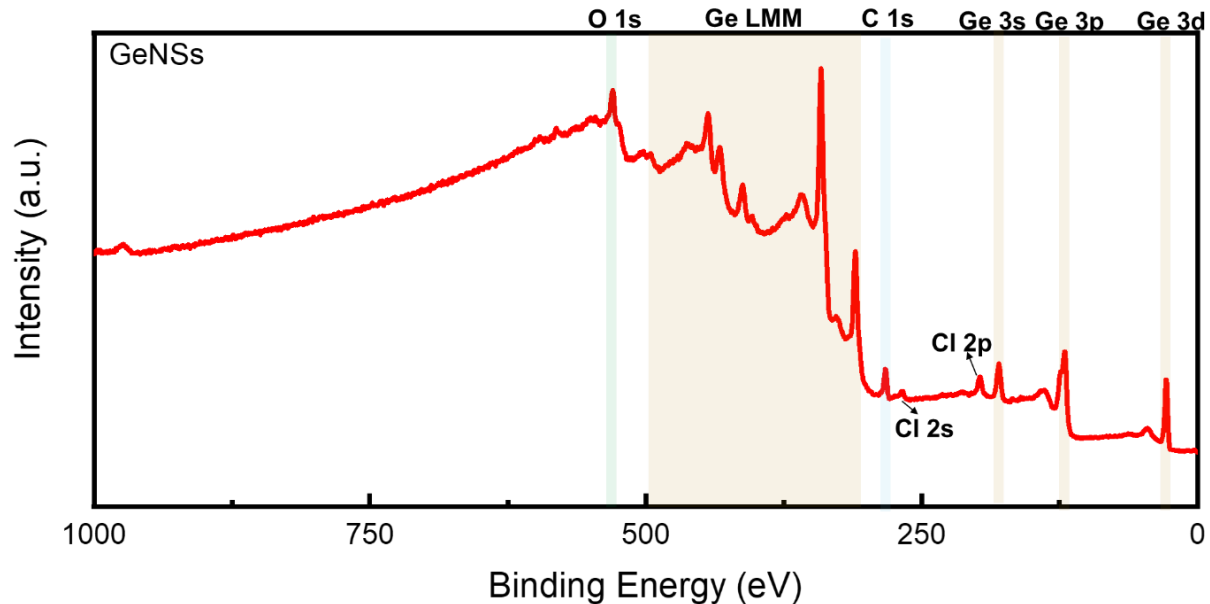
Figure 2.7. A representative survey XP spectrum of GeNSs.

XPS provides complementary information related to material composition, as well as bonding environment, and oxidation states of accessible elements in the materials in question. The survey spectrum of the parent GeNSs reveals they comprise Ge, as well as trace Cl (i.e., 1.2 atomic%) and O (i.e., 5.1 atomic%) (Figure 2.7). In contrast, and consistent with our FTIR and XRD analyses (vide supra), survey XP spectra of the M@GeNSs show evidence of oxidation and corresponding metal particles (Figure 2.8). Deconvolution of the Ge 3d region of the high-resolution XP spectra gave insight into the speciation of Ge atoms within the parent and metal decorated GeNSs. Parent nanosheets (Figure 2.9) show the expected characteristic Ge emission of germanane at 29.8 eV as well as some Ge^{2+} (31.2 eV; 3.5% of Ge) and Ge^{4+} (32.5 eV; 6.2% of Ge). The metal loadings of M@GeNSs were calculated based upon compositions determined from XP survey spectra integration (Table 2.1). The metal loading decreased from Ag, Pd, Cu, Au, and Pt, following the same trend as the charge of the metal ions (i.e., Ag^+, Pd^{2+}, Cu^{2+}, Au^{3+}, and Pt^{4+}).
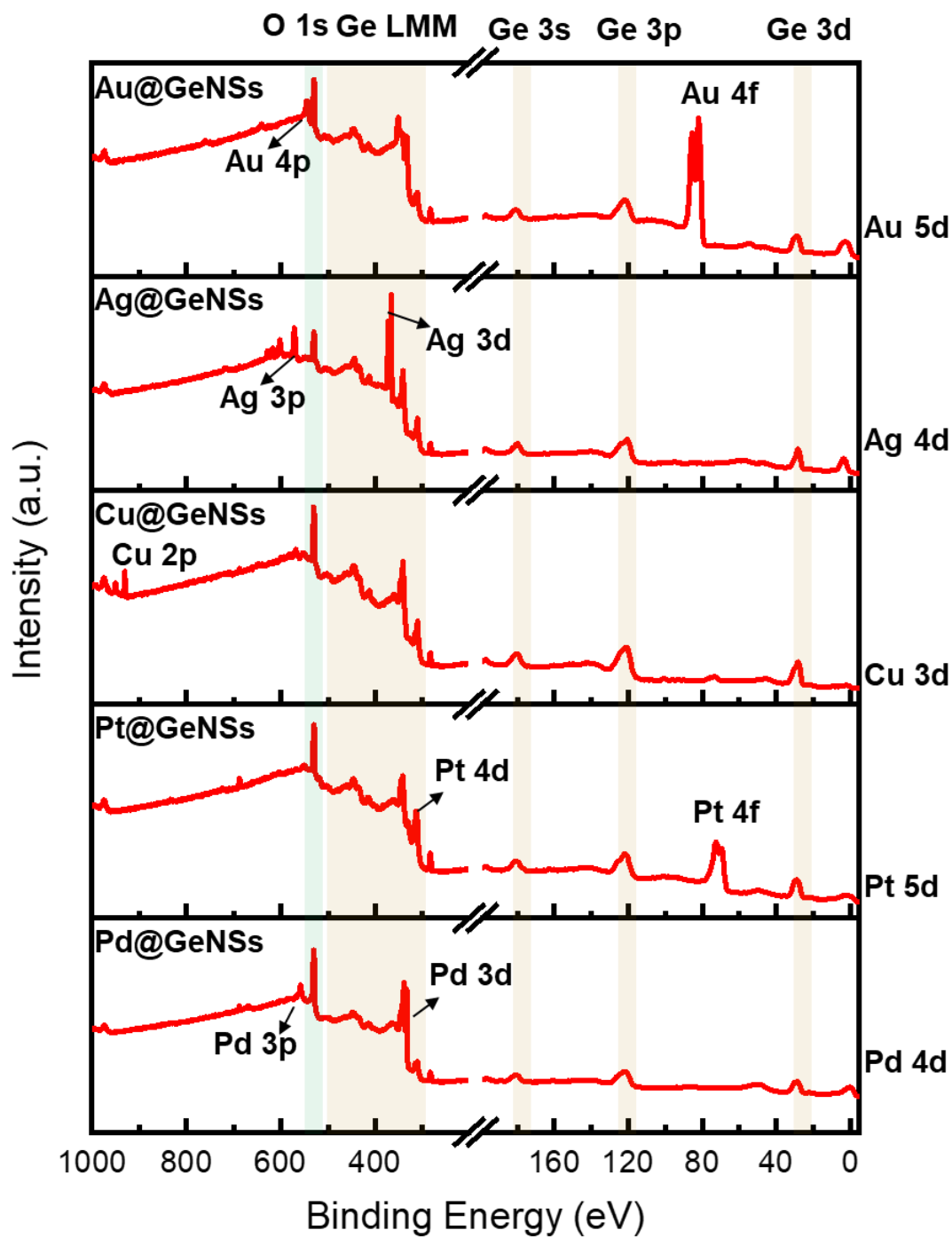
Figure 2.8. Representative survey XP spectra of (a) Au@GeNSs (b) Ag@GeNSs, (c) Cu@GeNSs, (d) Pt@GeNSs and (e) Pd@GeNSs
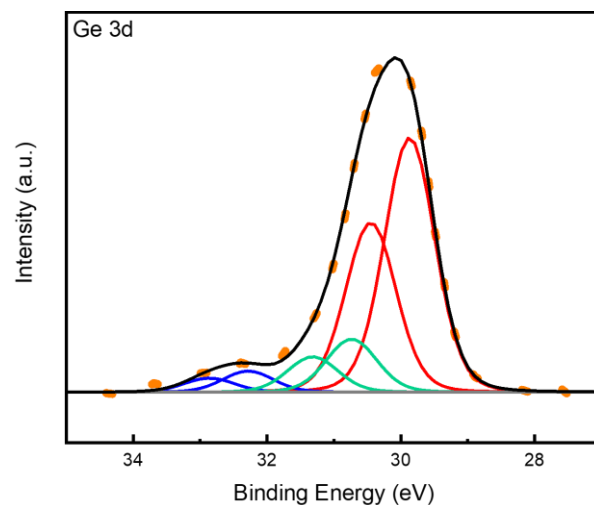
Figure 2.9. A representative high-resolution XP spectrum of Ge 3d region of GeNSs.

Table 2.1. Summary of XPS data.

M@GeNSs (M=)	Au	Ag	Cu	Pd	Pt
Ge 3d regions(eV)	29.8	29.7	29.7	29.8	29.7
Metal regions(eV)[a]	83.8	368.2	932.8	335.2	70.7
	(84.0)	(368.2)	(933.0)	(335.0)	(71.0)
M/Ge ratio[b]	0.063	0.081	0.072	0.075	0.058

[a] Values in parentheses represent the standard metallic binding energies.[25] [b] The ratios were calculated from the atomic percentage of metal and Ge obtained from the survey spectra in question.
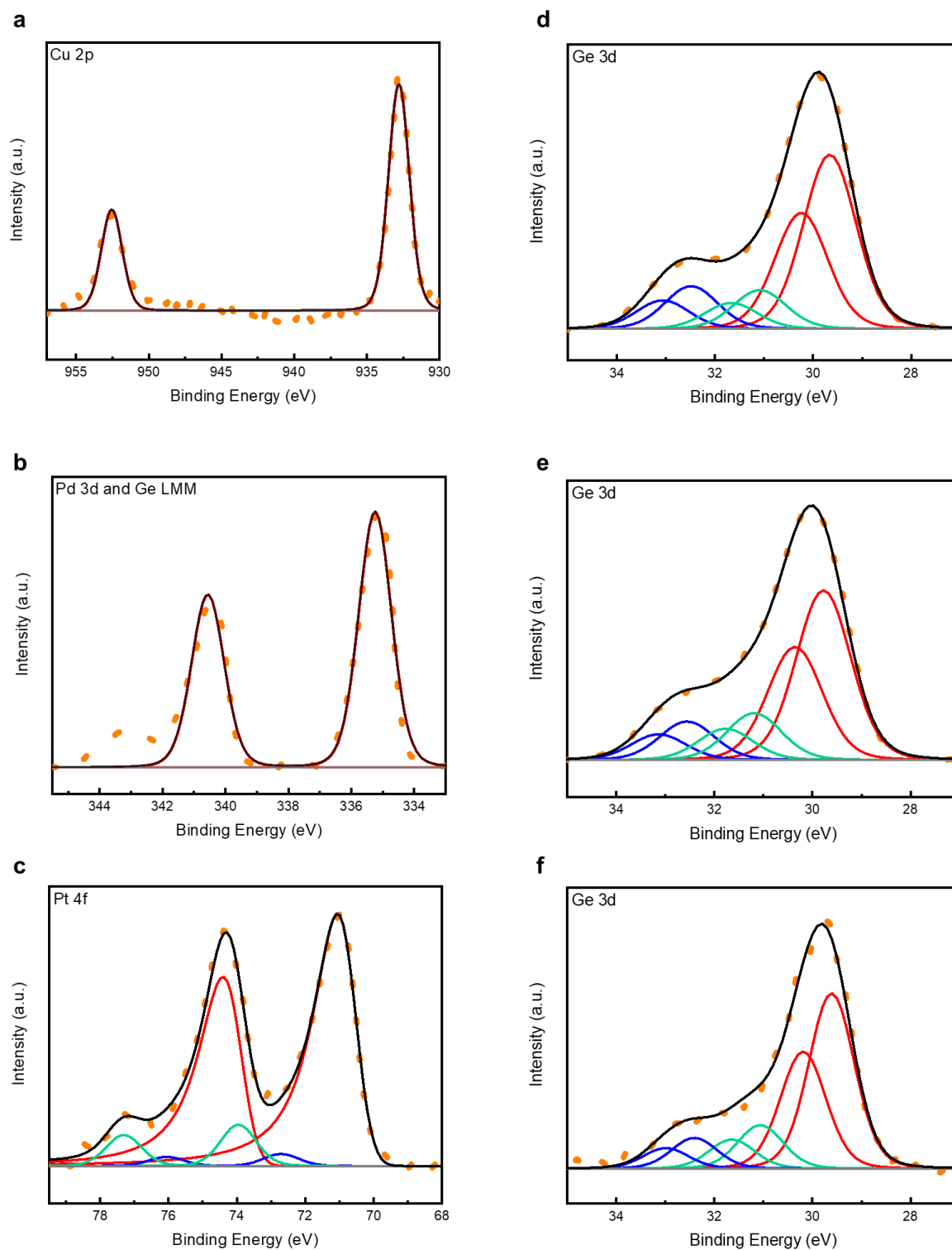
Figure 2.10. Representative high-resolution XP spectra of (a, d) Cu@GeNSs, (b, e) Pd@GeNSs and (c, f) Pt@GeNSs. Corresponding metal (left) and Ge 3d (right) regions are presented in rows.

In all cases, the high-resolution XP spectra of M@GeNSs showed emissions associated with the corresponding metal (i.e., Au, Ag, Cu, Pd, and Pt) deposits and the underlying GeNSs (Figure 2.10). For convenience, the present discussion will be limited to the XP spectra of M@GeNSs (M = Au or Ag). Fitting the Ge 3d spectra provides a binding energy of 29.8 eV that has been previously attributed to Ge in the nanosheets.[24] We also note components appearing at 31.3 and 32.5 eV that have previously been attributed to Ge^{2+} and Ge^{4+} species, respectively (Figures 2.4c and f).[29] The XP spectra of Au and Ag decorated M@GeNSs (Figures 2.4b and e) show emissions at binding energies characteristic of the corresponding metallic state (i.e., Au $4f_{7/2}$, 83.8 eV; Ag $3d_{5/2}$, 368.2 eV). Corresponding data for M@GeNSs (M = Cu, Pd, Pt) are provided in Table 2.1 and Figure 2.10.
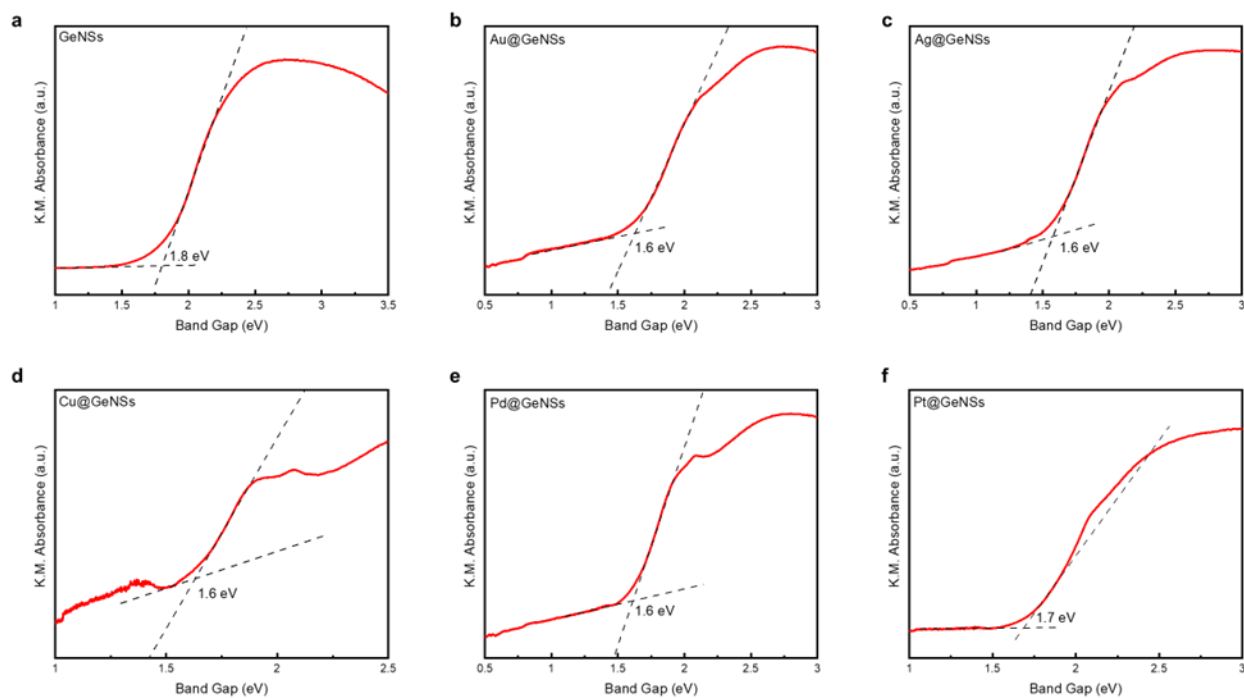
Figure 2.11. Representative diffuse reflectance spectra of Ge nanosheets and M@GeNSs.

Diffuse reflectance spectroscopy allows direct measurement of the optical band gap of solids. The optical direct band gaps of M@GeNS are smaller than that of GeNSs (i.e., 1.8 eV) in

the range of 1.6 to 1.7 eV and show no obvious dependence on metal speciation. Urbach tails were observed in the analyses of all samples (Figure 2.11) and show some sample to sample variation consistent with varying degrees of disorder and oxidation.[21] Additional absorption edges above 2 eV were also noted that are readily attributed to the metal nanoparticles on the GeNS surfaces.[8]
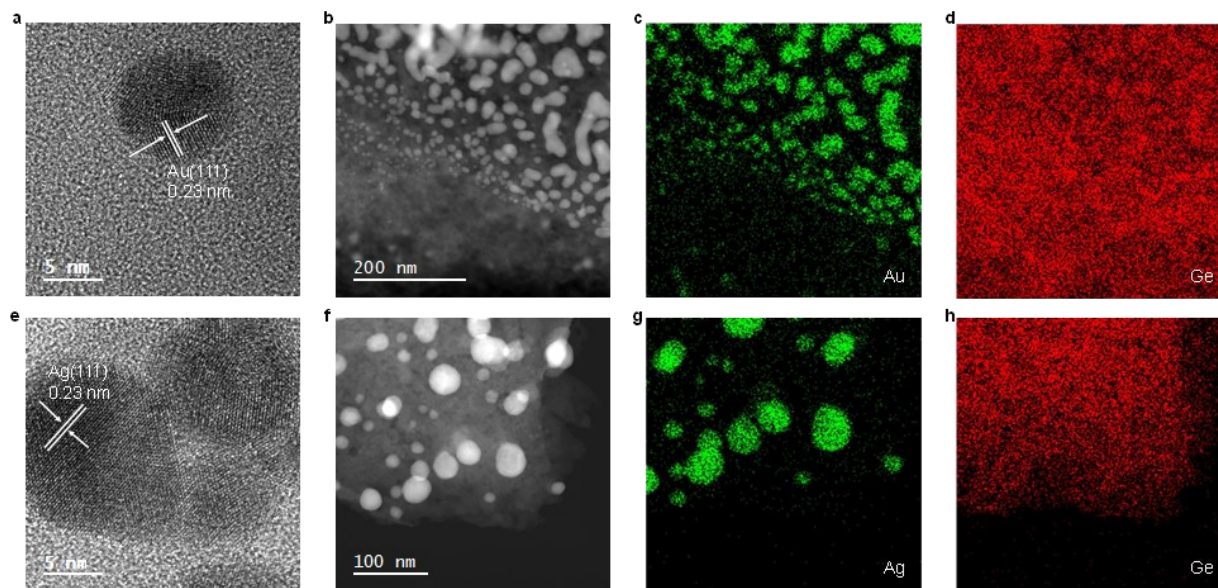
Figure 2.12. TEM and EDX analysis of Au@GeNSs (Top) and Ag@GeNSs (Bottom). High-resolution images (a and e) showing characteristic metal (111) lattice spacing. HAADF-STEM images (b and f) and corresponding EDX mapping of the indicated elements (c, d, g, h).

Electron microscopy of M@GeNSs reveals information regarding material nano-morphology. High-resolution transmission electron microscopy (HRTEM) images confirm the deposition of nanocrystalline Au and Ag particles onto the GeNS surfaces (Figures 2.12a, e and 2.13). Brightfield TEM reveals the deposited metal nanoparticles are pseudospherical with dimensions in the range of 2.7 to 18.8 nm consistent with the observed XRD reflection peak broadening (Figure 2.14).[30] High-angle annular dark-field scanning transmission electron microscopy (HAADF-STEM) images show M@GeNS morphologies consistent with bright field imaging and confirm MNPs are distributed across the NS surfaces with no evidence of ordering

(Figure 2.12b and f). Finally, EDX mapping and spectra confirms co-localization of morphological features in brightfield and HAADF-STEM comprise the target metal (Figures 2.12, 2.13 and 2.15).
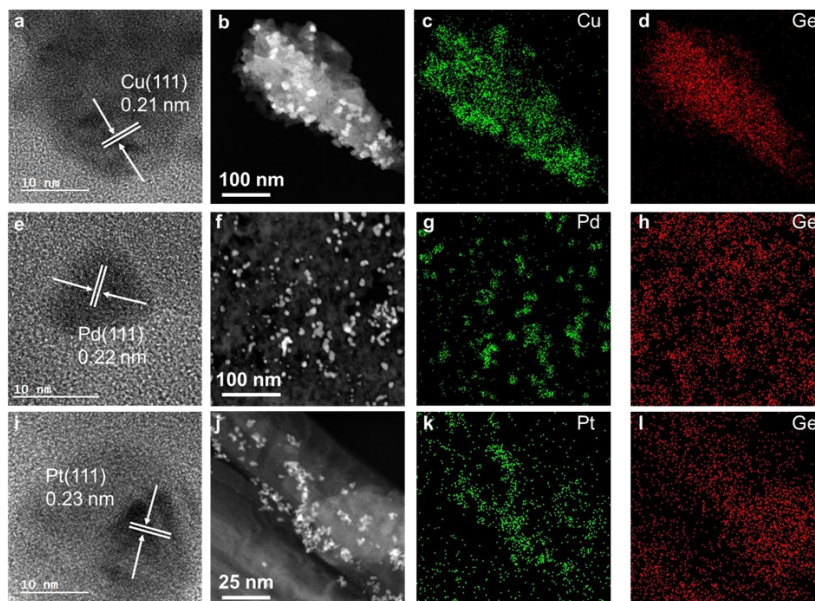
Figure 2.13. Representative HRTEM, HAADF-STEM images and EDX mapping of (a-d) Cu@GeNSs, (e-h) Pd@GeNSs, and (i-l) Pt@GeNSs.
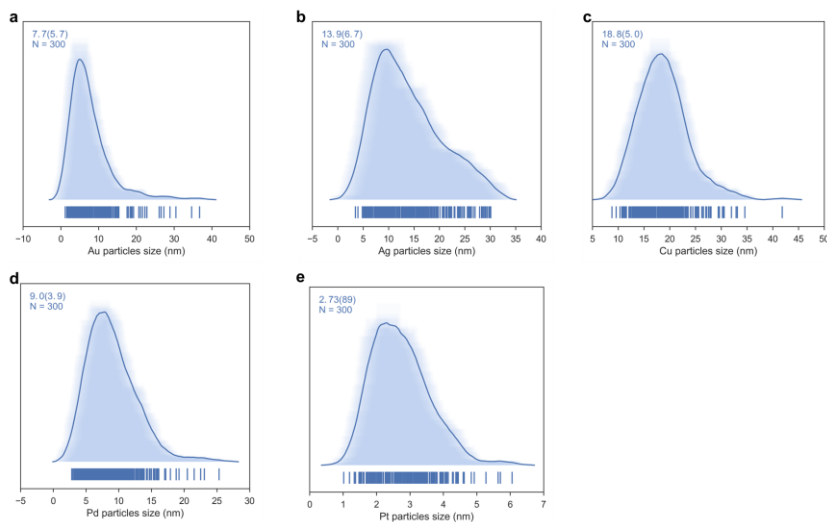
Figure 2.14. Representative average shift histograms for metal nanoparticles on (a) Au@GeNSs (b) Ag@GeNSs, (c) Cu@GeNSs, (d) Pd@GeNSs and (e) Pt@GeNSs.
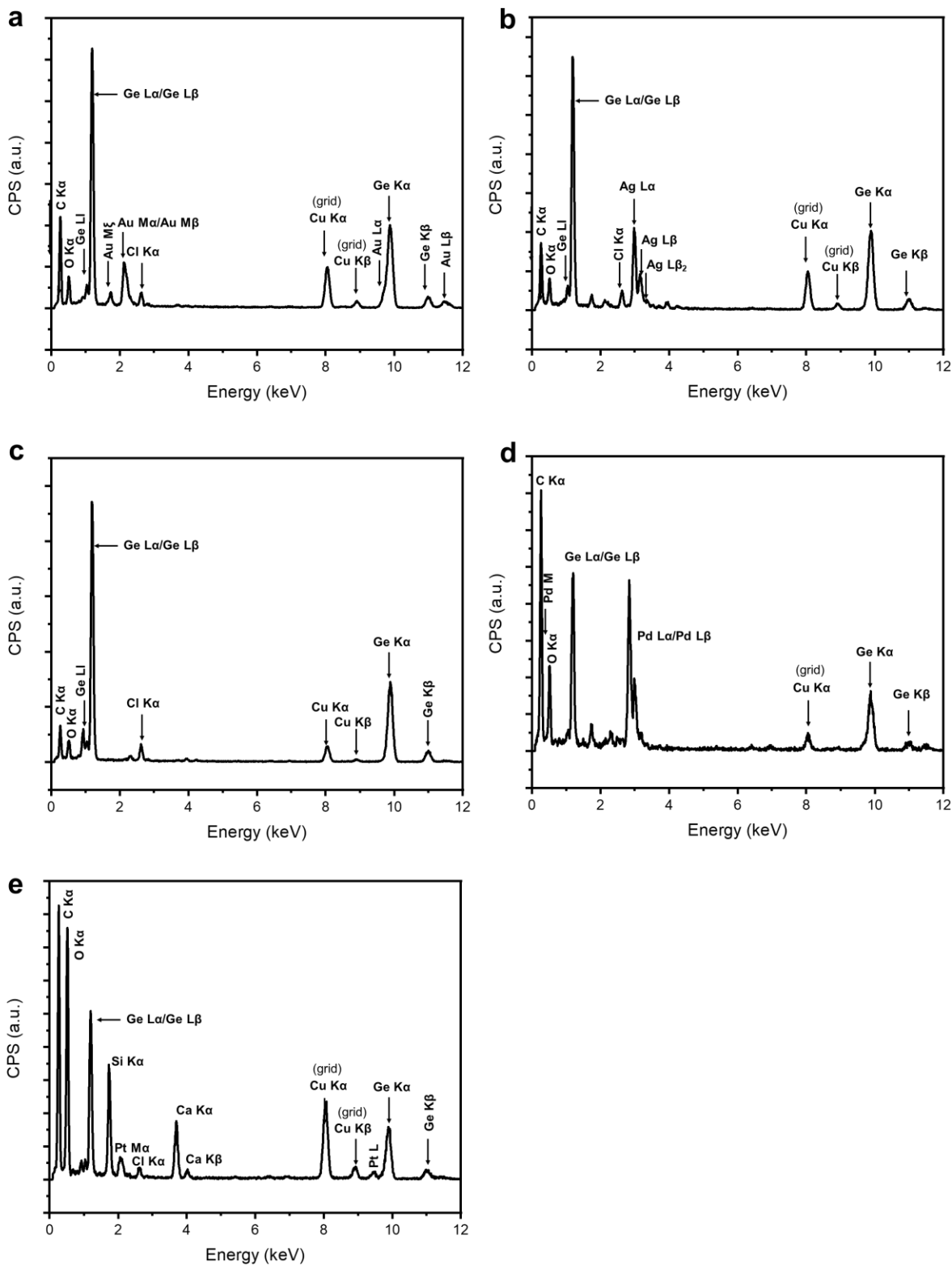
Figure 2.15. Representative EDX spectra for (a) Au@GeNSs (b) Ag@GeNSs, (c) Cu@GeNSs, (d) Pd@GeNSs, and (e) Pt@GeNSs.

With a series of M@GeNSs in hand, we chose to explore their possible catalytic activity in light-activated aerobic oxidation of neat benzyl alcohol. This reaction was chosen because the primary source of benzaldehyde is the gas-phase oxidation of toluene[31] or liquid-phase oxidation of benzyl alcohol.[32] Established reactions provide complex byproducts (i.e., benzoic acid and benzyl benzoate) and low conversion efficiencies.[33] Given the established importance of benzaldehyde to cinnamaldehyde, exploring new catalytic pathways to its production is of interest.[11] The photochemical reaction conditions investigated as part of the present study are provided in the Experimental section. Gas chromatography-mass spectrometry (GC-MS) analysis of aliquots extracted from the reaction mixture at regular, predetermined time intervals provided a convenient means for monitoring of the reaction progress.

A comparison of the corresponding reactivity of GeNSs, freestanding metal nanoparticles (MNPs), physical mixtures of freestanding metal nanoparticles and GeNSs (MNPs+GeNSs), and M@GeNSs under identical conditions provides insight into the cooperative roles of the components (Figure 2.16 and Table 2.2). Upon first inspection it is immediately clear the oxidation of benzyl alcohol does not proceed in the absence of light or in an inert (i.e., N_2) environment.
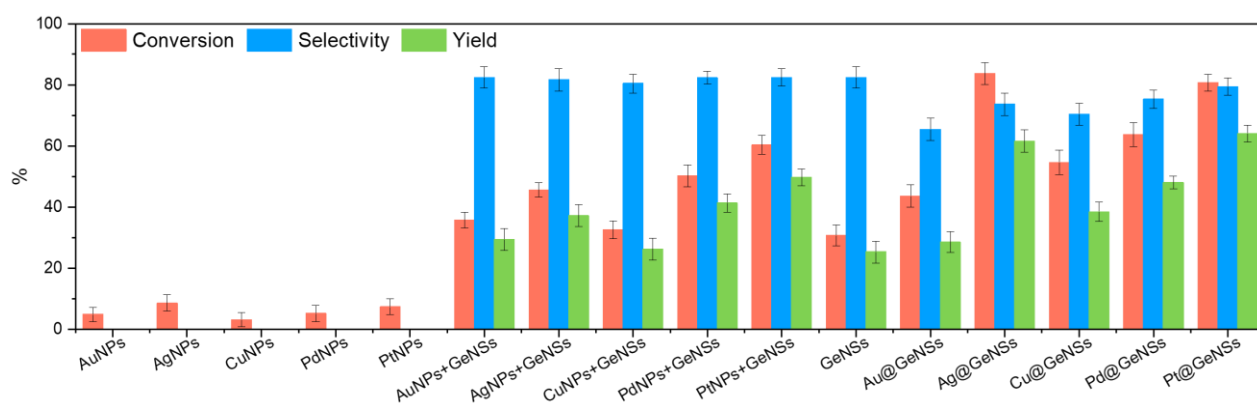
Figure 2.16. Photocatalytic oxidation performance: Conversion, selectivity and yield of reaction displayed by each of the catalysts for the aerobic oxidation of BA. Associated error bars correspond to mean +/- SD (N = 3).

72

Table 2.2. Summary of photocatalytic oxidation performance of benzyl alcohol to produce benzaldehyde.

	Conversion (%)	Selectivity (%)	Yield (%)	AQE (%)
GeNSs	30.7	82.4	25.3	2.79
Au@GeNSs	43.6	65.4	28.6	3.97
Ag@GeNSs	83.7	73.7	61.6	7.61
Cu@GeNSs	54.6	70.4	38.5	4.97
Pd@GeNSs	63.7	75.3	48.1	5.79
Pt@GeNSs	80.7	79.4	64.1	7.34

Table 2.3. Comparison of the photocatalytic oxidation of benzyl alcohol to produce benzaldehyde using free metal particles, M@GeNSs, as well as physical mixtures of free metal nanoparticles and GeNSs (MNPs+GeNSs).

Conversion (%)	Au	Ag	Cu	Pd	Pt
M@GeNSs	43.6	83.7	54.6	63.7	80.7
MNPs+GeNSs	35.7	45.6	32.5	50.2	60.3
MNPs	4.85	8.66	3.15	5.22	7.36

We also note that the identity of the catalyst is important. The oxidation of benzyl alcohol to benzaldehyde is not efficiently catalyzed by freestanding metal nanoparticles (i.e., <10% conversion). In this regard, yield and percent selectivity were not evaluated for these systems. Equivalent evaluation of parent, hydrogen-terminated GeNSs show a 30.7% conversion, 82.4% selectivity, and 25.3% yield; GeNSs simultaneously provide the lowest conversion and yield, as well as the highest selectivity of any nanosheet system investigated here. Of import, we also noted the presence of benzoic acid in the product mixture obtained from GeNS suggesting over-oxidation is possible.
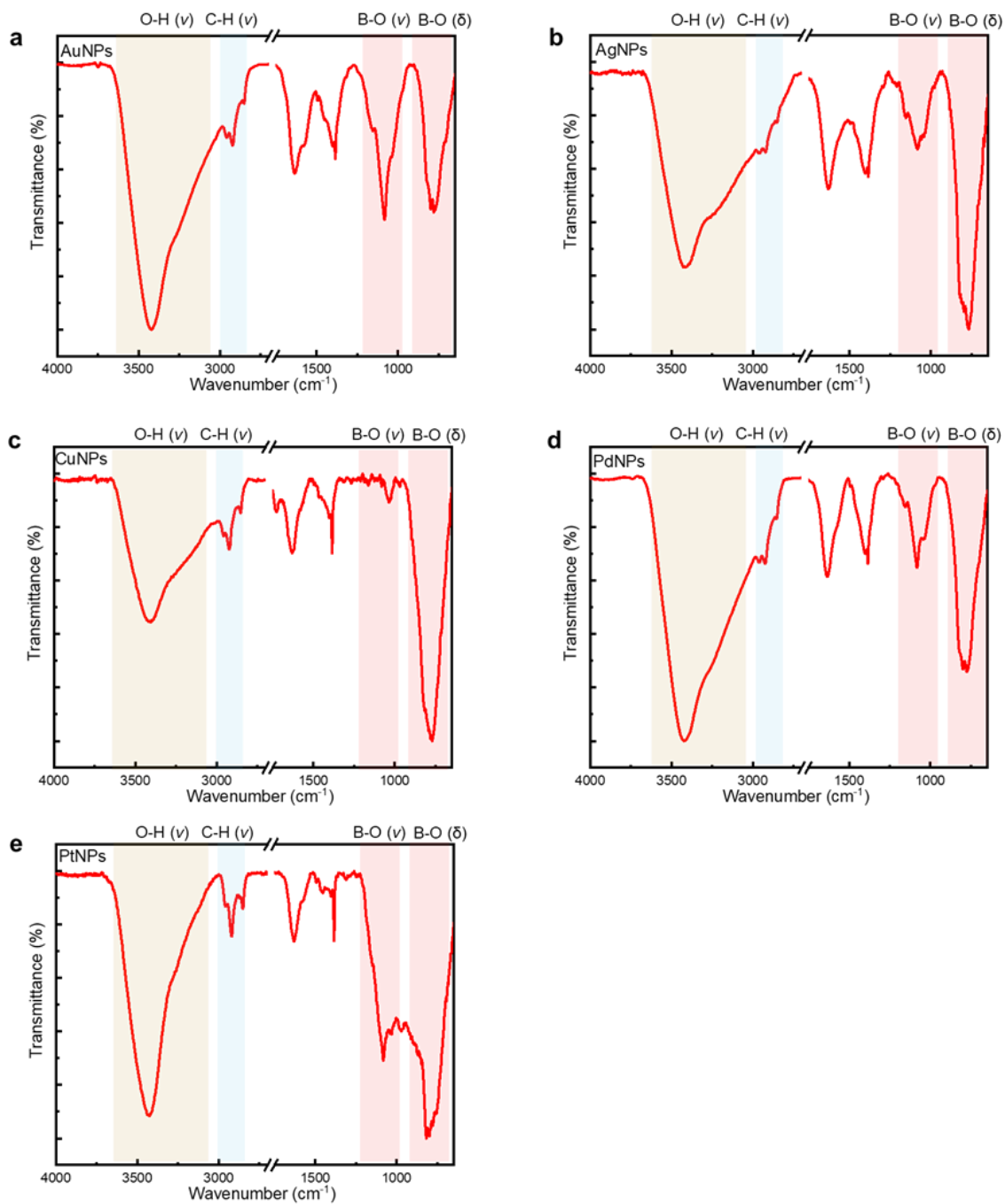
Figure 2.17. Representative FTIR spectra of the indicated metal nanoparticles.

To investigate the impact of introducing MNPs on the catalytic activity of M@GeNSs we first explored the reactivity of physical mixtures of MNPs and GeNSs (i.e., MNPs+GeNSs; M = Au, Ag, Cu, Pd, Pt). In all cases, introducing metal nanoparticles prepared via solution phase sodium borohydride reduction (i.e., mixtures) provided an apparent increase in percent conversion (Table 2.3); however, closer inspection reveals the new higher percent conversion correlates with the straightforward combination of the precent conversions realized by the GeNSs and MNPs alone. This suggests the two nanomaterials are acting independently. Consistent with these observations, FTIR analysis of MNPs (Figure 2.17) suggests they are passivated with O-H and B-O containing functionalities that would prevent direct interaction between the MNPs and GeNSs.[34] A negligible difference between the dimensions of freestanding metal particles and metal particles on GeNSs excludes the influence of metal particle sizes (Table 2.4). The question remains: does intimate contact between MNPs and GeNSs influence reactivity.

Table 2.4. Representative nanoparticle size distributions for metal nanoparticles and M@GeNSs obtaining from measuring 300 nanoparticles under TEM.

Sizes (nm)	Au	Ag	Cu	Pd	Pt
M@GeNSs	7.7 ± 5.7	13.9 ± 6.7	18.8 ± 7.0	9.0 ± 3.9	2.7 ± 0.8
MNPs	8.3 ± 5.3	14.3 ± 6.1	20.1 ± 6.5	9.2 ± 3.3	3.2 ± 0.6

As noted above, the reducing nature of the hydride surface (i.e., Ge–H) on GeNSs provides a convenient approach toward interfacing GeNSs with MNPs to provide a metal–semiconductor hybrid (i.e., M@GeNSs). FTIR and XPS analyses of these materials (Figure 2.4, 2.6 and 2.10) suggest the surfaces of the MNPs in these systems are accessible to solution borne reactants and make these intriguing catalyst candidates. In all cases, other than for reactions involving Au@GeNSs, we note a statistically relevant increase in percent conversion for M@GeNSs catalysts when compared to a straightforward combination of GeNSs, MNPs, and MNP + GeNSs.

Ag@GeNSs exhibit the highest conversion (i.e., 83.7%) with an apparent quantum efficiency (AQE; Table 2.2) of 7.6%. The high-resolution XP spectra of Ag@GeNSs after the reaction showed emissions associated with the corresponding metallic Ag and Ag_2O (Figure 2.18a). The oxidized Ag can further participate in the oxidation of benzyl alcohol without additional oxygen; this would increase conversion while decreasing selectivity (i.e., 73.7%).[35, 36] Pt@GeNSs show a slightly lower conversion compared to the Ag analogue (i.e., 80.7%) and higher selectivity for benzaldehyde (i.e., 79.4%) that when combined leads to a higher yield of 64.1%.
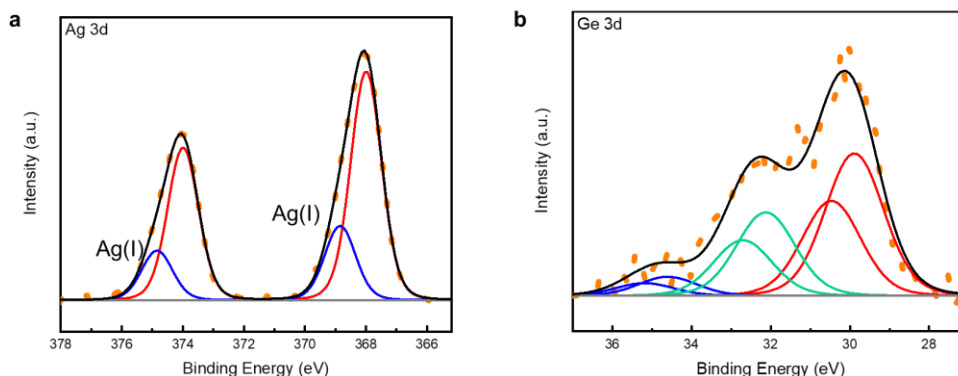
Figure 2.18. Representative high-resolution XP spectra of a) Ag 3d regions of Ag@GeNSs after the photooxidation of benzyl alcohol to produce benzaldehyde showing Ag(I) species, (b) Ge 3d regions after photooxidation of benzyl alcohol to produce benzaldehyde.

The catalytic performance of different loads of Ag on the GeNSs is shown in Table 2.5. The conversion of benzyl alcohol increased from 64.6% to 85.4% with increasing Ag loading. However, the selectivity decreased from 76.2% to 71.2% due to the over oxidation of benzaldehyde to benzoic acid by excess Ag.[35] As a result, 5% Ag@GeNSs gave the highest yield of 61.6% (Table 2.5). We also note that the presented Ag@GeNSs achieve a considerable conversion rate and selectivity in a short time and moderate condition compared to the already reported literature (Table 2.6).[16, 35, 37-42]

Table 2.5. Effect of Ag loading on catalytic performance of Ag@GeNSs in selective oxidation of benzyl alcohol to benzaldehyde.

Loading of Ag Ag@GeNSs	1%	2.5%	5%	10%
Conversion (%)	64.6	70.2	83.7	85.4
Selectivity (%)	76.2	74.6	73.7	71.2
Yield (%)	49.2	52.4	61.6	60.8

Table 2.6. Reported studies on the selective oxidation of benzyl alcohol.

Catalyst	Irradiation source	T (K)	t(h)	Solvent	Conversion (%)	Selectivity (%)
Ag@GeNSs	**Hg lamp (140 W, 366 nm)**	**RT**	**4**	**H_2O**	**83.7**	**73.7**
Ru/g-C$_3$N$_4$[37]	UV LED (220 W, 390 nm)	RT	4	H_2O	73	72
Ir/TiO$_2$[16]	Hg lamp (250 W, 315 nm)	333	6	N/A	8.9	92
Pt/TiO$_2$[38]	Xe lamp (250 W, 420 nm)	727	2	H_2O	87	68
Au/CeO$_2$[35]	Vis LED (220 W, 530 nm)	RT	10	H_2O	52	99
Ag/SBA[39]	N/A	595	1	N/A	74.8	85.2
Au-Pd/TiO$_2$[40]	N/A	393	10	N/A	51.7	76.7
Pd/TiO$_2$[41]	N/A	363	6	N/A	4.5	85.9
Cu/TiO$_2$[42]	N/A	393	6	N/A	1.1	99.9
Cu-Pd/TiO$_2$[42]	N/A	393	6	N/A	35.9	98.7

A possible mechanism for the presented catalytic activity of M@GeNSs is shown in Figure 2.19. Initial exposure to UV light homolytically cleaved a Ge–Ge bond providing a "Ge·" radical that can react with surface adsorbed BA. This process leads to the liberation of hydrogen gas and attachment of an R–O moiety to the surface of the GeNS (where R = benzyl) and reformation of

the Ge–Ge bond which preserves the integrity of the GeNS. Subsequently, light-induced homolytic cleavage of the benzyl C–H bond provides a carbon-based "C·" radical that can directly react with molecular oxygen that is adsorbed to adjacent MNPs and ultimately lead to the liberation of benzaldehyde.[16, 43] Of particular note, this process will also lead to partial oxidation of the underlying GeNS which is evident in the presented XPS and FTIR analyses (Figure 2.18b and 2.20).

To leverage M@GeNSs as a photocatalyst, the catalyst should ideally exhibit high recovery and reusability. For convenience, we used Ag@GeNSs as an illustration (Figure 2.21f) to test the reusability of the present systems. For freestanding Ag@GeNSs the conversion efficiency decreased by nearly half its original value due to the poor recovery after only five cycles; this is not unexpected given the small amount of catalyst employed (ca. 40 mg). The nanoscale Ag@GeNSs suspension in the reaction mixture was lost during analyses and recycling. In light of the poor recyclability of the powder catalyst, we prepared Ag@GeNSs thin films to improve their reuse. Ag@GeNS thin films were characterized using XRD, XPS, and SEM (Figure 2.21). These analyses revealed that the GeNS crystallinity maintained after the film formation and the intense reflections characteristic of metallic Ag confirm the successful deposition of Ag NPs. High-resolution XP spectra of the Ge 3d region show characteristic emissions from the Ge in the nanosheet at 29.8 eV as well as two less intense emissions from Ge^{2+} and Ge^{4+}. The Ag 3d region showed an emission at 368.2 eV corresponding to metallic Ag. Secondary electron SEM images confirm the expected morphology of GeNSs thin film (Figure 2.21b and 2.22) and after the deposition of Ag, many dispersed particles with approximate dimensions of ca. 20 nm are noted on the GeNS surfaces (Figure 2.21e and 2.22).
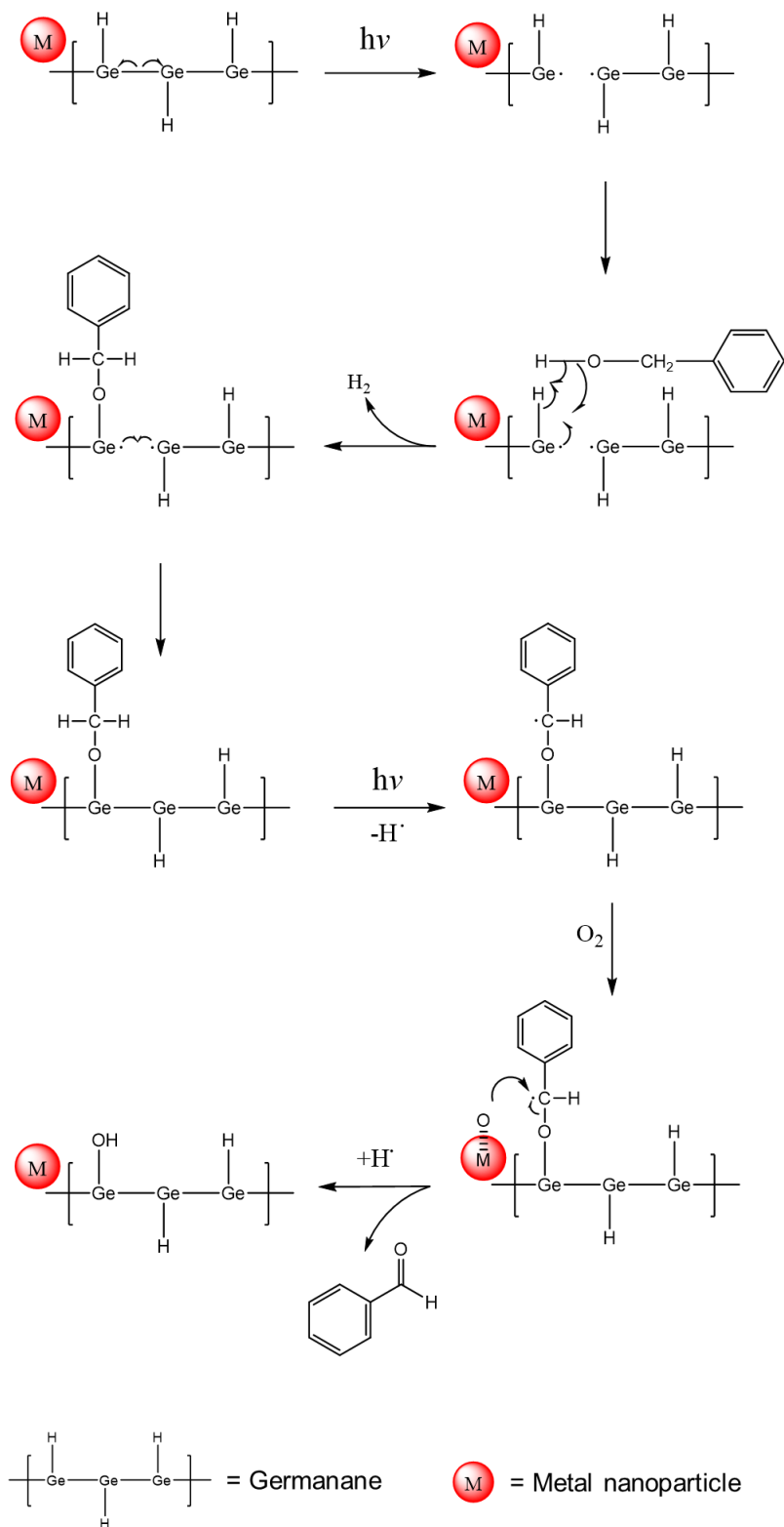
Figure 2.19. Proposed mechanism for the presented catalytic activity of M@GeNSs in the photooxidation of benzyl alcohol to produce benzaldehyde.
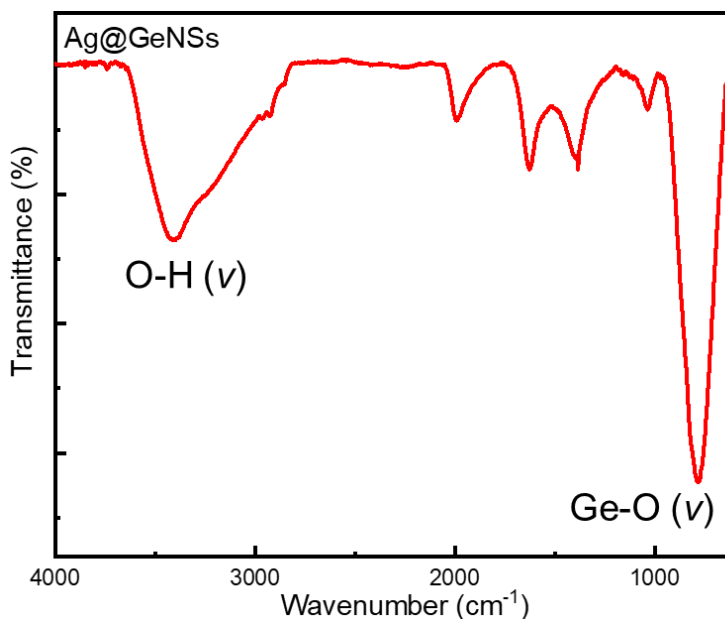
Figure 2.20. Representative FTIR spectrum of Ag@GeNSs after the photooxidation of benzyl alcohol to produce benzaldehyde.
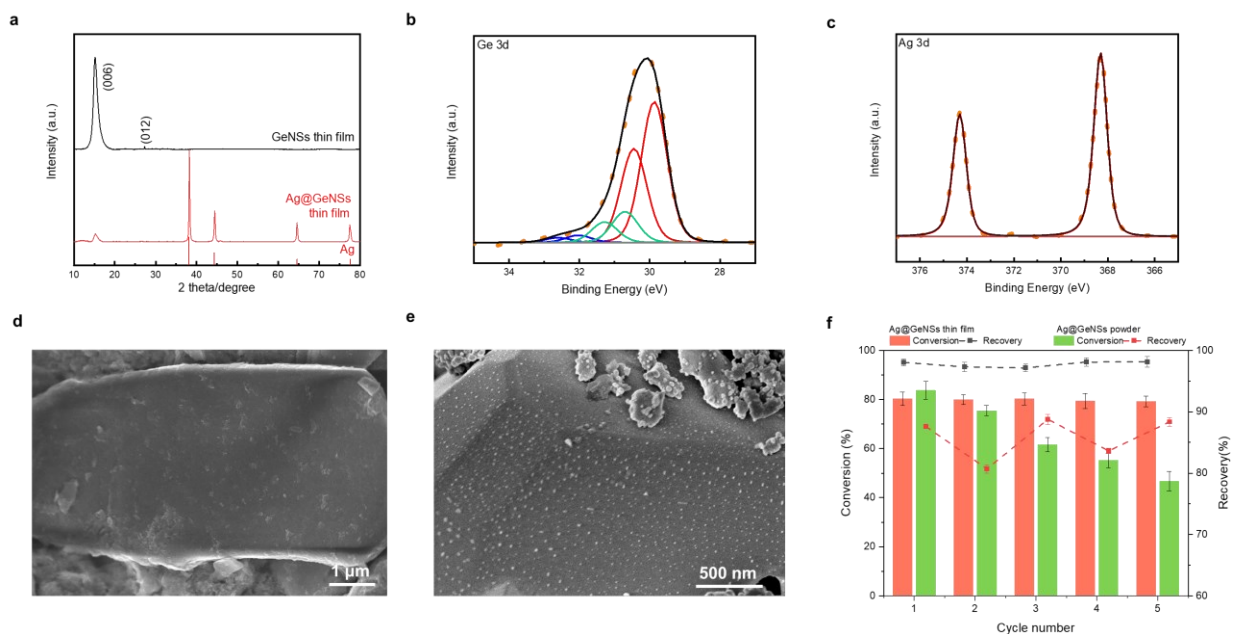
Figure 2.21. Characterization and photocatalytic performance of Ag@GeNS thin films: PXRD patterns of (a) Ag@GeNSs and GeNS thin films. High resolution XP spectra of (b) Ge 3d region and (c) Ag 3d region. SEM images of (d) GeNS and (e) Ag@GeNS thin films. Photocatalytic activity and recovery comparison of Ag@GeNS thin film and powder in 5 reaction cycles.

80

The Ag@GeNSs thin films were evaluated under the same photocatalytic conditions as their freestanding counterparts (Figure 2.21f and Table 2.7). From these analyses, we note a marked improvement in recyclability over freestanding systems with thin films showing an average of 97.7% recovery and 79.8% conversion percent over 5 cycles. Although the catalytic performance during the first cycle is not as high as Ag@GeNSs powder, the excellent recovery provides long-term cycling.
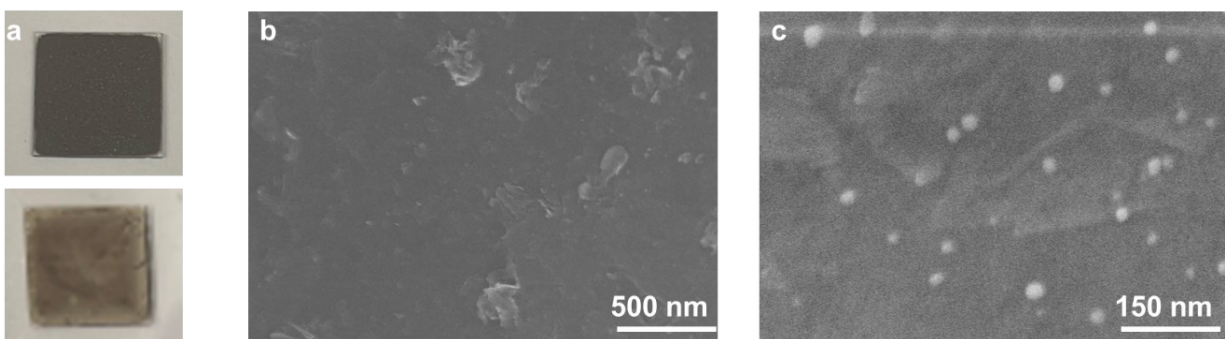
Figure 2.22. (a) Photos of Ge nanosheet thin film before (top) and after (bottom) Ag deposition. High-resolution SEM images of (b) GeNS and (c) Ag@GeNS thin films

Table 2.7. Photocatalytic oxidation activity of benzyl alcohol to benzaldehyde and recovery comparison of Ag@GeNS thin films and powders.

	Cycle 1	Cycle 2	Cycle 3	Cycle 4	Cycle 5
Ag@GeNS thin films					
Conversion (%)	80.2	79.9	80.2	79.4	79.2
Recovery (%)	98.0	97.3	97.1	98.4	98.1
Ag@GeNS powders					
Conversion (%)	83.7	75.5	61.6	55.2	46.7
Recovery (%)	87.6	80.7	88.8	83.6	88.3

2.7 Summary and Outlook

Herein, we have demonstrated a facile method for introducing a variety of adherent metal nanoparticles (Au, Ag, Cu, Pd, Pt) to the surfaces of GeNSs. XRD and XPS analyses confirm that the GeNS structure remained intact during the deposition process and metal nanoparticles were

formed. Further, TEM studies revealed the morphology of the M@GeNSs and showed the metal nanoparticles were distributed over the entire GeNS surface. The presented materials were subsequently interrogated as photocatalysts for the selective visible light-induced oxidation of benzyl alcohol. The M@GeNSs possess a higher conversion efficiency compared to a straightforward mixture of freestanding metal nanoparticles prepared via solution reduction and GeNSs. The synergistic effect of the intimately linked metal nanoparticles and GeNSs in M@GeNSs strongly favors the production of benzaldehyde via oxygen-atom transfer from metal nanoparticles to the product. Furthermore, thin films of metal-decorated GeNSs prepared via dropcasting provide for convenient catalyst recovery and recyclability.

2.8 References

1. Huey, W. L. B.; Goldberger, J. E., Covalent Functionalization of Two-dimensional Group 14 Graphane Analogues. *Chem. Soc. Rev.* **2018,** *47* (16), 6201-6223.
2. Jiang, S.; Krymowski, K.; Asel, T.; Arguilla, M. Q.; Cultrara, N. D.; Yanchenko, E.; Yang, X.; Brillson, L. J.; Windl, W.; Goldberger, J. E., Tailoring the Electronic Structure of Covalently Functionalized Germanane via the Interplay of Ligand Strain and Electronegativity. *Chem. Mater.* **2016,** *28* (21), 8071-8077.
3. Helbich, T.; Lyuleeva, A.; Ludwig, T.; Scherf, L. M.; Fässler, T. F.; Lugli, P.; Rieger, B., One-Step Synthesis of Photoluminescent Covalent Polymeric Nanocomposites from 2D Silicon Nanosheets. *Adv. Funct. Mater.* **2016,** *26* (37), 6711-6718.
4. Hartman, T.; Sofer, Z., Beyond Graphene: Chemistry of Group 14 Graphene Analogues: Silicene, Germanene, and Stanene. *ACS Nano* **2019,** *13* (8), 8566-8576.
5. Liu, Z.; Lou, Z.; Li, Z.; Wang, G.; Wang, Z.; Liu, Y.; Huang, B.; Xia, S.; Qin, X.; Zhang, X.; Dai, Y., GeH: a Novel Material as a Visible-light Driven Photocatalyst for Hydrogen Evolution. *Chem. Commun.* **2014,** *50* (75), 11046-11048.
6. Liu, Z.; Wang, Z.; Sun, Q.; Dai, Y.; Huang, B., Methyl-terminated Germanane $GeCH_3$ Synthesized by Solvothermal Method with Improved Photocatalytic Properties. *Appl. Surf. Sci.* **2019,** *467-468*, 881-888.
7. Ng, S.; Sturala, J.; Vyskocil, J.; Lazar, P.; Martincova, J.; Plutnar, J.; Pumera, M., Two-Dimensional Functionalized Germananes as Photoelectrocatalysts. *ACS Nano* **2021,** *15* (6), 11681-11693.
8. Qian, C.; Sun, W.; Hung, D. L. H.; Qiu, C.; Makaremi, M.; Hari Kumar, S. G.; Wan, L.; Ghoussoub, M.; Wood, T. E.; Xia, M.; Tountas, A. A.; Li, Y. F.; Wang, L.; Dong, Y.; Gourevich, I.; Singh, C. V.; Ozin, G. A., Catalytic CO_2 Reduction by Palladium-decorated Silicon–hydride Nanosheets. *Nat. Catal.* **2018,** *2* (1), 46-54.
9. Zhao, F.; Feng, Y.; Wang, Y.; Zhang, X.; Liang, X.; Li, Z.; Zhang, F.; Wang, T.; Gong, J.; Feng, W., Two-dimensional Gersiloxenes with Tunable Bandgap for Photocatalytic H_2 Evolution and CO_2 Photoreduction to CO. *Nat. Commun.* **2020,** *11* (1), 1443.
10. Aizawa, M.; Cooper, A. M.; Malac M.; Buriak, J. M., Silver Nano-Inukshuks on Germanium. *Nano Lett*., **2005**, *5* (5), 815-819.
11. Richmond, H. H., US Pat., 73966147A, 1950.
12. Enache, D. I.; Edwards, J. K.; Landon, P.; Solsona-Espriu, B.; Carley, A. F.; Herzing, A. A.; Watanabe, M.; Kiely, C. J.; Knight, D. W.; Hutchings, G. J., Solvent-Free Oxidation of Primary Alcohols to Aldehydes Using Au-Pd/TiO_2 Catalysts. *Science* **2006,** *311* (5759), 362-365.
13. Long, J.; Xie, X.; Xu, J.; Gu, Q.; Chen, L.; Wang, X., Nitrogen-Doped Graphene Nanosheets as Metal-Free Catalysts for Aerobic Selective Oxidation of Benzylic Alcohols. *ACS Catal.* **2012,** *2* (4), 622-631.
14. Furukawa, S.; Shishido, T.; Teramura, K.; Tanaka, T., Photocatalytic Oxidation of Alcohols over TiO_2 Covered with Nb_2O_5. *ACS Catal.* **2011,** *2* (1), 175-179.
15. Patel, M. A.; Luo, F.; Khoshi, M. R.; Rabie, E.; Zhang, Q.; Flach, C. R.; Mendelsohn, R.; Garfunkel, E.; Szostak, M.; He, H., P-Doped Porous Carbon as Metal Free Catalysts for Selective Aerobic Oxidation with an Unexpected Mechanism. *ACS Nano* **2016,** *10* (2),

2305-2315.

16. Feng, W.; Wu, G.; Li, L.; Guan, N., Solvent-free Selective Photocatalytic Oxidation of Benzyl Alcohol over Modified TiO_2. *Green Chem.* **2011,** *13* (11), 3265-3272.

17. Huang, X.; Akdim, O.; Douthwaite, M.; Wang, K.; Zhao, L.; Lewis, R. J.; Pattisson, S.; Daniel, I. T.; Miedziak, P. J.; Shaw, G.; Morgan, D. J.; Althahban, S. M.; Davies, T. E.; He, Q.; Wang, F.; Fu, J.; Bethell, D.; McIntosh, S.; Kiely, C. J.; Hutchings, G. J., Au–Pd Separation Enhances Bimetallic Catalysis of Alcohol Oxidation. *Nature* **2022,** *603* (7900), 271-275.

18. Qamar, M.; Elsayed, R. B.; Alhooshani, K. R.; Ahmed, M. I.; Bahnemann, D. W., Highly Efficient and Selective Oxidation of Aromatic Alcohols Photocatalyzed by Nanoporous Hierarchical Pt/Bi_2WO_6 in Organic Solvent-free Environment. *ACS Appl. Mater. Interfaces* **2015,** *7* (2), 1257-1269.

19. Jia, L.; Wang, D.-H.; Huang, Y.-X.; Xu, A.-W.; Yu, H.-Q., Highly Durable N-Doped Graphene/CdS Nanocomposites with Enhanced Photocatalytic Hydrogen Evolution from Water under Visible Light Irradiation. *J. of Phys. Chem. C* **2011,** *115* (23), 11466-11473.

20. Helbich, T.; Lyuleeva, A.; Höhlein, I. M. D.; Marx, P.; Scherf, L. M.; Kehrle, J.; Fässler, T. F.; Lugli, P.; Rieger, B., Radical-Induced Hydrosilylation Reactions for the Functionalization of Two-Dimensional Hydride Terminated Silicon Nanosheets. *Chem.– Eur. J.* **2016,** *22* (18), 6194-6198.

21. Bianco, E.; Butler, S.; Jiang, S.; Restrepo, O. D.; Windl, W.; Goldberger, J. E., Stability and Exfoliation of Germanane: A Germanium Graphane Analogue. *ACS Nano* **2013,** *7* (5), 4414-4421.

22. Zhang, Q.; Li, N.; Goebl, J.; Lu, Z.; Yin, Y., A Systematic Study of the Synthesis of Silver Nanoplates: Is Citrate a "Magic" Reagent? *J. Am. Chem. Soc.* **2011,** *133* (46), 18931-18939.

23. Anderson, S. L.; Luber, E. J.; Olsen, B. C.; Buriak, J. M., Substance over Subjectivity: Moving beyond the Histogram. *Chem. Mater.* **2016,** *28* (17), 5973-5975.

24. Yu, H.; Helbich, T.; Scherf, L. M.; Chen, J.; Cui, K.; Fässler, T. F.; Rieger, B.; Veinot, J. G. C., Radical-Initiated and Thermally Induced Hydrogermylation of Alkenes on the Surfaces of Germanium Nanosheets. *Chem. Mater.* **2018,** *30* (7), 2274-2280.

25. NIST X-ray Photoelectron Spectroscopy Database, NIST Standard Reference Database Number 20, National Institute of Standards and Technology, Gaithersburg MD, 20899 (2000).

26. Holzwarth, U.; Gibson, N., The Scherrer Equation Versus the 'Debye-Scherrer equation'. *Nat. Nanotechnol.* **2011,** *6* (9), 534-534.

27. Cultrara, N. D.; Wang, Y.; Arguilla, M. Q.; Scudder, M. R.; Jiang, S.; Windl, W.; Bobev, S.; Goldberger, J. E., Synthesis of 1T, 2H, and 6R Germanane Polytypes. *Chem. Mater.* **2018,** *30* (4), 1335-1343.

28. Khomenkova, L.; Lehninger, D.; Kondratenko, O.; Ponomaryov, S.; Gudymenko, O.; Tsybrii, Z.; Yukhymchuk, V.; Kladko, V.; von Borany, J.; Heitmann, J., Effect of Ge Content on the Formation of Ge Nanoclusters in Magnetron-Sputtered $GeZrO_x$-Based Structures. *Nanoscale Res. Lett.* **2017,** *12* (1), 196.

29. Yu, H.; Thiessen, A. N.; Hossain, M. A.; Kloberg, M. J.; Rieger, B.; Veinot, J. G. C., Thermally Induced Dehydrogenative Coupling of Organosilanes and H-Terminated Silicon Quantum Dots onto Germanane Surfaces. *Chem. Mater.* **2020**, *32* (11), 4536-4543.

30.   Holder, C. F.; Schaak, R. E., Tutorial on Powder X-ray Diffraction for Characterizing Nanoscale Materials. *ACS Nano* **2019**, *13* (7), 7359-7365.

31.   Brückner, A., A New Approach to Study the Gas-phase Oxidation of Toluene: Probing Active Sites in Vanadia-based Catalysts under Working Conditions. *Appl. Catal. A-Gen.* **2000**, *200* (1), 287-297.

32.   Zhan, G.; Hong, Y.; Mbah, V. T.; Huang, J.; Ibrahim, A.-R.; Du, M.; Li, Q., Bimetallic Au–Pd/MgO as Efficient Catalysts for Aerobic Oxidation of Benzyl Alcohol: A Green Bio-reducing Preparation Method. *Appl. Catal. A-Gen.* **2012**, *439-440*, 179-186.

33.   Ferraz, C. P.; Garcia, M. A. S.; Teixeira-Neto, É.; Rossi, L. M., Oxidation of Benzyl Alcohol Catalyzed by Gold Nanoparticles under Alkaline Conditions: Weak vs. Strong Bases. *RSC Adv*. **2016**, *6* (30), 25279-25285.

34.   Gautam, C.; Yadav, A. K.; Singh, A. K., A Review on Infrared Spectroscopy of Borate Glasses with Effects of Different Additives. *ISRN Ceram*. **2012**, *2012*, 1-17.

35.   Ma, L.; Jia, l.; Guo, X.; Xiang, L., Catalytic Activity of Ag/SBA-15 for Low-temperature Gas-phase Selective Oxidation of Benzyl Alcohol to Benzaldehyde. *Chin. J. Catal.* **2014**, *35* (1), 108-119.

36.   Jia, L.; Zhang, S.; Gu, F.; Ping, Y.; Guo, X.; Zhong, Z.; Su, F., Highly Selective Gas-phase Oxidation of Benzyl Alcohol to Benzaldehyde Over Silver-containing Hexagonal Mesoporous Silica. *Microporous and Mesoporous Mater.* **2012**, *149* (1), 158-165.

37.   Lima, M. J.; Tavares, P. B.; Silva, A. M. T.; Silva, C. G.; Faria, J. L. Selective Photocatalytic Oxidation of Benzyl Alcohol to Benzaldehyde by Using Metal-loaded g-C_3N_4 Photocatalysts. *Catal. Today* **2017**, *287* (1), 70-77.

38.   Zhai, W.; Xue, S.; Zhu, A.; Luo, Y.; Tian, Y. Plasmon-Driven Selective Oxidation of Aromatic Alcohols to Aldehydes in Water with Recyclable Pt/TiO_2 Nanocomposites. *ChemCatChem* **2011**, *3* (1), 127−130.

39.   Tanaka, A.; Hashimoto, K.; Kominami, H. Selective Photocatalytic Oxidation of Aromatic Alcohols to Aldehydes in an Aqueous Suspension of Gold Nanoparticles Supported on Cerium (IV) Oxide under Irradiation of Green Light. *Chem. Commun.* **2011**, *47* (37), 10446−10448.

40.   Li, X.; Feng, J.; Sun, J.; Wang, Z.; Zhao, W. Solvent-Free Catalytic Oxidation of Benzyl Alcohol over Au-Pd Bimetal Deposited on TiO_2: Comparison of Rutile, Brookite, and Anatase. *Nanoscale Res. Lett.* **2019**, *14* (1), 394.

41.   Sun, J.; Han, Y.; Fu, H.; Qu, X.; Xu, Z.; Zheng, S. Au@Pd/TiO_2 with Atomically Dispersed Pd as Highly Active Catalyst for Solvent-free Aerobic Oxidation of Benzyl Alcohol. *Chem. Eng. J.* **2017**, *313* (1), 1–9.

42.   Alshammari, H.M. Synthesis of Palladium and Copper Nanoparticles Supported on TiO_2 for Oxidation Solvent-Free Aerobic Oxidation of Benzyl Alcohol. *Processes* **2021**, *9* (9), 1590.

43.   Xie, F.; Zhang, Y.; He, X.; Li, H.; Qiu, X.; Zhou, W.; Huo, S.; Tang, Z., First Achieving Highly Selective Oxidation of Aliphatic Alcohols to Aldehydes over Photocatalysts. *J Mater. Chem. A* **2018**, *6* (27), 13236-13243.

3. Chapter 3: Facile Synthesis of High-Entropy Alloy Nanoparticles on Germanane, Ge nanoparticles and Wafers[b]

The preparation and prototype application of high-entropy alloy nanoparticles (HEA NPs) have emerged as an intriguing area of research.[1] The attention being paid to these materials arises, in part, because they possess complex multi-element compositions and high-entropy solid-solution structures that provide tunable reactivity and enhanced stability that are particularly attractive for catalyst design.[2] The initial breakthrough in the general synthesis of HEA NPs that exhibit a wide compositional range (including many immiscible combinations) and large numbers of constituent elements (up to eight), was realized via "carbo-thermal shock" synthesis.[3] Subsequently, a variety of other synthesis procedures have emerged, including vapor phase spark discharge, rapid radiative heating or annealing, low-temperature hydrogen spillover, and microwave heating.[4-8] Many of these methods require specialized and costly infrastructure, and simple solution-based methods remain few in number.[9] To date, a variety of substrates (e.g., carbon nanosheets,[10] carbon nanofibers,[11] graphene,[12] TiO_2,[7] MoS_2[13]) have been demonstrated as promising supports for HEA NPs, showing enhanced stability and catalytic performance. Notably, germanium-based materials have yet to be explored as a potential support for HEA NPs.

As described in Chapter 1, Germanane (GeNS) is a 2-dimensional semiconductor that shares similarities with graphene; its atoms are arranged in a structure that closely resembles that of the (111) surfaces of hydrogen-terminated Ge.[14] This material possesses an optical band gap ranging from 1.4 - 1.7 eV that depends on surface chemistry,[15] and it has been successfully integrated into prototype devices, such as transistors and Li-ion batteries.[16,17] The use of metal heterostructures containing germanane and other 2D semiconductors, such as Si-doped germanane, presents new opportunities due to their unique optical and electronic properties.[18] For example, coupling the reactivity of metals with the optical properties of graphene has led to photocatalysts capable of water splitting,[19] while interfacing plasmonic metal nanoparticles with the electronic properties of germanane could yield materials with potential applications in solar energy conversion, photodetection, and sensing. To date, investigation of germanane-metal heterostructures has been limited, in part, because there are few examples of methods that provide these emerging materials.[20]

In Chapter 2, we described the preparation of metal nanoparticle-decorated germanane (M@GeNSs) via a solution-based method and demonstrated their reactivity in the selective photocatalytic aerobic oxidation of benzyl alcohol.[21] This success led us to investigate the possibility of depositing high-entropy alloy nanoparticles (HEA NPs) onto germanane surfaces using a variation of our surface-mediated reduction method. Previous syntheses of HEA NPs with an elemental composition of AuAgCuPdPt have been limited to a top-down approach utilizing cryo-milling.[22] Drawing inspiration from our previous report involving monometallic nanomaterial deposition on GeNSs, here we demonstrate the deposition of HEA NPs (AuAgCuPdPt) onto germanane surfaces (Figure 3.1). Subsequent to deposition, we successfully liberate freestanding HEA NPs from the GeNSs via UV light irradiation and demonstrate the

resulting NPs maintain their single-phase solid solution structure. With these promising results in hand, we explore the scope of various Ge-based substrates as platforms for growing HEA NPs. Knowing germanium nanoparticles (GeNPs) could exhibit similar Ge-H surface moieties and that they are readily prepared,[23] we also investigate these materials as reducing substrates for HEA NP growth. We conclude this study by extending our method to hydrogen-terminated Ge (100) wafers.
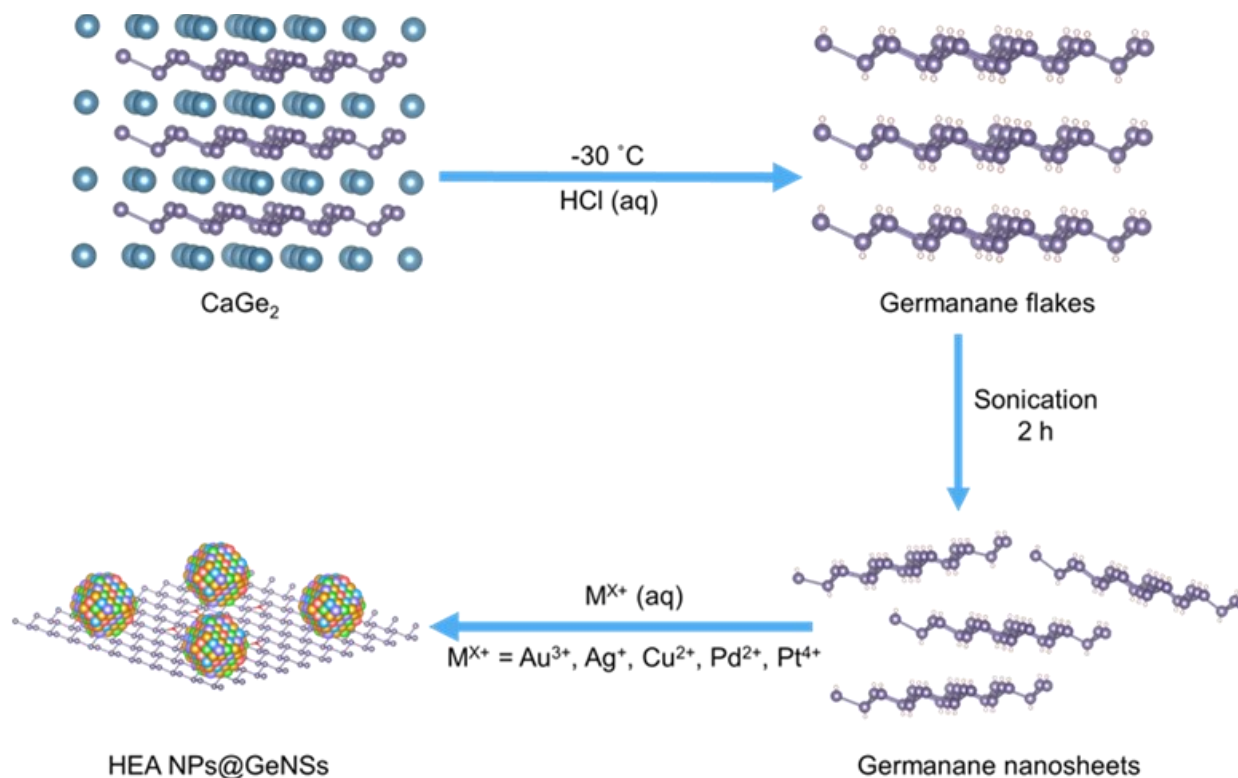
Figure 3.1. A pictorial representation of the formation of high-entropy nanoparticles on germanane.

3.1 Materials and Methods

3.1.1 Materials

Germanium (Ge, 99.999%), calcium (Ca, 99.0%), gold chloride ($AuCl_3$, 99.99%), silver nitrate ($AgNO_3$, 99.9999%), copper chloride ($CuCl_2$, 99.999%), palladium chloride ($PdCl_2$, 99.9%), platinum chloride ($PtCl_4$, 99.999%) and hypophosphorous acid solution (50 wt.% H_3PO_2 in water)

were purchased from Sigma-Aldrich. Sodium hydroxide (NaOH) pellets, ammonium hydroxide (28-30 wt.% NH_4OH), hydrofluoric acid (electronic grade, 48-50% HF) hydrochloric acid (37 wt.%, HCl), ethanol (anhydrous), isopropyl alcohol (anhydrous), acetone (HPLC grade) and toluene (HPLC grade) were purchased from Fisher Scientific. Germanium dioxide (GeO_2, 99.99%) was purchased from Gelest. Milli-Q (18.2 MΩ·cm at 25 °C) water was used for all experiments. All organic solvents were dried using an Innovative Technology, Inc. Grubbs-type solvent purification system. $CaGe_2$ and GeNSs were synthesized with the same methods as in the Chapter 2.

3.1.2 Synthesis of High-Entropy Alloy Nanoparticles-decorated Germanium Nanosheets (HEA NPs@GeNSs)

To prepare high entropy alloy nanoparticles-decorated germanium nanosheets (HEA NPs@GeNSs; HEA NPs= Au, Ag, Cu, Pt, Pd), germanane powder (73 mg; 1 mmol) was dispersed in 4 mL Milli-Q water. The mixture was sonicated in a bath sonicator for 2 hours to yield a red suspension of exfoliated GeNSs. Subsequently, an appropriate amount (0.01 mmol) of the anhydrous metal salt in question ($AuCl_3$, $AgNO_3$, $CuCl_2$, $PdCl_2$ and $PtCl_4$) was dissolved in 1 mL of Milli-Q water together. The mixed metal salts solution (i.e., 0.1 mL) was added into the GeNS dispersion at room temperature under subdued light, resulting in a change of color from red to black. The mixture was stirred for 10 min, and the product was recovered by centrifugation and washed with Milli-Q water three times. The product was then dried for 12 hours under vacuum and subsequently stored in a nitrogen-filled glovebox under subdued light. Typical mass yields for this procedure were 45 mg.

3.1.3 Liberation of High-Entropy Alloy Nanoparticles (HEA NPs)

To liberate the HEA NPs from the HEA NPs@GeNSs , HEA NPs@GeNSs powder (100 mg) was dispersed in 5 mL of Milli-Q water. The suspension was stirred and irradiated with a 360 nm UV LED light source for 24 h under a N_2 atmosphere. After decomposition, the product was washed and centrifuged with 3 mL of Milli-Q water three time. The resulting product was then dried for 12 hours under vacuum and subsequently stored in a nitrogen-filled glovebox in subdued light.

3.1.4 Synthesis of Germanium Hydroxide

Germanium hydroxide was prepared using a modified literature synthesis.[23] GeO_2 (5 g) was added to a solution of 25 g NaOH in 35 mL of water in a 250 mL round-bottom flask and stirred until the white powder is dissolved. The mixture was then acidified slowly to pH 1 using an 80 mL solution of water and concentrated HCl (1:1), followed by the addition of 35 mL of hypophosphorous acid in water (50 wt% H_3PO_2). The mixture was refluxed at 120°C for 4 hours under flowing Ar. The reaction was allowed to cool to 90°C before adding 50 mL of NH_4OH slowly through the condenser, which precipitated brown $Ge(OH)_2$ out of solution. **Caution!** The reaction with ammonium hydroxide is very exothermic. The brown precipitate was collected by vacuum filtration and purified by twice re-dispersing and stirring in 300 mL of water. After the final collection by vacuum filtration, the brown-orange product was allowed to dry overnight on a double manifold vacuum.

3.1.5 Synthesis of Germanium Nanoparticles (GeNPs)

Brown $Ge(OH)_2$ powder was placed in a quartz boat and loaded into a Thermofisher Lindberg/Blue M tube furnace equipped with a quartz tube. The tube was charged with flowing

argon gas (10 cm^3/s) and the furnace was ramped to 400 °C at a rate of 5 °C/min. After holding at the peak temperature for 1 hour, the furnace was cooled naturally to room temperature before collecting the sample, which was then weighed and transferred to a vial for storage. Hydride-terminated germanium nanoparticles were released from the sample through ethanolic hydrofluoric acid (HF) etching, using a modified literature procedure.[24] **Caution!** HF is dangerous; extreme care and compliance with local regulations is required. In a 50 mL Teflon PFA (perflouroalkoxy) beaker, 0.1 g of the composite was dispersed in 6 mL of a mixture of ethanol and water (1:1), followed by the addition of 3 mL of concentrated HCl and 2 mL of aqueous (49 %) HF. The mixture was stirred for 1 hour before extracting the liberated germanium nanoparticles with toluene into test tubes. The resulting dark brown colloidal solution was subjected to centrifugation at 5,000 rpm for 5 minutes to obtain a dark brown pellet. This process was repeated twice more, dispersing the nanoparticle pellet in dry toluene between each centrifugation, and removing the supernatant.

3.1.6 Synthesis of High-Entropy Alloy Nanoparticles from Germanium Nanoparticles (HEA NPs@GeNPs)

To prepare high entropy alloy nanoparticles from germanium nanoparticles (HEA NPs@GeNPs; HEA NPs = Au, Ag, Cu, Pt, Pd), germanium nanoparticles (72 mg; 1 mmol) were dispersed in 4 mL distilled water. Subsequently, a mixed metal salt solution (0.1 mL, 0.01 mmol/L) was added to the GeNPs dispersion at room temperature, in subdued light, resulting in a color change from brown to black. The mixture was stirred for 10 minutes, and the product was recovered by centrifugation and washed with Milli-Q water three times. The product was then

dried for 12 hours under vacuum and stored in a nitrogen-filled glovebox, while being shielded from light. Typical mass yields for this procedure were 50 mg.

3.1.7 Synthesis of High-Entropy Alloy Nanoparticles on Ge Wafer

A germanium shard was precleaned with acetone, isopropyl alcohol, and Milli-Q water to remove surface native oxide and dried under a nitrogen stream. Immediately thereafter, the germanium sample was immersed in a 5 mL mixed metal salt solution (0.05 mmol/L) in a glass vial and kept in the dark for 10 minutes. Subsequently, the shard was carefully removed from the solution and rinsed three times with 5 mL of Milli-Q water. Finally, the shard was dried in a stream of flowing N_2 gas and transferred to a nitrogen-filled glovebox, where it was maintained under subdued light.

3.2 Material Characterization

3.2.1 Fourier Transformed Infrared (FTIR) Spectroscopy

FTIR analyses were performed using a Thermo Nicolet 8700 FTIR Spectrometer and Continuum FTIR Microscope. Samples were prepared by drop coating a toluene dispersion of the solid sample in question onto an electronics-grade Si-wafer (N-type, 100 surface, 100 μm thickness and 10 ohm·cm resistivity) and dried under flowing nitrogen.

3.2.2 Electron Microscopy

Transmission electron microscopy (TEM) bright and dark field images were acquired using a JEOL JEM-ARM200CF S/TEM electron microscope at an accelerating voltage of 200 kV. High resolution (HR) TEM images were processed using Gatan Digital Micrograph software (Version 3.4.1). TEM samples were prepared by depositing a drop of a dilute toluene suspension of the sample in question onto a holey or ultra-thin carbon coated copper grid (obtained from Electron

Microscopy Inc.). The grid bearing the sample was kept in a vacuum chamber at a base pressure of 0.2 bar for at least 24 h prior to data collection. The particle size distribution was assembled as an average shifted histogram as described by Buriak *et al.* for at least 300 particles in TEM. The average shifted histogram averaged the different histogram shapes formed by shifting the bin origin.[25]

Secondary electron scanning electron microscopy (SEM) images were acquired using a Hitachi S4800 FESEM electron microscope at an accelerating voltage of 25 kV. Samples were mounted on a stainless-steel stub by using a conductive tape.

3.2.3 X-ray Photoelectron Spectroscopy (XPS)

XPS analyses were performed using a Kratos Axis Ultra instrument operating in energy spectrum mode at 210 W. The base and operating chamber pressure were maintained at 10^{-7} Pa. A monochromatic Al Kα source ($\lambda = 8.34$ Å) was used to irradiate the samples, and the spectra were obtained with an electron take-off angle of 90°. CasaXPS software (VAMAS) was used to interpret high-resolution spectra. All spectra were internally calibrated to the C 1s emission (284.8 eV) of adventitious carbon. After calibration, a Shirley-type background was applied to remove most of the extrinsic loss structure. The Ge 3d region were deconvoluted into the Ge $3d_{5/2}$ and $3d_{3/2}$ spin-orbit couple for the element Ge and the energy separation of these doublets was fixed at 0.58 eV and the Ge $3d_{3/2}$ to $3d_{5/2}$ area was fixed at 0.67.[26] For the high-resolution XP spectra of metals, the spin-orbit couple energy separation and area were fixed and the spectral envelope was fit using a Lorentzian asymmetric line shape LA(a, b, n) where a and b define the asymmetry and n defines the Gaussian width. The various spectral regions were fit as follows: Au 4f was deconvoluted into the Au $4f_{7/2}$ and $4f_{5/2}$ spin-orbit couple and the energy separation of these doublets was fixed at 3.70 eV and the Au $4f_{5/2}$ to $4f_{7/2}$ area ratio was fixed at 0.75.[26] Ag 3d was deconvoluted into the

Ag $3d_{5/2}$ and $3d_{3/2}$ spin-orbit couple and the energy separation of these doublets was fixed at 6.00 eV and the Ag $3d_{3/2}$ to $3d_{5/2}$ area ration was fixed at 0.67.[26] Cu 2p was deconvoluted into the Cu $2p_{3/2}$ and $2p_{1/2}$ spin-orbit couple and the energy separation of these doublets was fixed at 19.75 eV and the Cu $2p_{1/2}$ and $2p_{3/2}$ area ratio was fixed at 0.50.[26] Pd 3d was deconvoluted into the Pd $3d_{5/2}$ and $3d_{3/2}$ spin-orbit couple and the energy separation of these doublets was fixed at 5.26 eV and the Pd $3d_{3/2}$ to $3d_{5/2}$ area ratio was fixed at 0.67.[26] Pt 4f was deconvoluted into the Pt $4f_{7/2}$ and $4f_{5/2}$ spin-orbit couple and the energy separation of these doublets was fixed at 3.35 eV and the Pt $4f_{5/2}$ to $4f_{7/2}$ area ratio was fixed at 0.75.[26]

3.2.4 Powder X-ray Diffraction (XRD)

XRD measurements were conducted on a Bruker D8 Advance diffractometer using Cu-$K_{\alpha1}$ (λ = 1.5406 Å) and $K_{\alpha2}$ (λ = 1.5444 Å) radiation. Powder samples were mounted on a zero-background Si crystal sample holder and scanned over 2θ ranges of 10 - 100° with a scan step of 0.0015 °/s. The instrumental broadening effect was considered by measuring a NIST LaB_6 standard sample with a same scanning speed. Jade 6 was used to fit the peak broadening with both size and strain effect. Synchrotron diffraction data were collected at the Canadian Light Source, utilizing the Brockhouse high energy wiggler (BXDS-WHE) beamline. The samples were prepared by loading them into polyimide Kapton with an inner diameter of 0.300 mm and outer diameter of 0.350 mm, using a magnetic sample holder in transmission mode. Powder data was collected using a Rayonix MX300HE 2D detector with a detector distance of 496.37 mm. The beam energy was set to 30.3383 keV, and the synchrotron radiation wavelength was calibrated using a LaB_6 standard, which was found to be 0.40867 Å. Prior to integration, the background from the empty Kapton was subtracted.

3.3 Results and Discussion

Germanane used in this study was prepared by deintercalation of $CaGe_2$ (Figure 3.1).[27] The resulting product was sonicated in water for 2 h to maximize exfoliation. Suspensions of GeNSs were then combined with an aqueous solution containing the metal salts of choice (i.e., $AuCl_3$, $AgNO_3$, $CuCl_2$, $PdCl_2$, $PtCl_4$). Upon adding a solution of mixed metal salts to the GeNS suspension, the Ge-H moieties on the GeNS surfaces immediately reacted with the aqueous metal ions resulting in the deposition of size-polydisperse HEA NPs (AuAgCuPdPt) onto the GeNS surfaces. This process was accompanied by the evolution of bubbles (presumably hydrogen) and a color change from red to black (Figure 3.2).
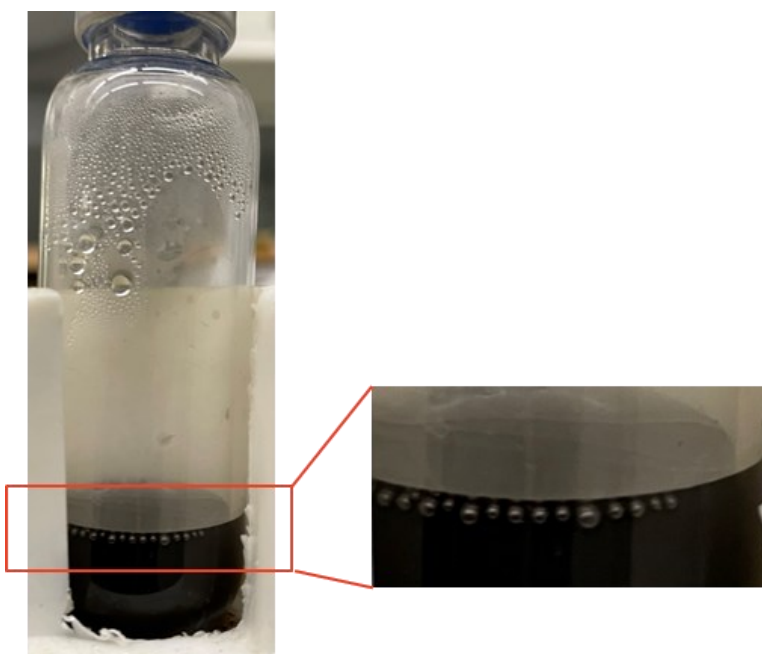
Figure 3.2. Photograph of the reaction forming HEA NPs@GeNSs showing evolution of hydrogen bubbles.
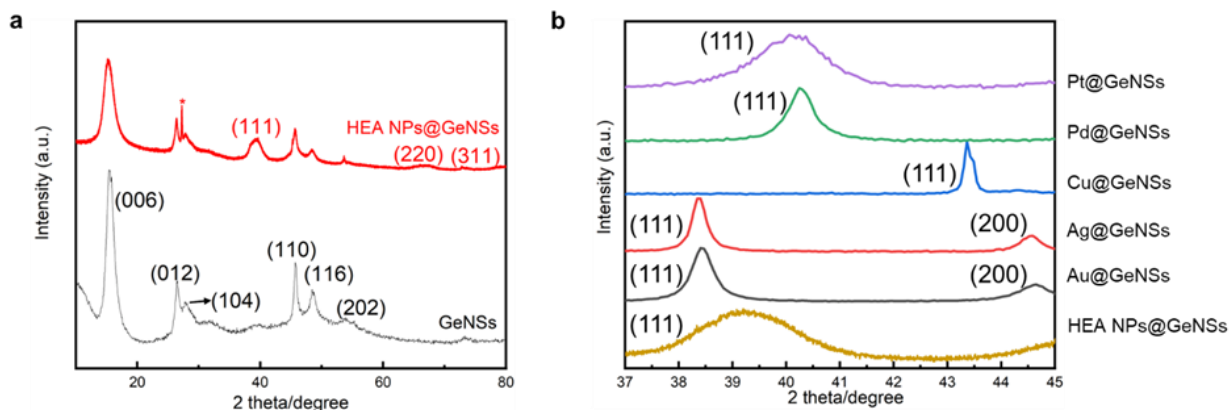
Figure 3.3. XRD patterns of (a) HEA NPs@GeNSs (red trace) and GeNSs (black trace). (b) A comparison of laboratory-based XRD patterns of M@GeNSs and HEA NPs@GeNSs from 37˚ to 45˚. (*) correspond to reflections arising from bulk Ge impurities.
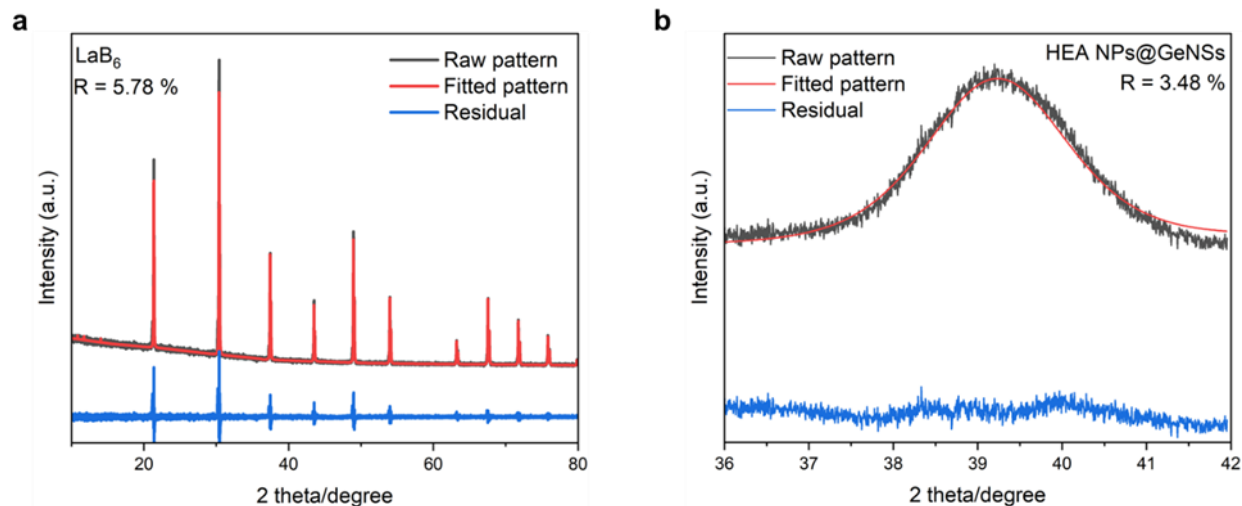
Figure 3.4. XRD patterns and corresponding fitting for (a) LaB_6 standard sample, and (b) the (111) reflection in the laboratory-based X-ray diffraction pattern for HEA NPs@GeNSs corresponding to an HEA nanocrystal domain size of approximately 5.5 nm.

Powder X-ray diffraction (XRD) was used to interrogate the HEA NPs deposited on the GeNSs (HEA NPs@GeNSs) and reveals their crystal structure. The XRD pattern of HEA NPs@GeNSs showed reflections characteristic of the GeNSs, as well as reflections arising from the nanoparticles. The HEA NP related features are weak and broad due to their small crystallite size (Figure 3.3a). The feature appearing in the range of 38° - 41° (Figure 3.3b) corresponds to the

(111) reflection of the single-phase solid solution HEA particles consistent with typical patterns reported for AuAgCuPdPt HEA NPs.[28] Evaluation of the peak broadening of this reflection was performed using the Scherrer equation after considering the effects of instrumental broadening (Figure 3.4a); this analysis provided approximate crystallite size of 5.5 nm when taking into account peak broadening arising from decreased size (Figure 3.4b).[29] We cannot account for strain contributions because we cannot determine a dependence on 2 theta. These results are consistent with the successful deposition of HEA NPs while retaining the GeNS structure. Synchrotron XRD analysis (Figure 3.5) showed a pattern with improved signal-to-noise ratio along with intense characteristic GeNS reflections[30] superimposed on the broad peak at 10.1° relating to the lattice parameter of 4.0607(3) Å for the FCC structure.
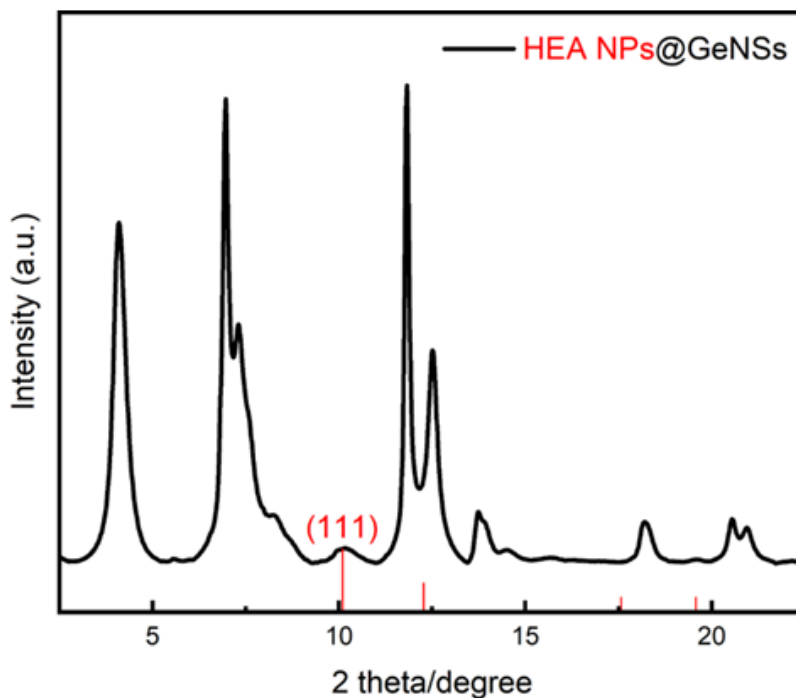
Figure 3.5. Synchrotron XRD (λ = 0.40867 Å) pattern of HEA NPs@GeNSs exhibiting the (111) reflections from the HEA NPs and other intense reflections from GeNSs.

To further investigate the nature of the HEA NPs@GeNSs, we evaluated the materials using Fourier-transform infrared (FTIR) and X-ray photoelectron (XPS) spectroscopies. The FTIR

spectrum (Figure 3.6) of the parent GeNSs showed intense features associated with Ge-H stretching (2000 cm^{-1}) and bending modes (830 cm^{-1} and 770 cm^{-1}).[31] Following deposition of the HEA NPs, the FTIR spectrum of HEA NPs@GeNSs displayed a prominent feature in the range of 700 to 890 cm^{-1} that we attribute to Ge-O vibrations.[32] We also observed that the intensities of Ge-H associated features diminished, although they were still obvious. Our observations are similar to previous reports for metal-decorated germanane[21] and silicane,[33] and are consistent with the surface hydride functionalities have reduced metal ions, leaving surface dangling bonds on the GeNSs that are subsequently oxidized to form Ge-O-Ge and Ge-O-H moieties.
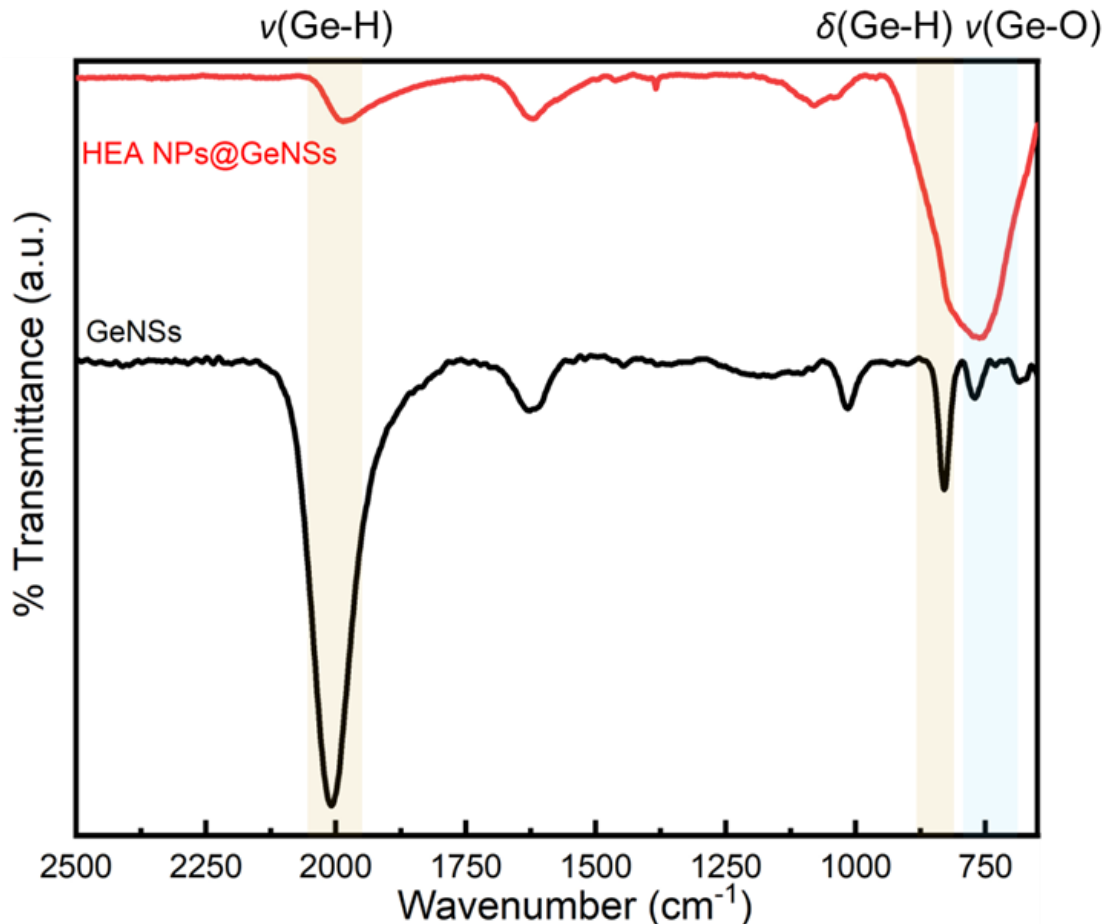
Figure 3.6. Representative FTIR spectra of GeNSs before (black) and after (red) HEA NPs deposition.

XPS provides additional information regarding composition, bonding environment, and oxidation states of elements in the presented materials. The survey XP spectrum of the HEA NPs@GeNSs was consistent with the FTIR and XRD analyses, showing evidence of oxidation and corresponding metal emissions (Figure 3.7). The metal amounts of the HEA NPs@GeNSs were calculated based on the compositions determined from the XP survey spectra integration, and the atomic percentage of each metal was approximately 2% (Table 3.1). We calculated the configuration entropy (1.61R) based on the atomic percentage indicating a high mixing entropy.
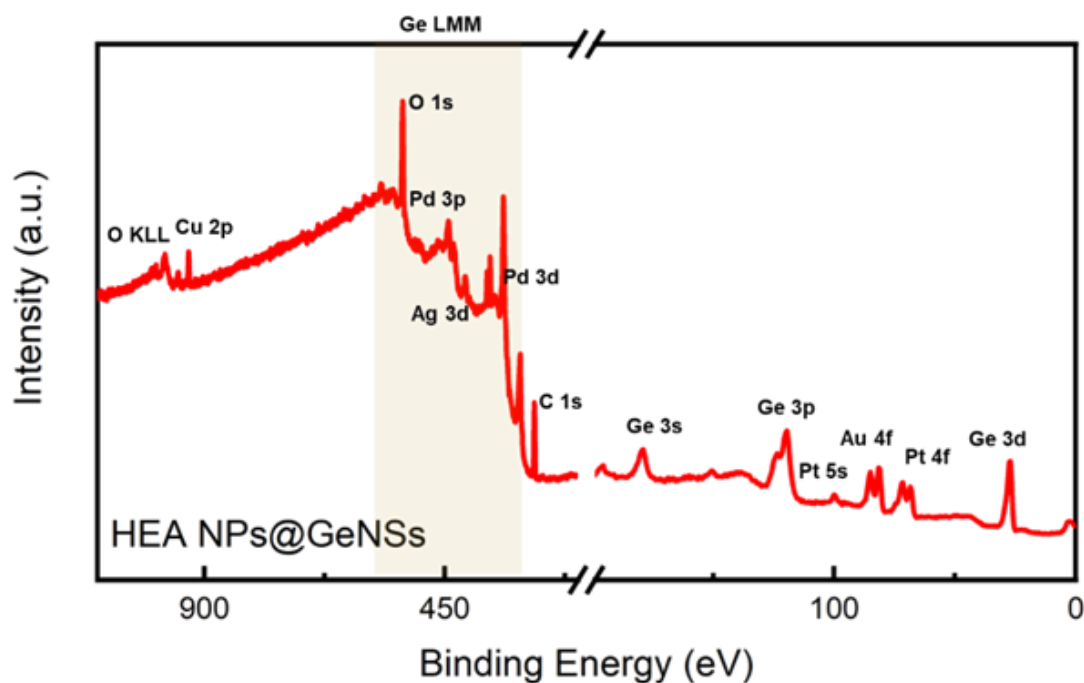
Figure 3.7. Representative survey XP spectrum of HEA NPs@GeNSs.

The high-resolution XP spectra of HEA NPs@GeNSs showed emissions associated with the corresponding metal (i.e., Au, Ag, Cu, Pd, and Pt) deposits and the underlying GeNSs (Figure 3.8). The Ge 3d spectra were fitted to reveal a binding energy of 29.8 eV, which has been previously attributed to Ge in the nanosheets.[30] We also note components appearing at 31.3 and 32.5 eV that have previously been attributed to Ge^{2+} and Ge^{4+} species, respectively (Figure 3.8a).[21]

The high resolution XP spectra of each metal (Figures 3.8b-f) show emissions at binding energies characteristic of the corresponding metallic state (i.e., Au $4f_{7/2}$, 83.9 eV; Ag $3d_{5/2}$, 367.9 eV; Cu $2p_{3/2}$, 932.5 eV; Pd $3d_{5/2}$, 335.2 eV; Pt $4f_{7/2}$, 71.0 eV).

Table 3.1. Summary of XPS data for HEA NPs@GeNSs.

	Ge 3d	Au 4f	Ag 3d	Cu 2p	Pd 3d	Pt 4f
Emission (eV)	29.8	83.9	367.9	932.5	335.2	71.0
Reference emission (eV)[a]	29.8	84.0	368.2	933.0	335.0	71.0
Atomic percentage (%)	20.7	1.94	2.03	2.16	2.17	1.99

[a] Reference metal emissions are from NIST X-ray Photoelectron Spectroscopy Database.[26]
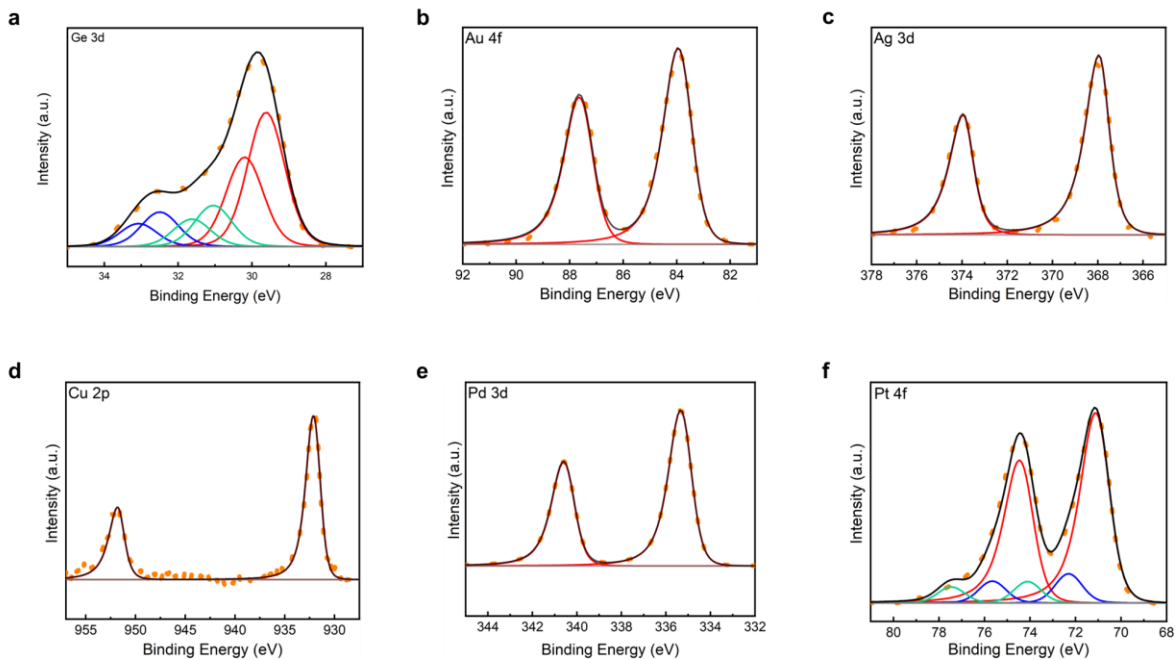
Figure 3.8. Representative high-resolution XP spectra of HEA NPs@GeNSs: (a) Ge 3d, (b) Au 4f, (c) Ag 3d, (d) Cu 3d, (e) Pd 3d and (f) Pt 4f regions.

Electron microscopy was used to study the morphology of HEA NPs@GeNSs. High-resolution transmission electron microscopy (HRTEM) images confirm the deposition of nanocrystalline HEA NPs onto the GeNS surfaces (Figure 3.9), while brightfield TEM reveals the deposited metal nanoparticles are pseudospherical with dimensions of 5.6 nm (Figure 3.10).[34]

High-angle annular dark-field scanning transmission electron microscopy (HAADF-STEM) (Figure 3.9b) shows HEA NPs@GeNS morphologies consistent with brightfield imaging and energy dispersive X-ray (EDX) mapping confirms the co-localization of all metals in the morphological features in darkfield and HAADF-STEM (Figures 3.9 c-i). The EDX spectrum (Figure 3.11) provides signatures for Ge (i.e., ca. 15 atom %) and the other five target metals (i.e., ca. 1.5 atom %). Taken together, and consistent with the XPS analysis, these data support our conclusion that the alloy is homogeneous and not subject to obvious surface segregation or phase separation.
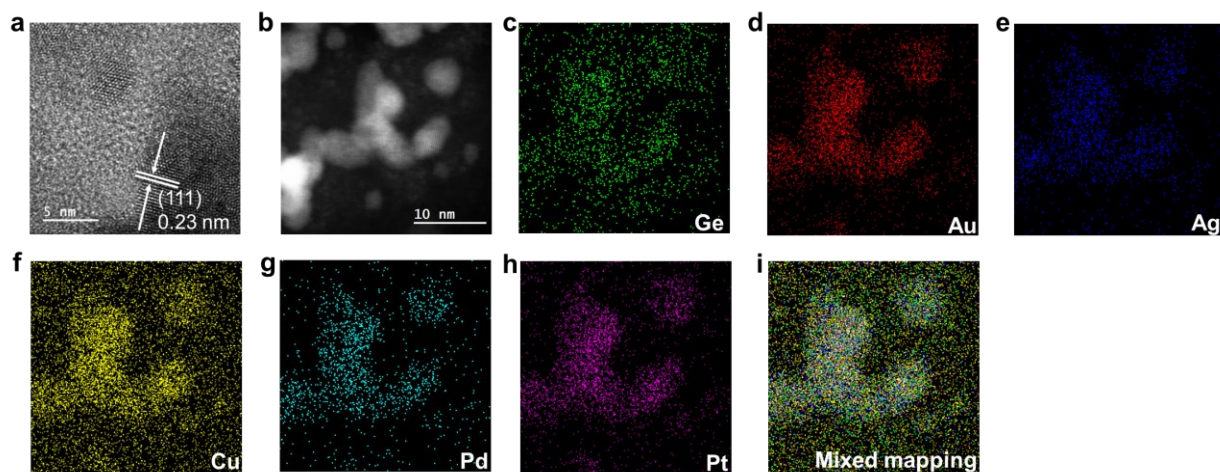
Figure 3.9. TEM and EDX analysis of HEA NPs@GeNSs. (a) High-resolution image showing characteristic metal (111) lattice spacing. (b) HAADF-STEM image and (c-i) corresponding EDX mapping of the indicated elements.

We also investigated the liberation of HEA NPs from GeNSs by exposing HEA NPs@GeNSs to UV light (Figure 3.12). Upon exposure to UV light, the GeNSs were destroyed and the liberated HEA NPs were collected by centrifugation. Consistent with liberation, powder XRD showed no reflections associated with the GeNSs. In addition, the XRD data (Figure 3.13a) indicates the HEA NPs display a characteristic face-centred cubic structure as evidence by (111), (200), and (220) reflections appearing at 39.3°, 45.9°, and 66.3°, respectively. Further analysis of

these broadened features using the Scherrer equation provided an estimated crystallite size of 6.1 nm (Figure 3.13b). After considering the dependence of peak broadening on diffraction angle, the broadening distribution of the HEA NPs (Figure 3.14) shows, not unexpectedly that there is also strain-induced broadening.
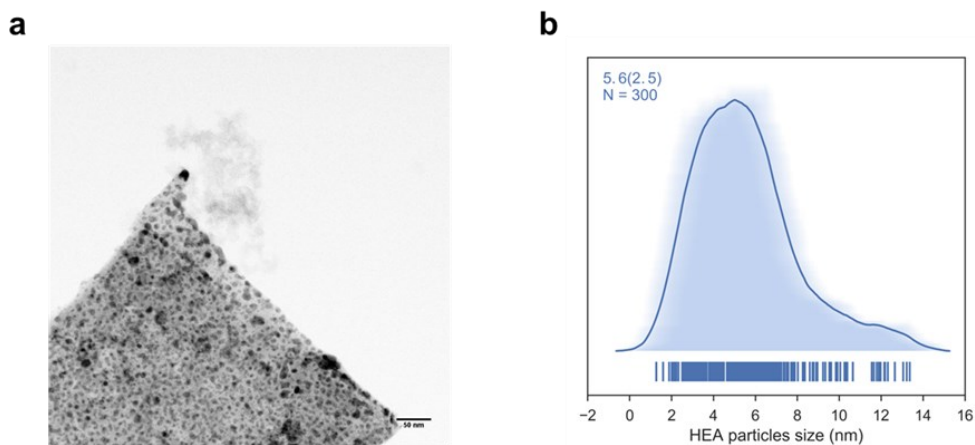
Figure 3.10. Representative (a) brightfield TEM image of HEA NPs@GeNSs and the associated (b) average shifted histogram for HEA particles on GeNSs.
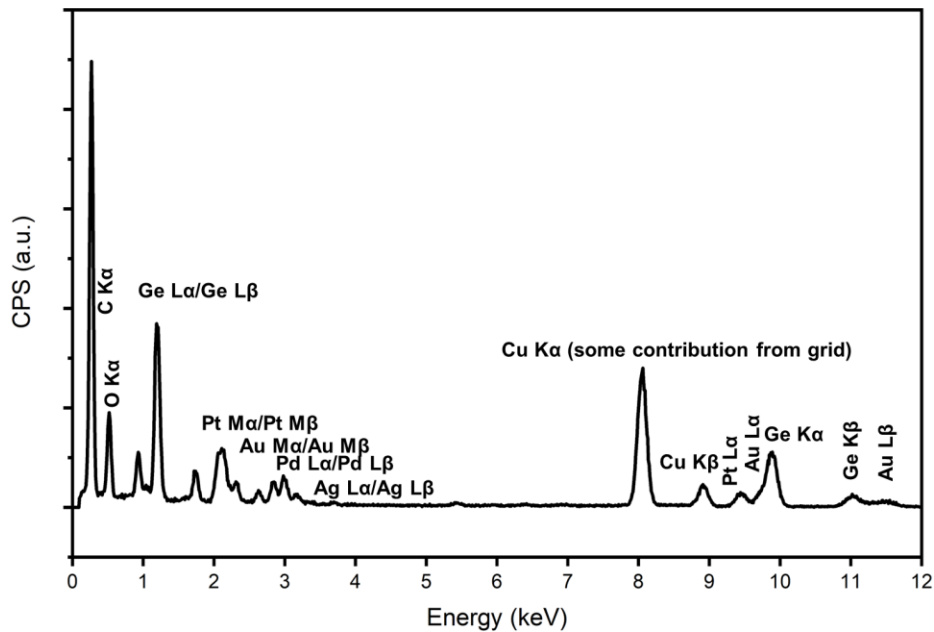
Figure 3.11. Representative EDX spectrum for HEA NPs@GeNSs.
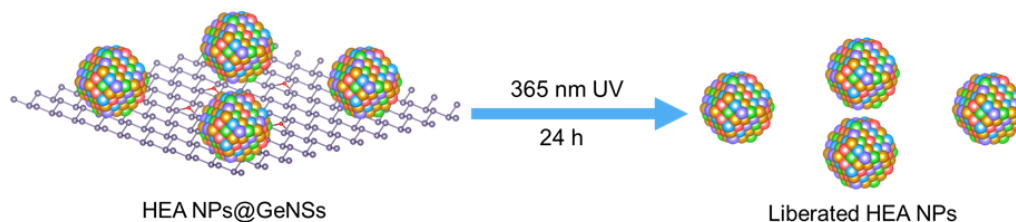
Figure 3.12. A pictorial illustration of the liberation of high-entropy nanoparticles from germanane.
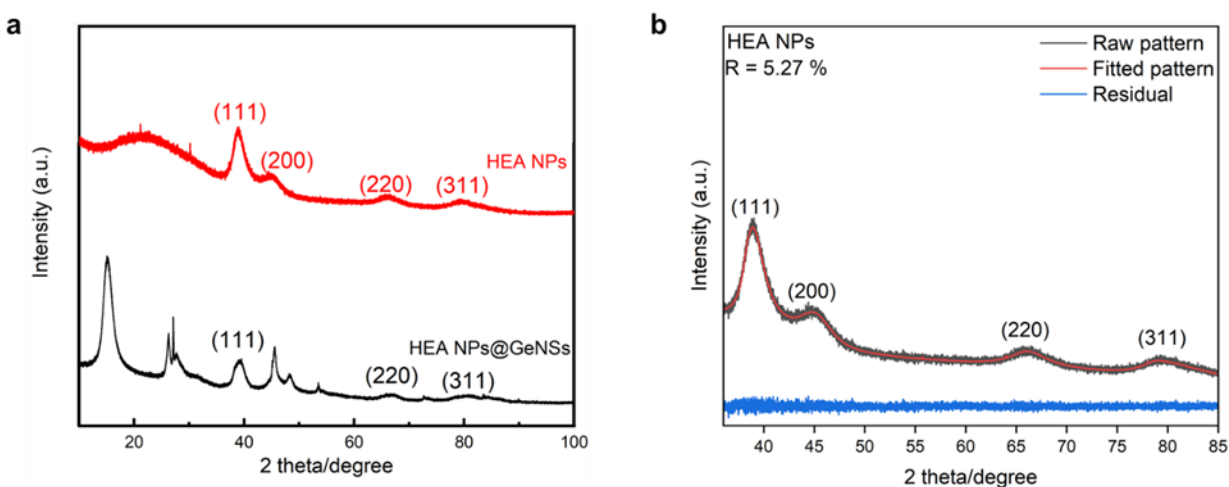
Figure 3.13. (a) Laboratory XRD patterns of liberated HEA NPs (red trace) and corresponding HEA NPs@GeNSs (black trace). (b) Fitting results of the (111) reflection in the laboratory-based X-ray diffraction pattern for liberated HEA NPs corresponding to an HEA nanocrystal domain size of 6.1 nm.

XPS was used to gain further information about the composition and the oxidation states of the constituent elements that make up the HEA NPs. The survey spectrum (Figure 3.15) revealed trace amounts of Ge (i.e., 1.72 atom %), O (i.e., 19.5 atom %) and mainly consisted of the five metal components (i.e., 14.0 atom % for each metal) in consistent with the XRD results. Not surprisingly, fitting the Ge 3d spectrum provided the components at 31.3 and 32.5 eV that are attributed to the residual oxidized Ge species.[21] The XP spectra of each metal (Figure 3.16) showed emissions at binding energies characteristic of the corresponding metallic state (i.e., Au $4f_{7/2}$, 83.7 eV; Ag $3d_{5/2}$, 367.8 eV; Cu $2p_{3/2}$, 932.4 eV; Pd $3d_{5/2}$, 335.1 eV; Pt $4f_{7/2}$, 70.9 eV, Table S3.2).

103

However, they also showed varying degrees of oxidation, as the decomposition of GeNSs exposed more of the HEA NP surface leading to some oxidation during liberation.
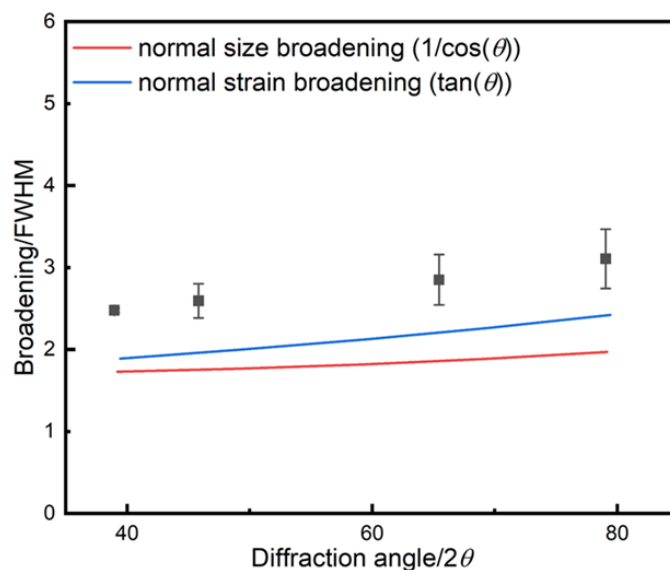
Figure 3.14. XRD peak broadening as a function of diffraction angle for liberated HEA NPs.

The morphology of the HEA NPs liberated from the GeNSs was evaluated using TEM. The brightfield TEM imaging (Figure 3.17a) revealed spherical HEA NPs. The size of the HEA NPs after liberation was found to be 5.9 ± 1.8 nm (Figure 3.17b), consistent with the preliberation dimensions size. EDX mapping (Figure 3.18) provided evidence of the co-localization of morphological features in HAADF-STEM images and confirmed the presence of the five target metals. The EDX spectrum (Figure 3.19) showed a negligible Ge signal (i.e., 0.05 atom %) and metal signals (i.e., ca. 15 atom %), indicating the successful liberation of the HEA NPs. The configuration entropy (1.61R) was calculated based on the atomic percentage indicating a high mixing entropy.

Having demonstrated the feasibility of using germanium nanosheets (GeNS) as a multipurpose reducing agent and substrate for the growth of high-entropy alloy nanoparticles (HEA NPs) we endeavored to explore the scope of Ge substrates that could do the same. We first

turned to H-terminated germanium nanoparticles (H-GeNPs) that were prepared via thermal disproportionation of 'Ge(OH)$_2$' followed by removal of the encapsulating oxide via aqueous HF etching.[23] Upon addition of the mixed metal ion solution previously used for HEA NP deposition on GeNSs, the Ge-H moieties on the GeNP surfaces facilitated the immediate reduction of metal ions and with deposition of size-polydisperse HEA NPs (AuAgCuPdPt) onto the GeNP surfaces (Figure 3.20).
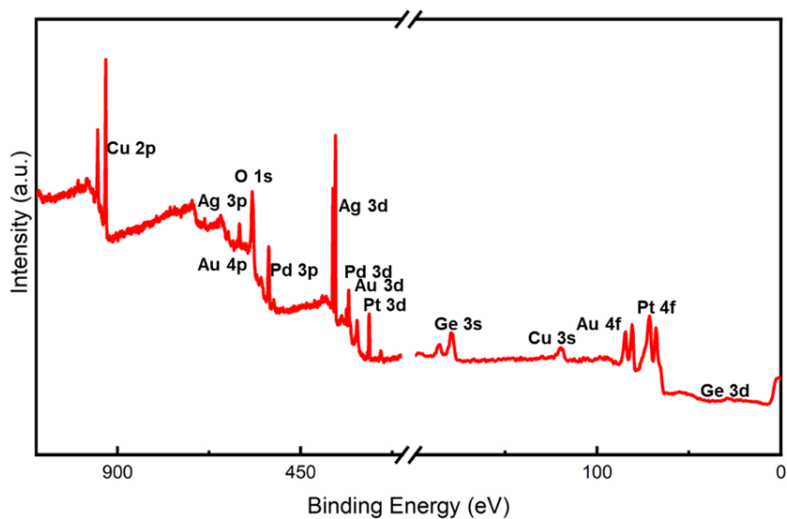
Figure 3.15. Representative survey XP spectrum of liberated HEA NPs.
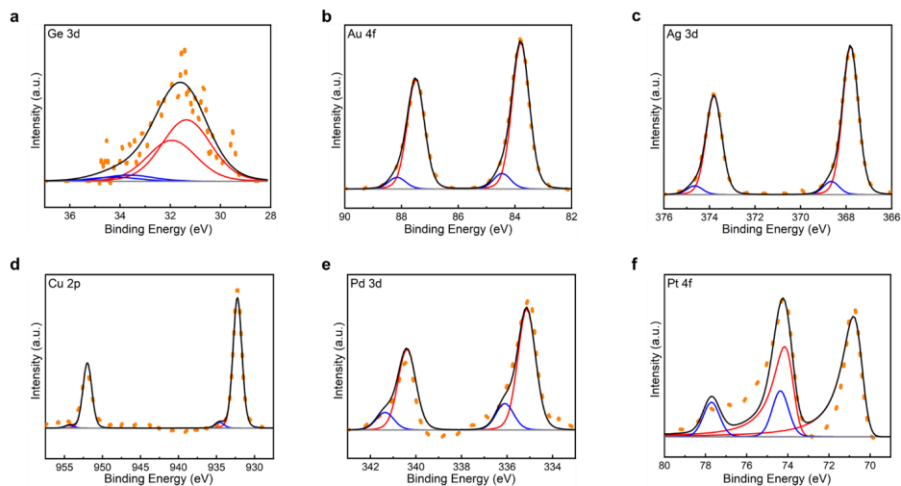
Figure 3.16. Representative high-resolution XP spectra of liberated HEA NPs: (a) Ge 3d, (b) Au 4f, (c) Ag 3d, (d) Cu 3d, (e) Pd 3d and (f) Pt 4f regions.

105

Table 3.2. Summary of XPS data for liberated HEA NPs.

	Ge 3d	Au 4f	Ag 3d	Cu 2p	Pd 3d	Pt 4f
Emission (eV)	31.3	83.7	367.8	932.4	335.1	70.9
Reference emission (eV)[a]	29.8	84.0	368.2	933.0	335.0	71.0
Atomic percentage (%)	1.72	14.35	13.99	14.27	13.51	14.86

[a] Reference metal emission are from NIST X-ray Photoelectron Spectroscopy Database.[26]
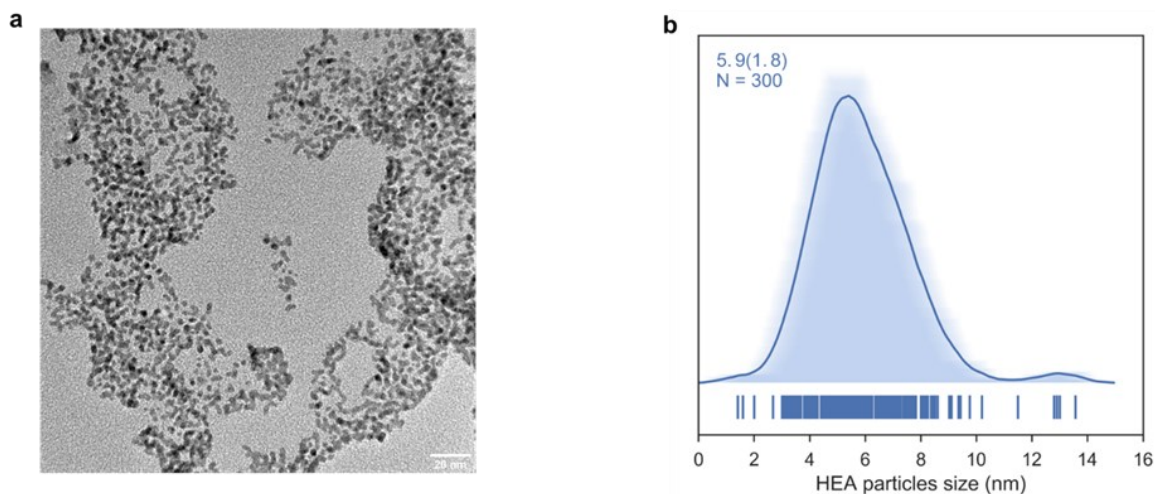
Figure 3.17. Representative (a) brightfield TEM image of HEA NPs and the associated (b) average shifted histogram.
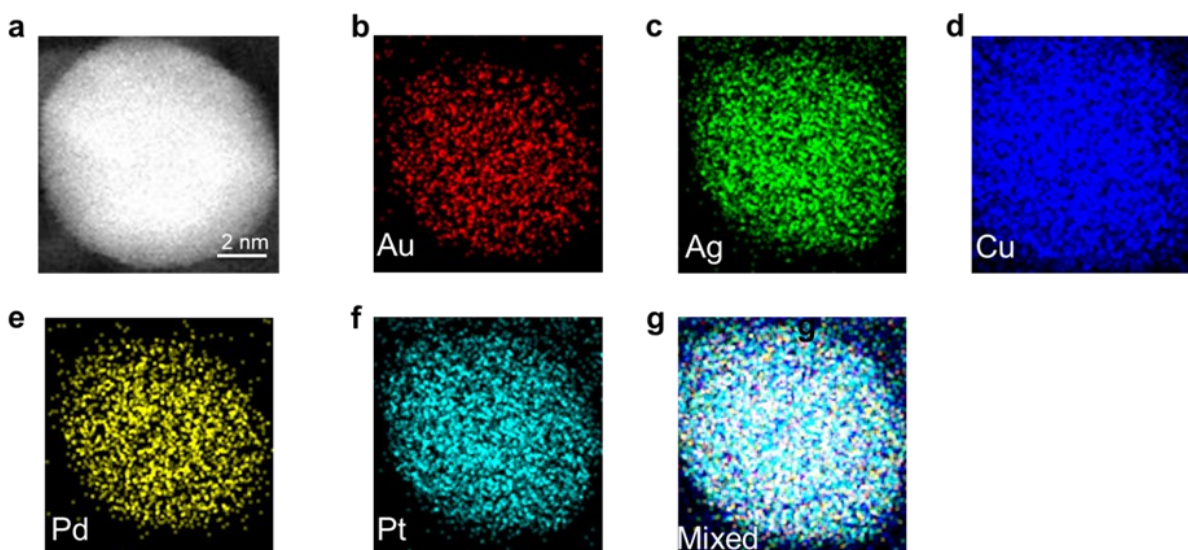
Figure 3.18. Representative HAADF-STEM images and EDX mapping of liberated HEA NPs.
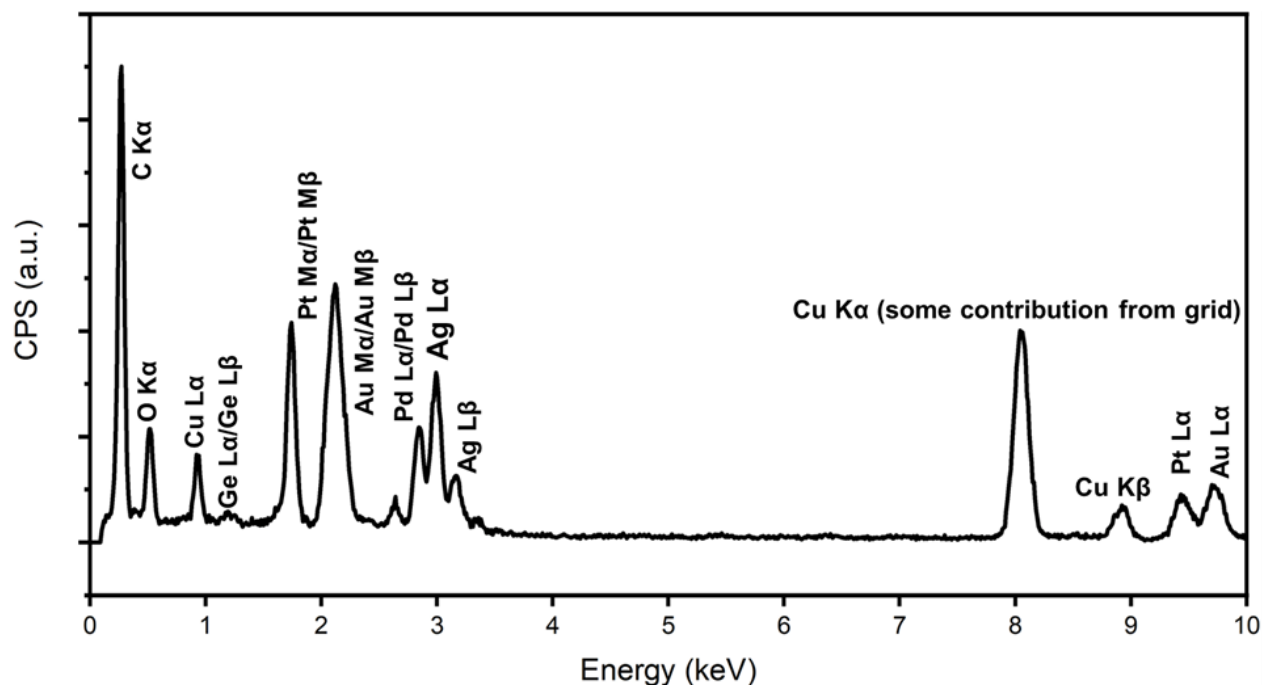
Figure 3.19. Representative EDX spectrum for HEA NPs liberated from GeNSs.
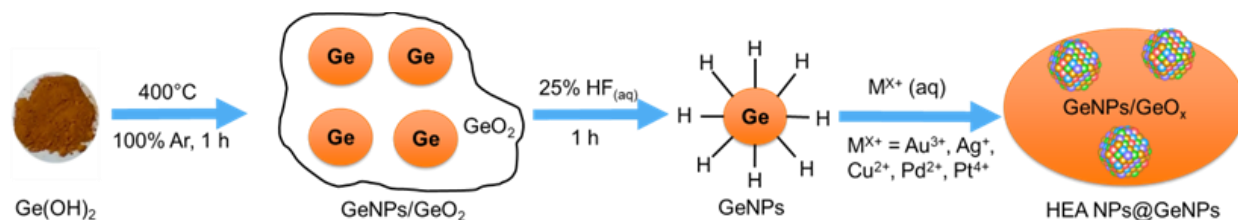
Figure 3.20. A pictorial illustration of the formation of high-entropy nanoparticles on GeNPs. GeNPs were prepared via thermal disproportion of 'Ge(OH)$_2$'. The GeNPs/GeO$_2$ were subsequently etched in the 25 % HF for 1 h to remove the oxide. The mixed aqueous solution of metal salts (i.e., AuCl$_3$, AgNO$_3$, CuCl$_2$, PdCl$_2$, and PtCl$_4$) was added into the aqueous suspension of GeNPs. Metal ions were reduced and deposited onto the germanane surfaces forming HEA NPs.

The HEA NPs@GeNPs were characterized using XRD and FTIR spectroscopy to investigate their crystal structure and bonding. The obtained HEA NPs@GeNPs possessed a single-phase solid solution crystal structure, as evidenced by the characteristic reflections of GeNP superimposed on a weak and broad peak within the 38°- 41° range (Figure 3.21a).[22] Scherrer analysis provided an estimate of crystallite size of 7.2 nm (Figure 3.21b). The FTIR spectrum showed a dominant Ge-O vibration feature in the range of 700 to 890 cm^{-1}, while the Ge-H

107

stretching at 2000 cm^{-1} was diminished (Figure 3.22),[23] indicating that the surface hydride

functionalities have reduced metal ions, leaving surface dangling bonds on the GeNPs that

subsequently oxidized to form Ge-O-Ge and Ge-O-H moieties. These results are consistent with

the previous observations on HEA NPs@GeNSs sample (vide supra).
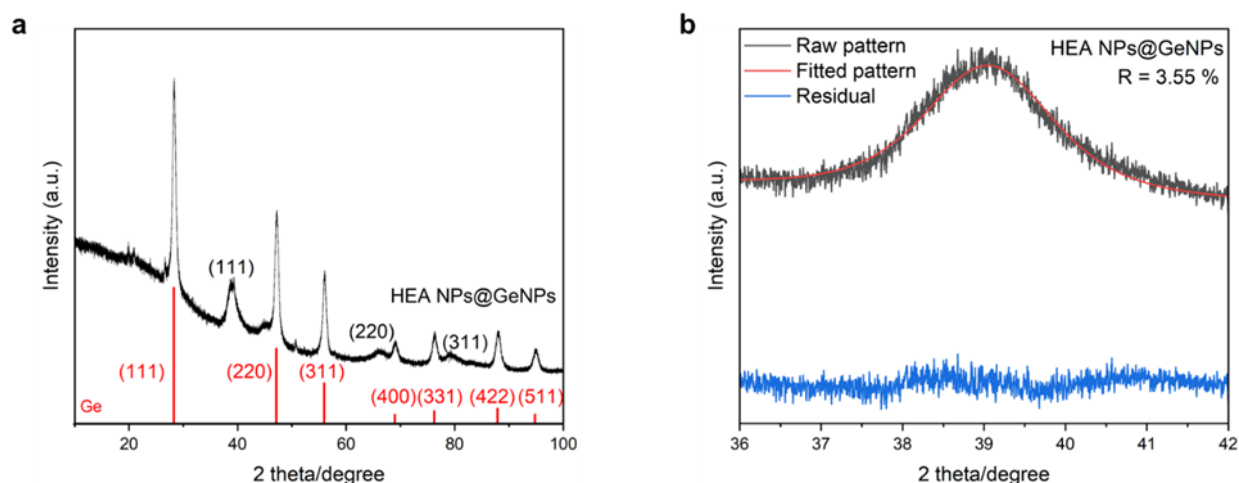
Figure 3.21. (a) Laboratory XRD pattern of HEA NPs@GeNPs (black trace). Characteristic reflections for bulk Ge (PDF# 79-0001) are provided for reference. (b) Fitting results of the (111) reflection in the laboratory-based X-ray diffraction pattern for HEA NPs@GeNPs corresponding to an HEA nanocrystal domain size of 7.2 nm.
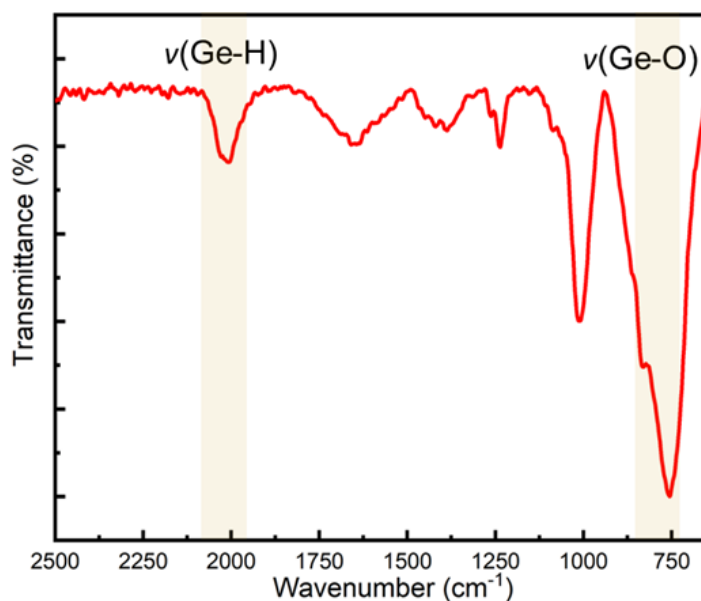
Figure 3.22. Representative FTIR spectrum of HEA NPs@GeNPs.

XPS was used to investigate the elemental composition and oxidation states of the resulting HEA NPs@GeNPs. The survey spectrum showed the expected metal emissions (approximately 1 atom %) and Ge (24.6 atom %) in the sample (Figure 3.23). The high-resolution spectra of each metal within HEA NPs@GeNPs exhibited characteristic metallic binding energies (Figure 3.24), including Au $4f_{7/2}$, 84.0 eV; Ag $3d_{5/2}$, 367.9 eV; Cu $2p_{3/2}$, 932.3 eV; Pd $3d_{5/2}$, 335.1 eV; and Pt $4f_{7/2}$, 71.0 eV (Table 3.3). The Ge 3d region provided a binding energy of 29.6 eV, consistent with the previous attribution of Ge in the nanoparticles.[24] Notably, the majority of Ge^{4+} species were observed at 32.5 eV, while some partial Ge^{2+} species were present at 31.7 eV. This observation suggests that the agglomeration of GeNPs during the reaction increased the likelihood of forming Ge-O-Ge bonds in the HEA NPs@GeNPs, resulting in a higher component of Ge^{4+} species.
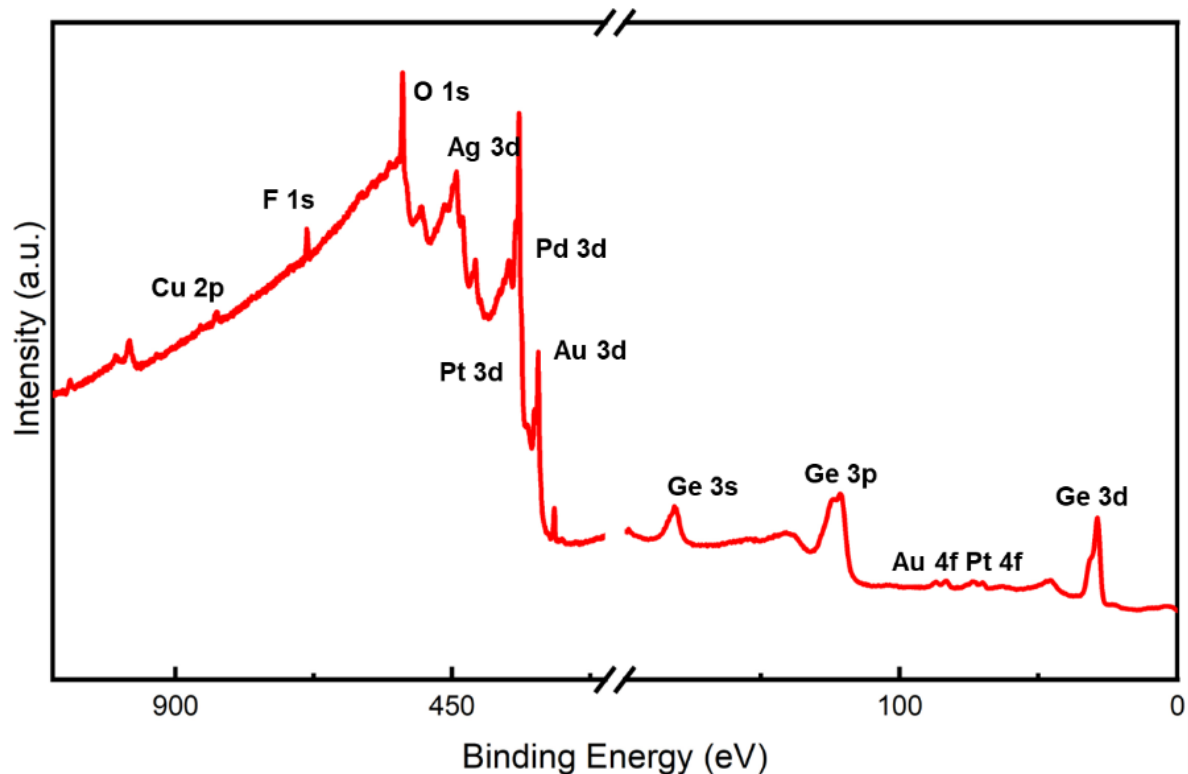
Figure 3.23. Representative survey XP spectrum of HEA NPs@GeNPs.
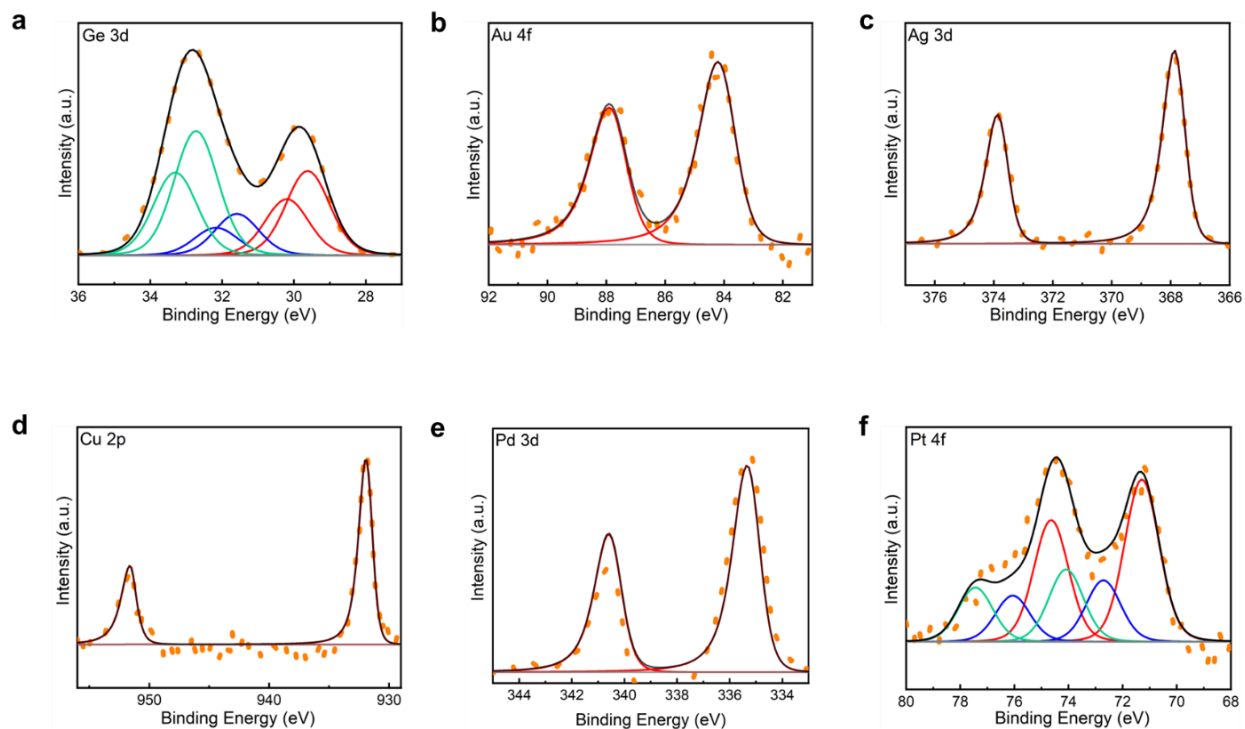
Figure 3.24. Representative high-resolution XP spectra of HEA NPs@GeNPs: (a) Ge 3d, (b) Au 4f, (c) Ag 3d, (d) Cu 3d, (e) Pd 3d and (f) Pt 4f regions.

Table 3.3. Summary of XPS data for HEA NPs@GeNPs.

	Ge 3d	Au 4f	Ag 3d	Cu 2p	Pd 3d	Pt 4f
Emission (eV)	29.6	84.0	367.9	932.3	335.1	71.0
Reference emission (eV)[a]	29.6	84.0	368.2	933.0	335.0	71.0
Atomic percentage (%)	24.6	0.86	1.01	0.96	0.87	0.99

[a] Reference metal emission are from NIST X-ray Photoelectron Spectroscopy Database.[26]
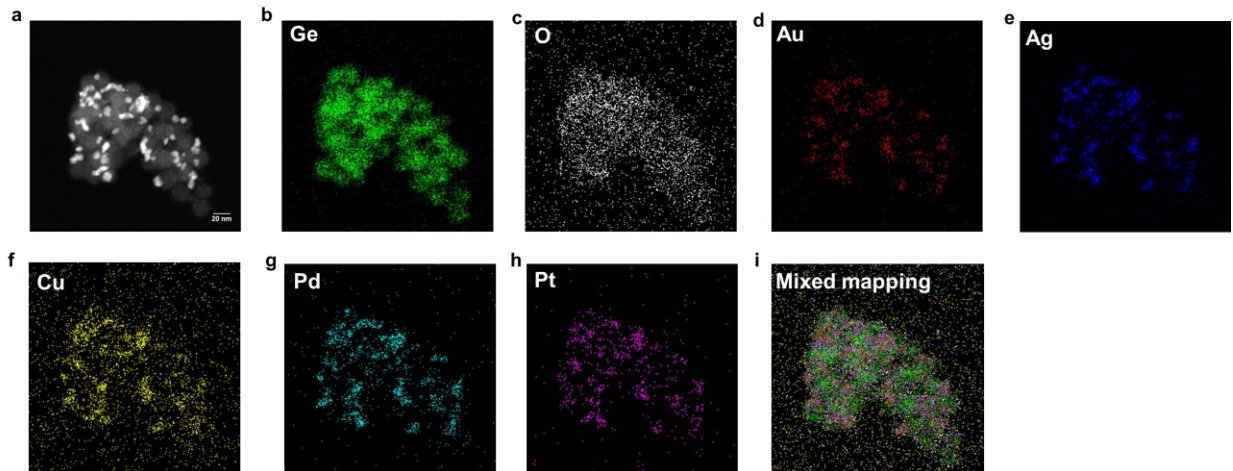
Figure 3.25. STEM and EDX analysis of HEA NPs@GeNPs. (a) HAADF-STEM image and (b-i) corresponding EDX mapping of the indicated elements.
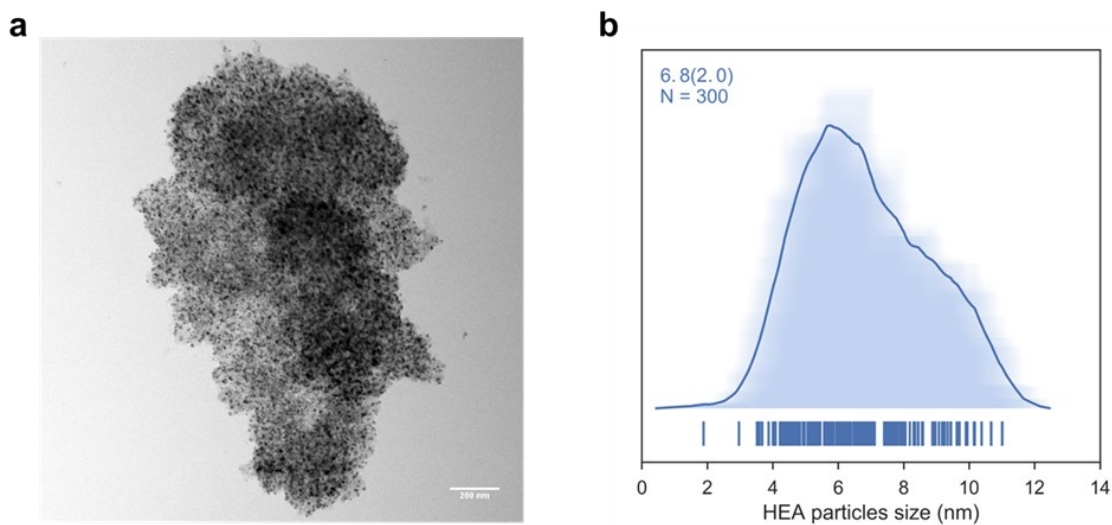
Figure 3.26. Representative (a) brightfield TEM image of HEA NPs@GeNPs and (b) average shifted histogram for HEA particles on GeNPs.

The morphology of HEA NPs@GeNPs was examined using a HAADF-STEM image (Figure 3.25a). The size of the deposited HEA NPs, as measured in the brightfield image (Figure 3.26), was 6.8 ± 2.0 nm in agreement with Scherrer analysis of the corresponding XRD pattern.[34] EDX mapping (Figure 3.25b-i) is consistent with the deposited alloy nanoparticles being homogenous and the GeNP substrate was partially oxidized, in agreement with the FTIR and XPS

111

results. The EDX spectrum (Figure 3.27) further indicated an elemental composition of Au (1.6 atom %), Ag (1.5 atom %), Cu (1.3 atom %), Pd (1.1 atom %), and Pt (1.4 atom %) which agrees with the chemical composition determined by XPS.
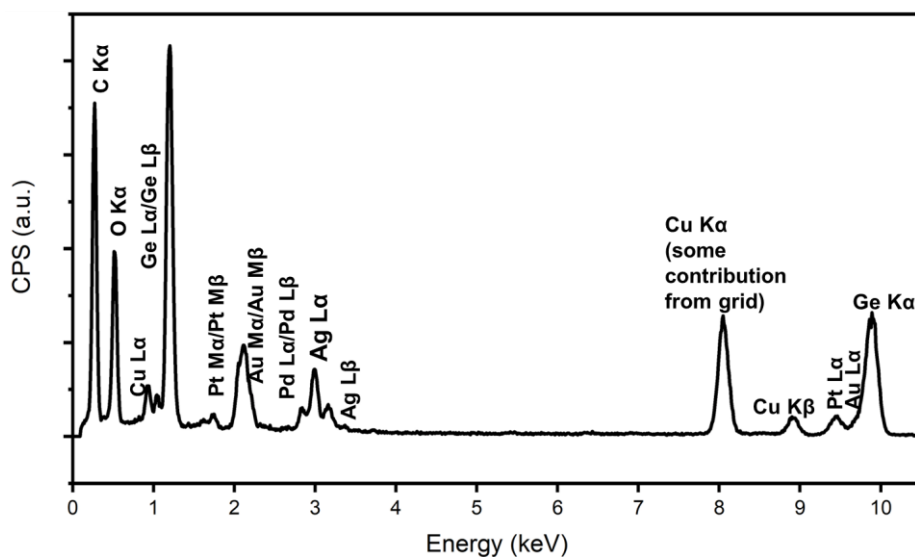
Figure 3.27. Representative EDX spectrum for HEA NPs@GeNPs.
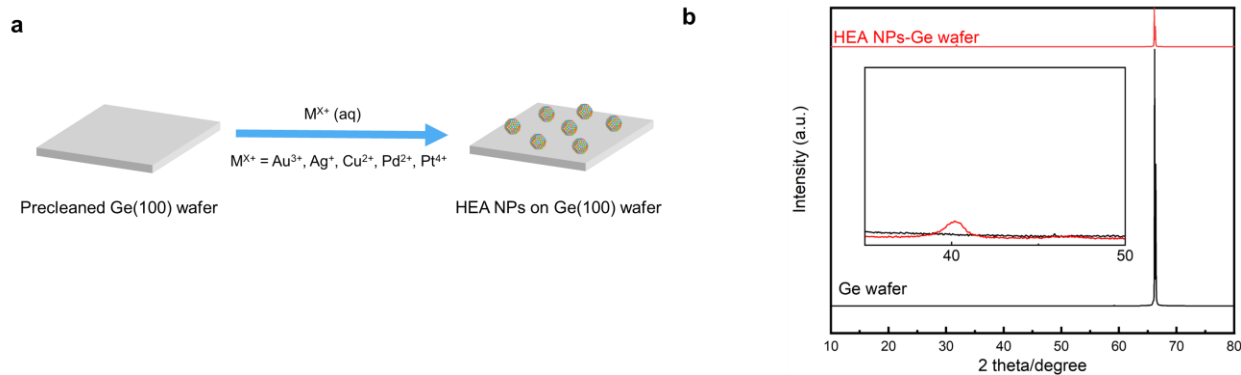
Figure 3.28. (a) Schematic illustration of the deposition of the HEA NPs on Ge(100) wafer. (b) XRD patterns of HEA NPs-Ge wafer and Ge(100) wafer.

Finally, we turned our attention to a bulk Ge wafer to explore the generalizability of our approach toward preparing HEA NPs. A precleaned Ge (100) wafer was immersed in a solution containing a predefined mixture of metal salts for 10 minutes. Doing so resulted in the deposition of HEA NPs on the Ge surface (Figure 3.28a). The solid solution structure of the deposited HEA

112

NPs was characterized using powder XRD (Figure 3.28b) and showed a diminished intensity of the preferential reflection (100) at 67°, suggesting the crystallinity of Ge (100) decreased due to the deposition, and a broad reflection at 38° - 41°. The HEA NPs had a crystalline domain size of 35.3 nm, as determined by the Scherrer equation.
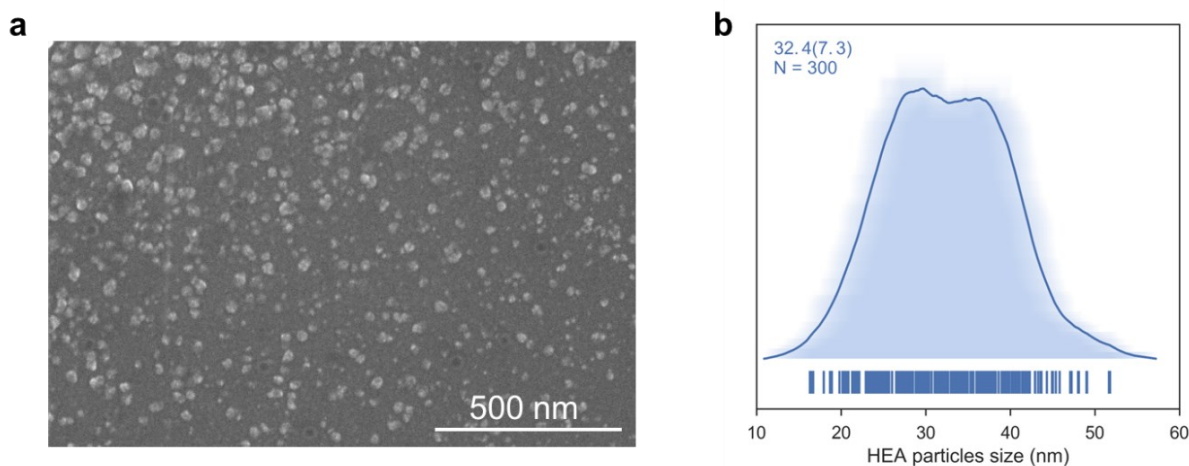
Figure 3.29. Representative (a) SEM image of HEA NPs-Ge wafer and (b) average shifted histogram for HEA NPs.
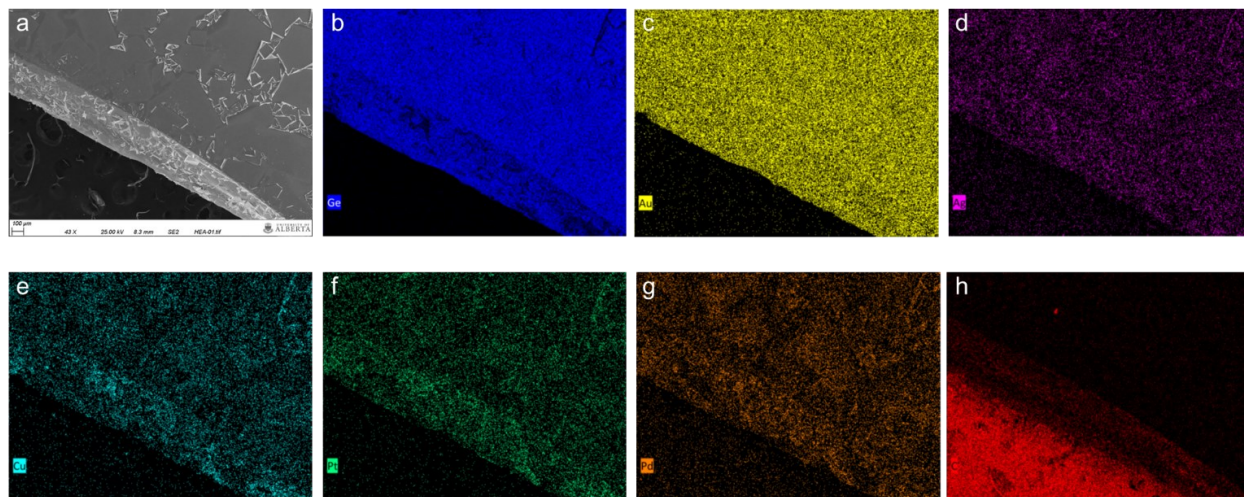
Figure 3.30. (a) Representative SEM image and (b-h) EDX mapping for HEA NPs-Ge wafer.

113
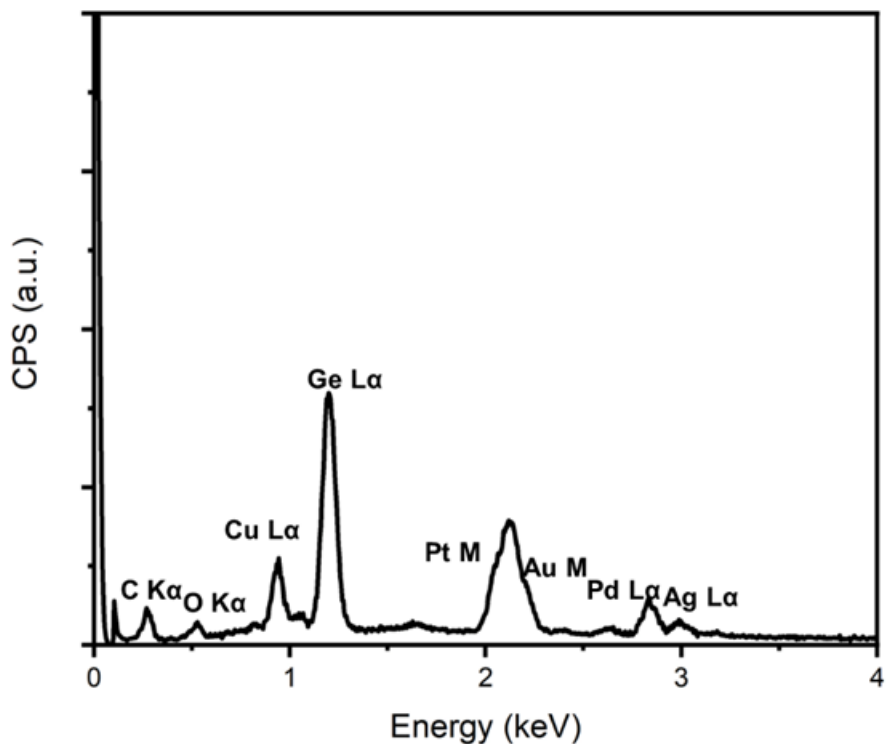
Figure 3.31. Representative SEM/EDX spectrum for HEA NPs-Ge wafer.
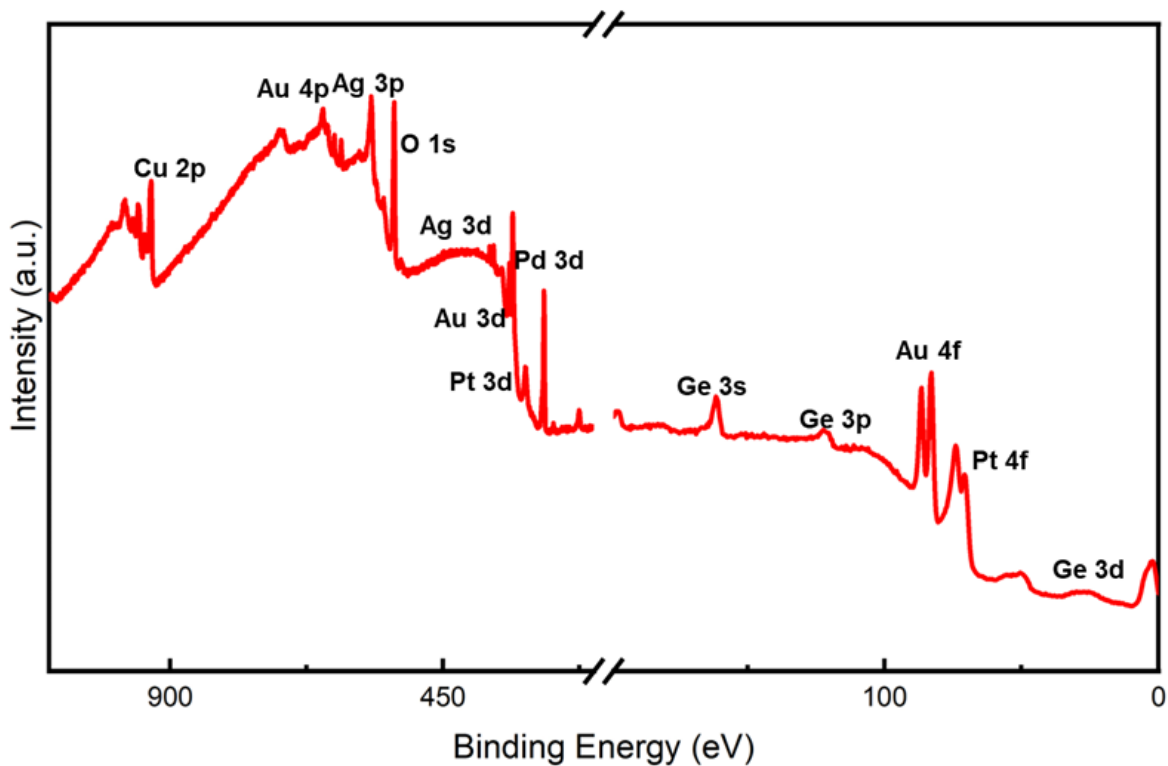
Figure 3.32. Representative survey XP spectrum of HEA NPs-Ge wafer.

114
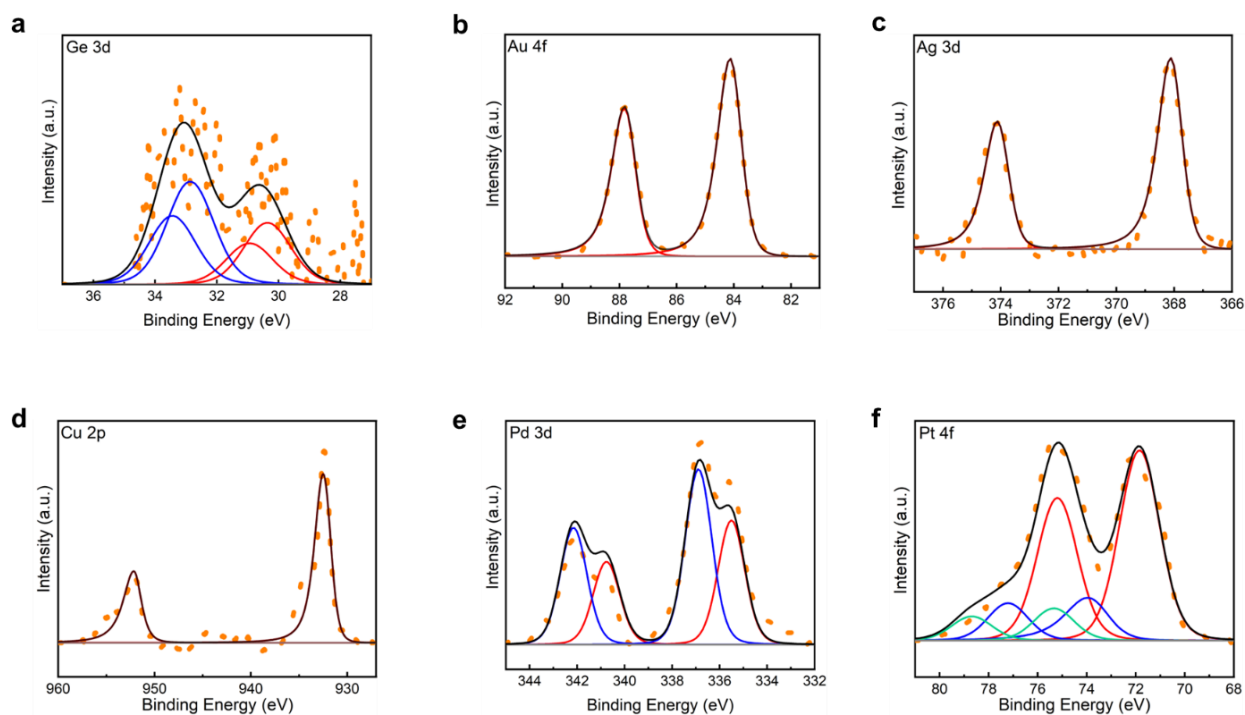
Figure 3.33. Representative high-resolution XP spectra of HEA NPs-Ge wafer: (a) Ge 3d, (b) Au 4f, (c) Ag 3d, (d) Cu 3d, (e) Pd 3d and (f) Pt 4f regions.

SEM imaging showed the deposited HEA NPs had an average size of 32.4 ± 7.3 nm on the surface of the Ge wafer, with no obvious evidence of localized substrate etching observed (Figure 3.29). SEM/EDX measurement (Figures 3.30 and 3.31) indicated a homogenous distribution of the metal elements, with an atomic composition of Au (4.78 atom %), Ag (3.10 atom %), Cu (3.39 atom %), Pd (3.85 atom %), and Pt (4.64 atom %).

Table 3.4. Summary of XPS data for HEA NPs-Ge wafer

	Ge 3d	Au 4f	Ag 3d	Cu 2p	Pd 3d	Pt 4f
Emission (eV)	31.3	83.7	368.0	932.4	335.5	70.8
Reference emission (eV)[a]	29.8	84.0	368.2	933.0	335.0	71.0
Atomic percentage (%)	9.27	6.53	4.97	5.39	5.79	5.64

[a] Reference metal emission is from NIST X-ray Photoelectron Spectroscopy Database.[26]

In comparison, the chemical composition of the material was investigated by XPS (Figure 3.32), which revealed a surface atomic ratio (Table 3.4) of Au (6.53 atom %), Ag (4.97 atom %), Cu (5.39 atom %), Pd (5.79 atom %), Pt (5.64 atom %), and Ge (9.27 atom%). The weaker Ge emission observed in contrast to previous GeNS and GeNP experiments was attributed to the larger size of the deposited HEA NPs, which limited XPS probing to depth. The high-resolution XP spectrum of the Ge 3d region (Figure 3.33) showed the presence of Ge^{1+} (binding energy at 30.3 eV) and Ge^{4+} (binding energy at 32.5 eV) species,[35] indicating that after the removal of the native oxide, the surface Ge undergoes hydrolysis in the water forming Ge-H and Ge-OH on the surface. The generated Ge-H simultaneously reduced the metal ions, resulting in the deposition of the HEA NPs, which is consistent with the SEM images where no obvious local etching was observed. Overall, our study provides new insights into the synthesis and characterization of HEA NPs on the Ge surface and highlights the potential applications of our synthetic method in the bulk Ge system.

3.4 Summary and Outlook

In this chapter we present a simple method for the deposition of adherent high-entropy alloy nanoparticles (AuAgCuPdPt) onto the surfaces of germanium nanosheets (GeNSs). Our investigation confirms the preservation of the structural integrity of the GeNS during the deposition process and the formation of high-entropy nanoparticles, as verified by X-ray diffraction (XRD) and X-ray photoelectron spectroscopy (XPS). Transmission electron microscopy (TEM) analysis reveals the distribution of the high-entropy alloy nanoparticles over the entire surface of the GeNS. The subsequent liberation of the nanoparticles from the GeNS through UV irradiation demonstrated their solid-solution structure and homogenous element

distribution. We also demonstrate that HEA NPs can be prepared on the surface of agglomerated GeNPs via a straightforward synthetic route. We concluded by extending our investigation to bulk Ge, where deposition of HEA NPs on the surface of a wafer was demonstrated.

3.5 References

1. Yao, Y.; Dong, Q.; Brozena, A.; Luo, J.; Miao, J.; Chi, M.; Wang, C.; Kevrekidis, I. G.; Ren, Z. J.; Greeley, J.; Wang, G.; Anapolsky, A.; Hu, L., High-entropy Nanoparticles: Synthesis-structure-property Relationships and Data-driven Discovery. *Science* **2022,** *376* (6589), eabn3103.
2. Glasscott, M. W.; Pendergast, A. D.; Goines, S.; Bishop, A. R.; Hoang, A. T.; Renault, C.; Dick, J. E., Electrosynthesis of High-entropy Metallic Glass Nanoparticles for Designer, Multi-functional Electrocatalysis. *Nat. Commun.* **2019,** *10* (1), 2650.
3. Yao, Y.; Huang, Z.; Xie, P.; Lacey, S. D.; Jacob, R. J.; Xie, H.; Chen, F.; Nie, A.; Pu, T.; Rehwoldt, M.; Yu, D.; Zachariah, M. R.; Wang, C.; Shahbazian-Yassar, R.; Li, J.; Hu, L., Carbothermal Shock Synthesis of High-entropy-alloy Nanoparticles. *Science* **2018,** *359* (6383), 1489-1494.
4. Chen, P.-C.; Liu, X.; Hedrick, J. L.; Xie, Z.; Wang, S.; Lin, Q.-Y.; Hersam, M. C.; Dravid, V. P.; Mirkin, C. A., Polyelemental Nanoparticle Libraries. *Science* **2016,** *352* (6293), 1565-1569.
5. Kumar, N.; Tiwary, C. S.; Biswas, K., Preparation of Nanocrystalline High-entropy Alloys via Cryomilling of Cast Ingots. *J. Mater. Sci.* **2018,** *53* (19), 13411-13423.
6. Gao, S.; Hao, S.; Huang, Z.; Yuan, Y.; Han, S.; Lei, L.; Zhang, X.; Shahbazian-Yassar, R.; Lu, J., Synthesis of High-entropy Alloy Nanoparticles on Supports by the Fast Moving Bed Pyrolysis. *Nat. Commun.* **2020,** *11* (1), 2016.
7. Mori, K.; Hashimoto, N.; Kamiuchi, N.; Yoshida, H.; Kobayashi, H.; Yamashita, H., Hydrogen Spillover-driven Synthesis of High-entropy Alloy Nanoparticles as a Robust Catalyst for CO_2 Hydrogenation. *Nat. Commun.* **2021,** *12* (1), 3884.
8. Qiao, H.; Saray, M. T.; Wang, X.; Xu, S.; Chen, G.; Huang, Z.; Chen, C.; Zhong, G.; Dong, Q.; Hong, M.; Xie, H.; Shahbazian-Yassar, R.; Hu, L., Scalable Synthesis of High Entropy Alloy Nanoparticles by Microwave Heating. *ACS Nano* **2021,** *15* (9), 14928-14937.
9. Wu, D.; Kusada, K.; Yamamoto, T.; Toriyama, T.; Matsumura, S.; Kawaguchi, S.; Kubota, Y.; Kitagawa, H., Platinum-Group-Metal High-Entropy-Alloy Nanoparticles. *J. Am. Chem. Soc.* **2020,** *142* (32), 13833-13838.
10. Zhu, G.; Jiang, Y.; Yang, H.; Wang, H.; Fang, Y.; Wang, L.; Xie, M.; Qiu, P.; Luo, W., Constructing Structurally Ordered High-Entropy Alloy Nanoparticles on Nitrogen-Rich Mesoporous Carbon Nanosheets for High-Performance Oxygen Reduction. *Adv. Mater.* **2022,** *34* (15), e2110128.
11. Huang, Z.; Yao, Y.; Pang, Z.; Yuan, Y.; Li, T.; He, K.; Hu, X.; Cheng, J.; Yao, W.; Liu, Y.; Nie, A.; Sharifi-Asl, S.; Cheng, M.; Song, B.; Amine, K.; Lu, J.; Li, T.; Hu, L.; Shahbazian-Yassar, R., Direct Observation of the Formation and Stabilization of Metallic Nanoparticles on Carbon Supports. *Nat. Commun.* **2020,** *11* (1), 6373.
12. Rekha, M. Y.; Mallik, N.; Srivastava, C., First Report on High Entropy Alloy Nanoparticle Decorated Graphene. *Sci. Rep.* **2018,** *8* (1), 8737.
13. Urs, K. M. B.; Katiyar, N. K.; Kumar, R.; Biswas, K.; Singh, A. K.; Tiwary, C. S.; Kamble, V., Multi-component (Ag-Au-Cu-Pd-Pt) Alloy Nanoparticle-decorated p-type 2D-molybdenum Disulfide (MoS_2) for Enhanced Hydrogen Sensing. *Nanoscale* **2020,** *12* (22), 11830-11841.

14. Huey, W. L. B.; Goldberger, J. E., Covalent functionalization of two-dimensional group 14 graphane analogues. *Chem. Soc. Rev.* **2018,** *47* (16), 6201-6223.

15. Jiang, S.; Krymowski, K.; Asel, T.; Arguilla, M. Q.; Cultrara, N. D.; Yanchenko, E.; Yang, X.; Brillson, L. J.; Windl, W.; Goldberger, J. E., Tailoring the Electronic Structure of Covalently Functionalized Germanane via the Interplay of Ligand Strain and Electronegativity. *Chem. Mater.* **2016,** *28* (21), 8071-8077.

16. Serino, A. C.; Ko, J. S.; Yeung, M. T.; Schwartz, J. J.; Kang, C. B.; Tolbert, S. H.; Kaner, R. B.; Dunn, B. S.; Weiss, P. S., Lithium-Ion Insertion Properties of Solution-Exfoliated Germanane. *ACS Nano* **2017,** *11* (8), 7995-8001.

17. Madhushankar, B. N.; Kaverzin, A.; Giousis, T.; Potsi, G.; Gournis, D.; Rudolf, P.; Blake, G. R.; van der Wal, C. H.; van Wees, B. J., Electronic Properties of Germanane Field-effect Transistors. *2D Mater.* **2017,** *4* (2), 021009.

18. Zhao, F.; Feng, Y.; Wang, Y.; Zhang, X.; Liang, X.; Li, Z.; Zhang, F.; Wang, T.; Gong, J.; Feng, W., Two-dimensional Gersiloxenes with Tunable Bandgap for Photocatalytic H_2 Evolution and CO_2 Photoreduction to CO. *Nat. Commun.* **2020,** *11* (1), 1443.

19. Chen, L. H.; Shen, H. T.; Chang, W. H.; Khalil, I.; Liao, S. Y.; W, A. Y.; Liu, S. C.; Chu, C. C.; Hsiao, V. K. S., Photocatalytic Properties of Graphene/Gold and Graphene Oxide/Gold Nanocomposites Synthesized by Pulsed Laser Induced Photolysis. *Nanomaterials (Basel)* **2020,** *10* (10), 1985.

20. Ng, S.; Pumera, M., 2D Functionalized Germananes: Synthesis and Applications. *Adv Mater* **2023,** *35* (7), e2207196.

21. Ni, C.; Chevalier, M.; Veinot, J. G. C., Metal Nanoparticle-decorated Germanane for Selective Photocatalytic Aerobic Oxidation of Benzyl Alcohol. *Nanoscale Adv.* **2022,** *5* (1), 228-236.

22. Nellaiappan, S.; Katiyar, N. K.; Kumar, R.; Parui, A.; Malviya, K. D.; Pradeep, K. G.; Singh, A. K.; Sharma, S.; Tiwary, C. S.; Biswas, K., High-Entropy Alloys as Catalysts for the CO_2 and CO Reduction Reactions: Experimental Realization. *ACS Catal.* **2020,** *10* (6), 3658-3663.

23. Javadi, M.; Picard, D.; Sinelnikov, R.; Narreto, M. A.; Hegmann, F. A.; Veinot, J. G. C., Synthesis and Surface Functionalization of Hydride-Terminated Ge Nanocrystals Obtained from the Thermal Treatment of $Ge(OH)_2$. *Langmuir* **2017,** *33* (35), 8757-8765.

24. Hossain, M. A.; Javadi, M.; Yu, H.; Thiessen, A. N.; Ikpo, N.; Oliynyk, A. O.; Veinot, J. G. C., Dehydrocoupling - an Alternative Approach to Functionalizing Germanium Nanoparticle Surfaces. *Nanoscale* **2020,** *12* (11), 6271-6278.

25. Anderson, S. L.; Luber, E. J.; Olsen, B. C.; Buriak, J. M., Substance over Subjectivity: Moving beyond the Histogram. *Chem. Mater.* **2016,** *28* (17), 5973-5975.

26. NIST X-ray Photoelectron Spectroscopy Database, NIST Standard Reference Database Number 20, National Institute of Standards and Technology, Gaithersburg MD, 20899 (2000).

27. Helbich, T.; Lyuleeva, A.; Ludwig, T.; Scherf, L. M.; Fässler, T. F.; Lugli, P.; Rieger, B., One-Step Synthesis of Photoluminescent Covalent Polymeric Nanocomposites from 2D Silicon Nanosheets. *Adv. Funct. Mater.* **2016,** *26* (37), 6711-6718.

28. Katiyar, N. K.; Dhakar, S.; Parui, A.; Gakhad, P.; Singh, A. K.; Biswas, K.; Tiwary, C. S.; Sharma, S., Electrooxidation of Hydrazine Utilizing High-Entropy Alloys: Assisting the Oxygen Evolution Reaction at the Thermodynamic Voltage. *ACS Catal.* **2021,** *11* (22),

14000-14007.

29. Holder, C. F.; Schaak, R. E., Tutorial on Powder X-ray Diffraction for Characterizing Nanoscale Materials. *ACS Nano* **2019,** *13* (7), 7359-7365.

30. Yu, H.; Helbich, T.; Scherf, L. M.; Chen, J.; Cui, K.; Fässler, T. F.; Rieger, B.; Veinot, J. G. C., Radical-Initiated and Thermally Induced Hydrogermylation of Alkenes on the Surfaces of Germanium Nanosheets. *Chem. Mater.* **2018,** *30* (7), 2274-2280.

31. Bianco, E.; Butler, S.; Jiang, S.; Restrepo, O. D.; Windl, W.; Goldberger, J. E., Stability and Exfoliation of Germanane: A Germanium Graphane Analogue. *ACS Nano* **2013,** *7* (5), 4414-4421.

32. Khomenkova, L.; Lehninger, D.; Kondratenko, O.; Ponomaryov, S.; Gudymenko, O.; Tsybrii, Z.; Yukhymchuk, V.; Kladko, V.; von Borany, J.; Heitmann, J., Effect of Ge Content on the Formation of Ge Nanoclusters in Magnetron-Sputtered $GeZrO_x$-Based Structures. *Nanoscale Res. Lett.* **2017,** *12* (1), 196.

33. Qian, C.; Sun, W.; Hung, D. L. H.; Qiu, C.; Makaremi, M.; Hari Kumar, S. G.; Wan, L.; Ghoussoub, M.; Wood, T. E.; Xia, M.; Tountas, A. A.; Li, Y. F.; Wang, L.; Dong, Y.; Gourevich, I.; Singh, C. V.; Ozin, G. A., Catalytic CO_2 Reduction by Palladium-decorated Silicon–hydride Nanosheets. *Nat. Catal.* **2018,** *2* (1), 46-54.

34. Bueno, S. L. A.; Leonardi, A.; Kar, N.; Chatterjee, K.; Zhan, X.; Chen, C.; Wang, Z.; Engel, M.; Fung, V.; Skrabalak, S. E., Quinary, Senary, and Septenary High Entropy Alloy Nanoparticle Catalysts from Core@Shell Nanoparticles and the Significance of Intraparticle Heterogeneity. *ACS Nano* **2022,** *16* (11), 18873-18885.

35. Zheng, Y.; Lapano, J.; Bruce Rayner, G.; Engel-Herbert, R., Native Oxide Removal from Ge Surfaces by Hydrogen Plasma. *J. Vac. Sci. Technol. A* **2018,** *36* (3), 031306.

4. Chapter 4: Synthesis of High-Entropy Germanides and Investigation of the Formation Process[c]

High-entropy alloy nanoparticles (HEA NPs) have emerged as a captivating and challenging class of materials.[1] The attention placed on these materials can be attributed to their multi-element compositions and high-entropy solid-solution structures, which impart tunable reactivity and enhanced stability and make HEA NPs suitable candidates in catalyst development.[2] The advancement in synthesis of HEA NPs, which exhibit a wide compositional range encompassing numerous immiscible metal combinations and incorporating up to eight constituent elements, was achieved using the "carbo-thermal shock" method.[3] Subsequently, several other procedures have been developed to prepare HEA NPs, including vapor phase spark discharge, rapid radiative heating or annealing, low-temperature hydrogen spillover, microwave heating, and colloidal methods.[4-13] In the wake of these advancements, diverse high-entropy compounds, such as oxides,[14] fluorides,[15] sulfides,[16] carbides,[17] nitrides,[18] silicide,[19] borides,[20] stannides,[21] and halide perovskites[22] have been demonstrated. It is noteworthy that germanides have remained unexplored as high-entropy nanomaterials.

Germanides are a class of materials that have garnered attention because of their potential thermoelectric and electronic applications.[23,24] These compounds are formed by combining

---

germanium with metallic elements such as iron, nickel, cobalt, and palladium.[25-28] Germanides are characterized by high electrical conductivity, low thermal conductivity, and favorable thermoelectric characteristics.[24, 29, 30] As such, germanides have emerged as promising active materials for thermoelectric generators, coolers, and electronic devices (e.g., transistors, diodes, integrated circuit interconnects).[27, 28, 30-32] The principles of high-entropy alloying can enhance thermoelectric performance and substantial progress has been achieved in the field of high-performance high-entropy alloy thermoelectrics.[23, 33, 34] Still, examples of high-entropy alloying involving germanides remain underexplored.[32]

In Chapter 3, we presented a solution-based method for preparing high-entropy alloy nanoparticle-decorated germanane (HEA NPs@GeNSs).[35] Using this method, we prepared HEA NPs (comprising Au, Ag, Cu, Pd, and Pt) on the surface of germanane. Recognizing that the Ge-H terminated surface germanane serves as a reducing agent and the underlying Ge atoms could potentially provide a Ge source that could facilitate the formation of high-entropy germanides (HEGs), we have now explored transforming HEA NPs@GeNSs into a HEG (AuAgCuPdPtGe) via rapid thermal annealing. These findings motivated us to target HEA NPs@GeNSs of different metal compositions and the formation of corresponding HEGs. Given that first-row transition metals (Sc, Ti, V, Cr, Mn, Fe, Co, Ni) can be incorporated into single-phase HEA NPs and are readily prepared as high-entropy oxides,[36] we chose to investigate several of these elements (i.e., V, Cr, Fe, Co, Ni) as potential components for high-entropy germanide formation.

Moreover, we have delved into the formation processes that yield HEGs using *in situ* heating X-ray diffraction and transmission electron microscopy. Our experimental observations revealed that at elevated temperatures (300 °C), germanane decomposes providing into germanium

nanoparticles that the high-entropy components subsequently diffuse into. At comparatively low temperatures, this process is slow with diffusion proceeding more rapidly when temperature exceeds 600 °C.

4.1 Materials and Methods

4.1.1 Material

Germanium (Ge, 99.999%), calcium (Ca, 99.0%), gold (III) chloride (AuCl$_3$, 99.99%), silver nitrate (AgNO$_3$, 99.9999%), copper (II) chloride (CuCl$_2$, 99.999%), palladium (II) chloride (PdCl$_2$, 99.9%) and platinum (IV) chloride (PtCl$_4$, 99.999%) were purchased from Sigma-Aldrich and hydrochloric acid (HCl, 37% w/w), ethanol (anhydrous), isopropyl alcohol (anhydrous), acetone (HPLC grade) and toluene (HPLC grade) were purchased from Fisher Scientific. Milli-Q (18.2 MΩ·cm at 25 °C) water was used for all experiments. All organic solvents were dried using an Innovative Technology, Inc. Grubbs-type solvent purification system.

4.1.2 Synthesis of High-Entropy Alloy Nanoparticles-decorated Germanium Nanosheets (HEA NPs@GeNSs)

To prepare high entropy alloy nanoparticles-decorated germanium nanosheets (HEA NPs@GeNSs; HEA = Au, Ag, Cu, Pt, Pd), germanane powder (73 mg; 1 mmol) was dispersed in 4 mL Milli-Q water. The mixture was sonicated in a bath sonicator for 2 hours to yield a red suspension of exfoliated GeNSs. Subsequently, an appropriate mass (0.01 mmol) of the anhydrous metal salt in question (AuCl$_3$, AgNO$_3$, CuCl$_2$, PdCl$_2$ and PtCl$_4$) was dissolved in 1 mL of Milli-Q water together. The metal salt solution (i.e., 0.1 ml) was then added into the GeNS dispersion at room temperature in subdued light and the original red suspensions turned black. The mixture was stirred for 10 min and the product was recovered by centrifugation and washed with Milli-Q water

three times. The product was dried for 12 h in vacuo and subsequently stored in nitrogen filled glovebox and subdued light. Typical mass yields for this procedure were 55 mg. The resulting material was characterized using XRD, XPS, and TEM.

4.1.3 Synthesis of AuAgCuPdPtGe High-Entropy Germanide

The above prepared HEA@GeNSs (0.5 g) was heated up to 800 °C at 1 °C/s under Ar flow in a tube furnace. After reaching the peak temperature, the sample was maintained at that temperature for 10 min and quenched to room temperature by removing the tube from the furnace and blowing the tube with constant N_2 gas. Upon cooling to room temperature, the resulting black solid was subsequently stored in nitrogen filled glovebox. Typical mass yields for this procedure were 100 mg. The resulting material was characterized using XRD, XPS, and TEM.

4.1.4 Synthesis of FeCoNiCrVGe High-Entropy Germanide

To prepare FeCoNiCrVGe high-entropy germanide, germanane powder (73 mg; 1 mmol) was dispersed in 4 mL anhydrous ethanol. The mixture was sonicated in a bath sonicator for 2 hours to yield a red suspension of exfoliated GeNSs. Subsequently, an appropriate mass (0.1 mmol) of the anhydrous metal salt in question ($FeCl_3$, $CoCl_2$, $NiCl_2$, $CrCl_2$ and VCl_3) was dissolved in 1 mL of anhydrous ethanol together. The metal salt solution (i.e., 0.1 ml) was then added into the GeNS dispersion while stirring at room temperature. The solvent was evaporated at 50 °C for 10 min using a Heidolph G5 rotary evaporator. The resulting slurry was heated to 800 °C at 1 °C/s under Ar flow in a tube furnace (Lindberg). After reaching the peak temperature, the sample was maintained at that temperature for 10 min and air quenched to room temperature by removing the tube from the furnace and blowing the tube with constant N_2 gas. Upon cooling to room

temperature, the resulting black solid was subsequently stored in nitrogen filled glovebox. The resulting material was characterized using XRD, XPS, and TEM.

4.2 Material Characterization

4.2.1 Fourier Transformed Infrared (FTIR) Spectroscopy

FTIR analyses were performed using a Thermo Nicolet 8700 FTIR Spectrometer and Continuum FTIR Microscope. Samples were prepared by drop coating a toluene dispersion of the solid sample in question onto an electronics-grade Si-wafer (N-type, 100 surface, 100 μm thickness and 10 ohm·cm resistivity) and dried under flowing nitrogen.

4.2.2 Electron Microscopy

Transmission electron microscopy (TEM) bright and dark field images were acquired using a JEOL JEM-ARM200CF S/TEM electron microscope at an accelerating voltage of 200 kV. High resolution (HR) TEM images were processed using Gatan Digital Micrograph software (Version 3.4.1). TEM samples were prepared by depositing a drop of a dilute toluene suspension of the sample in question onto a holey or ultra-thin carbon coated copper grid or molybdenum grid (obtained from Electron Microscopy Inc.). The grid bearing the sample was kept in a vacuum chamber at a base pressure of 0.2 bar for at least 24 h prior to data collection. The particles size distribution was assembled as an average shifted histogram as described by Buriak et al. for at least 300 particles in TEM. The average shifted histogram averaged the different histogram shapes formed by shifting the bin origin.[37]

In situ heating TEM experiments were conducted using the DENSsolutions Wildfire in situ heating TEM sample holder. TEM samples were prepared by depositing a drop (5 μL) of a dilute

ethanol suspension of metal salts and GeNSs onto a DENSsolutions Wildfire Si_3N_4 nano-chip. The heating program was monitored by DENSsolutions Impulse software. After collecting the images and EDX mapping at room temperature, the samples were heated up to 800 °C at 1 °C/s and kept at 800 °C for 10 min. Then the samples were cooled down to room temperature at 20 °C/s.

4.2.3 X-ray Photoelectron Spectroscopy (XPS)

XPS analyses were performed using a Kratos Axis Ultra instrument operating in energy spectrum mode at 210 W. The base and operating chamber pressure were maintained at 10^{-7} Pa. A monochromatic Al Kα source ($\lambda = 8.34$ Å) was used to irradiate the samples, and the spectra were obtained with an electron take-off angle of 90°. CasaXPS software (VAMAS) was used to interpret high-resolution spectra. All spectra were internally calibrated to the C 1s emission (284.8 eV) of adventitious carbon. After calibration, a Shirley-type background was applied to remove most of the extrinsic loss structure. The Ge 3d region were deconvoluted into the Ge $3d_{5/2}$ and $3d_{3/2}$ spin-orbit couple for the element Ge and the energy separation of these doublets was fixed at 0.58 eV and the Ge $3d_{3/2}$ to $3d_{5/2}$ area was fixed at 0.67.[31] For the high-resolution XP spectra of metals, the spin-orbit couple energy separation and area were fixed and the spectral envelope was fit using a Lorentzian asymmetric line shape LA(a, b, n) where a and b define the asymmetry and n defines the Gaussian width. The various spectral regions were fit as follows: Au 4f was deconvoluted into the Au $4f_{7/2}$ and $4f_{5/2}$ spin-orbit couple and the energy separation of these doublets was fixed at 3.70 eV and the Au $4f_{5/2}$ to $4f_{7/2}$ area ratio was fixed at 0.75.[38] Ag 3d was deconvoluted into the Ag $3d_{5/2}$ and $3d_{3/2}$ spin-orbit couple and the energy separation of these doublets was fixed at 6.00 eV and the Ag $3d_{3/2}$ to $3d_{5/2}$ area ration was fixed at 0.67.[38] Cu 2p was deconvoluted into the Cu $2p_{3/2}$ and $2p_{1/2}$ spin-orbit couple and the energy separation of these doublets was fixed at 19.75 eV and the Cu $2p_{1/2}$ and $2p_{3/2}$ area ratio was fixed at 0.50.[38] Pd 3d was deconvoluted into the Pd $3d_{5/2}$

and $3d_{3/2}$ spin-orbit couple and the energy separation of these doublets was fixed at 5.26 eV and the Pd $3d_{3/2}$ to $3d_{5/2}$ area ratio was fixed at 0.67.[38] Pt 4f was deconvoluted into the Pt $4f_{7/2}$ and $4f_{5/2}$ spin-orbit couple and the energy separation of these doublets was fixed at 3.35 eV and the Pt $4f_{5/2}$ to $4f_{7/2}$ area ratio was fixed at 0.75.[38] Fe 2p was deconvoluted into the Fe $2p_{3/2}$ and $2p_{1/2}$ spin-orbit couple and the energy separation of these doublets was fixed at 13.1 eV and the Fe $2p_{1/2}$ and $2p_{3/2}$ area ratio was fixed at 0.50. Co 2p was deconvoluted into the Co $2p_{3/2}$ and $2p_{1/2}$ spin-orbit couple and the energy separation of these doublets was fixed at 14.99 eV and the Co $2p_{1/2}$ and $2p_{3/2}$ area ratio was fixed at 0.50. Ni 2p was deconvoluted into the Ni $2p_{3/2}$ and $2p_{1/2}$ spin-orbit couple and the energy separation of these doublets was fixed at 17.3 eV and the Ni $2p_{1/2}$ and $2p_{3/2}$ area ratio was fixed at 0.50. Cr 2p was deconvoluted into the Cr $2p_{3/2}$ and $2p_{1/2}$ spin-orbit couple and the energy separation of these doublets was fixed at 9.3 eV and the Cr $2p_{1/2}$ and $2p_{3/2}$ area ratio was fixed at 0.50. V 2p was deconvoluted into the V $2p_{3/2}$ and $2p_{1/2}$ spin-orbit couple and the energy separation of these doublets was fixed at 7.6 eV and the V $2p_{1/2}$ and $2p_{3/2}$ area ratio was fixed at 0.50.[38]

4.2.4 Powder X-ray Diffraction (XRD)

XRD was performed using a Bruker D8 Advance diffractometer (Cu-$K_{\alpha1}$ (λ = 1.5406 Å) and $K_{\alpha2}$ (λ = 1.5444 Å) radiation). Samples were prepared by mounting the powder in question on a zero background Si crystal sample holder. XRD patterns were scanned between 2θ ranges of 10 - 80° with a scan step of 0.06 °/s. The instrumental broadening effect was considered by measuring a NIST LaB_6 standard sample with a same scanning speed. Jade 6 was used to fit the peak broadening with both size and strain effect. The lattice parameter for the AuAgCuPdPtGe HEG and FeCoNiCrVGe HEG was calculated using the lattice parameter of the AuAgCuPdPt and FeCoNiCrV HEA and the lattice parameter of Ge based on Vegard's Law.

$$a_{HEA_{(1-x)}Ge_x} = (1-x)a_{HEA_{(1-x)}} + xa_{Ge_x}$$

In situ XRD experiments were performed using a Bruker D8 Discover diffractometer (Cu-Kα1 (λ = 1.5406 Å) and Kα2 (λ = 1.5444 Å) radiation) with an Anton Paar DHS 1100 heating stage. Samples were prepared by mounting the powder in question on a zero background Si crystal sample holder. The samples were heated up to 800 °C at 1 °C/s under N_2 flow inside the dome of the heating stage and kept at each desired temperature (200 °C, 300 °C, 400 °C, 500 °C, 600 °C, 700 °C, 750 °C and 800 °C) for XRD measurement. XRD patterns were scanned between 2θ ranges of 10 - 80° with a scan step of 0.06 °/s and subtracted the background from the dome measured at room temperature. After finishing the heating program, the samples were cooled down to room temperature by circulating the dome with N_2 flow.

4.3 Results and Discussion

Germanane used in the present study was prepared by deintercalation of $CaGe_2$ (Figure 3.1).[39] Following the deintercalation process, the resulting product was placed in distilled water and the mixture was subjected to a bath sonicator for 2 hours to achieve optimal exfoliation. Subsequently, the exfoliated germanane was combined with an aqueous solution containing the desired metal salts (i.e., $AuCl_3$, $AgNO_3$, $CuCl_2$, $PdCl_2$, $PtCl_4$). The Ge-H on the surfaces of the germanane immediately reacted with the aqueous metal ions[35] leading to the formation of size-polydisperse HEA NPs (AuAgCuPdPt) on the surfaces of the germanane (Figure 3.1). The resulting HEA NPs@GeNS powder was collected and heated to 800 °C at 1 °C/s in flowing Ar. After annealing at the peak temperature for 10 min, the product was rapidly cooled to room temperature by removing the tube from the furnace and flushing the reaction tube with a constant flow of N_2 gas. This process led to the formation of the desired AuAgCuPdPtGe HEG (Figure 4.1).
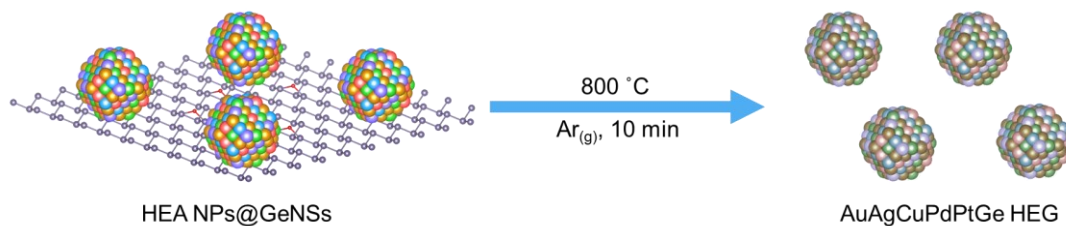
Figure 4.1. A pictorial representation of the formation of high-entropy germanide (HEG: AuAgCuPdPtGe) from high-entropy alloy nanoparticles decorated germanane (HEA NPs@GeNSs). HEA NPs@GeNSs were rapid annealed at 800 °C under Ar flow for 10 minutes. The products were collected after rapidly cooling to room temperature. (Note: For clarity, hydrogen atoms on the germanane surfaces are not shown.)

Powder X-ray diffraction (XRD) was used to examine the crystal structure of AuAgCuPdPtGe HEG. The XRD pattern of HEA NPs@GeNSs (Figure 4.2) showed characteristic reflections of HEA NPs and GeNSs.[35] After annealing, the pattern of HEG (AuAgCuPdPtGe) exhibited characteristic FCC reflections. Notably, these reflections exhibited a slight shift to higher angles (27.33°, 45.35°, 53.78°, 66.07°, 72.89°) in comparison to Ge reflections (27.28°, 45.30°, 53.69°, 65.99°, 72.81°) consistent with the incorporation of multiple elements (i.e., Au, Ag, Cu, Pd, Pt) into the Ge crystal structure resulting in a strained lattice.[15] We determined the lattice parameter for the AuAgCuPdPtGe HEG using Vegard's Law (Figure 4.3). A deviation from the linear variation of the lattice parameters was observed for the AuAgCuPdPtGe HEG suggesting strain is present that arises from the incorporation of the small atoms (i.e., Au, Ag, Cu, Pd, Pt).[40] We also noted a typical GeO_2 pattern in the XRD analysis, which we confidently attribute to arising from the crystallization of residual oxidized surface germanium species.[41] The broadening of the HEG reflections was evaluated using the Scherrer equation and provided an estimated approximate crystallite size of 62.8 ± 1.9 nm.[42] Consistent with our lattice parameter data, consideration of the diffraction angle dependence of peak broadening on diffraction angle (Figure 4.4) also reveals that strain-induced broadening is manifesting in the AuAgCuPdPtGe HEG system.[35]
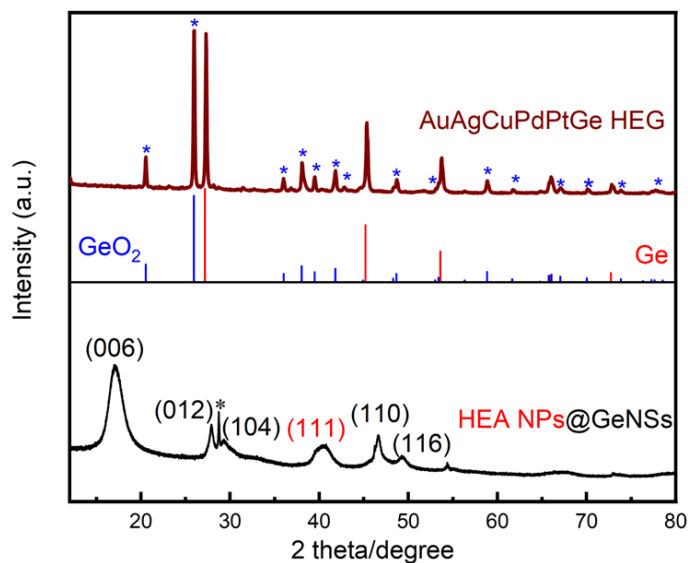
Figure 4.2. A comparison of XRD patterns of HEA NPs@GeNSs and AuAgCuPdPtGe HEG. (*) correspond to GeO_2 reflections. Ge and GeO_2 reflections are from PDF#89-9345 and 83-2477. The asterisk corresponds to reflections arising from the Ge impurity that from the synthesis of GeNSs.
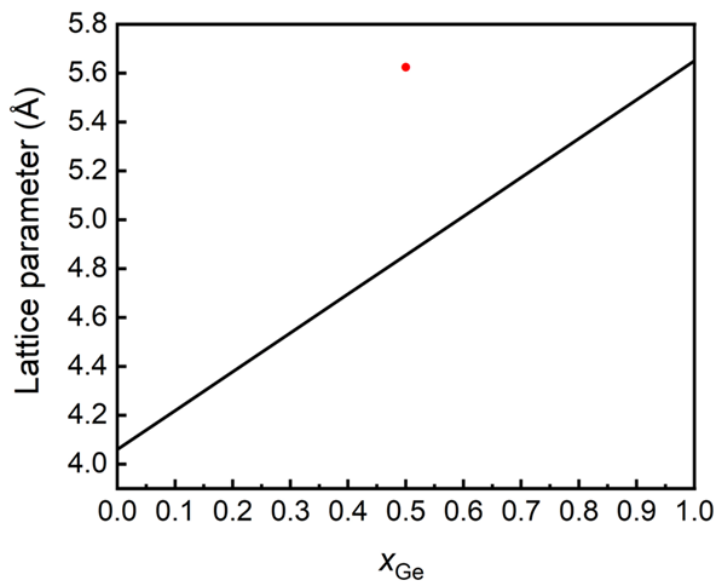
Figure 4.3 A plot of the lattice parameter as a function of the mole fraction of Ge in AuAgCuPdPtGe HEG by using Vegard's law. The red dot represents the experiment lattice parameter calculated from the XRD reflections using Bragg's law.
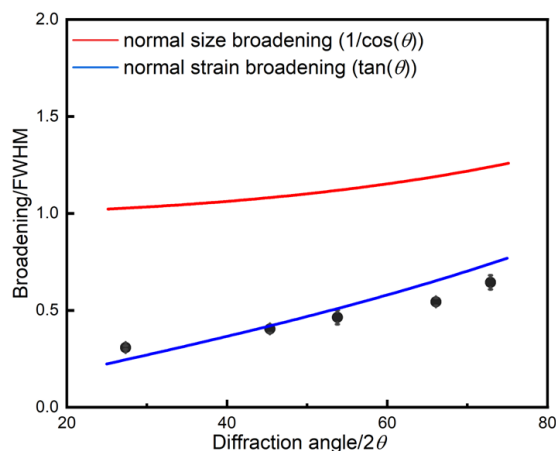
Figure 4.4. XRD peak broadening distribution for AuAgCuPdPtGe HEG.

To further investigate the nature of the AuAgCuPdPtGe HEG, we interrogated the product using Fourier-transform infrared (FTIR) and X-ray photoelectron spectroscopy (XPS). The FTIR spectrum (Figure 4.5) of the parent HEA NPs@GeNSs exhibited prominent features attributed to Ge-H stretching modes at 2000 cm^{-1} and Ge-O stretching modes in the range of 700 to 890 cm^{-1}.[35] Following annealing, the FTIR spectrum of the resulting AuAgCuPdPtGe HEG displayed no discernible feature at 2000 cm^{-1}. The absence of the Ge-H stretching mode is consistent with thermal cleavage of Ge-H bonds.[43]
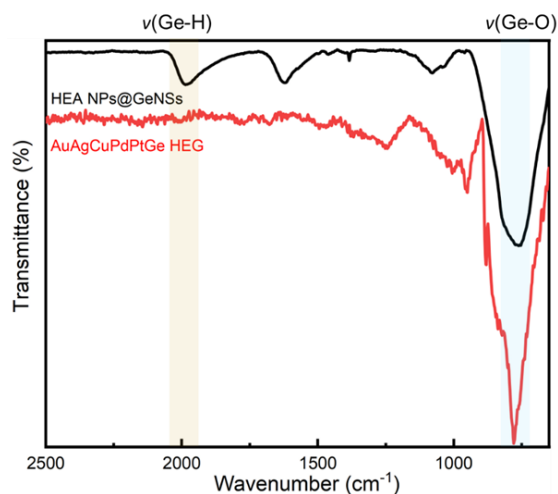
Figure 4.5. Representative FTIR spectra of HEA NPs@GeNSs before (black) and after (red) AuAgCuPdPtGe HEG formation.

131

XPS provides additional insight into the material composition, bonding environment, and oxidation states of elements in the present materials. The survey XP spectrum of the AuAgCuPdPtGe HEG corroborated the findings from FTIR and XRD analyses, revealing evidence of oxidation and corresponding metal emissions (Figure 4.6). Integration of the emission peaks in the survey XP spectra provided quantification of the compositions of the AuAgCuPdPtGe HEG. The surface atomic percentages for each metal were approximately 14 atomic %, while that of Ge was around 27.1 atomic %. These results provide an approximate composition of $Au_{0.54}Ag_{0.53}Cu_{0.55}Pd_{0.55}Pt_{0.53}Ge$ (Table 4.1), in which higher Ge amount results from residual GeO_2 noted in the XRD and FTIR analyses.
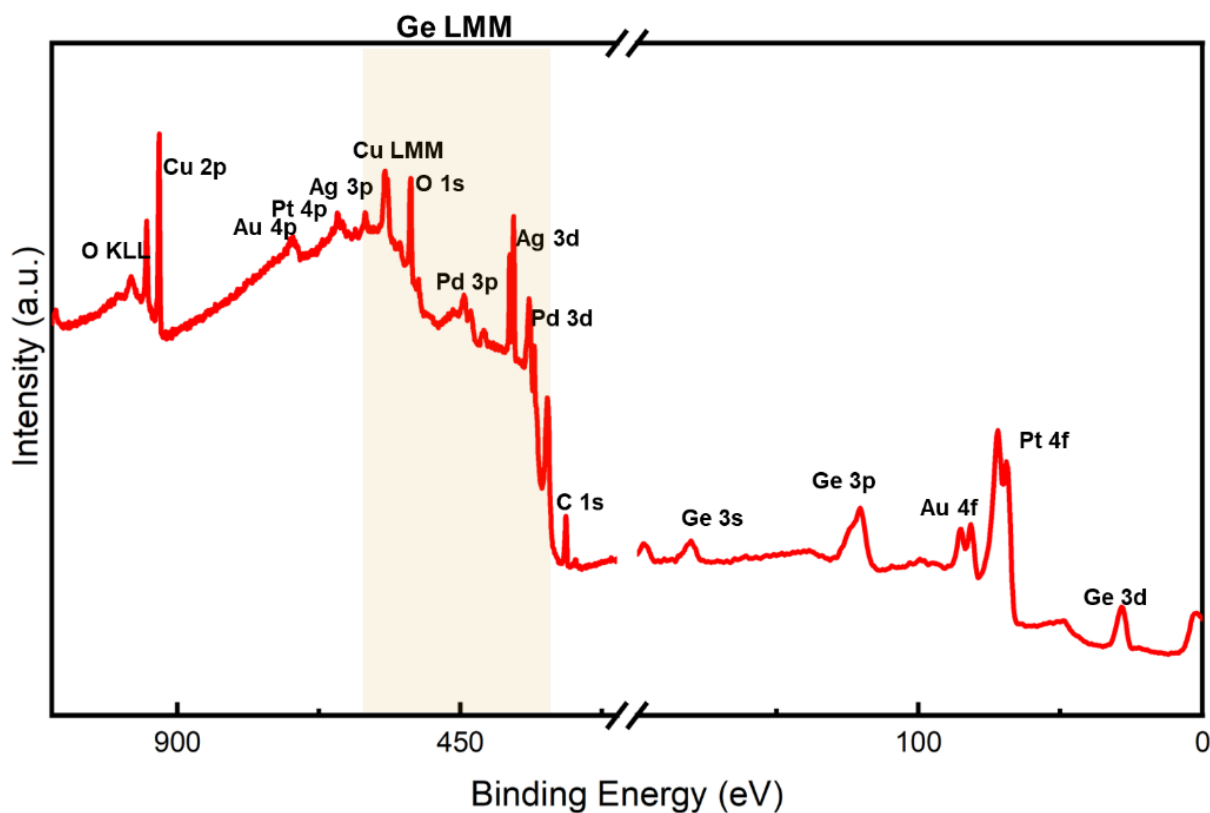
Figure 4.6. Representative survey XP spectrum of AuAgCuPdPtGe HEG.

Table 4.1. Summary of XPS data for AuAgCuPdPtGe HEG.

	Ge 3d	Au 4f	Ag 3d	Cu 2p	Pd 3d	Pt 4f
Emission (eV)	29.5	84.0	368.0	932.1	335.0	71.0
Reference emission (eV)[a]	29.8	84.0	368.2	933.0	335.0	71.0
Atomic percentage (%)	24.2	14.8	15.2	15.3	15.1	15.4
Eletronegativity[b]	2.01	2.54	1.93	1.90	2.20	2.28

[a] Reference metal emissions are from NIST X-ray Photoelectron Spectroscopy Database.
[b] Eletronegativities are from CRC Handbook for Chemistry and Physics, 95th ed., 2014, CRC Press.

High-resolution XP spectra of the AuAgCuPdPtGe HEG revealed emissions associated with the corresponding metals (Au, Ag, Cu, Pd, and Pt) and Ge (Figure 4.7). The Ge 3d spectra showed a shift to a lower binding energy of 29.5 eV, when compared to Ge in the GeNSs (29.8 eV).[44] This shift is in agreement with the Ge atoms in the HEG being bonded to atoms that are less electronegative than hydrogen. Among the constituent metals in the present AuAgCuPdPtGe HEG, only Ge, Cu, and Ag fit this criterion (Table 4.1). We also note that the measured binding energy of Ge in AuAgCuPdPtGe HEG is comparable to that of crystalline germanium (c-Ge; 29.5 eV),[39] suggesting a random mixing effect has averaged the influence of the electronegativity of atoms neighboring germanium. Additionally, we note fit components in the Ge 3d emission appearing at 31.3 and 32.5 eV that have previously been attributed to Ge^{2+} and Ge^{4+} species, arise from the presence of GeO_2 (Figures 4.7a) that are consistent with our XRD and FTIR analyses.[39] Turning our attention to the metal constituents, the XP spectra of each showed emissions at binding energies characteristic of their corresponding metallic state (i.e., Au $4f_{7/2}$, 84.0 eV; Ag $3d_{5/2}$, 368.0 eV; Cu $2p_{3/2}$, 932.1 eV; Pd $3d_{5/2}$, 335.0 eV; Pt $4f_{7/2}$, 71.0 eV). These findings are attributed to the random

distribution of atoms in the high-entropy germanide structure,[45] and support the successful formation of the HEG.
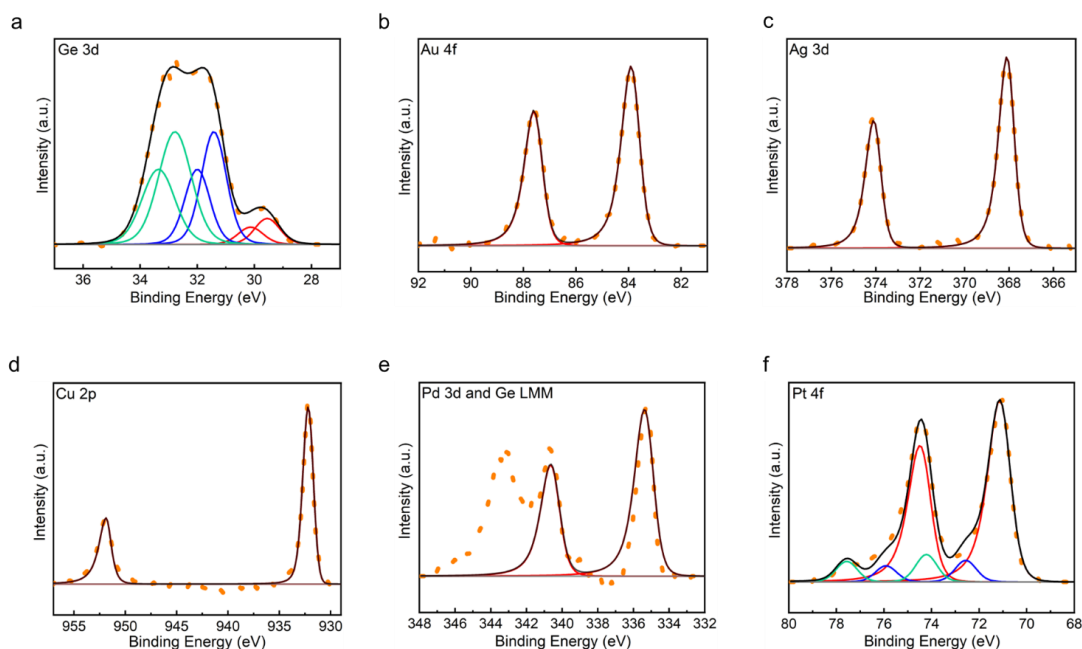
Figure 4.7. Representative high-resolution XP spectra of AuAgCuPdPtGe HEG: (a) Ge 3d, (b) Au 4f, (c) Ag 3d, (d) Cu 3d, (e) Pd 3d and Ge LMM, and (f) Pt 4f regions.

Electron microscopy techniques were employed for the investigation of the nano-morphology of the AuAgCuPdPtGe HEG. High-resolution transmission electron microscopy (HRTEM) image (Figure 4.8a) confirms the formation of pseudospherical HEG particles with dimensions 63.4 ± 4.5 nm (Figure 4.9a), while highly crystalline GeO_2 was observed surrounding the germanide (Figure 4.9b). Low-resolution bright-field TEM imaging (Figure 4.9c) shows the polydispersity of the AuAgCuPdPtGe HEG surrounded with crystalline GeO_2. High-angle annular dark-field scanning transmission electron microscopy (HAADF-STEM) images show AuAgCuPdPtGe HEG morphologies consistent with bright-field imaging (Figure 4.8b) and EDX mapping confirms co-localization of all metals and Ge in the morphological features (Figure 4.8c-h). On rare occasions localized element distribution mapping may vary slightly. We propose this

134

arises from inhomogeneous distribution of metal salts used to prepare the HEA NPs@GeNSs. The EDX spectrum (Figure 4.10) provides signatures for Ge (i.e., ca. 21 atom%) and the other five target metals (i.e., ca. 6 atom%). Collectively, these findings, with XPS analyses, support the conclusion that the germanide exhibits homogeneity and there is no evidence of surface segregation or phase separation.
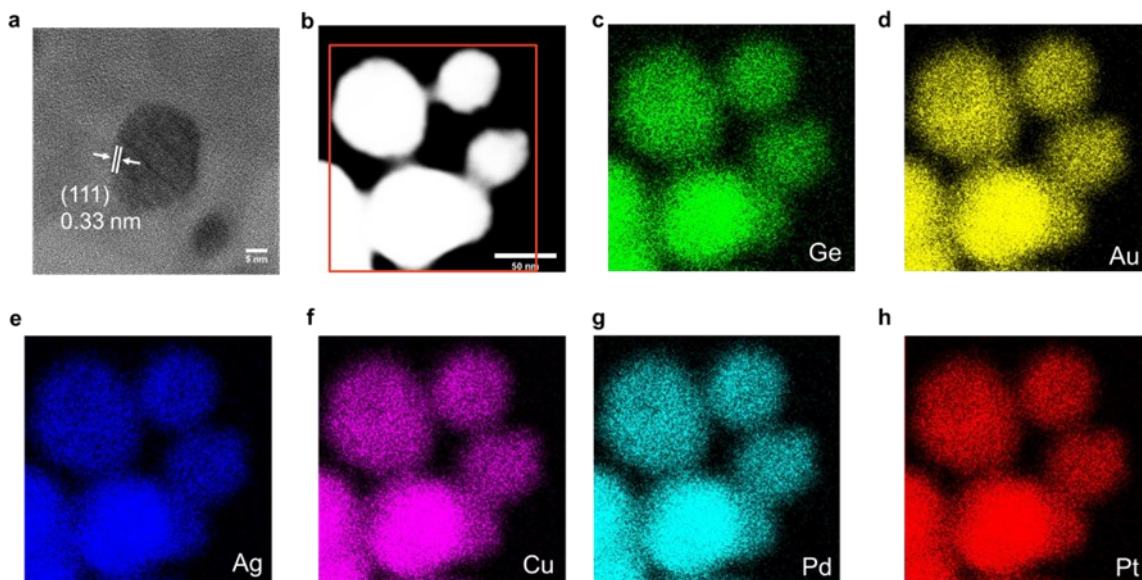
Figure 4.8. TEM and EDX analysis of AuAgCuPdPtGe HEG. (a) High-resolution image showing characteristic (111) lattice spacing. (b) HAADF-STEM image and (c-h) corresponding EDX mapping of the indicated elements.
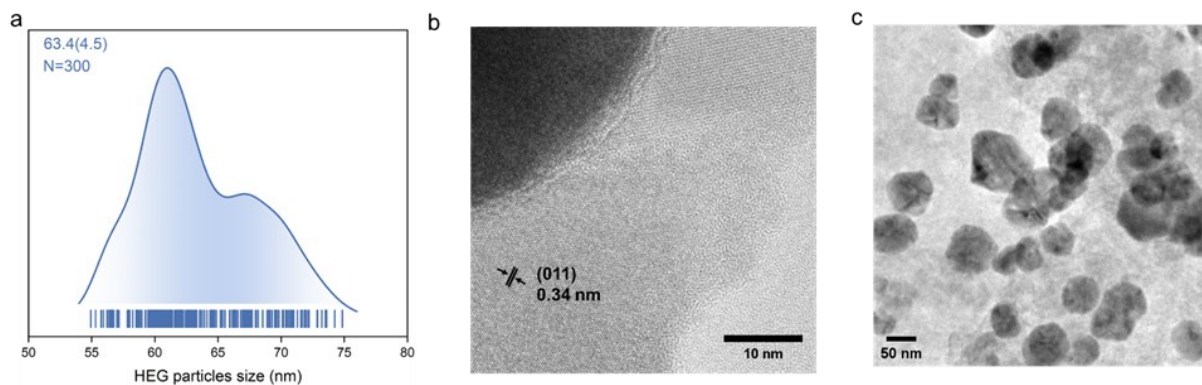
Figure 4.9. Representative (a) average shifted histogram for AuAgCuPdPtGe HEG and (b) high-resolution TEM image of AuAgCuPdPtGe HEG showing GeO_2 (011) lattice spacing. (c) low-resolution bright-field TEM image of AuAgCuPdPtGe HEG.
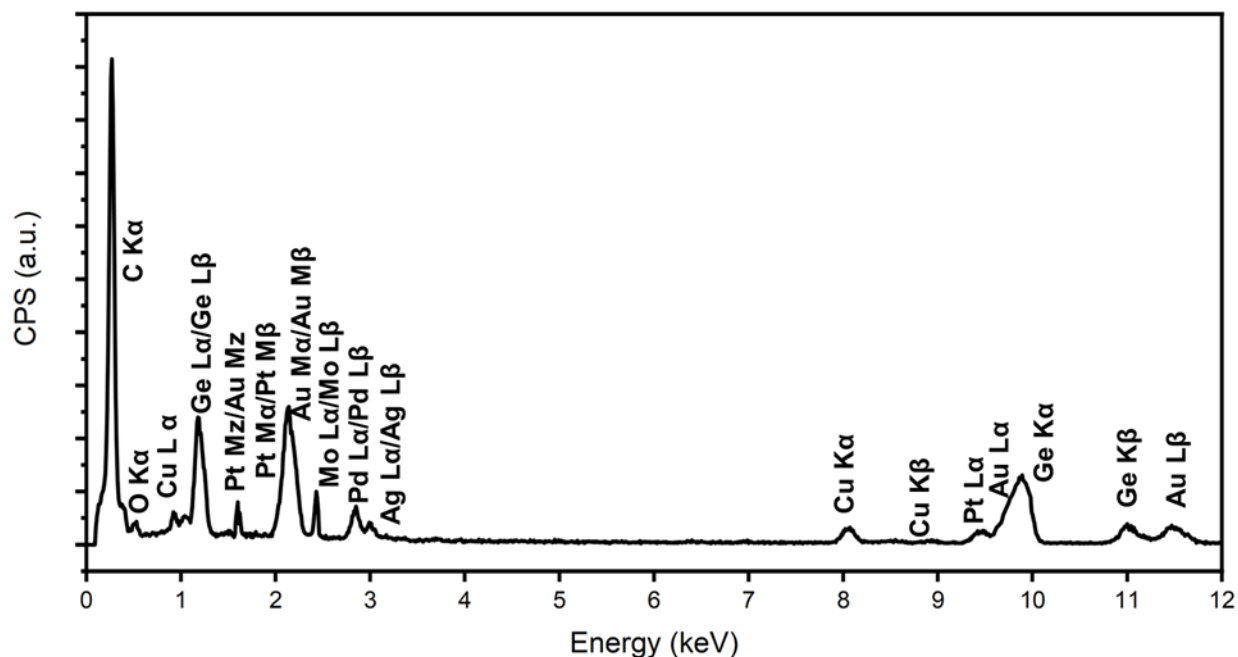
Figure 4.10. A representative EDX spectrum for AuAgCuPdPtGe HEG. Mo signal results from the grid.

Having demonstrated the feasibility of annealing HEA NPs@GeNSs as a convenient approach to preparing high-entropy germanides, we explored using alternative metals exhibiting lower redox potentials. While previous studies have focused on noble metals possessing positive redox potentials, we directed our attention to the first-row transition metals, V, Cr, Fe, Co, and Ni. The negative redox potentials of these transition metals hinder the direct reduction of the metal ion by GeNSs for metal nanoparticles deposition. To address this, we synthesized a FeCoNiCrVGe HEG by initially mixing GeNSs with a solution comprising metal salts (i.e., $FeCl_3$, VCl_3, $CrCl_2$, $CoCl_2$, $NiCl_2$) followed by solvent removal through rotary evaporation. The resulting slurry was heated to 800 °C at 1 °C/s under Ar flow. The sample was maintained at the peak temperature for 10 minutes, after which the product was quenched to room temperature by removing the tube from the furnace and flushing the tube with N_2 gas (Figure 4.10).

136
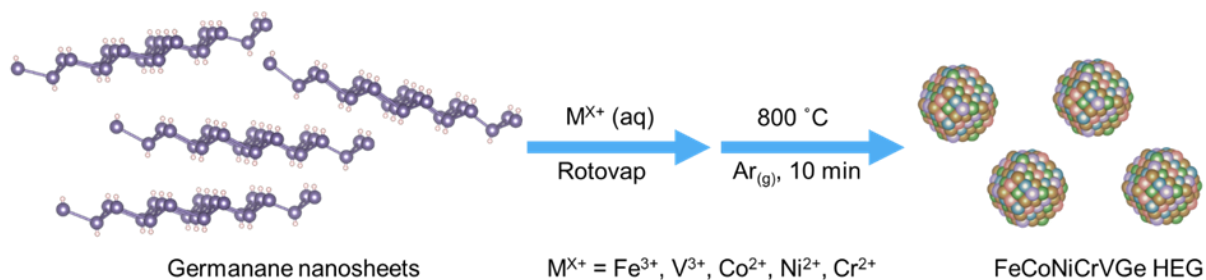
Figure 4.11. A pictorial representation of the synthesis of FeCoNiCrVGe HEG.

The crystal structure and bonding of FeCoNiCrVGe HEG were investigated using XRD and FTIR spectroscopy. The XRD analysis (Figure 4.12) is dominated by the characteristic reflections from GeNSs. No salt related reflections are noted because of their low concentration. After annealing (Figure 4.12) FCC reflections from FeCoNiCrVGe HEG were observed while no reflections associated with GeNSs were detected. We also note that the reflections associated with the FeCoNiCrVGe HEG appeared at slightly higher angles (27.32°, 45.34°, 53.74°, 66.06°, 72.90°) compared to the Ge reflections (27.28°, 45.30°, 53.69°, 65.99°, 72.81°). The reflections of GeO_2 were also observed, but with lower intensity in comparison with the AuAgCuPdPtGe HEG. This finding suggests the metal salts-loaded GeNSs precursor contained fewer oxidized Ge surface species and implies that the GeNSs exhibited limited reactivity toward the metal salts used (i.e., $FeCl_3$, VCl_3, $CrCl_2$, $CoCl_2$, $NiCl_2$). Scherrer analysis provided an estimated crystallite size of 55.3 ± 1.7 nm and the broadening distribution of the FeCoNiCrVGe HEG indicated the presence of strain-induced broadening (Figure 4.13a). We also determined the lattice parameter for the FeCoNiCrVGe HEG using Vegard's Law (Figure 4.13b) and found that a similar deviation from the linear variation of the lattice parameters due to the incorporation of the small atoms. In the FTIR spectrum of the precursor (Figure 4.14), a dominant Ge-H stretching vibration was observed at 2000 cm^{-1}; of note there is no apparent Ge-O vibration feature in the range of 700 to 800 cm^{-1}.[35]

Consistent with the presented XRD analyses, after annealing a significant Ge-O peak emerged at 800 cm^{-1} and there is no evidence of the Ge-H feature.
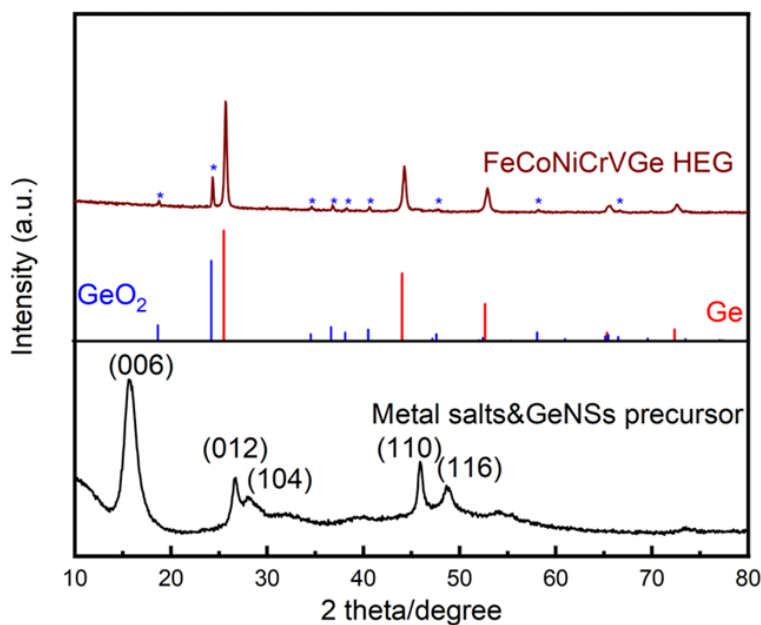
Figure 4.12. A comparison of XRD patterns of metal salts&GeNSs precursor and FeCoNiCrVGe HEG. (*) correspond to GeO$_2$ reflections. Ge and GeO$_2$ reflections are from PDF#89-4562 and 83-2477.
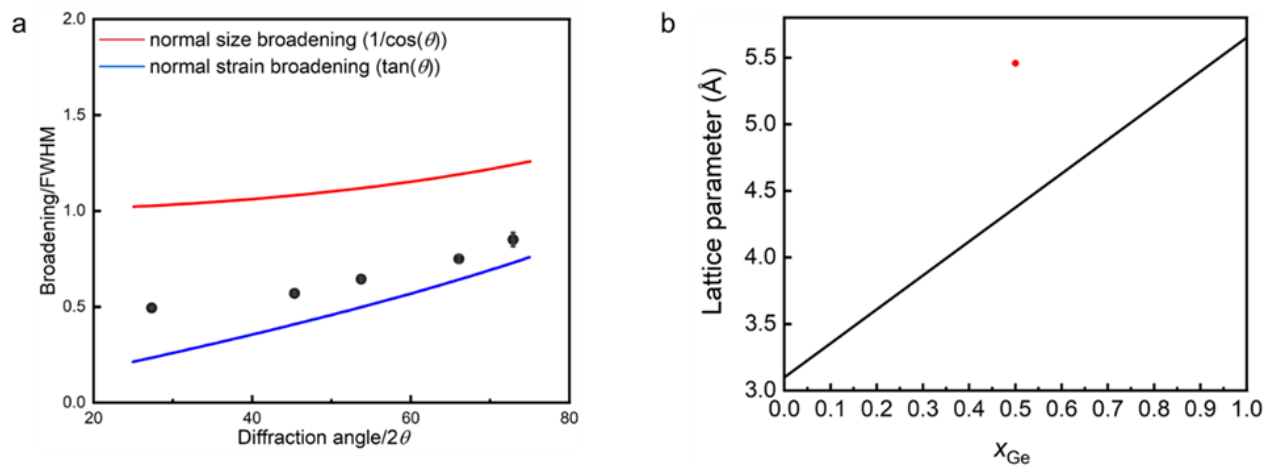
Figure 4.13. (a) XRD peak broadening distribution for the FeCoNiCrVGe HEG. (b) A plot of the lattice parameter as a function of the mole fraction of Ge in FeCoNiCrVGe HEG by using Vegard's law. The red dot represents the experiment lattice parameter calculated from the XRD reflections using Bragg's law.
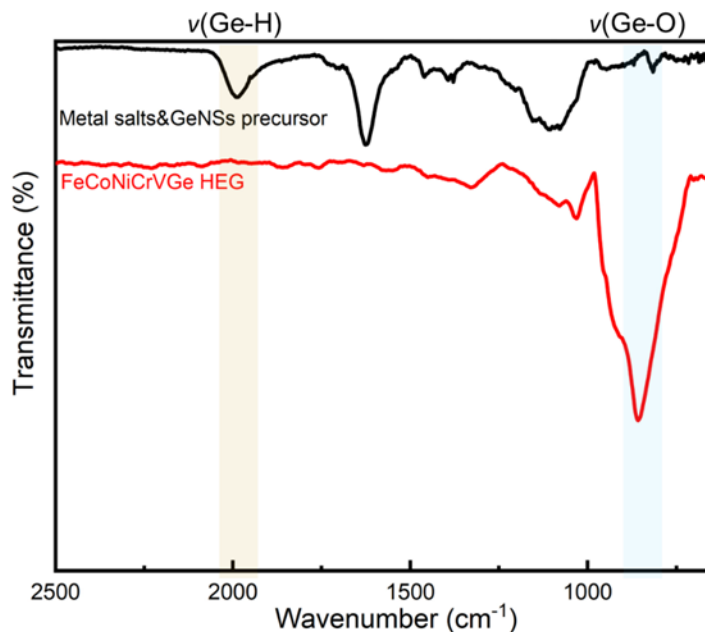
Figure 4.14. Representative FTIR spectra of metal salts&GeNSs precursor (black) and FeCoNiCrVGe HEG (red).

XPS was used to investigate the elemental composition and oxidation states of the resulting FeCoNiCrVGe HEG. The survey spectrum (Figure 4.15) showed the expected metal (approximately 15 atomic %) and Ge (24.2 atomic %) emissions, indicating an approximate composition of $Fe_{0.63}Co_{0.62}Ni_{0.64}Cr_{0.63}V_{0.61}Ge$ (Table 4.2) ; as with the AuAgCuPdPtGe HEG, we note higher proportions of Ge that we attribute to the presence of GeO_2. The high-resolution spectra of the metal components within the FeCoNiCrVGe HEG exhibited high oxidation states (Figure 4.16; V^{3+} $2p_{3/2}$, 515.7 eV; Cr^{3+} $2p_{3/2}$, 576.9 eV; Fe^{2+} $2p_{3/2}$, 709.6 eV; Co^{2+} $2p_{3/2}$, 779.6 eV and Ni^{+} $2p_{3/2}$, 853.0 eV) and the metal emissions are shifted to higher binding energies compared to their metallic state. This shift is attributed to the comparatively high electronegativity of Ge when relative to the metals (Table 4.2).[46, 47] The difference in electronegativity between the elements affects their binding energies, with a larger difference resulting in greater shift.[20] Correspondingly, the Ge 3d region (Figure 4.16a) provided a binding energy of 29.2 eV which was lower than the

139

binding energy of c-Ge (29.5 eV). This shift in Ge 3 d binding energy is consistent with the average electronegativity of neighboring atoms is lower than that of Ge itself.[47] It should be noted that all of the metals (Fe, Co, Ni, Cr, V) in the HEG exhibit lower electronegativities compared to the previous noble metals and Ge (Table 4.2).
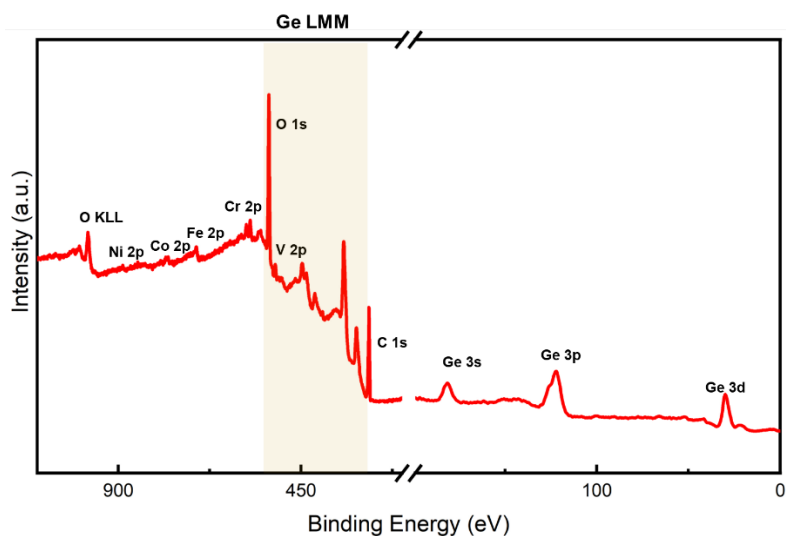
Figure 4.15. Representative survey XP spectrum of FeCoNiCrVGe HEG.
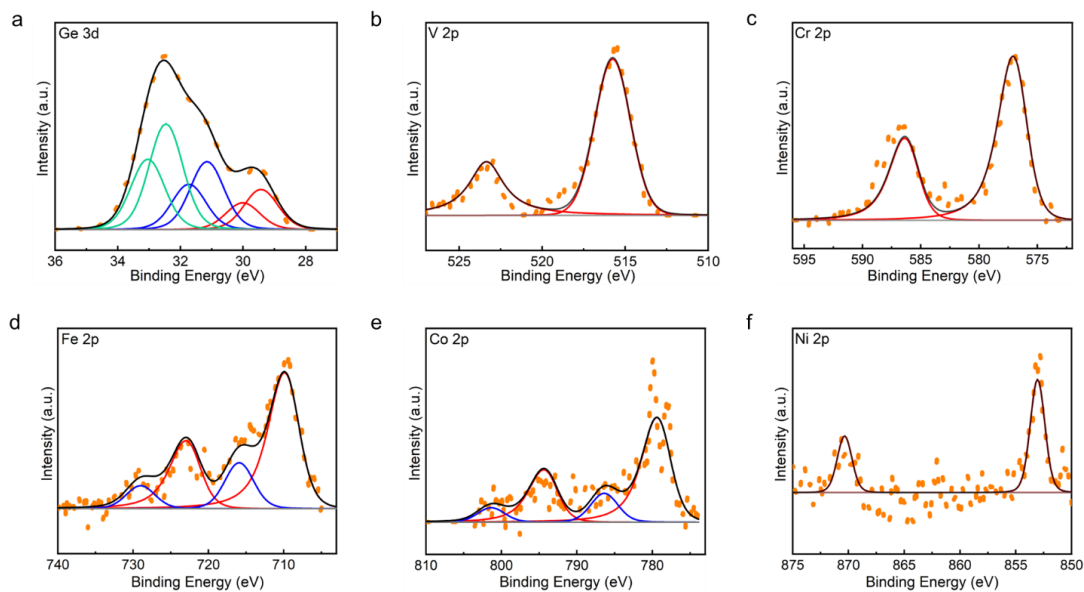
Figure 4.16. Representative high-resolution XP spectra of FeCoNiCrVGe HEG: (a) Ge 3d, (b) V 2p, (c) Cr 2p, (d) Fe 2p, (e) Co 2p and (f) Ni 2p regions.

140

Table 4.2. Summary of XPS data for FeCoNiCrVGe HEG.

	Ge 3d	V 2p	Cr 2p	Fe 2p	Co 2p	Ni 2p
Emission (eV)	29.2	515.7	576.9	709.6	779.6	853.0
Reference emission (eV)[a]	29.5; Ge	515.7; V^{3+}	576.9; Cr^{3+}	709.6; Fe^{2+}	779.6; Co^{2+}	853.0; Ni^{+}
Atomic percentage (%)	24.2	14.8	15.2	15.3	15.1	15.4
Eletronegativity[b]	2.01	1.63	1.66	1.83	1.88	1.91

[a] Reference metal emissions are from NIST X-ray Photoelectron Spectroscopy Database.

[b] Eletronegativities are from CRC Handbook for Chemistry and Physics, 91st ed., 2010–2011, CRC Press.
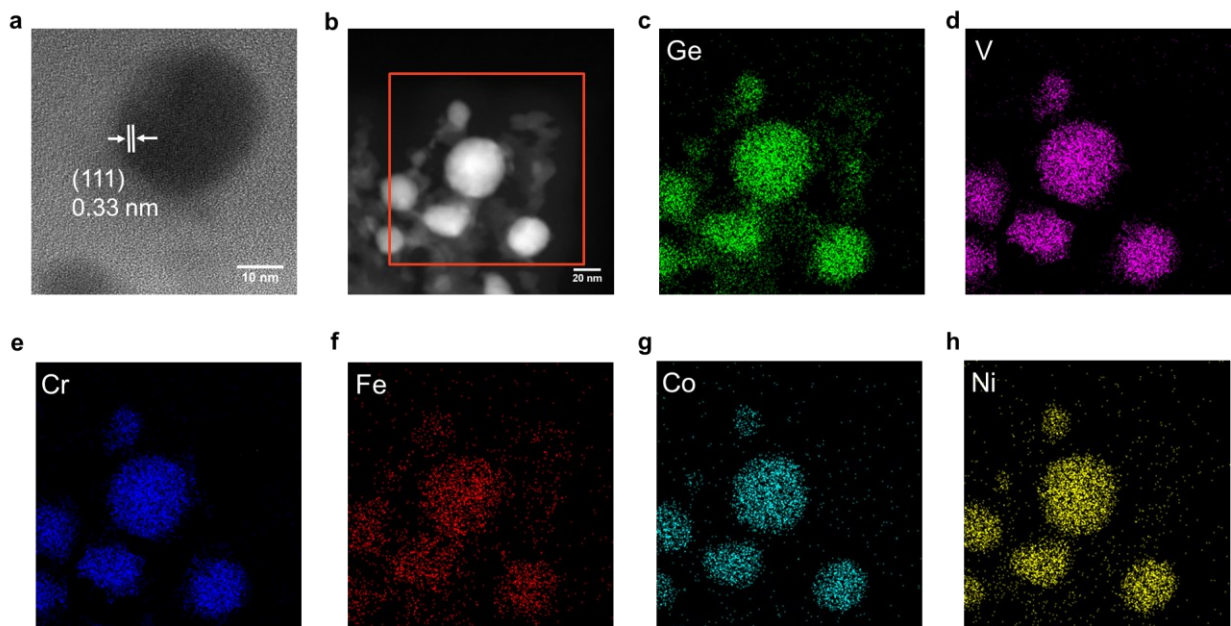
Figure 4.17. TEM and EDX analysis of FeCoNiCrVGe HEG. (a) High-resolution image showing characteristic (111) lattice spacing. (b) HAADF-STEM image and (c-h) corresponding EDX mapping of the indicated elements.

HRTEM imaging (Figure 4.17a) confirmed the formation of FeCoNiCrVGe HEG with particles dimension of be 55.8 ± 3.4 nm (Figure 4.18a) and low-resolution bright-field TEM imaging (Figure 4.18b) shows the polydispersity of the FeCoNiCrVGe HEG. Morphology of our FeCoNiCrVGe HEG was further interrogated using HAADF-STEM imaging (Figure 4.17b) while EDX mapping provided evidence of the co-localization of morphological features in HAADF-STEM images and the presence of the five target metals (Fe, Co, Ni, Cr, V) and Ge. The EDX spectrum (Figure 4.19) further indicated an elemental composition of Fe (1.6 atom %), Co (1.5 atom %), Ni (1.3 atom %), Cr (1.1 atom %), V (1.4 atom %) and Ge (6.4 atom %) which agrees with the composition determined using XPS.
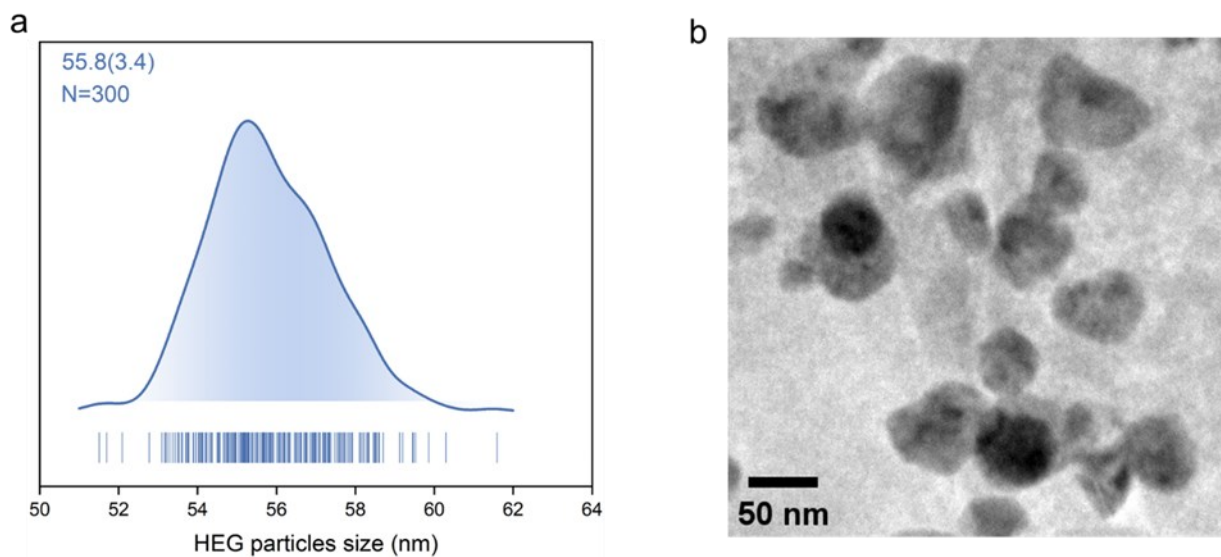
Figure 4.18. Representative (a) average shifted histogram for FeCoNiCrVGe HEG and (c) low-resolution bright-field TEM image of FeCoNiCrVGe HEG.
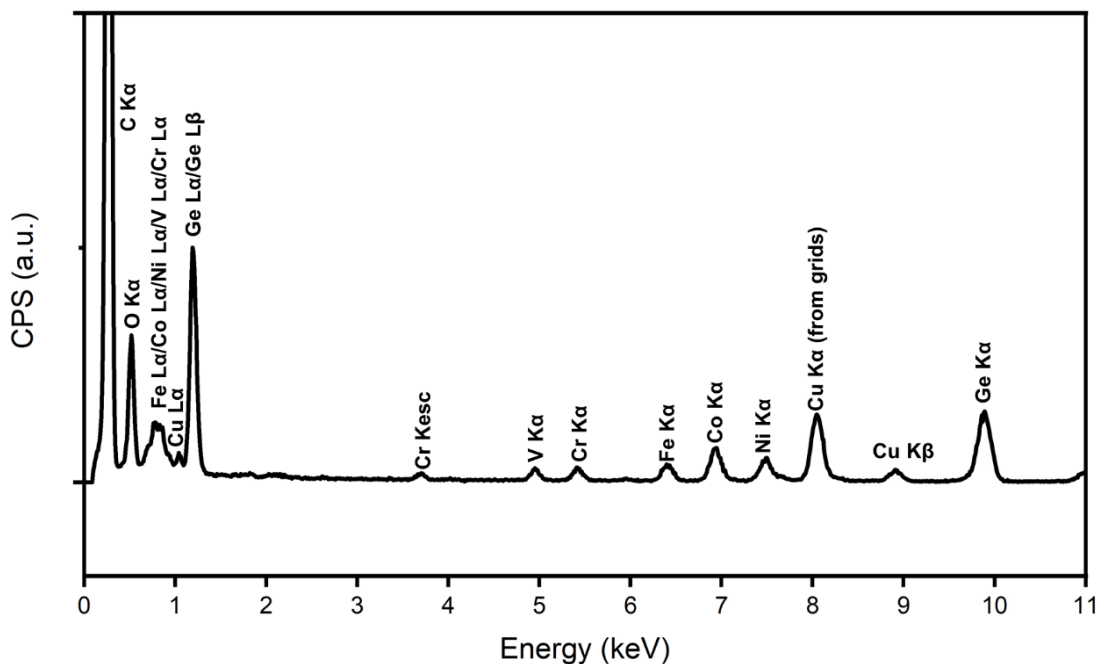
Figure 4.19. Representative EDX spectrum for FeCoNiCrVGe HEG.

To gain a more complete understanding of the processes leading to the transformation of HEA NPs@GeNSs to an AuAgCuPdPtGe HEG we performed *in situ* heating XRD experiments. These experiments captured the diffraction pattern of the HEA NPs@GeNSs from room temperature to 800 ˚C (Figure 4.20a). A dome (Figure 4.21a) was used to maintain an inert N_2 atmosphere during the heating process and its background contribution (Figure 4.21b) was subtracted from the resulting XRD diffraction pattern. During the heating process, a gradual decrease in the intensity of the (006) reflection of GeNSs (15.5˚) was noted at 200 ˚C, and it completely disappeared at 300 ˚C, suggesting the decomposition of GeNSs.[43] At and above 300 ˚C, broad reflections characteristic of a cubic Ge crystal structure began to emerge, signifying the formation of nanosized Ge crystals. With increased temperature, these reflections narrowed indicative of increasing crystallite size and structure ordering.[48] Based on Scherrer analyses,[49] the average crystallite size were calculated from the XRD patterns and provided an increase in average crystallite size from 1.6 to 61.8 nm as the annealing temperature increased from 300 to 800 °C

143

(Figure 4.21a). Additionally, the appearance of sharp intensity reflections corresponding to hexagonal GeO_2 crystal structure was observed after 700 ˚C. This finding is consistent with the crystallization of surface Ge oxide species at high temperatures[41] and is in agreement with previous *ex situ* XRD measurement. During heating, these peaks shifted to lower degrees due to the thermal expansion at high temperature[50] before shifting back after cooling.

For comparison, the formation of the FeCoNiCrVGe HEG was also investigated by *in situ* heating XRD. The XRD patterns of FeCoNiCrVGe HEG during the heating process from room temperature to 800 ˚C (Figure 4.20b) showed a similar evolution to that observed for the formation of AuAgCuPdPtGe HEG. The reflection assigned to GeNSs at 15.5˚ also decreased at 200 ˚C and disappeared at 300 ˚C, indicating the decomposition of GeNSs occurred at 200 ˚C and completed at 300 ˚C,[43] just as observed in the case of AuAgCuPdPtGe HEG. Furthermore, broad intensity reflections corresponding to a cubic Ge crystal structure appeared at 400 ˚C. As the temperature increased, these reflections became sharpened, indicating an increase in crystallite size and structural ordering, similar to the behavior observed in the AuAgCuPdPtGe HEG transformation. Using the Scherrer equation, the average crystallite sizes were calculated from the XRD patterns and showed an increase from 2.2 to 55.3 nm as the annealing temperature increased from 300 to 800 °C (Figure 4.22a). While AuAgCuPdPtGe HEG displayed reflections arising from hexagonal GeO_2 with higher intensities at 700 ˚C, FeCoNiCrVGe HEG showed these reflections of hexagonal GeO_2 with much lower intensities at 800 ˚C. This suggests that more GeNSs remained unreacted with the transition metal salts (i.e., $FeCl_3$, VCl_3, $CrCl_2$, $CoCl_2$, $NiCl_2$) and the formation of hexagonal GeO_2 originated from trace surface oxidation of GeNSs (Figure 4.23).[51]
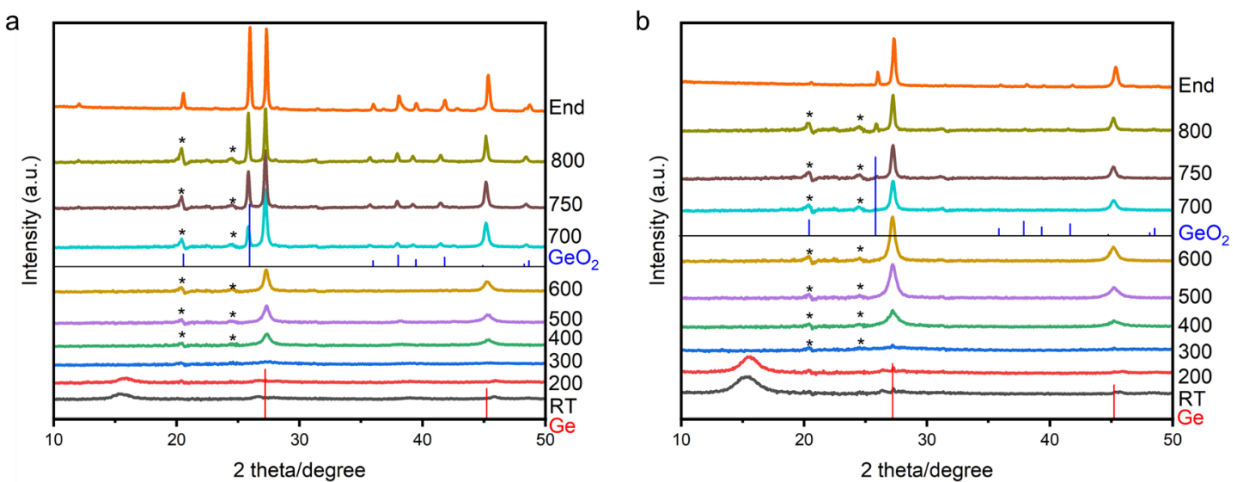
Figure 4.20. *In situ* heating XRD results of (a) AuAgCuPdPtGe HEG and (b) FeCoNiCrVGe HEG. (*) correspond to the reflections from the dome of in situ XRD heating stage. Ge and GeO_2 reflections are from PDF#89-3833 and 83-2477.
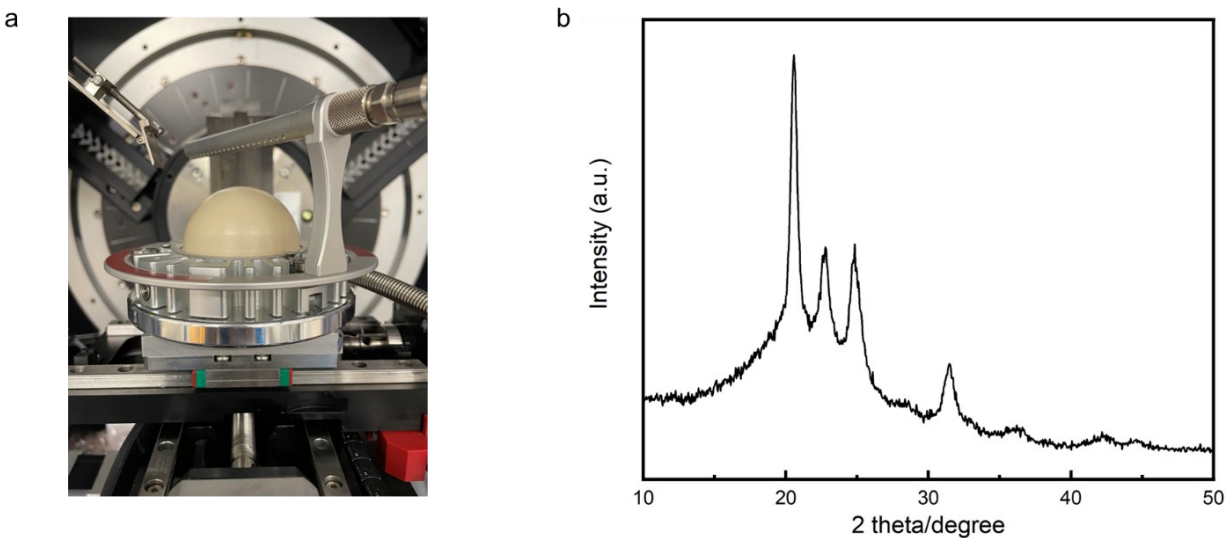
Figure 4.21. (a) Photograph of the *in situ* XRD heating stage with the dome. (b)XRD pattern of the dome of the *in situ* XRD heating stage.
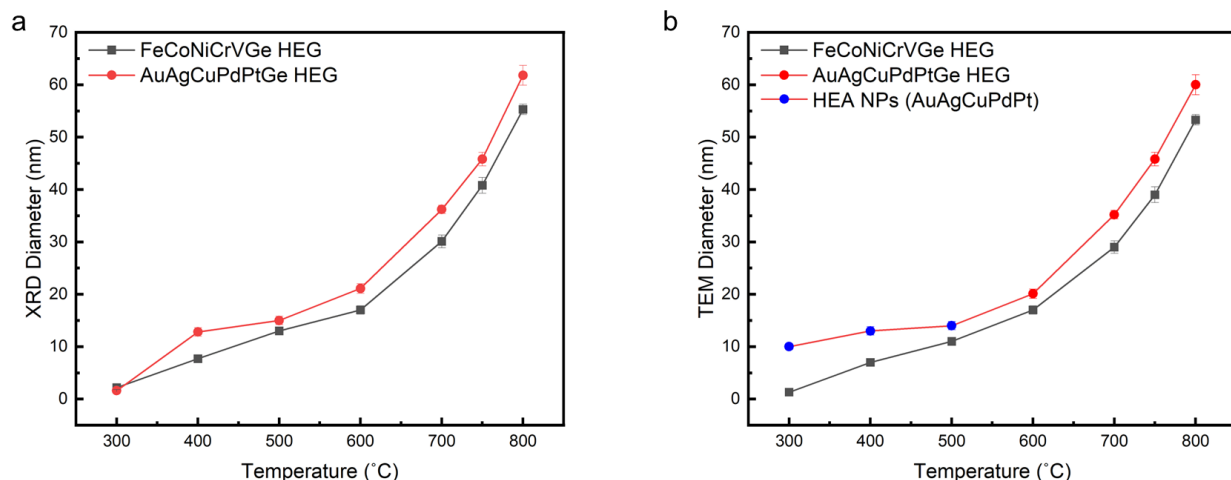
Figure 4.22. (a) Average size of HEGs derived from the XRD results and (b) average size of HEA NPs and HEG derived from the TEM results.
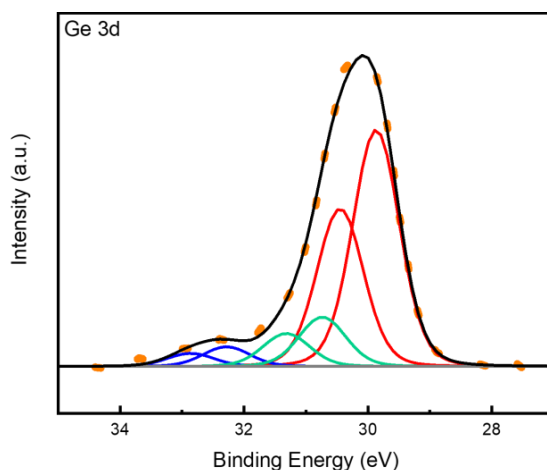
Figure 4.23. A representative high-resolution XP spectrum of Ge 3d region of metal salts&GeNSs precursor.

To monitor the structural evolution of FeCoNiCrVGe HEG in real time, *in situ* heating STEM experiments were performed; representative movie is presented in Movie S1. The HAADF-STEM images of the same location (Figure 4.24) captured the morphological changes of GeNS upon heating from room temperature to 800 ˚C and ultimately leading to the formation of the FeCoNiCrVGe HEG. There was no significant change observed in the GeNS below 300 °C, consistent with this initial heating stage primarily involving the breaking of Ge-H bonds, with

146

hydrogen radicals subsequently reducing the metal salts to form metal atoms. Above 300 °C, GeNS began decomposing into Ge, resulting in the formation of small grains, while metal atoms diffused into the structure.[52, 53] Notably, the grain size increases slowly below 600 °C, but grows rapidly at 600 °C and above. The TEM particle sizes (Figure 4.22b) measured during the heating process showed an increase from 1.3 to 53.3 nm, which is in agreement with the previous in situ heating XRD results. Observations from the contrast-enhanced images (Figure 4.25) revealed the presence of small nanoparticles around the germanide at 700 °C, which grew larger at 800 °C. These nanoparticles resulted from the growth of metal atoms that were reduced from excess metal salts on the *in situ* heating nanochip instead the GeNS. EDX mapping (Figure 4.26) further confirmed the morphology of GeNSs in HAADF-STEM and revealed the presence of the five target metal salts before heating. After heating, EDX mapping (Figure 4.27) indicated the co-localization of morphological features characteristic of FeCoNiCrVGe HEG. The EDX spectrum (Figure 4.28 and 4.29) showed a notable decrease in the Cl signal (*i.e.,* from 3.43 to 0.05 atomic %), while the signals corresponding to Ge and the other five metal signals remained around 3 atomic % after heating. This finding suggests a successful transformation from metal salts&GeNS precursor to FeCoNiCrVGe HEG.
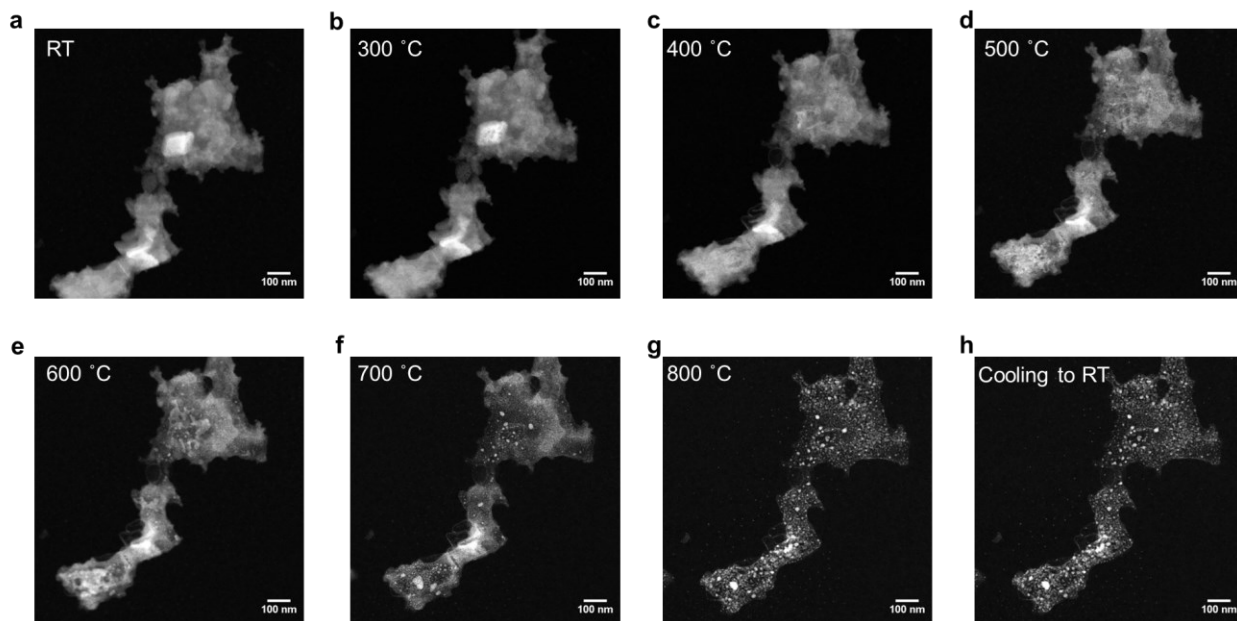
Figure 4.24. HAADF-STEM images of FeCoNiCrVGe HEG at the same location during the *in situ* heating experiment from room temperature to 800 ˚C (a-g) and after cooling down to room temperature (h). The sample slightly shifted due to the thermal drift.
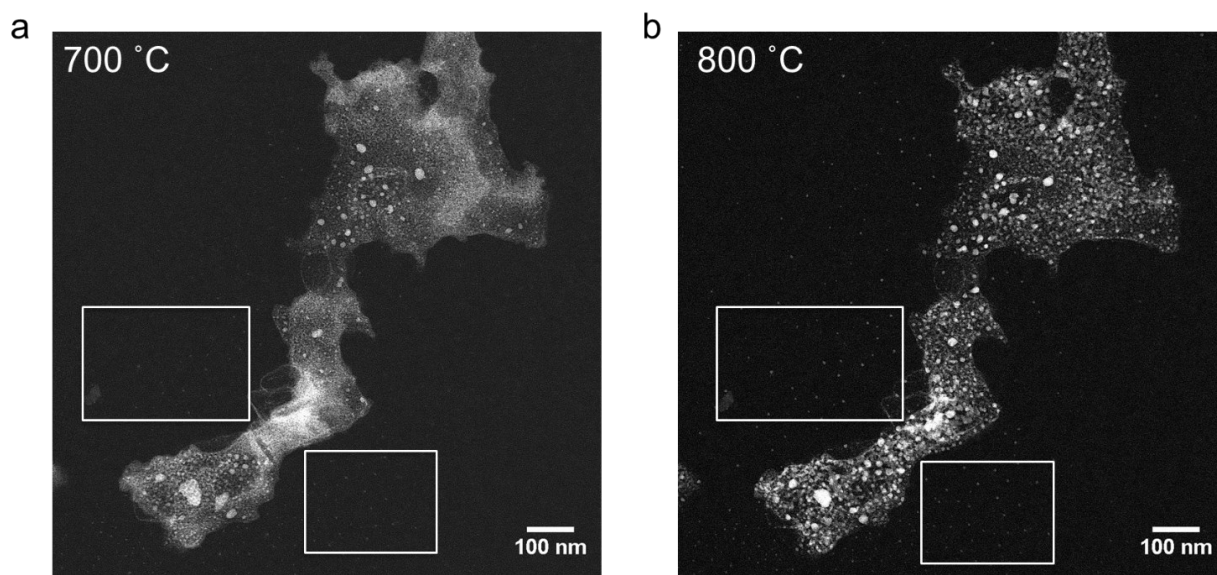
Figure 4.25. Enhanced HAADF-STEM images of FeCoNiCrVGe HEG at the same location during the *in situ* heating experiment at 700 ˚C and 800 ˚C. (Boxes highlight regions where small metal nanoparticles arising from the reduction of excess metal salts have formed on the in situ heating nanochip.)

148
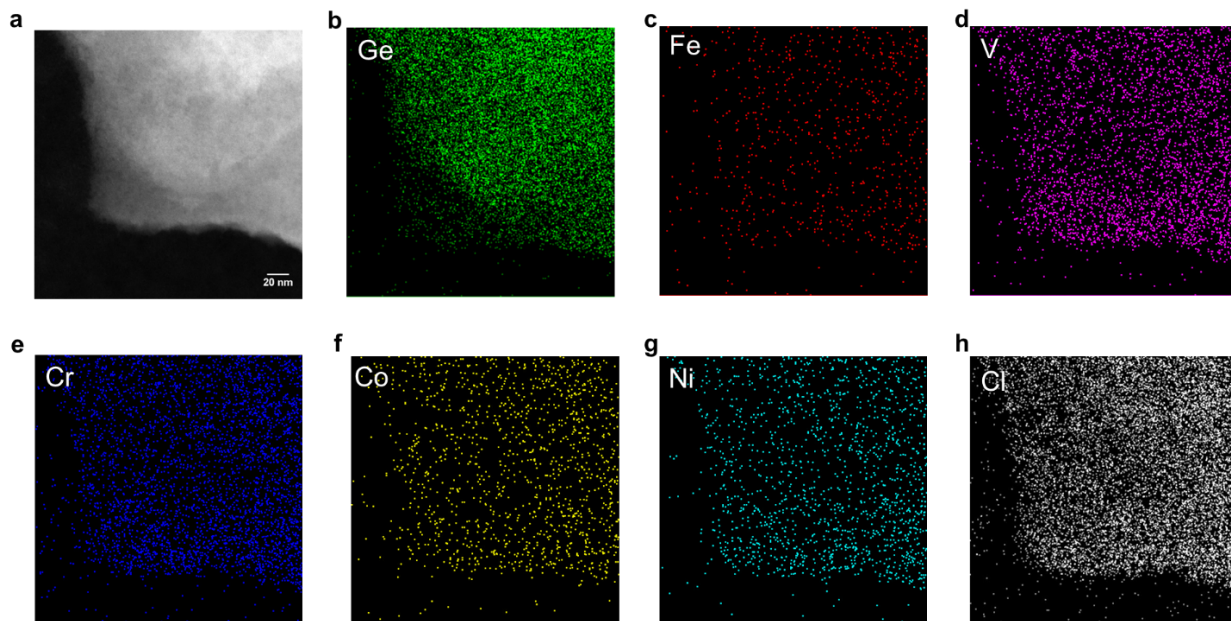
Figure 4.26. Representative HAADF-STEM images and EDX mapping of metal salts&GeNSs.
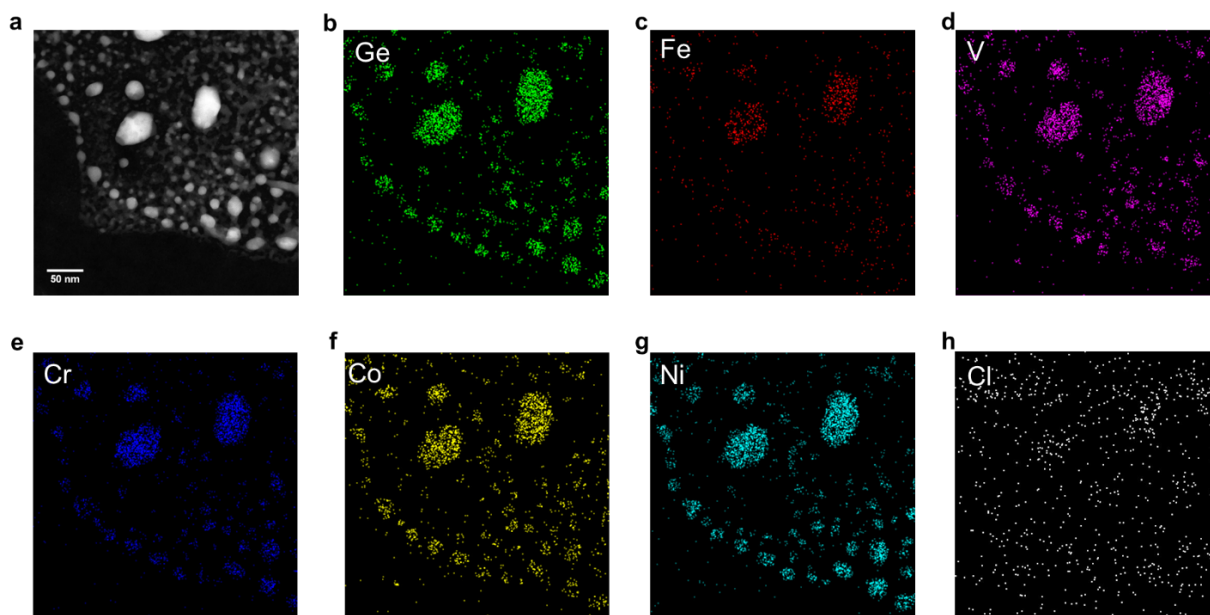
Figure 4.27. Representative HAADF-STEM images and EDX mapping of FeCoNiCrVGe HEG.
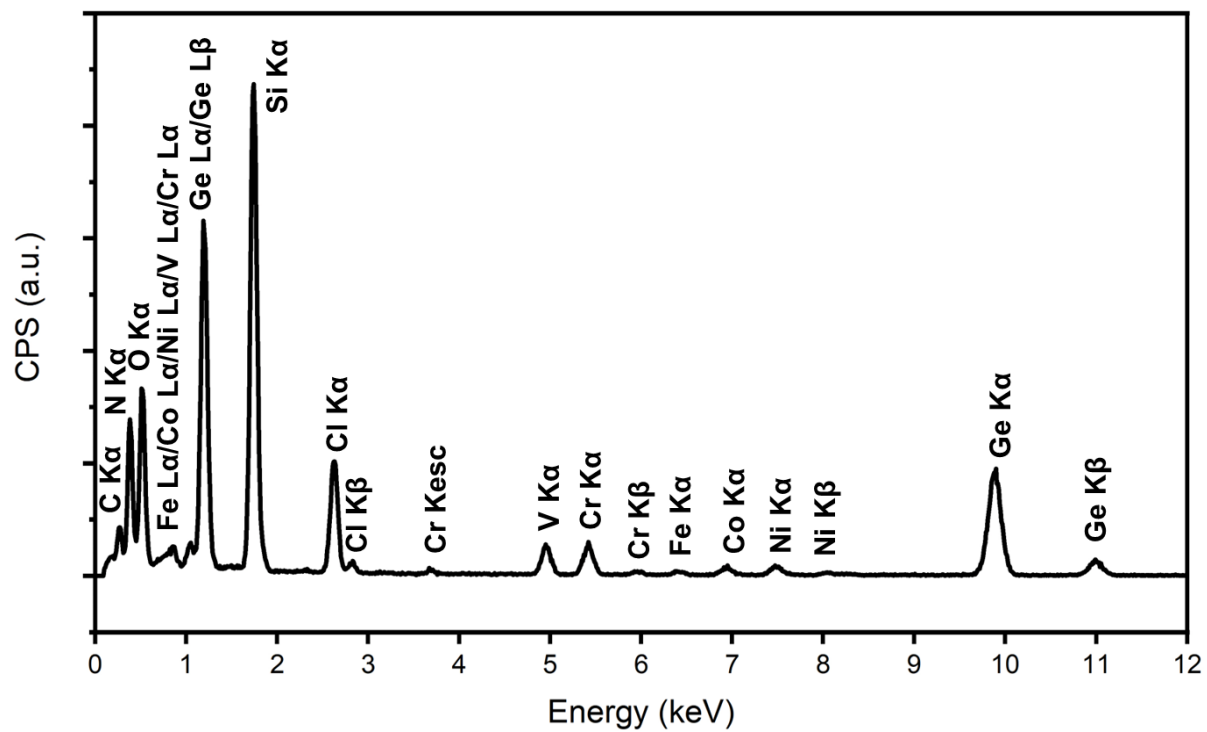
Figure 4.28. A representative EDX spectrum for metal salts&GeNSs. Si and N signals result from the Si_3N_4 chip.
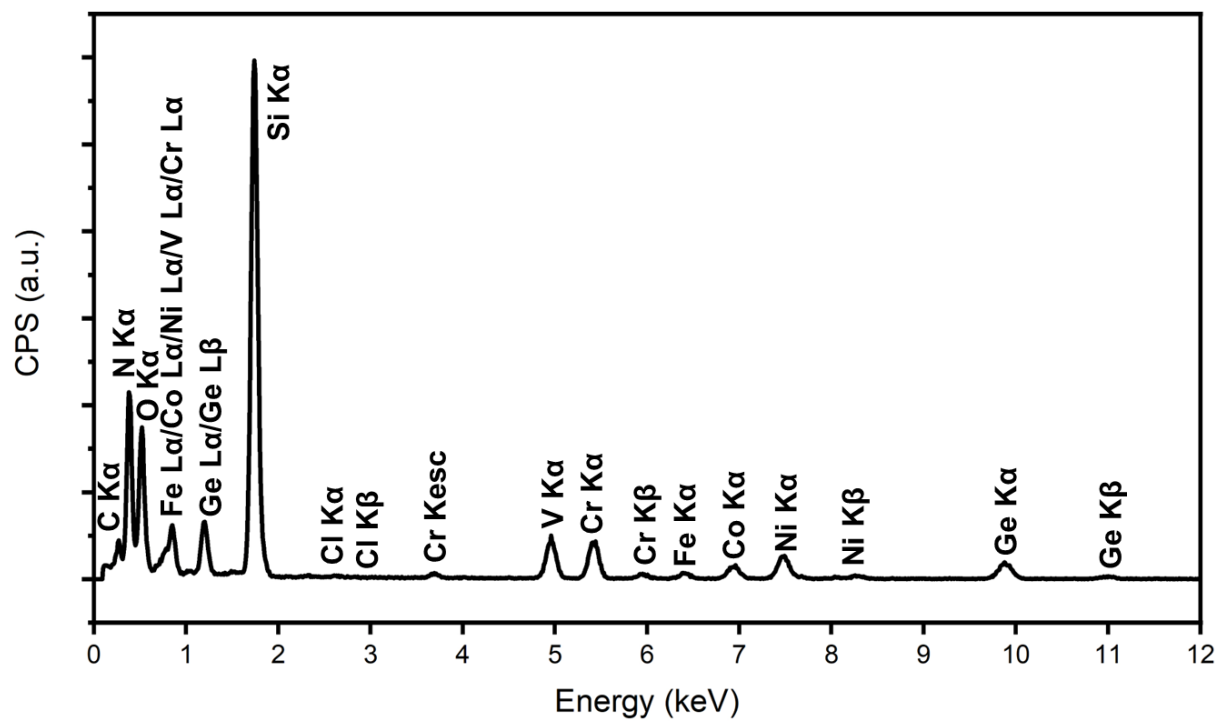
Figure 4.29. A representative EDX spectrum for FeCoNiCrVGe HEG. Si and N signals result from the Si_3N_4 chip.
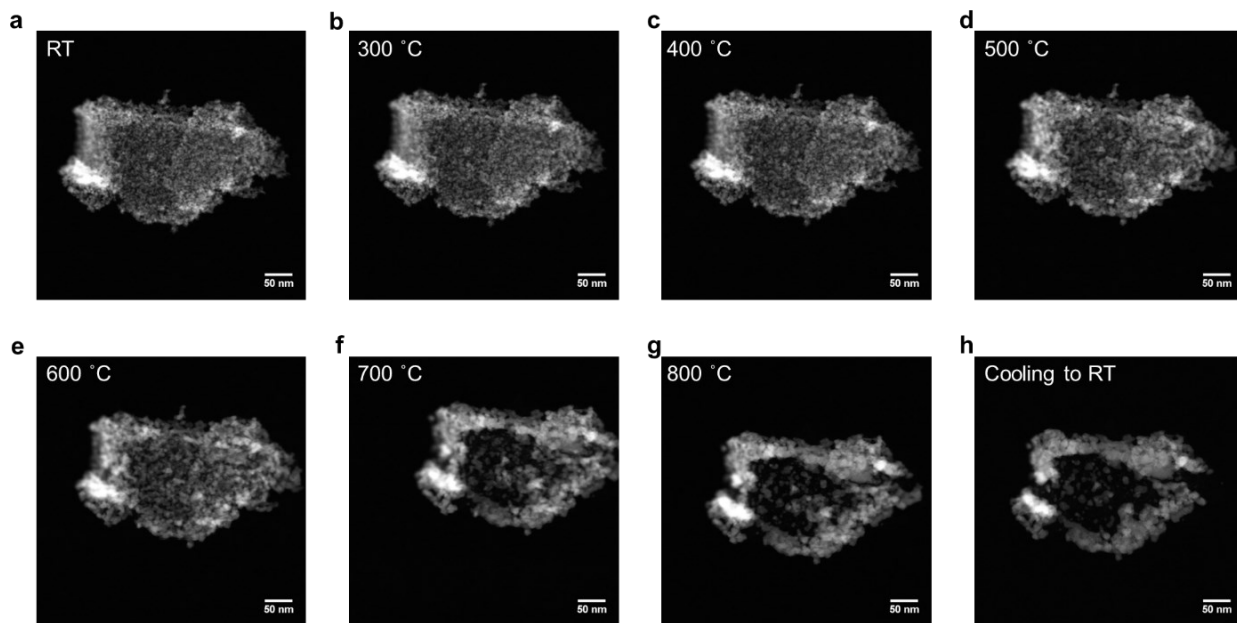
Figure 4.30. HAADF-STEM images of AuAgCuPdPtGe HEG at the same location during the *in situ* heating experiment from room temperature to 800 ˚C (a-g) and after cooling down to room temperature (h). The sample shifted slightly due to the thermal drift.
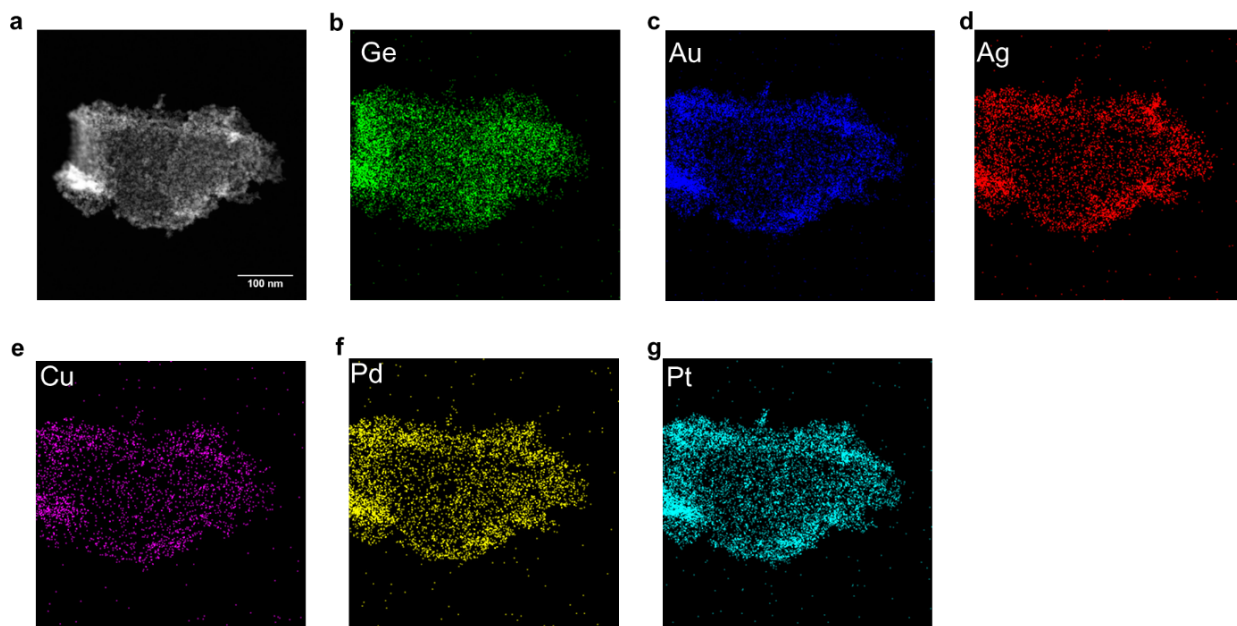
Figure 4.31. Representative HAADF-STEM images and EDX mapping of HEA NPs@GeNSs.
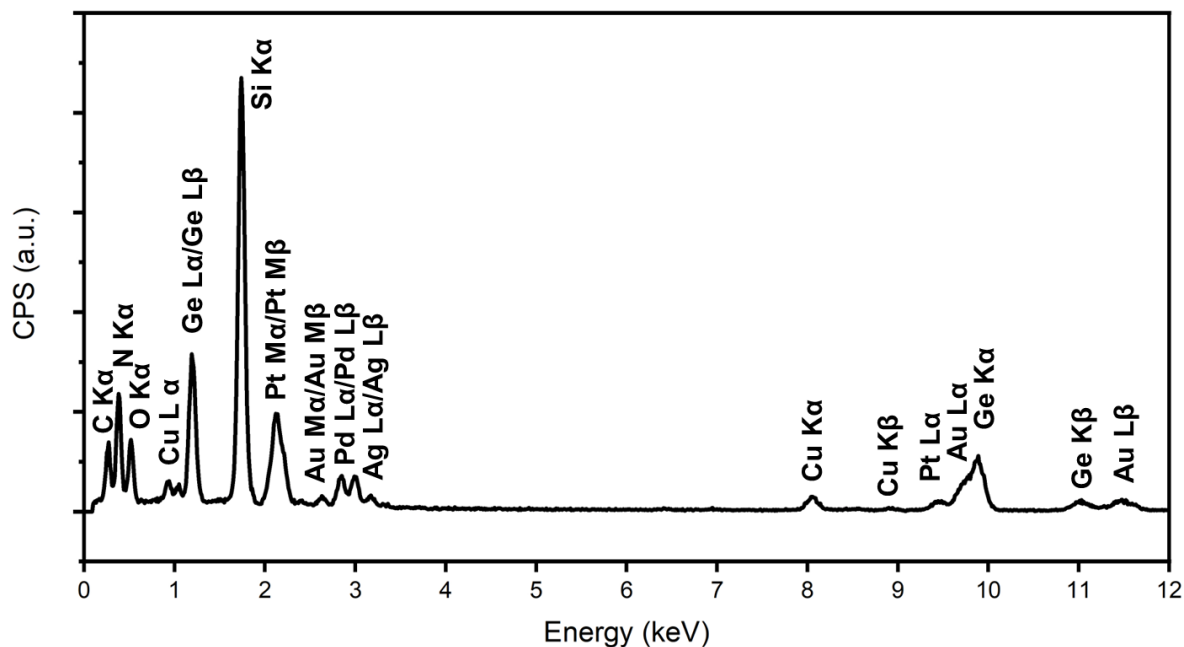
Figure 4.32. A representative EDX spectrum for HEA NPs@GeNSs. Si and N signals result from the Si_3N_4 chip.
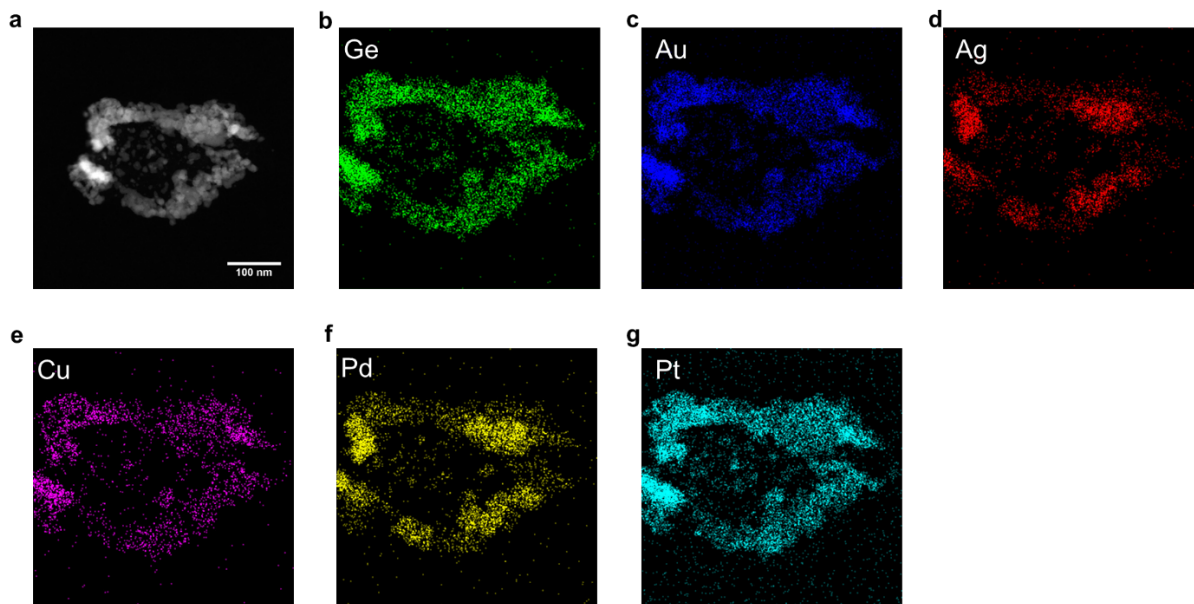
Figure 4.33. Representative HAADF-STEM images and EDX mapping of AuAgCuPdPtGe HEG.

To provide a comparison, the transformation process of HEA NPs@GeNSs to AuAgCuPdPtGe HEG was also investigated using *in situ* heating STEM experiments, as presented in Movie S2. The HAADF-STEM images of the same location (Figure 4.30) showed the

morphology evolution of the nanosheets as they were heated from room temperature to 800 ˚C. Below 300 ˚C, no significant morphological changes were observed, indicating a similar initial stage involving the breakage of Ge-H bonds. After 300 ˚C, it became challenging to observe the transformation of underlying GeNSs to Ge since they were covered by the HEA NPs. Instead, the surface HEA NPs disappear, suggesting that they diffused into the underlying Ge. Above 600 ˚C, the fast growth of larger particles from the small grains was observed. The sizes of the particles measured from the TEM (Figure 4.23b) also showed a slower growth stage before 600 ˚C, followed by a faster growth stage after 600 ˚C, consistent with previous *in situ* XRD results. Unlike the FeCoNiCrVGe HEG, no obvious nanoparticles were observed around the nanosheets region, demonstrating that the transformation in this case primarily involves the diffusion of HEA NPs into the Ge. EDX mapping and spectrum (Figure 4.31 and 4.32) further confirmed the morphology of HEA NPs@GeNSs in HAADF-STEM, which comprised the HEA NPs before heating.[28] After heating, the EDX mapping and spectrum (Figure 4.33 and 4.34) showed co-localization of morphological features of AuAgCuPdPtGe HEG nanoparticles.
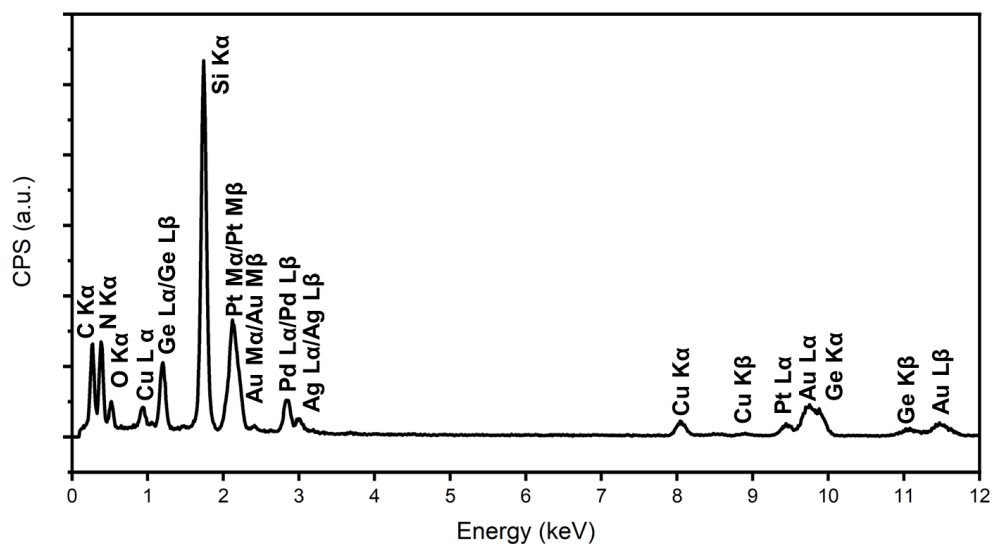
Figure 4.34. A representative EDX spectrum for AuAgCuPdPtGe HEG. Si and N signals result from the Si$_3$N$_4$ chip.

4.4 Summary and Outlook

The present study has successfully demonstrated a method for preparing two types of high-entropy germanide ($Au_{0.54}Ag_{0.53}Cu_{0.55}Pd_{0.55}Pt_{0.53}Ge$ and $Fe_{0.63}Co_{0.62}Ni_{0.64}Cr_{0.63}V_{0.61}Ge$) using a rapid thermal annealing. HEG formation was verified by XRD and XPS, which provided evidence of their structure and elemental composition/oxidation states, respectively. Transmission electron microscopy further revealed that the HEGs possessed a near equal concentrations of all the constituent elements and exhibited a homogenous distribution throughout the material. The transformation processes were subsequently investigated by in situ heating in XRD and STEM. HEG formation involved the decomposition of GeNSs during the initial stages, followed by a slow grain growth process through atom diffusion at temperatures below 600 °C, and finally a rapid grain growth process at higher temperatures. These findings provide valuable insights into the formation and growth mechanisms of HEGs. The ability to synthesize and characterize these HEGs paves the way for future investigations into their unique properties and potential applications in fields such as materials science, electronics, and catalysis.

4.5 References

1. Yao, Y.; Dong, Q.; Brozena, A.; Luo, J.; Miao, J.; Chi, M.; Wang, C.; Kevrekidis, I. G.; Ren, Z. J.; Greeley, J.; Wang, G.; Anapolsky, A.; Hu, L., High-entropy Nanoparticles: Synthesis-structure-property Relationships and Data-driven Discovery. *Science* **2022,** *376* (6589), eabn3103.

2. Glasscott, M. W.; Pendergast, A. D.; Goines, S.; Bishop, A. R.; Hoang, A. T.; Renault, C.; Dick, J. E., Electrosynthesis of High-entropy Metallic Glass Nanoparticles for Designer, Multi-functional Electrocatalysis. *Nat. Commun.* **2019,** *10* (1), 2650.

3. Yao, Y.; Huang, Z.; Xie, P.; Lacey, S. D.; Jacob, R. J.; Xie, H.; Chen, F.; Nie, A.; Pu, T.; Rehwoldt, M.; Yu, D.; Zachariah, M. R.; Wang, C.; Shahbazian-Yassar, R.; Li, J.; Hu, L., Carbothermal Shock Synthesis of High-entropy-alloy Nanoparticles. *Science* **2018,** *359* (6383), 1489-1494.

4. Chen, P.-C.; Liu, X.; Hedrick, J. L.; Xie, Z.; Wang, S.; Lin, Q.-Y.; Hersam, M. C.; Dravid, V. P.; Mirkin, C. A., Polyelemental Nanoparticle Libraries. *Science* **2016,** *352* (6293), 1565-1569.

5. Kumar, N.; Tiwary, C. S.; Biswas, K., Preparation of Nanocrystalline High-entropy Alloys via Cryomilling of Cast Ingots. *J. Mater. Sci.* **2018,** *53* (19), 13411-13423.

6. Gao, S.; Hao, S.; Huang, Z.; Yuan, Y.; Han, S.; Lei, L.; Zhang, X.; Shahbazian-Yassar, R.; Lu, J., Synthesis of High-entropy Alloy Nanoparticles on Supports by the Fast Moving Bed Pyrolysis. *Nat. Commun.* **2020,** *11* (1), 2016.

7. Mori, K.; Hashimoto, N.; Kamiuchi, N.; Yoshida, H.; Kobayashi, H.; Yamashita, H., Hydrogen Spillover-driven Synthesis of High-entropy Alloy Nanoparticles as a Robust Catalyst for CO_2 Hydrogenation. *Nat. Commun.* **2021,** *12* (1), 3884.

8. Qiao, H.; Saray, M. T.; Wang, X.; Xu, S.; Chen, G.; Huang, Z.; Chen, C.; Zhong, G.; Dong, Q.; Hong, M.; Xie, H.; Shahbazian-Yassar, R.; Hu, L., Scalable Synthesis of High Entropy Alloy Nanoparticles by Microwave Heating. *ACS Nano* **2021,** *15* (9), 14928-14937.

9. Zhu, G.; Jiang, Y.; Yang, H.; Wang, H.; Fang, Y.; Wang, L.; Xie, M.; Qiu, P.; Luo, W. Constructing Structurally Ordered High-Entropy Alloy Nanoparticles on Nitrogen-Rich Mesoporous Carbon Nanosheets for High-Performance Oxygen Reduction. *Adv. Mater.* **2022**, *34* (15), e2110128.

10. Cao, G.; Liang, J.; Guo, Z.; Yang, K.; Wang, G.; Wang, H.; Wan, X.; Li, Z.; Bai, Y.; Zhang, Y.; Liu, J.; Feng, Y.; Zheng, Z.; Lu, C.; He, G.; Xiong, Z.; Liu, Z.; Chen, S.; Guo, Y.; Zeng, M.; Lin, J.; Fu, L. Liquid Metal for High-Entropy Alloy Nanoparticles Synthesis. *Nature* **2023**, *619* (7968), 73-77.

11. Hashimoto, N.; Mori, K.; Yamashita, H. In Situ Investigation on the Formation Mechanism of High-Entropy Alloy Nanoparticles Induced by Hydrogen Spillover. *J. Phys. Chem. C*, **2023**, *127* (42), 20786-20793.

12. Kar, N.; McCoy, M.; Wolfe, J.; Bueno, S. L. A.; Shafei, I. H.; Skrabalak, S. E. Retrosynthetic Design of Core–Shell Nanoparticles for Thermal Conversion to Monodisperse High-Entropy Alloy Nanoparticles. *Nat. Synth.* **2024**, *3* (2), 175-184.

13. Kang, Y.; Cretu, O.; Kikkawa, J.; Kimoto, K.; Nara, H.; Nugraha, A. S.; Kawamoto, H.; Eguchi, M.; Liao, T.; Sun, Z.; Asahi, T.; Yamauchi, Y. Mesoporous Multimetallic Nanospheres with Exposed Highly Entropic Alloy Sites. *Nat. Commun.* **2023**, *14* (1), 4182.

14. Sarkar, A.; Velasco, L.; Wang, D.; Wang, Q.; Talasila, G.; de Biasi, L.; Kubel, C.; Brezesinski, T.; Bhattacharya, S. S.; Hahn, H.; Breitung, B., High Entropy Oxides for Reversible Energy Storage. *Nat. Commun.***2018,** *9* (1), 3400.

15. Wang, T.; Chen, H.; Yang, Z.; Liang, J.; Dai, S., High-Entropy Perovskite Fluorides: A New Platform for Oxygen Evolution Catalysis. *J. Am. Chem. Soc.* **2020,** *142* (10), 4550-4554.

16. McCormick, C. R.; Schaak, R. E., Simultaneous Multication Exchange Pathway to High-Entropy Metal Sulfide Nanoparticles. *J. Am. Chem. Soc.* **2021**, *143* (2), 1017-1023.

17. Sure, J.; Sri Maha Vishnu, D.; Kim, H. K.; Schwandt, C., Facile Electrochemical Synthesis of Nanoscale (TiNbTaZrHf)C High-Entropy Carbide Powder. *Angew. Chem., Int. Ed.* **2020,** *59* (29), 11830-11835.

18. Jin, T.; Sang, X.; Unocic, R. R.; Kinch, R. T.; Liu, X.; Hu, J.; Liu, H.; Dai, S., Mechanochemical-Assisted Synthesis of High-Entropy Metal Nitride via a Soft Urea Strategy. *Adv. Mater.* **2018,** *30* (23), e1707512.

19. Yi, G.; Ding, Y.; Cheng, Y.; Zhang, P.; Wang, X.; Liang, X., Development and Oxidation Behavior of High Entropy Silicide (NbMoTaWV)Si$_2$ Coatings on NbMoTaWV Alloy. *J. Alloys Compd.* **2022,** *916*, 165384

20. Dong, S.; Li, Q.; Hu, H.; Zhang, X.; Li, Y.; Ye, K.; Hou, W.; He, J.; Zhao, H., Application of Rare-Earth High Entropy Boride in Electrocatalytic Hydrogen Evolution Reaction. *Appl. Surf. Sci.* **2023,** *615*, 156413

21. Soliman, S. S.; Dey, G. R.; McCormick, C. R.; Schaak, R. E. Temporal Evolution of Morphology, Composition, and Structure in the Formation of Colloidal High-Entropy Intermetallic Nanoparticles. *ACS Nano* **2023**, *17* (16), 16147-16159.

22. Folgueras, M. C.; Jiang, Y.; Jin, J.; Yang, P. High-Entropy Halide Perovskite Single Crystals Stabilized by Mild Chemistry. *Nature* **2023**, *621* (7978), 282-288.

23. Shi, X. L.; Zou, J.; Chen, Z. G., Advanced Thermoelectric Design: From Materials and Structures to Devices. *Chem. Rev.* **2020,** *120* (15), 7399-7515.

24. Rabie, M. A.; Mirza, S.; Hu, Y.; Haddara, Y. M., Cobalt Germanide Contacts: Growth Reaction, Phase Formation Models, and Electrical Properties. *J. Mater. Sci. Mater. Electron.* **2019,** *30* (11), 10031-10063.

25. Götsch, T.; Stöger-Pollach, M.; Thalinger, R.; Penner, S., The Nanoscale Kirkendall Effect in Pd-Based Intermetallic Phases. *J. Phys. Chem. C* **2014,** *118* (31), 17810-17818.

26. Vaughn, D. D.; Sun, D.; Moyer, J. A.; Biacchi, A. J.; Misra, R.; Schiffer, P.; Schaak, R. E., Solution-Phase Synthesis and Magnetic Properties of Single-Crystal Iron Germanide Nanostructures. *Chem. Mater.* **2013,** *25* (21), 4396-4401.

27. Yan, C.; Higgins, J. M.; Faber, M. S.; Lee, P. S.; Jin, S., Spontaneous Growth and Phase Transformation of Highly Conductive Nickel Germanide Nanowires. *ACS Nano* **2011,** *5* (6), 5006-5014.

28. Yoon, H.; Seo, K.; Bagkar, N.; In, J.; Park, J.; Kim, J.; Kim, B., Vertical Epitaxial Co$_5$Ge$_7$ Nanowire and Nanobelt Arrays on A Thin Graphitic Layer for Flexible Field Emission Displays. *Adv. Mater.* **2009,** *21* (48), 4979-4982.

29. Peng, W.; Chanakian, S.; Zevalkink, A., Crystal Chemistry and Thermoelectric Transport of Layered AM$_2$X$_2$compounds. *Inorg. Chem. Front.* **2018,** *5* (8), 1744-1759.

30. Yoon, H.; Kang, T.; Lee, J. M.; Kim, S.-i.; Seo, K.; Kim, J.; Park, W. I.; Kim, B., Epitaxially Integrating Ferromagnetic Fe$_{1.3}$Ge Nanowire Arrays on Few-Layer Graphene. *J. Phys.Chem. Lett.* **2011,** *2* (9), 956-960.

31. Tang, J.; Wang, C.-Y.; Xiu, F.; Lang, M.; Chu, L.-W.; Tsai, C.-J.; Chueh, Y.-L.; Chen, L.-J.; Wang, K. L., Oxide-Confined Formation of Germanium Nanowire Heterostructures for High-Performance Transistors. *ACS Nano* **2011,** *5* (7), 6008-6015.

32. Mao, J.; Kim, H. S.; Shuai, J.; Liu, Z.; He, R.; Saparamadu, U.; Tian, F.; Liu, W.; Ren, Z., Thermoelectric Properties of Materials Near the Band Crossing Line in Mg$_2$Sn–Mg$_2$Ge–Mg$_2$Si system. *Acta Mater.* **2016,** *103*, 633-642.

33. Zhang, R. Z.; Gucci, F.; Zhu, H.; Chen, K.; Reece, M. J., Data-Driven Design of Ecofriendly Thermoelectric High-Entropy Sulfides. *Inorg Chem* **2018,** *57* (20), 13027-13033.

34. Fan, Z.; Wang, H.; Wu, Y.; Liu, X. J.; Lu, Z. P., Thermoelectric High-Entropy Alloys with Low Lattice Thermal Conductivity. *RSC Adv.* **2016,** *6* (57), 52164-52170.

35. Ni, C.; O'Connor, K. M.; Trach, J.; Butler, C.; Rieger, B.; Veinot, J. G. C., Facile Synthesis of High-Entropy Alloy Nanoparticles on Germanane, Ge Nanoparticles and Wafers. *Nanoscale Horiz。* **2023,** *8* (9), 1217-1225.

36. Song, B.; Yang, Y.; Rabbani, M.; Yang, T. T.; He, K.; Hu, X.; Yuan, Y.; Ghildiyal, P.; Dravid, V. P.; Zachariah, M. R.; Saidi, W. A.; Liu, Y.; Shahbazian-Yassar, R., In Situ Oxidation Studies of High-Entropy Alloy Nanoparticles. *ACS Nano* **2020,** *14* (11), 15131-15143.

37. Anderson, S. L.; Luber, E. J.; Olsen, B. C.; Buriak, J. M., Substance over Subjectivity: Moving beyond the Histogram. *Chem. Mater.* **2016,** *28* (17), 5973-5975.

38. NIST X-ray Photoelectron Spectroscopy Database, NIST Standard Reference Database Number 20, National Institute of Standards and Technology, Gaithersburg MD, 20899 (2000).

39. Yu, H.; Helbich, T.; Scherf, L. M.; Chen, J.; Cui, K.; Fässler, T. F.; Rieger, B.; Veinot, J. G. C., Radical-Initiated and Thermally Induced Hydrogermylation of Alkenes on the Surfaces of Germanium Nanosheets. *Chem. Mater.* **2018,** *30* (7), 2274-2280.

40. Mukherjee, S.; Nag, A.; Kocevski, V.; Santra, P. K.; Balasubramanian, M.; Chattopadhyay, S.; Shibata, T.; Schaefers, F.; Rusz, J.; Gerard, C.; Eriksson, O.; Segre C. U.; Sarma, D. D., Microscopic Description of the Evolution of the Local Structure and an Evaluation of the Chemical Pressure Concept in a Solid Solution *Phys. Rev. B*, **2014**, *89* (22), 224105.

41. Nalam, P. G.; Das, D.; Tan, S.; Ramana, C. V., Controlled Phase Stabilization Enabled Tunable Optical Properties of Nanocrystalline GeO$_2$ Films. *ACS Appl. Electron. Mater.* **2022,** *4* (6), 3115-3124.

42. Holzwarth, U.; Gibson, N., The Scherrer Equation Versus the 'Debye-Scherrer equation'. *Nat. Nanotechnol.* **2011,** *6* (9), 534-534.

43. Bianco, E.; Butler, S.; Jiang, S.; Restrepo, O. D.; Windl, W.; Goldberger, J. E., Stability and Exfoliation of Germanane: A Germanium Graphane Analogue. *ACS Nano* **2013,** *7* (5), 4414-4421.

44. Yu, H.; Thiessen, A. N.; Hossain, M. A.; Kloberg, M. J.; Rieger, B.; Veinot, J. G. C., Thermally Induced Dehydrogenative Coupling of Organosilanes and H-Terminated Silicon Quantum Dots onto Germanane Surfaces. *Chem. Mater.* **2020**, *32* (11), 4536-4543.

45.   Bueno, S. L. A.; Leonardi, A.; Kar, N.; Chatterjee, K.; Zhan, X.; Chen, C.; Wang, Z.; Engel, M.; Fung, V.; Skrabalak, S. E. Quinary, Senary, and Septenary High Entropy Alloy Nanoparticle Catalysts from Core@Shell Nanoparticles and the Significance of Intraparticle Heterogeneity. *ACS Nano* **2022**, *16* (11), 18873-18885.

46.   Smith, E. M.; Streyer, W. H.; Nader, N.; Vangala, S.; Grzybowski, G.; Soref, R.; Wasserman, D.; Cleary, J. W. Metal Germanides for Practical on-Chip Plasmonics in the Mid Infrared. *Opt. Mater. Express,* **2018**, *8* (4), 968-982

47.   Beekman, M.; Kauzlarich, S. M.; Doherty, L.; Nolas, G. S. Zintl Phases as Reactive Precursors for Synthesis of Novel Silicon and Germanium-Based Materials. *Materials (Basel)* **2019**, *12* (7), 1139.

48.   Su, L.; Chen, X.; Xu, L.; Eldred, T.; Smith, J.; DellaRova, C.; Wang, H.; Gao, W., Visualizing the Formation of High-Entropy Fluorite Oxides from an Amorphous Precursor at Atomic Resolution. *ACS Nano* **2022,** *16* (12), 21397-21406.

49.   Patterson, A. L., The Scherrer Formula for X-Ray Particle Size Determination. *Phys. Rev.* **1939,** *56* (10), 978-982.

50.   Okada, Y.; Tokumaru, Y., Precise determination of lattice parameter and thermal expansion coefficient of silicon between 300 and 1500 K. *J. Appl. Phys.* **1984,** *56* (2), 314-320.

51.   Ni, C.; Chevalier, M.; Veinot, J. G. C. Metal nanoparticle-decorated germanane for selective photocatalytic aerobic oxidation of benzyl alcohol. *Nanoscale. Adv.* **2022**, *5* (1), 228-236.

52.   El Hajraoui, K.; Luong, M. A.; Robin, E.; Brunbauer, F.; Zeiner, C.; Lugstein, A.; Gentile, P.; Rouviere, J. L.; Den Hertog, M., In Situ Transmission Electron Microscopy Analysis of Aluminum-Germanium Nanowire Solid-State Reaction. *Nano. Lett.* **2019,** *19* (5), 2897-2904.

53.   El Hajraoui, K.; Robin, E.; Zeiner, C.; Lugstein, A.; Kodjikian, S.; Rouviere, J. L.; Den Hertog, M., In Situ Transmission Electron Microscopy Analysis of Copper-Germanium Nanowire Solid-State Reaction. *Nano. Lett.* **2019,** *19* (12), 8365-8371.

5. Chapter 5: Summary and Outlook

5.1 Summary

High-entropy materials have demonstrated considerable potential for a range of emerging energy-related processes and seem particularly well-suited for catalysis and thermoelectric applications.[1] The compositional flexibility of high-entropy materials enables fine-tuning of needed functionalities. The aim of the research outlined in this Thesis was to explore germanium-based nanostructures for the synthesis of high-entropy alloy nanoparticles and compounds.

Chapter 1 gave a brief introduction to the basic principles of high-entropy alloys, nanoparticles and compounds. The chapter describes the first discovery of high-entropy alloys and briefly discusses their properties. The reduction in size of high-entropy alloys to the nanoscale for catalytic applications results in a synergistic effect and, even in a relatively short time, has garnered significant attention. The synthesis of high-entropy alloy nanoparticles was subsequently introduced, with a focus on the pivotal concept of rapid heating and cooling. A comprehensive compilation of high-entropy functional compounds, encompassing oxides, carbides, nitrides, borides, silicides, sulfides and halides was also incorporated into this Chapter. Finally, the chapter concludes by describing in detail two categories of germanium nanostructures, namely nanoparticles and nanosheets, along with a detailed discussion of their respective synthetic methodologies.

Chapter 2 presents a facile method for introducing a variety of adherent metal nanoparticles (Au, Ag, Cu, Pd, Pt) to the surfaces of GeNSs. XRD and XPS analyses confirm that the GeNS structure remained intact during the deposition process and metal nanoparticles were formed.

Further to this, TEM studies revealed the morphology of the M@GeNSs and showed the metal nanoparticles were distributed over the entire GeNS surface. The presented materials were subsequently investigated as photocatalysts for the selective visible light-induced oxidation of benzyl alcohol to benzaldehyde. The M@GeNSs possess a higher conversion efficiency compared to a mixture of freestanding metal nanoparticles prepared via solution reduction and GeNSs. The direct linking metal nanoparticles to GeNSs in M@GeNSs strongly favors the production of benzaldehyde and is a clear demonstration of a synergistic effect. Thin films of metal-decorated GeNSs prepared via dropcasting provide for convenient catalyst recovery and recyclability, an important consideration in possible catalytic applications of this type of system.

Chapter 3 describes the deposition of high-entropy alloy nanoparticles (HEA NPs) onto the surfaces of germanane, germanium nanoparticles (GeNPs) and bulk Ge via a surface-mediated reduction. Techniques such as XRD, FTIR, XPS, and TEM confirmed their structure, composition, and morphology. After deposition, freestanding HEA NPs can be successfully liberated from the GeNSs via UV light irradiation; the resulting NPs maintain their single-phase solid solution structure after liberation. This methodology was extended to both hydrogen-terminated Ge nanoparticles and Ge (100) wafers with similar results.

Chapter 4 introduces a method for preparing two types of high-entropy germanide (HEG: AuAgCuPdPtGe and FeCoNiCrVGe) using a rapid thermal annealing process. The synthesis of the HEGs was verified by XRD and XPS, which provided evidence of the desired elements and their oxidation states. TEM analysis further revealed that the HEGs possessed a near equal composition of all the alloy elements and exhibited a homogenous distribution throughout the material. The formation and growth mechanisms of the HEGs was studied using *in situ* heating XRD and TEM experiments. The observed HEG formation involved the initial decomposition of

160

germanane (GeNSs) occurring below 300 °C, followed by a gradual grain growth via atom diffusion at temperatures below 600 °C. A rapid grain growth process was then seen to occur at elevated temperatures.

5.2 Future Work

5.2.1 Microwave-Assisted Synthesis of Mesoporous High-Entropy Alloy Nanoparticles Using F127 as Soft Template

As introduced in Chapter 1, the synthesis of mesoporous HEA NPs has been achieved by wet chemistry methods.[2] The mesoporous nanoparticles exhibited a core-shell structure with a Pd-rich core and Rh/Ru-rich shell that resulted differences in reduction order during the prolonged heating.[2] The use of microwave heating for the preparation of nanomaterials has become increasingly popular over the past decade.[3] Its unique attributes, including rapid heating and the minimization of temperature gradients, have been shown to accelerate reaction rates and facilitate the synthesis of high-entropy alloy nanoparticles.[4] In a study not reported in this Thesis, we employed microwave heating to synthesize mesoporous HEA NPs (RhAgCuPdPt) with the aim of reducing the reaction time. The synthesis used F127 and L-AA as pore-directing and reducing agents, respectively. In a typical synthesis, F127 was dissolved in 0.8 mL DMF with continuous stirring in a 20 mL microwave tube. Aqueous solutions of metal precursors, in the desired ratio, and L-AA were added to initiate micellization. The tube was sealed and placed in the microwave reactor (Biotage Initiator). With vigorous stirring, the mixture was heated to 130 °C in 1 min and then held for 1 min at this temperature, after which it was rapidly cooled to 55 °C. The final mesoporous HEA NPs were collected by centrifugation, and the micelles were washed with

acetone/water several times. It is important to note that the overall reaction time (ramping and heating time) was reduced to two minutes.
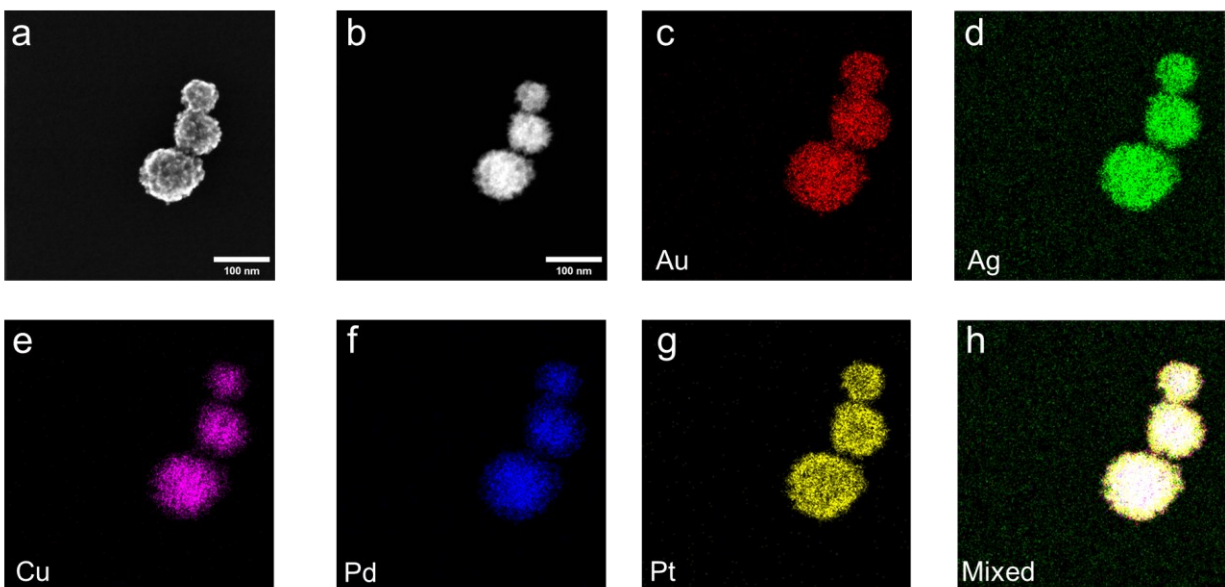
Figure 5.1. TEM and EDX analysis of mesoporous HEA NPs. (a) SE-STEM image, (b) HAADF-STEM image and (c-h) corresponding EDX mapping of the indicated elements.

Electron microscopy was used to study the morphology of mesoporous HEA NPs. Secondary electron scanning transmission electron microscopy (SE-STEM) image (Figure 5.1a) and high-angle annular dark-field scanning transmission electron microscopy (HAADF-STEM) image (Figure 5.1b) showed mesoporous morphologies and energy dispersive X-ray (EDX) mapping confirmed the co-localization of all metals in the morphological features in SE- and HAADF-STEM (Figures 5.1c-h).

XPS was used to investigate the elemental composition and oxidation states of the resulting mesoporous HEA NPs. The high-resolution spectra of each metal within the NPs exhibited characteristic metallic state (Figure 5.2a-e), including Rh $3d_{5/2}$, 307.6 eV; Ag $3d_{5/2}$, 368.0 eV; Cu $2p_{3/2}$, 932.1 eV; Pd $3d_{5/2}$, 335.0 eV; Pt $4f_{7/2}$, 71.0 eV. XRD pattern (Figure 5.2f) indicates the

mesoporous HEA NPs display a characteristic face-centred cubic structure as evidence by (111), (200), (220) and (311) reflections appearing at 39.5°, 45.9°, 67.2° and 81.1°, respectively.
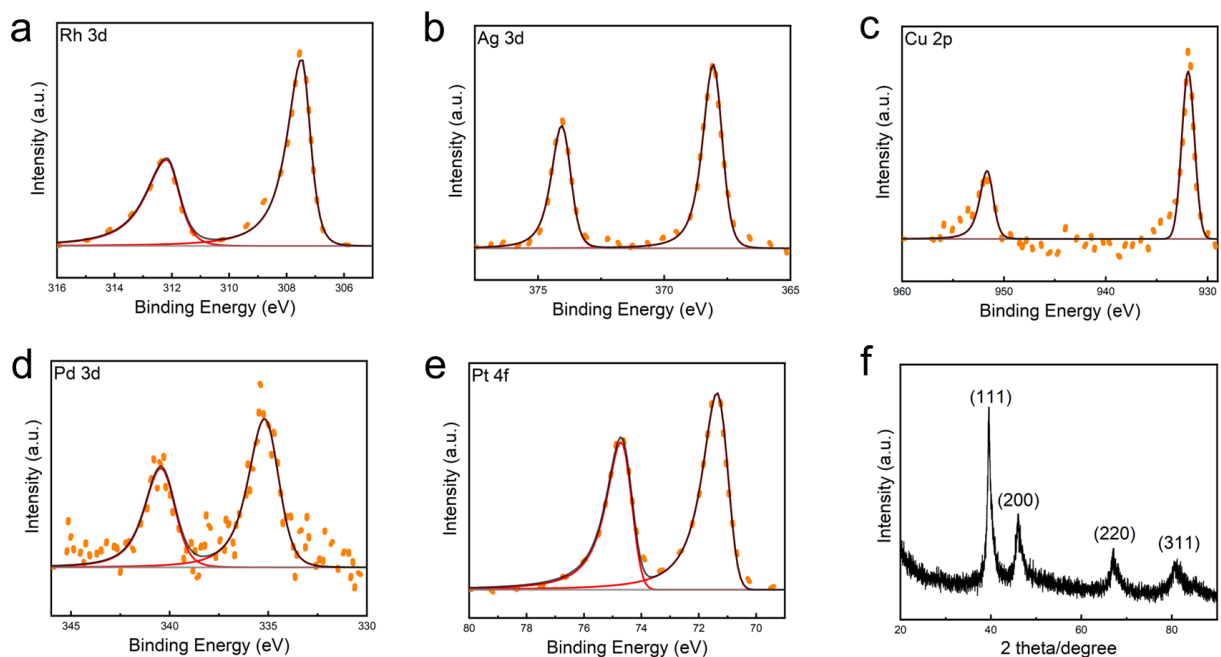
Figure 5.2. Representative high-resolution XP spectra of mesoporous HEA NPs: (a) Rh 3d, (b) Ag 3d, (c) Cu 2p, (d) Pd 3d and (e) Pt 4f regions. (f) XRD pattern of mesoporous HEA NPs.

5.2.2 Synthesis of Mesoporous High-Entropy Alloy Nanoparticles Using KIT-6 as Hard Template

The hard-templating method uses inorganic materials, such as ordered mesoporous silicas, as rigid templates in the synthesis of mesoporous nanomaterials. This method utilizes a carefully controlled nano-casting process to replicate the shape and structure of the hard templates.[5] Korea Advanced Institute of Science and Technology-6 (KIT-6) is an example of commercially available ordered mesoporous silica used in the synthesis of mesoporous metal nanostructures.[6] In our hands, KIT-6 can be used as a suitable hard template for the synthesis of mesoporous HEA NPs; a description of results not reported in this Thesis is as follows. The HEA NPs/KIT-6 composite is

typically obtained through a direct nano-casting process, wherein HEA NPs (AuRhCuPdPt) are introduced within ordered mesoporous KIT-6. The scaffold is then removed by using HF resulting in the liberation of mesoporous HEA NPs.

SE-STEM (Figure 5.3a) and HAADF-STEM images (Figure 5.3b) illustrate the mesoporous silica morphology. Within this structure, HEA NPs are observed to have propagated within the mesopores, with some nanoparticles extending beyond the confines of the mesoporous framework. EDX mapping provides additional corroboration by revealing the co-localization of HEA NPs and silica in both SE- and HAADF-STEM images (Figures 5.3c-j) and shows the successful integration of HEA NPs within the mesoporous silica matrix.
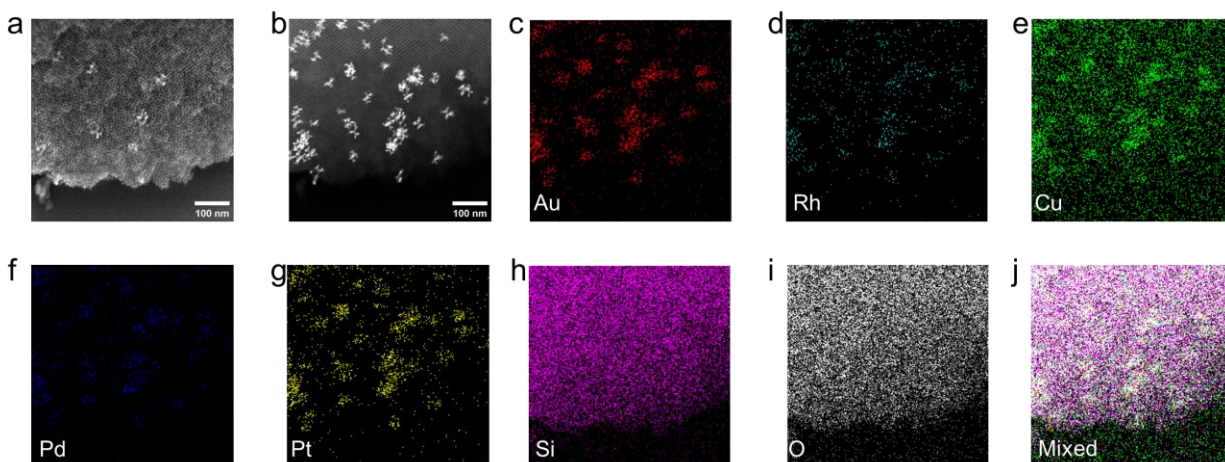
Figure 5.3. TEM and EDX analysis of HEA NPs/KIT-6. (a) SE-STEM image, (b) HAADF-STEM image and (c-j) corresponding EDX mapping of the indicated elements.
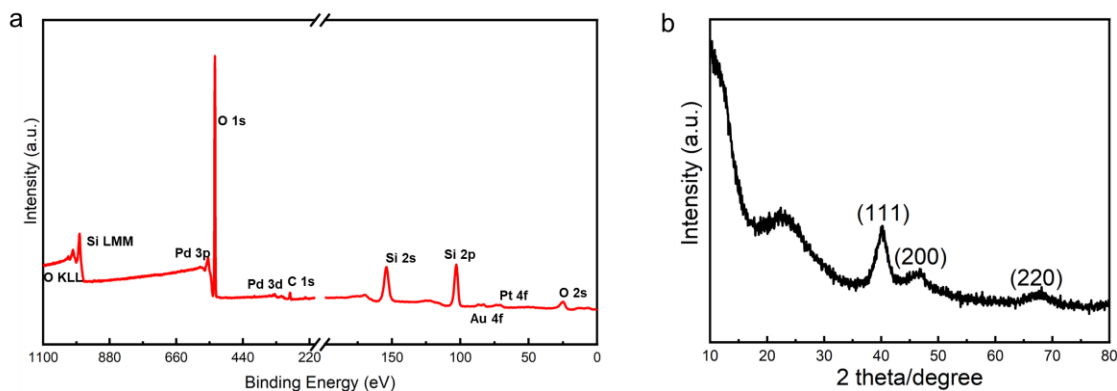
Figure 5.4. (a) Representative survey XP spectrum and (b) XRD patterns of HEA NPs/KIT-6.

The survey XP spectrum of HEA NPs/KIT-6 (Figure 5.4a) showed prominent Si (30.1 atom %) and O (60.1 atom %) emission consistent with the composition of SiO_2. O Notably, minimal emissions of Pd, Au, and Pt (0.2 atom %) were observed in the spectrum suggesting that the majority of the HEA NPs were located within the silica pore rather than the surface. XRD pattern (Figure 5.4b) revealed (111), (200) and (220) reflections characteristic of HEA NPs superimposed on the reflection from 20° to 30° arising from amorphous silica template.[5]
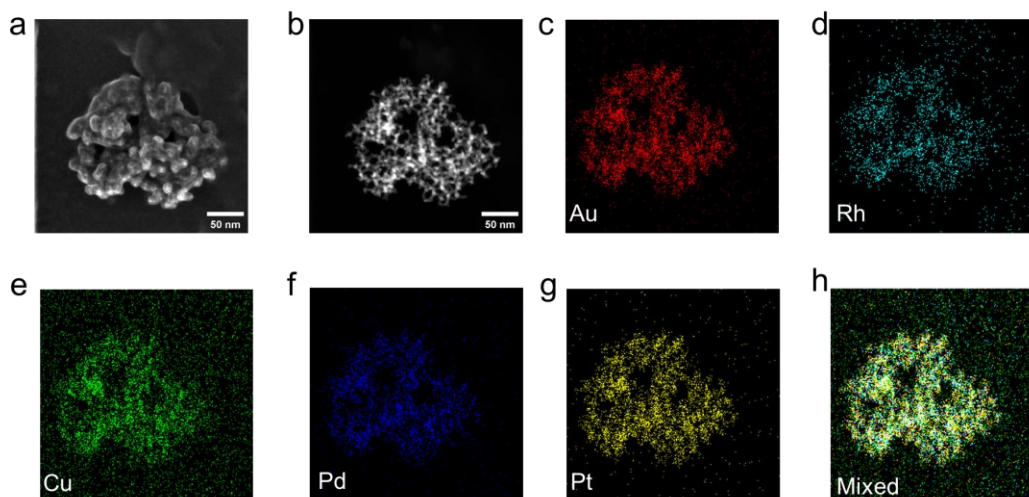
Figure 5.5. TEM and EDX analysis of mesoporous HEA NPs. (a) SE-STEM image, (b) HAADF-STEM image and (c-h) corresponding EDX mapping of the indicated elements.

After the removal of KIT-6 template via HF etching, SE-STEM (Figure 5.5a) and HAADF-STEM images (Figure 5.5b) displayed the mesoporous channel of the HEA NPs corresponding to the pores of removed KIT-6. SE-STEM was less definitive in this regard due to the electron beam induced deposition of carbon.[7] EDX mapping further confirmed the co-localization of morphological features in SE-STEM and HAADF-STEM comprise the target metal (Figures 5.5c-h).

The high-resolution XP spectra of each metal (Figure 5.6) showed emissions at binding energies characteristic of the corresponding metallic state (i.e., Au $4f_{7/2}$, 83.7 eV; Rh $3d_{5/2}$, 307.7 eV; Cu $2p_{3/2}$, 931.8 eV; Pd $3d_{5/2}$, 335.2 eV; Pt $4f_{7/2}$, 70.9 eV). XRD pattern (Figure 5.6f) display a characteristic face-centred cubic structure as evidence by (111), (200), and (220) reflections appearing at 40.1°, 46.7°, and 67.7° respectively, indicating the successful liberation of the HEA NPs from the KIT-6 template.
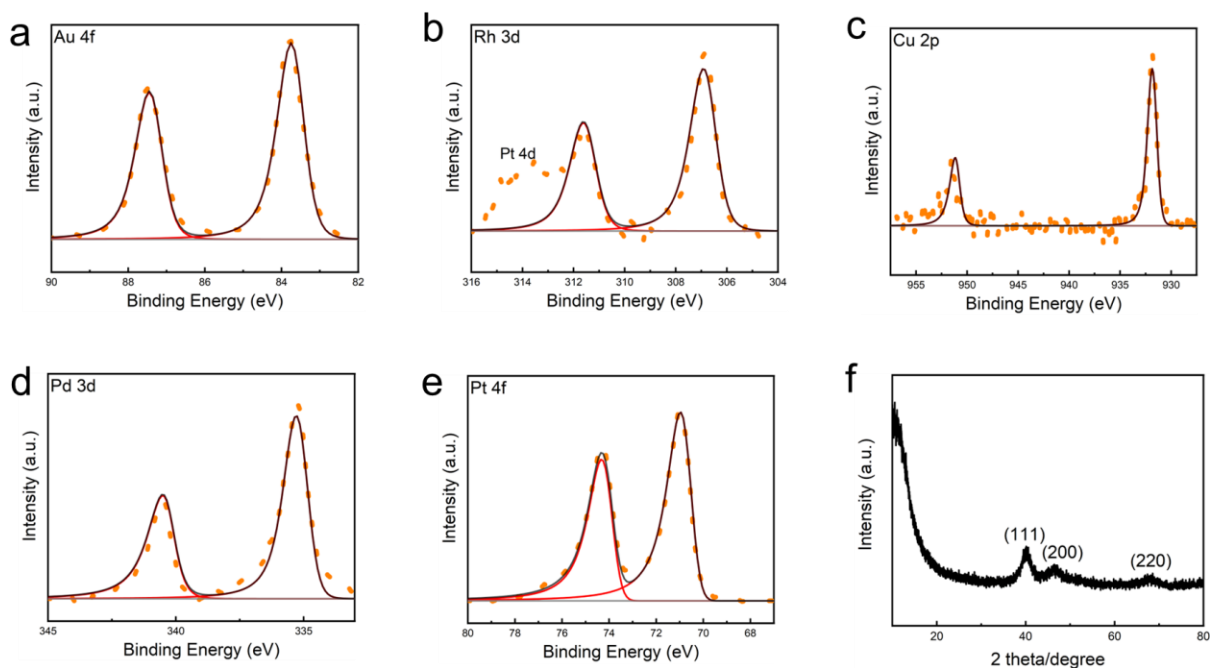
Figure 5.6. Representative high-resolution XP spectra of mesoporous HEA NPs: (a) Au 4f, (b) Rh 3d, (c) Cu 2p, (d) Pd 3d and (e) Pt 4f regions. (f) XRD pattern of mesoporous HEA NPs.

166

5.2.3 Synthesis of Mesoporous High-Entropy Alloy Nanoparticles Using SBA-15 as Hard Template

Santa Barbara Amorphous-15 (SBA-15) represents another example of ordered mesoporous silica.[8] This commercial material is characterized by a structurally hexagonal configuration and has also found application in the synthesis of mesoporous metal nanostructures.[9] In a parallel manner to the utilization of KIT-6, SBA-15 was employed as a hard template for the synthesis of mesoporous HEA NPs (AuRhCuPdPt). This approach leverages the well-defined mesoporous structure of SBA-15 to impart organization and structural characteristics to the synthesized mesoporous HEA NPs, demonstrating the versatility of ordered mesoporous silicas in nanomaterial synthesis methodologies.
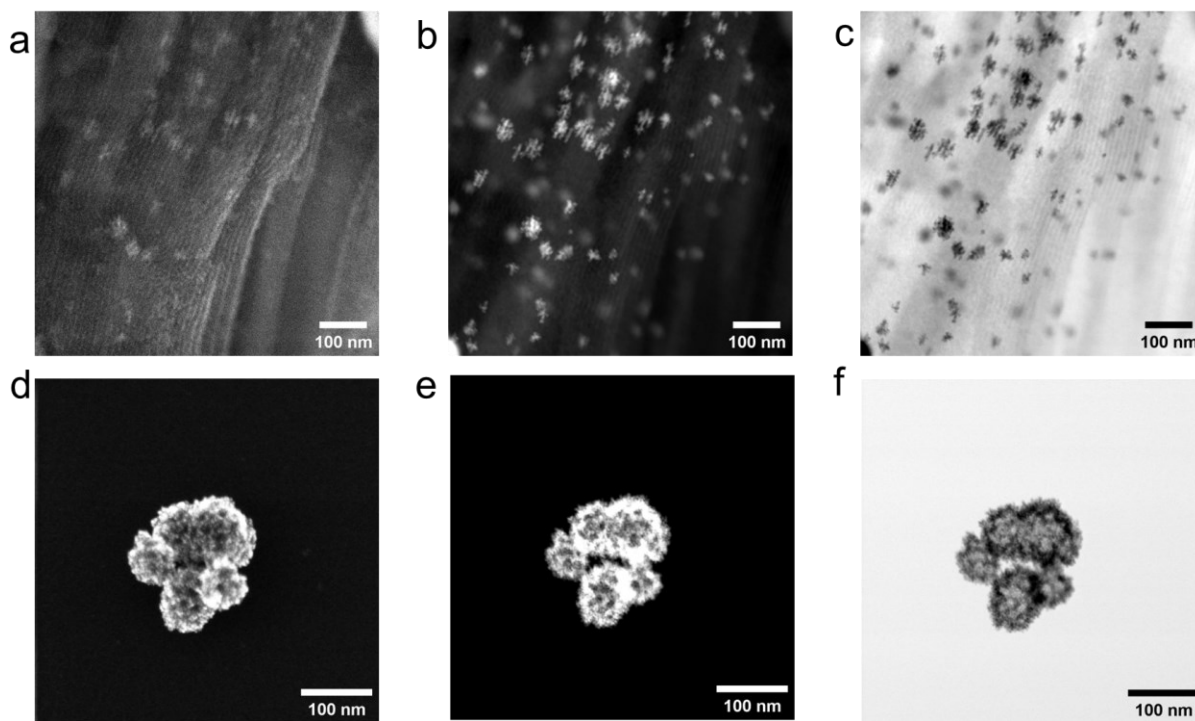
Figure 5.7. (a) SE-, (b) HAADF- and (c) BF-STEM images of HEA NPs/SBA-15. (d) SE-STEM, (e) HAADF-STEM and (f) BF-STEM images of mesoporous HEA NPs after the removal of SBA-15.

STEM was used to investigate the morphology of mesoporous HEA NPs before and after the removal of SBA-15 template (Figure 5.7). The differences between SE-, HAADF- and BF-STEM images suggested that a significant portion of the HEA NPs was situated within the mesopores of the SBA-15 template. After template removal, STEM images reveal the mesoporous characteristics of the HEA NPs, with no residual template evident. EDX mapping provided additional validation and was particularly pertinent with respective to the elemental composition and spatial alignment. Observations reinforced the premise that the mesoporous structure aws effectively maintained, further supporting the successful synthesis and template removal process.
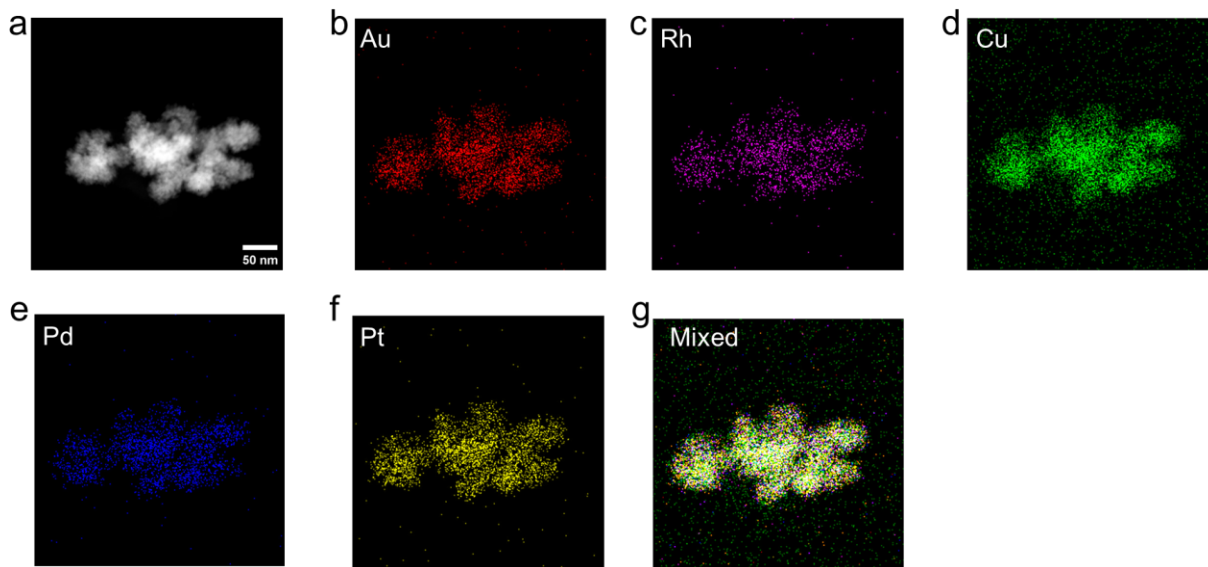
Figure 5.8. TEM and EDX analysis of mesoporous HEA NPs. (a) HAADF-STEM image and (b-g) corresponding EDX mapping of the indicated elements.

The high-resolution XP spectra obtained for each metal species (Figure 5.9) exhibited distinct emission peaks corresponding to the binding energies inherent to their metallic states. Specifically, the Au $4f_{7/2}$ emission at 84.1 eV, the Rh $3d_{5/2}$ emission at 307.4 eV, the Cu $2p_{3/2}$ emission at 932.5 eV, the Pd $3d_{5/2}$ emission at 335.6 eV, and the Pt $4f_{7/2}$ emission at 71.1 eV were all indicative of their respective metallic states. Furthermore, XRD pattern (Figure 5.9f) manifested

168

well-defined reflections at 40.1°, 46.7°, and 67.6°, corresponding to the (111), (200), and (220) reflections, respectively. These distinct diffraction peaks served as evidence for the successful liberation of the HEA NPs from the SBA-15 template.

The synthesized HEA NPs/silica composites can be used as the precursor to the high-entropy silicide (HES). Suni Guo will continue to explore the transformation of HEA NPs/silica composites to HES via magnesiothermic or aluminothermic reaction.
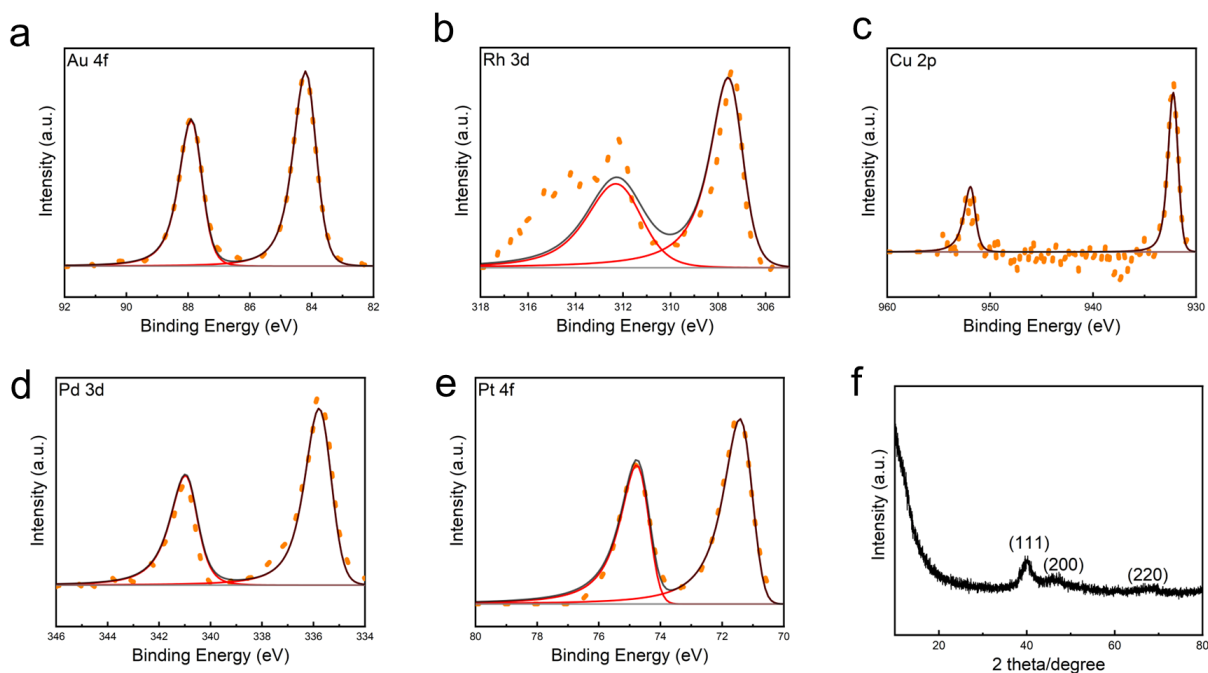
Figure 5.9. Representative high-resolution XP spectra of mesoporous HEA NPs: (a) Au 4f, (b) Rh 3d, (c) Cu 2p, (d) Pd 3d and (e) Pt 4f regions. (f) XRD pattern of mesoporous HEA NPs.

This Thesis provide tunable methods for the synthesis of high-entropy materials. In the future direction, this can be extended with the idea of engineering of new catalytic systems. Moreover, there remains a substantial need for an in-depth exploration of the applications of HEA NPs within the catalysis field. Particularly, the application of these nanomaterials in water splitting and CO_2 reduction systems. By elucidating the catalytic performance of HEA NPs in these specific

applications, valuable insights can be gained, paving the way for potential advancements in the development of sustainable and efficient catalytic systems.

Although current high-entropy materials (HEM) discoveries based on traditional trial and error method is possible, resulted-based driven HEM research is costly and slow. The discovery and synthesis of HEM would greatly benefit from the advancement of high-throughput synthesis and artificial intelligence (AI) assisted screening. The autonomous laboratory that integrates synthesis, characterization and optimization has successfully demonstrated discovery and synthesis of targeted small organic molecules, photocatalyst with multiobjective optimized reaction, lead-free perovskite thin films and air-stable inorganic compounds.[10-13] Recently, the development of disordered enthalpy-entropy descriptor (DEED), a descriptor that captures the balance between entropy gains and enthalpy costs, allowed the correct classification of functional synthesizability of high-entropy compounds and discovered new single-phase high-entropy carbonitrides and borides.[14] We can envision that the extension of DEED to other types of high-entropy materials and the combination of high-throughput synthesis enable further autonomous discovery of high-entropy materials with optimized composition and property.

5.3 References

1. Ma, Y.; Ma, Y.; Wang, Q.; Schweidler, S.; Botros, M.; Fu, T.; Hahn, H.; Brezesinski, T.; Breitung, B. High-Entropy Energy Materials: Challenges and New Opportunities. *Energy Environ. Sci.* **2021**, *14* (5), 2883-2905.
2. Kang, Y.; Cretu, O.; Kikkawa, J.; Kimoto, K.; Nara, H.; Nugraha, A. S.; Kawamoto, H.; Eguchi, M.; Liao, T.; Sun, Z.; Asahi, T.; Yamauchi, Y. Mesoporous Multimetallic Nanospheres with Exposed Highly Entropic Alloy Sites. *Nat. Commun.* **2023**, *14* (1), 4182.
3. Atkins, T. M.; Thibert, A.; Larsen, D. S.; Dey, S.; Browning, N. D.; Kauzlarich, S. M. Femtosecond Ligand/Core Dynamics of Microwave-Assisted Synthesized Silicon Quantum Dots in Aqueous Solution. *J. Am. Chem. Soc.* **2011** *133* (51), 20664-20667.
4. Qiao, H.; Saray, M. T.; Wang, X.; Xu, S.; Chen, G.; Huang, Z.; Chen, C.; Zhong, G.; Dong, Q.; Hong, M.; Xie, H.; Shahbazian-Yassar, R.; Hu, L. Scalable Synthesis of High Entropy Alloy Nanoparticles by Microwave Heating. *ACS Nano* **2021**, *15* (9), 14928-14937.
5. Peng, L.; Peng, H.; Li, W.; Zhao, D. Monomicellar Assembly to Synthesize Structured and Functional Mesoporous Carbonaceous Nanomaterials. *Nat. Protoc.* **2023**, *18* (4), 1155-1178.
6. Fang, J.; Zhang, L.; Li, J.; Lu, L.; Ma, C.; Cheng, S.; Li, Z.; Xiong, Q.; You, H. A General Soft-Enveloping Strategy in the Templating Synthesis of Mesoporous Metal Nanostructures. *Nat. Commun.* **2018**, *9* (1), 521.
7. Soong, C.; Woo, P.; Hoyle, D. Contamination Cleaning of TEM/SEM Samples with the ZONE Cleaner. *Microsc. Today* **2012**, *20* (6), 44-48.
8. Kleitz, F.; Choi, S. H.; Ryoo, R. Cubic *Ia3d* Large Mesoporous Silica: Synthesis and Replication to Platinum Nanowires, Carbon Nanorods and Carbon Nanotubes. *Chem. Commun.* **2003**, (17), 2136-2137.
9. Wang, H.; Jeong, H. Y.; Imura, M.; Wang, L.; Radhakrishnan, L.; Fujita, N.; Castle, T.; Terasaki, O.; Yamauchi, Y. Shape- and Size-Controlled Synthesis in Hard Templates: Sophisticated Chemical Reduction for Mesoporous Monocrystalline Platinum Nanoparticles. *J. Am. Chem. Soc.* **2011**, *133* (37), 14526-14529.
10. Coley, C. W.; Thomas, D. A., 3rd; Lummiss, J. A. M.; Jaworski, J. N.; Breen, C. P.; Schultz, V.; Hart, T.; Fishman, J. S.; Rogers, L.; Gao, H.; Hicklin, R. W.; Plehiers, P. P.; Byington, J.; Piotti, J. S.; Green, W. H.; Hart, A. J.; Jamison, T. F.; Jensen, K. F. A Robotic Platform for Flow Synthesis of Organic Compounds Informed by AI Planning. *Science* **2019**, *365* (6453), eaax1566.
11. Slattery, A.; Wen, Z.; Tenblad, P.; Sanjose-Orduna, J.; Pintossi, D.; den Hartog, T.; Noel, T. Automated Self-Optimization, Intensification, and Scale-up of Photocatalysis in Flow. *Science* **2024**, *383* (6681), eadj1817.
12. Sun, S.; Hartono, N. T. P.; Ren, Z. D.; Oviedo, F.; Buscemi, A. M.; Layurova, M.; Chen, D. X.; Ogunfunmi, T.; Thapa, J.; Ramasamy, S.; Settens, C.; DeCost, B. L.; Kusne, A. G.; Liu, Z.; Tian, S. I. P.; Peters, I. M.; Correa-Baena, J.-P.; Buonassisi, T. Accelerated Development of Perovskite-Inspired Materials via High-Throughput Synthesis and Machine-Learning Diagnosis. *Joule* **2019**, *3* (6), 1437-1451.
13. Szymanski, N. J.; Rendy, B.; Fei, Y.; Kumar, R. E.; He, T.; Milsted, D.; McDermott, M. J.; Gallant, M.; Cubuk, E. D.; Merchant, A.; Kim, H.; Jain, A.; Bartel, C. J.; Persson, K.;

Zeng, Y.; Ceder, G. An Autonomous Laboratory for the Accelerated Synthesis of Novel Materials. *Nature* **2023**, *624* (7990), 86-91.

14. Divilov, S.; Eckert, H.; Hicks, D.; Oses, C.; Toher, C.; Friedrich, R.; Esters, M.; Mehl, M. J.; Zettel, A. C.; Lederer, Y.; Zurek, E.; Maria, J. P.; Brenner, D. W.; Campilongo, X.; Filipovic, S.; Fahrenholtz, W. G.; Ryan, C. J.; DeSalle, C. M.; Crealese, R. J.; Wolfe, D. E.; Calzolari, A.; Curtarolo, S. Disordered Enthalpy-Entropy Descriptor for High-Entropy Ceramics discovery. *Nature* **2024**, *625* (7993), 66-73.

Bibliography

1. Martinón-Torres, M.; Valcárcel Rojas, R.; Sáenz Samper, J.; Guerra, M. F. Metallic Encounters in Cuba: The technology, exchange and meaning of metals before and after Columbus. *J. Anthropol. Archaeol.* **2012**, *31* (4), 439-454.

2. Nakaya, Y.; Furukawa, S. Catalysis of Alloys: Classification, Principles, and Design for a Variety of Materials and Reactions. *Chem. Rev.* **2023**, *123* (9), 5859-5947.

3. Yeh, J. W.; Chen, S. K.; Lin, S. J.; Gan, J. Y.; Chin, T. S.; Shun, T. T.; Tsau, C. H.; Chang, S. Y. Nanostructured High-Entropy Alloys with Multiple Principal Elements: Novel Alloy Design Concepts and Outcomes. *Adv. Eng. Mater.* **2004**, *6* (5), 299-303.

4. Cantor, B.; Chang, I. T. H.; Knight, P.; Vincent, A. J. B. Microstructural Development in Equiatomic Multicomponent Alloys. *Mater. Sci. Eng. A* **2004**, *375-377*, 213-218.

5. Senkov, O. N.; Wilks, G. B.; Miracle, D. B.; Chuang, C. P.; Liaw, P. K. Refractory High-Entropy Alloys. *Intermetallics* **2010**, *18* (9), 1758-1765.

6. Senkov, O. N.; Wilks, G. B.; Scott, J. M.; Miracle, D. B. Mechanical Properties of $Nb_{25}Mo_{25}Ta_{25}W_{25}$ and $V_{20}Nb_{20}Mo_{20}Ta_{20}W_{20}$ Refractory High Entropy Alloys. *Intermetallics* **2011**, *19* (5), 698-706.

7. Senkov, O. N.; Scott, J. M.; Senkova, S. V.; Miracle, D. B.; Woodward, C. F. Microstructure and Room Temperature Properties of a High-Entropy TaNbHfZrTi Alloy. *J. Alloys Compd.* **2011**, *509* (20), 6043-6048.

8. Sahlberg, M.; Karlsson, D.; Zlotea, C.; Jansson, U. Superior Hydrogen Storage in High Entropy Alloys. *Sci. Rep.* **2016**, *6*(1), 36770.

9. Karlsson, D.; Ek, G.; Cedervall, J.; Zlotea, C.; Moller, K. T.; Hansen, T. C.; Bednarcik, J.; Paskevicius, M.; Sorby, M. H.; Jensen, T. R.; Jansson, U.; Sahlberg, M. Structure and Hydrogenation Properties of a HfNbTiVZr High-Entropy Alloy. *Inorg. Chem.* **2018**, *57* (4), 2103-2110.

10. George, E. P.; Raabe, D.; Ritchie, R. O. High-entropy Alloys. *Nat. Rev. Mater.* **2019**, *4* (8), 515-534.

11. Xin, Y.; Li, S.; Qian, Y.; Zhu, W.; Yuan, H.; Jiang, P.; Guo, R.; Wang, L. High-Entropy Alloys as a Platform for Catalysis: Progress, Challenges, and Opportunities. *ACS Catal.* **2020**, *10* (19), 11280-11306.

12. Li, H.; Shin, K.; Henkelman, G. Effects of Ensembles, Ligand, and Strain on Adsorbate Binding to Alloy Surfaces. *J. Chem. Phys* **2018**, *149* (17), 174705.

13. Yao, Y.; Dong, Q.; Brozena, A.; Luo, J.; Miao, J.; Chi, M.; Wang, C.; Kevrekidis, I. G.; Ren, Z. J.; Greeley, J.; Wang, G.; Anapolsky, A.; Hu, L. High-entropy nanoparticles: Synthesis-structure-property relationships and data-driven discovery. *Science* **2022**, *376* (6589), eabn3103.

14. Yao, Y.; Huang, Z.; Xie, P.; Lacey, S. D.; Jacob, R. J.; Xie, H.; Chen, F.; Nie, A.; Pu, T.; Rehwoldt, M.; Yu, D.; Zachariah, M. R.; Wang, C.; Shahbazian-Yassar, R.; Li, J.; Hu, L. Carbothermal Shock Synthesis of High-entropy-alloy Nanoparticles. *Science* **2018**, *359* (6383), 1489-1494.

15. Gao, S.; Hao, S.; Huang, Z.; Yuan, Y.; Han, S.; Lei, L.; Zhang, X.; Shahbazian-Yassar, R.; Lu, J. Synthesis of High-entropy Alloy Nanoparticles on Supports by the Fast Moving Bed Pyrolysis. *Nat. Commun.* **2020**, *11* (1), 2016.

16. Feng, J.; Chen, D.; Pikhitsa, P. V.; Jung, Y.-h.; Yang, J.; Choi, M. Unconventional Alloys Confined in Nanoparticles: Building Blocks for New Matter. *Matter* **2020**, *3* (5), 1646-1663.

17. Yang, Y.; Song, B.; Ke, X.; Xu, F.; Bozhilov, K. N.; Hu, L.; Shahbazian-Yassar, R.; Zachariah, M. R. Aerosol Synthesis of High Entropy Alloy Nanoparticles. *Langmuir* **2020**, *36* (8), 1985-1992.

18. Mori, K.; Hashimoto, N.; Kamiuchi, N.; Yoshida, H.; Kobayashi, H.; Yamashita, H. Hydrogen Spillover-driven Synthesis of High-entropy Alloy Nanoparticles as a Robust Catalyst for CO_2 Hydrogenation. *Nat. Commun.* **2021**, *12* (1), 3884.

19. Qiao, H.; Saray, M. T.; Wang, X.; Xu, S.; Chen, G.; Huang, Z.; Chen, C.; Zhong, G.; Dong, Q.; Hong, M.; Xie, H.; Shahbazian-Yassar, R.; Hu, L. Scalable Synthesis of High Entropy Alloy Nanoparticles by Microwave Heating. *ACS Nano* **2021**, *15* (9), 14928-14937.

20. Bagot, P. A. J.; Kruska, K.; Haley, D.; Carrier, X.; Marceau, E.; Moody, M. P.; Smith, G. D. W. Oxidation and Surface Segregation Behavior of a Pt–Pd–Rh Alloy Catalyst. *J. Phys. Chem. C* **2014**, *118* (45), 26130-26138.

21. Fei, H.; Dong, J.; Wan, C.; Zhao, Z.; Xu, X.; Lin, Z.; Wang, Y.; Liu, H.; Zang, K.; Luo, J.; Zhao, S.; Hu, W.; Yan, W.; Shakir, I.; Huang, Y.; Duan, X. Microwave-Assisted Rapid Synthesis of Graphene-Supported Single Atomic Metals. *Adv. Mater.* **2018**, *30* (35), e1802146.

22. Ju, Z.; Qi, X.; Sfadia, R.; Wang, M.; Tseng, E.; Panchul, E. C.; Carter, S. A.; Kauzlarich, S. M. Single-Crystalline Germanium Nanocrystals Via a Two-Step Microwave-Assisted Colloidal Synthesis from GeI_4. *ACS Mater. Au* **2022**, *2* (3), 330-342.

23. Zhong, G.; Xu, S.; Cui, M.; Dong, Q.; Wang, X.; Xia, Q.; Gao, J.; Pei, Y.; Qiao, Y.; Pastel, G.; Sunaoshi, T.; Yang, B.; Hu, L. Rapid, High-Temperature, in Situ Microwave Synthesis of Bulk Nanocatalysts. *Small* **2019**, *15* (47), e1904881.

24. Renteria, J. D.; Ramirez, S.; Malekpour, H.; Alonso, B.; Centeno, A.; Zurutuza, A.; Cocemasov, A. I.; Nika, D. L.; Balandin, A. A. Strongly Anisotropic Thermal Conductivity of Free-Standing Reduced Graphene Oxide Films Annealed at High Temperature. *Adv. Funct. Mater*. **2015**, *25* (29), 4664-4672.

25. Bondesgaard, M.; Broge, N. L. N.; Mamakhel, A.; Bremholm, M.; Iversen, B. B. General Solvothermal Synthesis Method for Complete Solubility Range Bimetallic and High-Entropy Alloy Nanocatalysts. *Adv. Funct. Mater.* **2019**, *29* (50), 1905933.

26. Wu, D.; Kusada, K.; Yamamoto, T.; Toriyama, T.; Matsumura, S.; Kawaguchi, S.; Kubota, Y.; Kitagawa, H. Platinum-Group-Metal High-Entropy-Alloy Nanoparticles. *J. Am. Chem. Soc.* **2020**, *142* (32), 13833-13838.

27. Chen, Y.; Zhan, X.; Bueno, S. L. A.; Shafei, I. H.; Ashberry, H. M.; Chatterjee, K.; Xu, L.; Tang, Y.; Skrabalak, S. E. Synthesis of Monodisperse High Entropy Alloy Nanocatalysts from Core@Shell Nanoparticles. *Nanoscale. Horiz.* **2021**, *6* (3), 231-237.

28. Bueno, S. L. A.; Leonardi, A.; Kar, N.; Chatterjee, K.; Zhan, X.; Chen, C.; Wang, Z.; Engel, M.; Fung, V.; Skrabalak, S. E. Quinary, Senary, and Septenary High Entropy Alloy Nanoparticle Catalysts from Core@Shell Nanoparticles and the Significance of Intraparticle Heterogeneity. *ACS Nano* **2022**, *16* (11), 18873-18885.

29. Kar, N.; McCoy, M.; Wolfe, J.; Bueno, S. L. A.; Shafei, I. H.; Skrabalak, S. E. Retrosynthetic Design of Core–Shell Nanoparticles for Thermal Conversion to Monodisperse High-entropy Alloy Nanoparticles. *Nat. Synth.* **2024**, *3*(2), 175-184.

30.   Xia, X.; Wang, Y.; Ruditskiy, A.; Xia, Y. 25th Anniversary Article: Galvanic Replacement: A Simple and Versatile Route to Hollow Nanostructures with Tunable and Well-Controlled Properties. *Adv. Mater.* **2013**, *25* (44), 6313-6333.

31.   Zou, Y.; Zhou, X.; Ma, J.; Yang, X.; Deng, Y. Recent Advances in Amphiphilic Block Copolymer Templated Mesoporous Metal-based Materials: Assembly Engineering and Applications. *Chem. Soc. Rev.* **2020**, *49* (4), 1173-1208.

32.   Jiang, B.; Li, C.; Imura, M.; Tang, J.; Yamauchi, Y. Multimetallic Mesoporous Spheres Through Surfactant-Directed Synthesis. *Adv. Sci*. **2015**, *2* (8), 1500112.

33.   De Marco, M. L.; Baaziz, W.; Sharna, S.; Devred, F.; Poleunis, C.; Chevillot-Biraud, A.; Nowak, S.; Haddad, R.; Odziomek, M.; Boissiere, C.; Debecker, D. P.; Ersen, O.; Peron, J.; Faustini, M. High-Entropy-Alloy Nanocrystal Based Macro- and Mesoporous Materials. *ACS Nano* **2022**, *16* (10), 15837-15849.

34.   Kang, Y.; Cretu, O.; Kikkawa, J.; Kimoto, K.; Nara, H.; Nugraha, A. S.; Kawamoto, H.; Eguchi, M.; Liao, T.; Sun, Z.; Asahi, T.; Yamauchi, Y. Mesoporous Multimetallic Nanospheres with Exposed Highly Entropic Alloy Sites. *Nat. Commun.* **2023**, *14* (1), 4182.

35.   Rekha, M. Y.; Mallik, N.; Srivastava, C. First Report on High Entropy Alloy Nanoparticle Decorated Graphene. *Sci Rep* **2018**, *8* (1), 8737.

36.   Urs, K. M. B.; Katiyar, N. K.; Kumar, R.; Biswas, K.; Singh, A. K.; Tiwary, C. S.; Kamble, V. Multi-component (Ag-Au-Cu-Pd-Pt) Alloy Nanoparticle-Decorated P-Type 2D-Molybdenum Disulfide (MoS_2) for Enhanced Hydrogen Sensing. *Nanoscale* **2020**, *12* (22), 11830-11841.

37.   Zhu, G.; Jiang, Y.; Yang, H.; Wang, H.; Fang, Y.; Wang, L.; Xie, M.; Qiu, P.; Luo, W. Constructing Structurally Ordered High-Entropy Alloy Nanoparticles on Nitrogen-Rich Mesoporous Carbon Nanosheets for High-Performance Oxygen Reduction. *Adv. Mater.* **2022**, *34* (15), e2110128.

38.   Pescara, B.; Mazzio, K. A. Morphological and Surface-State Challenges in Ge Nanoparticle Applications. *Langmuir* **2020**, *36* (40), 11685-11701.

39.   Wind, L.; Sistani, M.; Song, Z.; Maeder, X.; Pohl, D.; Michler, J.; Rellinghaus, B.; Weber, W. M.; Lugstein, A. Monolithic Metal-Semiconductor-Metal Heterostructures Enabling Next-Generation Germanium Nanodevices. *ACS Appl. Mater. Interfaces* **2021**, *13* (10), 12393-12399.

40.   Rost, C. M.; Sachet, E.; Borman, T.; Moballegh, A.; Dickey, E. C.; Hou, D.; Jones, J. L.; Curtarolo, S.; Maria, J. P. Entropy-Stabilized Oxides. *Nat. Commun.* **2015**, *6* (1), 8485.

41.   Zhang, R.Z.; Reece, M. J. Review of High Entropy Ceramics: Design, Synthesis, Structure and Properties. *J. Mater. Chem. A* **2019**, *7* (39), 22148-22162.

42.   Boyjoo, Y.; Wang, M.; Pareek, V. K.; Liu, J.; Jaroniec, M. Synthesis and Applications of Porous Non-Silica Metal Oxide Submicrospheres. *Chem. Soc. Rev.* **2016**, *45* (21), 6013-6047.

43.   Wang, G.; Qin, J.; Feng, Y.; Feng, B.; Yang, S.; Wang, Z.; Zhao, Y.; Wei, J. Sol-Gel Synthesis of Spherical Mesoporous High-Entropy Oxides. *ACS Appl. Mater. Interfaces* **2020**, *12* (40), 45155-45164.

44.   Wang, K.; Chen, L.; Xu, C.; Zhang, W.; Liu, Z.; Wang, Y.; Ouyang, J.; Zhang, X.; Fu, Y.; Zhou, Y. Microstructure and Mechanical Properties of (TiZrNbTaMo)C High-Entropy Ceramic. *J. Mater. Sci. Technol.* **2020**, *39*, 99-105.

45. Sure, J.; Sri Maha Vishnu, D.; Kim, H. K.; Schwandt, C. Facile Electrochemical Synthesis of Nanoscale (TiNbTaZrHf)C High-Entropy Carbide Powder. *Angew. Chem., Int. Ed.* **2020**, *59* (29), 11830-11835.

46. Jin, T.; Sang, X.; Unocic, R. R.; Kinch, R. T.; Liu, X.; Hu, J.; Liu, H.; Dai, S. Mechanochemical-Assisted Synthesis of High-Entropy Metal Nitride via a Soft Urea Strategy. *Adv. Mater.* **2018**, *30* (23), e1707512.

47. Gild, J.; Zhang, Y.; Harrington, T.; Jiang, S.; Hu, T.; Quinn, M. C.; Mellor, W. M.; Zhou, N.; Vecchio, K.; Luo, J. High-Entropy Metal Diborides: A New Class of High-Entropy Materials and a New Type of Ultrahigh Temperature Ceramics. *Sci. Rep.* **2016**, *6*, 37946.

48. Dong, S.; Li, Q.; Hu, H.; Zhang, X.; Li, Y.; Ye, K.; Hou, W.; He, J.; Zhao, H. Application of Rare-Earth High Entropy Boride in Electrocatalytic Hydrogen Evolution Reaction. *Appl. Surf. Sci.* **2023**, *615*, 156413.

49. Qin, Y.; Liu, J.-X.; Li, F.; Wei, X.; Wu, H.; Zhang, G.-J. A High Entropy Silicide by Reactive Spark Plasma Sintering. *J. Adv. Ceram.* **2019**, *8* (1), 148-152.

50. Wang, T.; Chen, H.; Yang, Z.; Liang, J.; Dai, S. High-Entropy Perovskite Fluorides: A New Platform for Oxygen Evolution Catalysis. *J. Am. Chem. Soc.* **2020**, *142* (10), 4550-4554.

51. Folgueras, M. C.; Jiang, Y.; Jin, J.; Yang, P. High-Entropy Halide Perovskite Single Crystals Sabilized by Mild Chemistry. *Nature* **2023**, *621* (7978), 282-288.

52. Zhang, R. Z.; Gucci, F.; Zhu, H.; Chen, K.; Reece, M. J. Data-Driven Design of Ecofriendly Thermoelectric High-Entropy Sulfides. *Inorg. Chem.* **2018**, *57* (20), 13027-13033.

53. McCormick, C. R.; Schaak, R. E. Simultaneous Multication Exchange Pathway to High-Entropy Metal Sulfide Nanoparticles. *J. Am. Chem. Soc.* **2021**, *143* (2), 1017-1023.

54. Chen, G. Z.; Fray, D. J.; Farthing, T. W. Direct Electrochemical Reduction of Titanium Dioxide to Titanium in Molten Calcium Chloride. *Nature* **2000**, *407* (6802), 361-364.

55. Folgueras, M. C.; Louisia, S.; Jin, J.; Gao, M.; Du, A.; Fakra, S. C.; Zhang, R.; Seeler, F.; Schierle-Arndt, K.; Yang, P. Ligand-Free Processable Perovskite Semiconductor Ink. *Nano Lett.* **2021**, *21* (20), 8856-8862.

56. Shi, X. L.; Zou, J.; Chen, Z. G., Advanced Thermoelectric Design: From Materials and Structures to Devices. *Chem. Rev.* **2020,** *120* (15), 7399-7515.

57. Rabie, M. A.; Mirza, S.; Hu, Y.; Haddara, Y. M., Cobalt Germanide Contacts: Growth Reaction, Phase Formation Models, and Electrical Properties. *J. Mater. Sci. Mater. Electron.* **2019,** *30* (11), 10031-10063.

58. Götsch, T.; Stöger-Pollach, M.; Thalinger, R.; Penner, S., The Nanoscale Kirkendall Effect in Pd-Based Intermetallic Phases. *J. Phys. Chem. C* **2014,** *118* (31), 17810-17818.

59. Vaughn, D. D.; Sun, D.; Moyer, J. A.; Biacchi, A. J.; Misra, R.; Schiffer, P.; Schaak, R. E., Solution-Phase Synthesis and Magnetic Properties of Single-Crystal Iron Germanide Nanostructures. *Chem. Mater.* **2013,** *25* (21), 4396-4401.

60. Yan, C.; Higgins, J. M.; Faber, M. S.; Lee, P. S.; Jin, S., Spontaneous Growth and Phase Transformation of Highly Conductive Nickel Germanide Nanowires. *ACS Nano* **2011,** *5* (6), 5006-5014.

61. Yoon, H.; Seo, K.; Bagkar, N.; In, J.; Park, J.; Kim, J.; Kim, B., Vertical Epitaxial Co_5Ge_7 Nanowire and Nanobelt Arrays on A Thin Graphitic Layer for Flexible Field Emission Displays. *Adv. Mater.* **2009,** *21* (48), 4979-4982.

62. Nakaya, Y.; Hayashida, E.; Asakura, H.; Takakusagi, S.; Yasumura, S.; Shimizu, K. I.; Furukawa, S. High-Entropy Intermetallics Serve Ultrastable Single-Atom Pt for Propane Dehydrogenation. *J. Am. Chem. Soc.* **2022**, *144* (35), 15944-15953.

63. Collings, P. J. Simple Measurement of the Band Gap in Silicon and Germanium. *Am. J. Phys.* **1980**, *48* (3), 197-199.

64. Maeda, Y.; Tsukamoto, N.; Yazawa, Y.; Kanemitsu, Y.; Masumoto, Y. Visible Photoluminescence of Ge Microcrystals Embedded in SiO_2 Glassy Matrices. *Appl. Phys. Lett.* **1991**, *59* (24), 3168-3170.

65. Maeda, Y. Visible Photoluminescence of Ge Microcrystals Embedded in SiO_2 Glassy Matrix: Evidence in Support of the Quantum-Confinement Mechanism. *Phys. Rev. B Condens. Matter Mater. Phys.* **1995**, *51* (3), 1658-1670.

66. Cho, S.; Kang, I. M.; Kim, K. R.; Park, B.; Cho, J. S. H.; Kang, S.; Kim, I. M.; Park, B. K. R.; Kang, I. Man. Silicon-Compatible High-Hole-Mobility Transistor with an Undoped Germanium Channel for Low-Power Application. *Appl. Phys. Lett.* **2013**, *103* (22), 222102.

67. Michel, J.; Liu, J.; Kimerling, L. C. High-Performance Ge-on-Si Photodetectors. *Nat. Photon.* **2010**, *4* (8), 527-534.

68. Yongping, D.; Ying, D.; Bapat, A.; Nowak, J. D.; Carter, C. B.; Kortshagen, U. R.; Campbell, S. A. Single Nanoparticle Semiconductor Devices. *IEEE Trans. Electron Devices* **2006**, *53* (10), 2525-2531.

69. Serino, A. C.; Ko, J. S.; Yeung, M. T.; Schwartz, J. J.; Kang, C. B.; Tolbert, S. H.; Kaner, R. B.; Dunn, B. S.; Weiss, P. S. Lithium-Ion Insertion Properties of Solution-Exfoliated Germanane. *ACS Nano* **2017**, *11* (8), 7995-8001.

70. Lee, D. C.; Pietryga, J. M.; Robel, I.; Werder, D. J.; Schaller, R. D.; Klimov, V. I. Colloidal Synthesis of Infrared-Emitting Germanium Nanocrystals. *J. Am. Chem. Soc.,* **2009**, *131* (10). 3436-3437.

71. Prabakar, S.; Shiohara, A.; Hanada, S.; Fujioka, K.; Yamamoto, K.; Tilley, R. D. Size Controlled Synthesis of Germanium Nanocrystals by Hydride Reducing Agents and Their Biological Applications. *Chem. Mater.* **2010**, *22* (2). 482-486.

72. Vaughn II, D. D.; Schaak, R. E. Synthesis, Properties and Applications of Colloidal Germanium and Germanium-Based Nanomaterials. *Chem. Soc. Rev.* **2013**, *42* (7), 2861–2879.

73. McVey, B. F. P.; Prabakar, S.; Gooding, J. J.; Tilley, R. D. Solution Synthesis, Surface Passivation, Optical Properties, Biomedical Applications, and Cytotoxicity of Silicon and Germanium Nanocrystals. *Chempluschem* **2017**, *82* (1), 60–73.

74. Nogales, E.; Montone, A.; Cardellini, F.; ndez, B. M.; Piqueras, J. Visible Cathodoluminescence from Mechanically Milled Germanium. *Semicond. Sci. Technol.* **2002**, *17* (12), 1267–1271.

75. Taylor, B. R.; Kauzlarich, S. M.; Delgado, G. R.; Lee, H. W. H. Solution Synthesis and Characterization of Quantum Confined Ge Nanoparticles. *Chem. Mater.* **1999**, *11* (9), 2493–2500.

76. Chiu, H. W.; Kauzlarich, S. M. Investigation of Reaction Conditions for Optimal Germanium Nanoparticle Production by a Simple Reduction Route. *Chem. Mater.* **2006**, *18* (4), 1023–1028.

77. Prabakar, S.; Shiohara, A.; Hanada, S.; Fujioka, K.; Yamamoto, K.; Tilley, R. D. Size Controlled Synthesis of Germanium Nanocrystals by Hydride Reducing Agents and Their Biological Applications. *Chem. Mater.* **2010**, *22* (2), 482–486.

78. Vaughn II, D. D.; Bondi, J. F.; Schaak, R. E. Colloidal Synthesis of Air-Stable Crystalline Germanium Nanoparticles with Tunable Sizes and Shapes. *Chem. Mater.* **2010**, *22* (22), 6103–6108.

79. Wang, W.; Huang, J.; Ren, Z. Synthesis of Germanium Nanocubes by a Low-Temperature Inverse Micelle Solvothermal Technique. *Langmuir* **2005**, *21* (2), 751–754.

80. Javadi, M.; Picard, D.; Sinelnikov, R.; Narreto, M. A.; Hegmann, F. A.; Veinot, J. G. C. Synthesis and Surface Functionalization of Hydride-Terminated Ge Nanocrystals Obtained from the Thermal Treatment of Ge(OH)$_2$. *Langmuir* **2017**. *33* (35), 8757–8765.

81. Hossain, M. A.; Javadi, M.; Yu, H.; Thiessen, A. N.; Ikpo, N.;Oliynyk, A. O.; Veinot, J. G. C. Dehydrocoupling – an Alternative Approach to Functionalizing Germanium Nanoparticle Surfaces. *Nanoscale* **2020**, *12* (11), 6271–6278.

82. Li, M.; Su, S.; Wong, H.S.; Li, L.; How 2D Semiconductors Could Extend Moore's Law. *Nature* **2019**, *567* (7748), 169-170.

83. Novoselov, K. S.; Mishchenko, A.; Carvalho, A.; Castro Neto, A. H. 2D Materials and Van der Waals Heterostructures. *Science* **2016**, *353* (6298), aac9439.

84. Huey, W. L. B.; Goldberger, J. E. Covalent Functionalization of Two-Dimensional Group 14 Graphane Analogues. *Chem. Soc. Rev.* **2018**, *47* (16), 6201-6223.

85. Jiang, S.; Krymowski, K.; Asel, T.; Arguilla, M. Q.; Cultrara, N. D.; Yanchenko, E.; Yang, X.; Brillson, L. J.; Windl, W.; Goldberger, J. E. Tailoring the Electronic Structure of Covalently Functionalized Germanane via the Interplay of Ligand Strain and Electronegativity. *Chem. Mater.* **2016**, *28* (21), 8071-8077.

86. Serino, A. C.; Ko, J. S.; Yeung, M. T.; Schwartz, J. J.; Kang, C. B.; Tolbert, S. H.; Kaner, R. B.; Dunn, B. S.; Weiss, P. S. Lithium-Ion Insertion Properties of Solution-Exfoliated Germanane. *ACS Nano* **2017**, *11* (8), 7995-8001.

87. Madhushankar, B. N.; Kaverzin, A.; Giousis, T.; Potsi, G.; Gournis, D.; Rudolf, P.; Blake, G. R.; van der Wal, C. H.; van Wees, B. J. Electronic Properties of Germanane Field-Effect Transistors. *2D Mater.* **2017**, *4* (2), 021009.

88. Vogg, G.; Brandt, M. S.; Stutzmann, M. Polygermyne—A Prototype System for Layered Germanium Polymers. *Adv. Mater.* **2000**, *12* (17), 1278-1281.

89. Bianco, E.; Butler, S.; Jiang, S.; Restrepo, O. D.; Windl, W.; Goldberger, J. E. Stability and Exfoliation of Germanane: A Germanium Graphane Analogue. *ACS Nano* **2013**, *7* (5), 4414-4421.

90. Jiang, S.; Butler, S.; Bianco, E.; Restrepo, O. D.; Windl, W.; Goldberger, J. E. Improving the stability and optical properties of germanane via one-step covalent methyl-termination. *Nat. Commun.* **2014**, *5* (1), 3389.

91. Ng, S.; Pumera, M., 2D Functionalized Germananes: Synthesis and Applications. *Adv. Mater.* **2023,** *35* (7), e2207196.

92. Hartman, T.; Sturala, J.; Plutnar, J.; Sofer, Z., Alkali Metal Arenides as a Universal Synthetic Tool for Layered 2D Germanene Modification. *Angew. Chem., Int. Ed.* **2019,** *58* (46), 16517-16522.

93. Choi, K.; Buriak, J. M., Hydrogermylation of Alkenes and Alkynes on Hydride-Terminated Ge(100) Surfaces. *Langmuir* **2000,** *16* (20), 7737-7741.

94.   Yu, H.; Helbich, T.; Scherf, L. M.; Chen, J.; Cui, K.; Fässler, T. F.; Rieger, B.; Veinot, J. G. C., Radical-Initiated and Thermally Induced Hydrogermylation of Alkenes on the Surfaces of Germanium Nanosheets. *Chem. Mater.* **2018,** *30* (7), 2274-2280.

95.   Yu, H.; Thiessen, A. N.; Hossain, M. A.; Kloberg, M. J.; Rieger, B.; Veinot, J. G. C., Thermally Induced Dehydrogenative Coupling of Organosilanes and H-Terminated Silicon Quantum Dots onto Germanane Surfaces. *Chem. Mater.* **2020**, *32* (11), 4536-4543.

96.   Huey, W. L. B.; Goldberger, J. E., Covalent Functionalization of Two-dimensional Group 14 Graphane Analogues. *Chem. Soc. Rev.* **2018,** *47* (16), 6201-6223.

97.   Jiang, S.; Krymowski, K.; Asel, T.; Arguilla, M. Q.; Cultrara, N. D.; Yanchenko, E.; Yang, X.; Brillson, L. J.; Windl, W.; Goldberger, J. E., Tailoring the Electronic Structure of Covalently Functionalized Germanane via the Interplay of Ligand Strain and Electronegativity. *Chem. Mater.* **2016,** *28* (21), 8071-8077.

98.   Helbich, T.; Lyuleeva, A.; Ludwig, T.; Scherf, L. M.; Fässler, T. F.; Lugli, P.; Rieger, B., One-Step Synthesis of Photoluminescent Covalent Polymeric Nanocomposites from 2D Silicon Nanosheets. *Adv. Funct. Mater.* **2016,** *26* (37), 6711-6718.

99.   Hartman, T.; Sofer, Z., Beyond Graphene: Chemistry of Group 14 Graphene Analogues: Silicene, Germanene, and Stanene. *ACS Nano* **2019,** *13* (8), 8566-8576.

100.   Ni, C.; O'Connor, K. M.; Trach, J.; Butler, C.; Rieger, B.; Veinot, J. G. C., Facile Synthesis of High-Entropy Alloy Nanoparticles on Germanane, Ge Nanoparticles and Wafers. *Nanoscale Horiz.* **2023,** *8* (9), 1217-1225.

101.   Liu, Z.; Lou, Z.; Li, Z.; Wang, G.; Wang, Z.; Liu, Y.; Huang, B.; Xia, S.; Qin, X.; Zhang, X.; Dai, Y., GeH: a Novel Material as a Visible-light Driven Photocatalyst for Hydrogen Evolution. *Chem. Commun.* **2014,** *50* (75), 11046-11048.

102.   Liu, Z.; Wang, Z.; Sun, Q.; Dai, Y.; Huang, B., Methyl-terminated Germanane $GeCH_3$ Synthesized by Solvothermal Method with Improved Photocatalytic Properties. *Appl. Surf. Sci.* **2019,** *467-468*, 881-888.

103.   Ng, S.; Sturala, J.; Vyskocil, J.; Lazar, P.; Martincova, J.; Plutnar, J.; Pumera, M., Two-Dimensional Functionalized Germananes as Photoelectrocatalysts. *ACS Nano* **2021,** *15* (6), 11681-11693.

104.   Qian, C.; Sun, W.; Hung, D. L. H.; Qiu, C.; Makaremi, M.; Hari Kumar, S. G.; Wan, L.; Ghoussoub, M.; Wood, T. E.; Xia, M.; Tountas, A. A.; Li, Y. F.; Wang, L.; Dong, Y.; Gourevich, I.; Singh, C. V.; Ozin, G. A., Catalytic CO_2 Reduction by Palladium-decorated Silicon–hydride Nanosheets. *Nat. Catal.* **2018,** *2* (1), 46-54.

105.   Zhao, F.; Feng, Y.; Wang, Y.; Zhang, X.; Liang, X.; Li, Z.; Zhang, F.; Wang, T.; Gong, J.; Feng, W., Two-dimensional Gersiloxenes with Tunable Bandgap for Photocatalytic H_2 Evolution and CO_2 Photoreduction to CO. *Nat. Commun.* **2020,** *11* (1), 1443.

106.   Aizawa, M.; Cooper, A. M.; Malac M.; Buriak, J. M., Silver Nano-Inukshuks on Germanium. *Nano Lett*., **2005**, *5* (5), 815-819.

107.   Richmond, H. H., US Pat., 73966147A, 1950.

108.   Enache, D. I.; Edwards, J. K.; Landon, P.; Solsona-Espriu, B.; Carley, A. F.; Herzing, A. A.; Watanabe, M.; Kiely, C. J.; Knight, D. W.; Hutchings, G. J., Solvent-Free Oxidation of Primary Alcohols to Aldehydes Using Au-Pd/TiO2 Catalysts. *Science* **2006,** *311* (5759), 362-365.

109.   Long, J.; Xie, X.; Xu, J.; Gu, Q.; Chen, L.; Wang, X., Nitrogen-Doped Graphene Nanosheets as Metal-Free Catalysts for Aerobic Selective Oxidation of Benzylic Alcohols.

ACS Catal. **2012,** *2* (4), 622-631.

110. Furukawa, S.; Shishido, T.; Teramura, K.; Tanaka, T., Photocatalytic Oxidation of Alcohols over TiO_2 Covered with Nb_2O_5. *ACS Catal.* **2011,** *2* (1), 175-179.

111. Patel, M. A.; Luo, F.; Khoshi, M. R.; Rabie, E.; Zhang, Q.; Flach, C. R.; Mendelsohn, R.; Garfunkel, E.; Szostak, M.; He, H., P-Doped Porous Carbon as Metal Free Catalysts for Selective Aerobic Oxidation with an Unexpected Mechanism. *ACS Nano* **2016,** *10* (2), 2305-2315.

112. Feng, W.; Wu, G.; Li, L.; Guan, N., Solvent-free Selective Photocatalytic Oxidation of Benzyl Alcohol over Modified TiO_2. *Green Chem.* **2011,** *13* (11), 3265-3272.

113. Huang, X.; Akdim, O.; Douthwaite, M.; Wang, K.; Zhao, L.; Lewis, R. J.; Pattisson, S.; Daniel, I. T.; Miedziak, P. J.; Shaw, G.; Morgan, D. J.; Althahban, S. M.; Davies, T. E.; He, Q.; Wang, F.; Fu, J.; Bethell, D.; McIntosh, S.; Kiely, C. J.; Hutchings, G. J., Au–Pd Separation Enhances Bimetallic Catalysis of Alcohol Oxidation. *Nature* **2022,** *603* (7900), 271-275.

114. Qamar, M.; Elsayed, R. B.; Alhooshani, K. R.; Ahmed, M. I.; Bahnemann, D. W., Highly Efficient and Selective Oxidation of Aromatic Alcohols Photocatalyzed by Nanoporous Hierarchical Pt/Bi_2WO_6 in Organic Solvent-free Environment. *ACS Appl. Mater. Interfaces* **2015,** *7* (2), 1257-1269.

115. Jia, L.; Wang, D.-H.; Huang, Y.-X.; Xu, A.-W.; Yu, H.-Q., Highly Durable N-Doped Graphene/CdS Nanocomposites with Enhanced Photocatalytic Hydrogen Evolution from Water under Visible Light Irradiation. *J. of Phys. Chem. C* **2011,** *115* (23), 11466-11473.

116. Helbich, T.; Lyuleeva, A.; Höhlein, I. M. D.; Marx, P.; Scherf, L. M.; Kehrle, J.; Fässler, T. F.; Lugli, P.; Rieger, B., Radical-Induced Hydrosilylation Reactions for the Functionalization of Two-Dimensional Hydride Terminated Silicon Nanosheets. *Chem.– Eur. J.* **2016,** *22* (18), 6194-6198.

117. Bianco, E.; Butler, S.; Jiang, S.; Restrepo, O. D.; Windl, W.; Goldberger, J. E., Stability and Exfoliation of Germanane: A Germanium Graphane Analogue. *ACS Nano* **2013,** *7* (5), 4414-4421.

118. Zhang, Q.; Li, N.; Goebl, J.; Lu, Z.; Yin, Y., A Systematic Study of the Synthesis of Silver Nanoplates: Is Citrate a "Magic" Reagent? *J. Am. Chem. Soc.* **2011,** *133* (46), 18931-18939.

119. Anderson, S. L.; Luber, E. J.; Olsen, B. C.; Buriak, J. M., Substance over Subjectivity: Moving beyond the Histogram. *Chem. Mater.* **2016,** *28* (17), 5973-5975.

120. Yu, H.; Helbich, T.; Scherf, L. M.; Chen, J.; Cui, K.; Fässler, T. F.; Rieger, B.; Veinot, J. G. C., Radical-Initiated and Thermally Induced Hydrogermylation of Alkenes on the Surfaces of Germanium Nanosheets. *Chem. Mater.* **2018,** *30* (7), 2274-2280.

121. NIST X-ray Photoelectron Spectroscopy Database, NIST Standard Reference Database Number 20, National Institute of Standards and Technology, Gaithersburg MD, 20899 (2000).

122. Holzwarth, U.; Gibson, N., The Scherrer Equation Versus the 'Debye-Scherrer equation'. *Nat. Nanotechnol.* **2011,** *6* (9), 534-534.

123. Cultrara, N. D.; Wang, Y.; Arguilla, M. Q.; Scudder, M. R.; Jiang, S.; Windl, W.; Bobev, S.; Goldberger, J. E., Synthesis of 1T, 2H, and 6R Germanane Polytypes. *Chem. Mater.* **2018,** *30* (4), 1335-1343.

124. Khomenkova, L.; Lehninger, D.; Kondratenko, O.; Ponomaryov, S.; Gudymenko, O.;

Tsybrii, Z.; Yukhymchuk, V.; Kladko, V.; von Borany, J.; Heitmann, J., Effect of Ge Content on the Formation of Ge Nanoclusters in Magnetron-Sputtered GeZrO$_x$-Based Structures. *Nanoscale Res. Lett.* **2017,** *12* (1), 196.

125. Yu, H.; Thiessen, A. N.; Hossain, M. A.; Kloberg, M. J.; Rieger, B.; Veinot, J. G. C., Thermally Induced Dehydrogenative Coupling of Organosilanes and H-Terminated Silicon Quantum Dots onto Germanane Surfaces. *Chem. Mater.* **2020**, *32* (11), 4536-4543.

126. Holder, C. F.; Schaak, R. E., Tutorial on Powder X-ray Diffraction for Characterizing Nanoscale Materials. *ACS Nano* **2019,** *13* (7), 7359-7365.

127. Brückner, A., A New Approach to Study the Gas-phase Oxidation of Toluene: Probing Active Sites in Vanadia-based Catalysts under Working Conditions. *Appl. Catal. A-Gen.* **2000**, *200* (1), 287-297.

128. Zhan, G.; Hong, Y.; Mbah, V. T.; Huang, J.; Ibrahim, A.-R.; Du, M.; Li, Q., Bimetallic Au–Pd/MgO as Efficient Catalysts for Aerobic Oxidation of Benzyl Alcohol: A Green Bio-reducing Preparation Method. *Appl. Catal. A-Gen.* **2012**, *439-440*, 179-186.

129. Ferraz, C. P.; Garcia, M. A. S.; Teixeira-Neto, É.; Rossi, L. M., Oxidation of Benzyl Alcohol Catalyzed by Gold Nanoparticles under Alkaline Conditions: Weak vs. Strong Bases. *RSC Adv.* **2016**, *6* (30), 25279-25285.

130. Gautam, C.; Yadav, A. K.; Singh, A. K., A Review on Infrared Spectroscopy of Borate Glasses with Effects of Different Additives. *ISRN Ceram.* **2012**, *2012*, 1-17.

131. Ma, L.; Jia, l.; Guo, X.; Xiang, L., Catalytic Activity of Ag/SBA-15 for Low-temperature Gas-phase Selective Oxidation of Benzyl Alcohol to Benzaldehyde. *Chin. J. Catal.* **2014**, *35* (1), 108-119.

132. Jia, L.; Zhang, S.; Gu, F.; Ping, Y.; Guo, X.; Zhong, Z.; Su, F., Highly Selective Gas-phase Oxidation of Benzyl Alcohol to Benzaldehyde Over Silver-containing Hexagonal Mesoporous Silica. *Microporous and Mesoporous Mater.* **2012**, *149* (1), 158-165.

133. Lima, M. J.; Tavares, P. B.; Silva, A. M. T.; Silva, C. G.; Faria, J. L. Selective Photocatalytic Oxidation of Benzyl Alcohol to Benzaldehyde by Using Metal-loaded g-C$_3$N$_4$ Photocatalysts. *Catal. Today* **2017**, *287* (1), 70-77.

134. Zhai, W.; Xue, S.; Zhu, A.; Luo, Y.; Tian, Y. Plasmon-Driven Selective Oxidation of Aromatic Alcohols to Aldehydes in Water with Recyclable Pt/TiO$_2$ Nanocomposites. *ChemCatChem* **2011**, *3* (1), 127−130.

135. Tanaka, A.; Hashimoto, K.; Kominami, H. Selective Photocatalytic Oxidation of Aromatic Alcohols to Aldehydes in an Aqueous Suspension of Gold Nanoparticles Supported on Cerium (IV) Oxide under Irradiation of Green Light. *Chem. Commun.* **2011**, *47* (37), 10446−10448.

136. Li, X.; Feng, J.; Sun, J.; Wang, Z.; Zhao, W. Solvent-Free Catalytic Oxidation of Benzyl Alcohol over Au-Pd Bimetal Deposited on TiO$_2$: Comparison of Rutile, Brookite, and Anatase. *Nanoscale Res. Lett.* **2019**, *14* (1), 394.

137. Sun, J.; Han, Y.; Fu, H.; Qu, X.; Xu, Z.; Zheng, S. Au@Pd/TiO$_2$ with Atomically Dispersed Pd as Highly Active Catalyst for Solvent-free Aerobic Oxidation of Benzyl Alcohol. *Chem. Eng. J.* **2017**, *313* (1), 1–9.

138. Alshammari, H.M. Synthesis of Palladium and Copper Nanoparticles Supported on TiO$_2$ for Oxidation Solvent-Free Aerobic Oxidation of Benzyl Alcohol. *Processes* **2021**, *9* (9), 1590.

139. Xie, F.; Zhang, Y.; He, X.; Li, H.; Qiu, X.; Zhou, W.; Huo, S.; Tang, Z., First Achieving

Highly Selective Oxidation of Aliphatic Alcohols to Aldehydes over Photocatalysts. *J Mater. Chem. A* **2018,** *6* (27), 13236-13243.

140. Yao, Y.; Dong, Q.; Brozena, A.; Luo, J.; Miao, J.; Chi, M.; Wang, C.; Kevrekidis, I. G.; Ren, Z. J.; Greeley, J.; Wang, G.; Anapolsky, A.; Hu, L., High-entropy Nanoparticles: Synthesis-structure-property Relationships and Data-driven Discovery. *Science* **2022,** *376* (6589), eabn3103.

141. Glasscott, M. W.; Pendergast, A. D.; Goines, S.; Bishop, A. R.; Hoang, A. T.; Renault, C.; Dick, J. E., Electrosynthesis of High-entropy Metallic Glass Nanoparticles for Designer, Multi-functional Electrocatalysis. *Nat. Commun.* **2019,** *10* (1), 2650.

142. Yao, Y.; Huang, Z.; Xie, P.; Lacey, S. D.; Jacob, R. J.; Xie, H.; Chen, F.; Nie, A.; Pu, T.; Rehwoldt, M.; Yu, D.; Zachariah, M. R.; Wang, C.; Shahbazian-Yassar, R.; Li, J.; Hu, L., Carbothermal Shock Synthesis of High-entropy-alloy Nanoparticles. *Science* **2018,** *359* (6383), 1489-1494.

143. Chen, P.-C.; Liu, X.; Hedrick, J. L.; Xie, Z.; Wang, S.; Lin, Q.-Y.; Hersam, M. C.; Dravid, V. P.; Mirkin, C. A., Polyelemental Nanoparticle Libraries. *Science* **2016,** *352* (6293), 1565-1569.

144. Kumar, N.; Tiwary, C. S.; Biswas, K., Preparation of Nanocrystalline High-entropy Alloys via Cryomilling of Cast Ingots. *J. Mater. Sci.* **2018,** *53* (19), 13411-13423.

145. Gao, S.; Hao, S.; Huang, Z.; Yuan, Y.; Han, S.; Lei, L.; Zhang, X.; Shahbazian-Yassar, R.; Lu, J., Synthesis of High-entropy Alloy Nanoparticles on Supports by the Fast Moving Bed Pyrolysis. *Nat. Commun.* **2020,** *11* (1), 2016.

146. Mori, K.; Hashimoto, N.; Kamiuchi, N.; Yoshida, H.; Kobayashi, H.; Yamashita, H., Hydrogen Spillover-driven Synthesis of High-entropy Alloy Nanoparticles as a Robust Catalyst for CO_2 Hydrogenation. *Nat. Commun.* **2021,** *12* (1), 3884.

147. Qiao, H.; Saray, M. T.; Wang, X.; Xu, S.; Chen, G.; Huang, Z.; Chen, C.; Zhong, G.; Dong, Q.; Hong, M.; Xie, H.; Shahbazian-Yassar, R.; Hu, L., Scalable Synthesis of High Entropy Alloy Nanoparticles by Microwave Heating. *ACS Nano* **2021,** *15* (9), 14928-14937.

148. Wu, D.; Kusada, K.; Yamamoto, T.; Toriyama, T.; Matsumura, S.; Kawaguchi, S.; Kubota, Y.; Kitagawa, H., Platinum-Group-Metal High-Entropy-Alloy Nanoparticles. *J. Am. Chem. Soc.* **2020,** *142* (32), 13833-13838.

149. Zhu, G.; Jiang, Y.; Yang, H.; Wang, H.; Fang, Y.; Wang, L.; Xie, M.; Qiu, P.; Luo, W., Constructing Structurally Ordered High-Entropy Alloy Nanoparticles on Nitrogen-Rich Mesoporous Carbon Nanosheets for High-Performance Oxygen Reduction. *Adv. Mater.* **2022,** *34* (15), e2110128.

150. Huang, Z.; Yao, Y.; Pang, Z.; Yuan, Y.; Li, T.; He, K.; Hu, X.; Cheng, J.; Yao, W.; Liu, Y.; Nie, A.; Sharifi-Asl, S.; Cheng, M.; Song, B.; Amine, K.; Lu, J.; Li, T.; Hu, L.; Shahbazian-Yassar, R., Direct Observation of the Formation and Stabilization of Metallic Nanoparticles on Carbon Supports. *Nat. Commun.* **2020,** *11* (1), 6373.

151. Rekha, M. Y.; Mallik, N.; Srivastava, C., First Report on High Entropy Alloy Nanoparticle Decorated Graphene. *Sci. Rep.* **2018,** *8* (1), 8737.

152. Urs, K. M. B.; Katiyar, N. K.; Kumar, R.; Biswas, K.; Singh, A. K.; Tiwary, C. S.; Kamble, V., Multi-component (Ag-Au-Cu-Pd-Pt) Alloy Nanoparticle-decorated p-type 2D-molybdenum Disulfide (MoS_2) for Enhanced Hydrogen Sensing. *Nanoscale* **2020,** *12* (22), 11830-11841.

153. Huey, W. L. B.; Goldberger, J. E., Covalent functionalization of two-dimensional group 14 graphane analogues. *Chem. Soc. Rev.* **2018,** *47* (16), 6201-6223.

154. Jiang, S.; Krymowski, K.; Asel, T.; Arguilla, M. Q.; Cultrara, N. D.; Yanchenko, E.; Yang, X.; Brillson, L. J.; Windl, W.; Goldberger, J. E., Tailoring the Electronic Structure of Covalently Functionalized Germanane via the Interplay of Ligand Strain and Electronegativity. *Chem. Mater.* **2016,** *28* (21), 8071-8077.

155. Serino, A. C.; Ko, J. S.; Yeung, M. T.; Schwartz, J. J.; Kang, C. B.; Tolbert, S. H.; Kaner, R. B.; Dunn, B. S.; Weiss, P. S., Lithium-Ion Insertion Properties of Solution-Exfoliated Germanane. *ACS Nano* **2017,** *11* (8), 7995-8001.

156. Madhushankar, B. N.; Kaverzin, A.; Giousis, T.; Potsi, G.; Gournis, D.; Rudolf, P.; Blake, G. R.; van der Wal, C. H.; van Wees, B. J., Electronic Properties of Germanane Field-effect Transistors. *2D Mater.* **2017,** *4* (2), 021009.

157. Zhao, F.; Feng, Y.; Wang, Y.; Zhang, X.; Liang, X.; Li, Z.; Zhang, F.; Wang, T.; Gong, J.; Feng, W., Two-dimensional Gersiloxenes with Tunable Bandgap for Photocatalytic H_2 Evolution and CO_2 Photoreduction to CO. *Nat. Commun.* **2020,** *11* (1), 1443.

158. Chen, L. H.; Shen, H. T.; Chang, W. H.; Khalil, I.; Liao, S. Y.; W, A. Y.; Liu, S. C.; Chu, C. C.; Hsiao, V. K. S., Photocatalytic Properties of Graphene/Gold and Graphene Oxide/Gold Nanocomposites Synthesized by Pulsed Laser Induced Photolysis. *Nanomaterials (Basel)* **2020,** *10* (10), 1985.

159. Ng, S.; Pumera, M., 2D Functionalized Germananes: Synthesis and Applications. *Adv Mater* **2023,** *35* (7), e2207196.

160. Ni, C.; Chevalier, M.; Veinot, J. G. C., Metal Nanoparticle-decorated Germanane for Selective Photocatalytic Aerobic Oxidation of Benzyl Alcohol. *Nanoscale Adv.* **2022,** *5* (1), 228-236.

161. Nellaiappan, S.; Katiyar, N. K.; Kumar, R.; Parui, A.; Malviya, K. D.; Pradeep, K. G.; Singh, A. K.; Sharma, S.; Tiwary, C. S.; Biswas, K., High-Entropy Alloys as Catalysts for the CO_2 and CO Reduction Reactions: Experimental Realization. *ACS Catal.* **2020,** *10* (6), 3658-3663.

162. Javadi, M.; Picard, D.; Sinelnikov, R.; Narreto, M. A.; Hegmann, F. A.; Veinot, J. G. C., Synthesis and Surface Functionalization of Hydride-Terminated Ge Nanocrystals Obtained from the Thermal Treatment of $Ge(OH)_2$. *Langmuir* **2017,** *33* (35), 8757-8765.

163. Hossain, M. A.; Javadi, M.; Yu, H.; Thiessen, A. N.; Ikpo, N.; Oliynyk, A. O.; Veinot, J. G. C., Dehydrocoupling - an Alternative Approach to Functionalizing Germanium Nanoparticle Surfaces. *Nanoscale* **2020,** *12* (11), 6271-6278.

164. Anderson, S. L.; Luber, E. J.; Olsen, B. C.; Buriak, J. M., Substance over Subjectivity: Moving beyond the Histogram. *Chem. Mater.* **2016,** *28* (17), 5973-5975.

165. NIST X-ray Photoelectron Spectroscopy Database, NIST Standard Reference Database Number 20, National Institute of Standards and Technology, Gaithersburg MD, 20899 (2000).

166. Helbich, T.; Lyuleeva, A.; Ludwig, T.; Scherf, L. M.; Fässler, T. F.; Lugli, P.; Rieger, B., One-Step Synthesis of Photoluminescent Covalent Polymeric Nanocomposites from 2D Silicon Nanosheets. *Adv. Funct. Mater.* **2016,** *26* (37), 6711-6718.

167. Katiyar, N. K.; Dhakar, S.; Parui, A.; Gakhad, P.; Singh, A. K.; Biswas, K.; Tiwary, C. S.; Sharma, S., Electrooxidation of Hydrazine Utilizing High-Entropy Alloys: Assisting the Oxygen Evolution Reaction at the Thermodynamic Voltage. *ACS Catal.* **2021,** *11* (22),

14000-14007.

168. Holder, C. F.; Schaak, R. E., Tutorial on Powder X-ray Diffraction for Characterizing Nanoscale Materials. *ACS Nano* **2019,** *13* (7), 7359-7365.

169. Yu, H.; Helbich, T.; Scherf, L. M.; Chen, J.; Cui, K.; Fässler, T. F.; Rieger, B.; Veinot, J. G. C., Radical-Initiated and Thermally Induced Hydrogermylation of Alkenes on the Surfaces of Germanium Nanosheets. *Chem. Mater.* **2018,** *30* (7), 2274-2280.

170. Bianco, E.; Butler, S.; Jiang, S.; Restrepo, O. D.; Windl, W.; Goldberger, J. E., Stability and Exfoliation of Germanane: A Germanium Graphane Analogue. *ACS Nano* **2013,** *7* (5), 4414-4421.

171. Khomenkova, L.; Lehninger, D.; Kondratenko, O.; Ponomaryov, S.; Gudymenko, O.; Tsybrii, Z.; Yukhymchuk, V.; Kladko, V.; von Borany, J.; Heitmann, J., Effect of Ge Content on the Formation of Ge Nanoclusters in Magnetron-Sputtered GeZrO$_x$-Based Structures. *Nanoscale Res. Lett.* **2017,** *12* (1), 196.

172. Qian, C.; Sun, W.; Hung, D. L. H.; Qiu, C.; Makaremi, M.; Hari Kumar, S. G.; Wan, L.; Ghoussoub, M.; Wood, T. E.; Xia, M.; Tountas, A. A.; Li, Y. F.; Wang, L.; Dong, Y.; Gourevich, I.; Singh, C. V.; Ozin, G. A., Catalytic CO$_2$ Reduction by Palladium-decorated Silicon–hydride Nanosheets. *Nat. Catal.* **2018,** *2* (1), 46-54.

173. Bueno, S. L. A.; Leonardi, A.; Kar, N.; Chatterjee, K.; Zhan, X.; Chen, C.; Wang, Z.; Engel, M.; Fung, V.; Skrabalak, S. E., Quinary, Senary, and Septenary High Entropy Alloy Nanoparticle Catalysts from Core@Shell Nanoparticles and the Significance of Intraparticle Heterogeneity. *ACS Nano* **2022,** *16* (11), 18873-18885.

174. Zheng, Y.; Lapano, J.; Bruce Rayner, G.; Engel-Herbert, R., Native Oxide Removal from Ge Surfaces by Hydrogen Plasma. *J. Vac. Sci. Technol. A* **2018,** *36* (3), 031306.

175. Yao, Y.; Dong, Q.; Brozena, A.; Luo, J.; Miao, J.; Chi, M.; Wang, C.; Kevrekidis, I. G.; Ren, Z. J.; Greeley, J.; Wang, G.; Anapolsky, A.; Hu, L., High-entropy Nanoparticles: Synthesis-structure-property Relationships and Data-driven Discovery. *Science* **2022**, *376* (6589), eabn3103.

176. Glasscott, M. W.; Pendergast, A. D.; Goines, S.; Bishop, A. R.; Hoang, A. T.; Renault, C.; Dick, J. E., Electrosynthesis of High-entropy Metallic Glass Nanoparticles for Designer, Multi-functional Electrocatalysis. *Nat. Commun.* **2019,** *10* (1), 2650.

177. Yao, Y.; Huang, Z.; Xie, P.; Lacey, S. D.; Jacob, R. J.; Xie, H.; Chen, F.; Nie, A.; Pu, T.; Rehwoldt, M.; Yu, D.; Zachariah, M. R.; Wang, C.; Shahbazian-Yassar, R.; Li, J.; Hu, L., Carbothermal Shock Synthesis of High-entropy-alloy Nanoparticles. *Science* **2018,** *359* (6383), 1489-1494.

178. Chen, P.-C.; Liu, X.; Hedrick, J. L.; Xie, Z.; Wang, S.; Lin, Q.-Y.; Hersam, M. C.; Dravid, V. P.; Mirkin, C. A., Polyelemental Nanoparticle Libraries. *Science* **2016,** *352* (6293), 1565-1569.

179. Kumar, N.; Tiwary, C. S.; Biswas, K., Preparation of Nanocrystalline High-entropy Alloys via Cryomilling of Cast Ingots. *J. Mater. Sci.* **2018,** *53* (19), 13411-13423.

180. Gao, S.; Hao, S.; Huang, Z.; Yuan, Y.; Han, S.; Lei, L.; Zhang, X.; Shahbazian-Yassar, R.; Lu, J., Synthesis of High-entropy Alloy Nanoparticles on Supports by the Fast Moving Bed Pyrolysis. *Nat. Commun.* **2020,** *11* (1), 2016.

181. Mori, K.; Hashimoto, N.; Kamiuchi, N.; Yoshida, H.; Kobayashi, H.; Yamashita, H., Hydrogen Spillover-driven Synthesis of High-entropy Alloy Nanoparticles as a Robust Catalyst for CO$_2$ Hydrogenation. *Nat. Commun.* **2021,** *12* (1), 3884.

182. Qiao, H.; Saray, M. T.; Wang, X.; Xu, S.; Chen, G.; Huang, Z.; Chen, C.; Zhong, G.; Dong, Q.; Hong, M.; Xie, H.; Shahbazian-Yassar, R.; Hu, L., Scalable Synthesis of High Entropy Alloy Nanoparticles by Microwave Heating. *ACS Nano* **2021,** *15* (9), 14928-14937.

183. Zhu, G.; Jiang, Y.; Yang, H.; Wang, H.; Fang, Y.; Wang, L.; Xie, M.; Qiu, P.; Luo, W. Constructing Structurally Ordered High-Entropy Alloy Nanoparticles on Nitrogen-Rich Mesoporous Carbon Nanosheets for High-Performance Oxygen Reduction. *Adv. Mater.* **2022,** *34* (15), e2110128.

184. Cao, G.; Liang, J.; Guo, Z.; Yang, K.; Wang, G.; Wang, H.; Wan, X.; Li, Z.; Bai, Y.; Zhang, Y.; Liu, J.; Feng, Y.; Zheng, Z.; Lu, C.; He, G.; Xiong, Z.; Liu, Z.; Chen, S.; Guo, Y.; Zeng, M.; Lin, J.; Fu, L. Liquid Metal for High-Entropy Alloy Nanoparticles Synthesis. *Nature* **2023,** *619* (7968), 73-77.

185. Hashimoto, N.; Mori, K.; Yamashita, H. In Situ Investigation on the Formation Mechanism of High-Entropy Alloy Nanoparticles Induced by Hydrogen Spillover. *J. Phys. Chem. C,* **2023,** *127* (42), 20786-20793.

186. Kar, N.; McCoy, M.; Wolfe, J.; Bueno, S. L. A.; Shafei, I. H.; Skrabalak, S. E. Retrosynthetic Design of Core–Shell Nanoparticles for Thermal Conversion to Monodisperse High-Entropy Alloy Nanoparticles. *Nat. Synth.* **2024,** *3* (2), 175-184.

187. Kang, Y.; Cretu, O.; Kikkawa, J.; Kimoto, K.; Nara, H.; Nugraha, A. S.; Kawamoto, H.; Eguchi, M.; Liao, T.; Sun, Z.; Asahi, T.; Yamauchi, Y. Mesoporous Multimetallic Nanospheres with Exposed Highly Entropic Alloy Sites. *Nat. Commun.* **2023,** *14* (1), 4182.

188. Sarkar, A.; Velasco, L.; Wang, D.; Wang, Q.; Talasila, G.; de Biasi, L.; Kubel, C.; Brezesinski, T.; Bhattacharya, S. S.; Hahn, H.; Breitung, B., High Entropy Oxides for Reversible Energy Storage. *Nat. Commun* .**2018,** *9* (1), 3400.

189. Wang, T.; Chen, H.; Yang, Z.; Liang, J.; Dai, S., High-Entropy Perovskite Fluorides: A New Platform for Oxygen Evolution Catalysis. *J. Am. Chem. Soc.* **2020,** *142* (10), 4550-4554.

190. McCormick, C. R.; Schaak, R. E., Simultaneous Multication Exchange Pathway to High-Entropy Metal Sulfide Nanoparticles. *J. Am. Chem. Soc.* **2021,** *143* (2), 1017-1023.

191. Sure, J.; Sri Maha Vishnu, D.; Kim, H. K.; Schwandt, C., Facile Electrochemical Synthesis of Nanoscale (TiNbTaZrHf)C High-Entropy Carbide Powder. *Angew. Chem., Int. Ed.* **2020,** *59* (29), 11830-11835.

192. Jin, T.; Sang, X.; Unocic, R. R.; Kinch, R. T.; Liu, X.; Hu, J.; Liu, H.; Dai, S., Mechanochemical-Assisted Synthesis of High-Entropy Metal Nitride via a Soft Urea Strategy. *Adv. Mater.* **2018,** *30* (23), e1707512.

193. Yi, G.; Ding, Y.; Cheng, Y.; Zhang, P.; Wang, X.; Liang, X., Development and Oxidation Behavior of High Entropy Silicide (NbMoTaWV)Si_2 Coatings on NbMoTaWV Alloy. *J. Alloys Compd.* **2022,** *916*, 165384

194. Dong, S.; Li, Q.; Hu, H.; Zhang, X.; Li, Y.; Ye, K.; Hou, W.; He, J.; Zhao, H., Application of Rare-Earth High Entropy Boride in Electrocatalytic Hydrogen Evolution Reaction. *Appl. Surf. Sci.* **2023,** *615*, 156413

195. Soliman, S. S.; Dey, G. R.; McCormick, C. R.; Schaak, R. E. Temporal Evolution of Morphology, Composition, and Structure in the Formation of Colloidal High-Entropy Intermetallic Nanoparticles. *ACS Nano* **2023,** *17* (16), 16147-16159.

196. Folgueras, M. C.; Jiang, Y.; Jin, J.; Yang, P. High-Entropy Halide Perovskite Single Crystals Stabilized by Mild Chemistry. *Nature* **2023,** *621* (7978), 282-288.

197.   Shi, X. L.; Zou, J.; Chen, Z. G., Advanced Thermoelectric Design: From Materials and Structures to Devices. *Chem. Rev.* **2020,** *120* (15), 7399-7515.

198.   Rabie, M. A.; Mirza, S.; Hu, Y.; Haddara, Y. M., Cobalt Germanide Contacts: Growth Reaction, Phase Formation Models, and Electrical Properties. *J. Mater. Sci. Mater. Electron.* **2019,** *30* (11), 10031-10063.

199.   Götsch, T.; Stöger-Pollach, M.; Thalinger, R.; Penner, S., The Nanoscale Kirkendall Effect in Pd-Based Intermetallic Phases. *J. Phys. Chem. C* **2014,** *118* (31), 17810-17818.

200.   Vaughn, D. D.; Sun, D.; Moyer, J. A.; Biacchi, A. J.; Misra, R.; Schiffer, P.; Schaak, R. E., Solution-Phase Synthesis and Magnetic Properties of Single-Crystal Iron Germanide Nanostructures. *Chem. Mater.* **2013,** *25* (21), 4396-4401.

201.   Yan, C.; Higgins, J. M.; Faber, M. S.; Lee, P. S.; Jin, S., Spontaneous Growth and Phase Transformation of Highly Conductive Nickel Germanide Nanowires. *ACS Nano* **2011,** *5* (6), 5006-5014.

202.   Yoon, H.; Seo, K.; Bagkar, N.; In, J.; Park, J.; Kim, J.; Kim, B., Vertical Epitaxial Co_5Ge_7 Nanowire and Nanobelt Arrays on A Thin Graphitic Layer for Flexible Field Emission Displays. *Adv. Mater.* **2009,** *21* (48), 4979-4982.

203.   Peng, W.; Chanakian, S.; Zevalkink, A., Crystal Chemistry and Thermoelectric Transport of Layered AM_2X_2 compounds. *Inorg. Chem. Front.* **2018,** *5* (8), 1744-1759.

204.   Yoon, H.; Kang, T.; Lee, J. M.; Kim, S.-i.; Seo, K.; Kim, J.; Park, W. I.; Kim, B., Epitaxially Integrating Ferromagnetic $Fe_{1.3}Ge$ Nanowire Arrays on Few-Layer Graphene. *J. Phys.Chem. Lett.* **2011,** *2* (9), 956-960.

205.   Tang, J.; Wang, C.-Y.; Xiu, F.; Lang, M.; Chu, L.-W.; Tsai, C.-J.; Chueh, Y.-L.; Chen, L.-J.; Wang, K. L., Oxide-Confined Formation of Germanium Nanowire Heterostructures for High-Performance Transistors. *ACS Nano* **2011,** *5* (7), 6008-6015.

206.   Mao, J.; Kim, H. S.; Shuai, J.; Liu, Z.; He, R.; Saparamadu, U.; Tian, F.; Liu, W.; Ren, Z., Thermoelectric Properties of Materials Near the Band Crossing Line in Mg_2Sn–Mg_2Ge–Mg_2Si system. *Acta Mater.* **2016,** *103*, 633-642.

207.   Zhang, R. Z.; Gucci, F.; Zhu, H.; Chen, K.; Reece, M. J., Data-Driven Design of Ecofriendly Thermoelectric High-Entropy Sulfides. *Inorg Chem* **2018,** *57* (20), 13027-13033.

208.   Fan, Z.; Wang, H.; Wu, Y.; Liu, X. J.; Lu, Z. P., Thermoelectric High-Entropy Alloys with Low Lattice Thermal Conductivity. *RSC Adv.* **2016,** *6* (57), 52164-52170.

209.   Ni, C.; O'Connor, K. M.; Trach, J.; Butler, C.; Rieger, B.; Veinot, J. G. C., Facile Synthesis of High-Entropy Alloy Nanoparticles on Germanane, Ge Nanoparticles and Wafers. *Nanoscale Horiz.* **2023,** *8* (9), 1217-1225.

210.   Song, B.; Yang, Y.; Rabbani, M.; Yang, T. T.; He, K.; Hu, X.; Yuan, Y.; Ghildiyal, P.; Dravid, V. P.; Zachariah, M. R.; Saidi, W. A.; Liu, Y.; Shahbazian-Yassar, R., In Situ Oxidation Studies of High-Entropy Alloy Nanoparticles. *ACS Nano* **2020,** *14* (11), 15131-15143.

211.   Anderson, S. L.; Luber, E. J.; Olsen, B. C.; Buriak, J. M., Substance over Subjectivity: Moving beyond the Histogram. *Chem. Mater.* **2016,** *28* (17), 5973-5975.

212.   NIST X-ray Photoelectron Spectroscopy Database, NIST Standard Reference Database Number 20, National Institute of Standards and Technology, Gaithersburg MD, 20899 (2000).

213. Yu, H.; Helbich, T.; Scherf, L. M.; Chen, J.; Cui, K.; Fässler, T. F.; Rieger, B.; Veinot, J. G. C., Radical-Initiated and Thermally Induced Hydrogermylation of Alkenes on the Surfaces of Germanium Nanosheets. *Chem. Mater.* **2018,** *30* (7), 2274-2280.

214. Mukherjee, S.; Nag, A.; Kocevski, V.; Santra, P. K.; Balasubramanian, M.; Chattopadhyay, S.; Shibata, T.; Schaefers, F.; Rusz, J.; Gerard, C.; Eriksson, O.; Segre C. U.; Sarma, D. D., Microscopic Description of the Evolution of the Local Structure and an Evaluation of the Chemical Pressure Concept in a Solid Solution *Phys. Rev. B*, **2014**, *89* (22), 224105.

215. Nalam, P. G.; Das, D.; Tan, S.; Ramana, C. V., Controlled Phase Stabilization Enabled Tunable Optical Properties of Nanocrystalline GeO_2 Films. *ACS Appl. Electron. Mater.* **2022,** *4* (6), 3115-3124.

216. Holzwarth, U.; Gibson, N., The Scherrer Equation Versus the 'Debye-Scherrer equation'. *Nat. Nanotechnol.* **2011,** *6* (9), 534-534.

217. Bianco, E.; Butler, S.; Jiang, S.; Restrepo, O. D.; Windl, W.; Goldberger, J. E., Stability and Exfoliation of Germanane: A Germanium Graphane Analogue. *ACS Nano* **2013,** *7* (5), 4414-4421.

217. Yu, H.; Thiessen, A. N.; Hossain, M. A.; Kloberg, M. J.; Rieger, B.; Veinot, J. G. C., Thermally Induced Dehydrogenative Coupling of Organosilanes and H-Terminated Silicon Quantum Dots onto Germanane Surfaces. *Chem. Mater.* **2020**, *32* (11), 4536-4543.

218. Bueno, S. L. A.; Leonardi, A.; Kar, N.; Chatterjee, K.; Zhan, X.; Chen, C.; Wang, Z.; Engel, M.; Fung, V.; Skrabalak, S. E. Quinary, Senary, and Septenary High Entropy Alloy Nanoparticle Catalysts from Core@Shell Nanoparticles and the Significance of Intraparticle Heterogeneity. *ACS Nano* **2022**, *16* (11), 18873-18885.

219. Smith, E. M.; Streyer, W. H.; Nader, N.; Vangala, S.; Grzybowski, G.; Soref, R.; Wasserman, D.; Cleary, J. W. Metal Germanides for Practical on-Chip Plasmonics in the Mid Infrared. *Opt. Mater. Express,* **2018**, *8* (4), 968-982

220. Beekman, M.; Kauzlarich, S. M.; Doherty, L.; Nolas, G. S. Zintl Phases as Reactive Precursors for Synthesis of Novel Silicon and Germanium-Based Materials. *Materials (Basel)* **2019**, *12* (7), 1139.

221. Su, L.; Chen, X.; Xu, L.; Eldred, T.; Smith, J.; DellaRova, C.; Wang, H.; Gao, W., Visualizing the Formation of High-Entropy Fluorite Oxides from an Amorphous Precursor at Atomic Resolution. *ACS Nano* **2022,** *16* (12), 21397-21406.

222. Patterson, A. L., The Scherrer Formula for X-Ray Particle Size Determination. *Phys. Rev.* **1939,** *56* (10), 978-982.

223. Okada, Y.; Tokumaru, Y., Precise determination of lattice parameter and thermal expansion coefficient of silicon between 300 and 1500 K. *J. Appl. Phys.* **1984,** *56* (2), 314-320.

224. Ni, C.; Chevalier, M.; Veinot, J. G. C. Metal nanoparticle-decorated germanane for selective photocatalytic aerobic oxidation of benzyl alcohol. *Nanoscale. Adv.* **2022**, *5* (1), 228-236.

225. El Hajraoui, K.; Luong, M. A.; Robin, E.; Brunbauer, F.; Zeiner, C.; Lugstein, A.; Gentile, P.; Rouviere, J. L.; Den Hertog, M., In Situ Transmission Electron Microscopy Analysis of Aluminum-Germanium Nanowire Solid-State Reaction. *Nano. Lett.* **2019,** *19* (5), 2897-2904.

226. El Hajraoui, K.; Robin, E.; Zeiner, C.; Lugstein, A.; Kodjikian, S.; Rouviere, J. L.; Den Hertog, M., In Situ Transmission Electron Microscopy Analysis of Copper-Germanium Nanowire Solid-State Reaction. *Nano. Lett.* **2019,** *19* (12), 8365-8371.

227. Ma, Y.; Ma, Y.; Wang, Q.; Schweidler, S.; Botros, M.; Fu, T.; Hahn, H.; Brezesinski, T.; Breitung, B. High-Entropy Energy Materials: Challenges and New Opportunities. *Energy Environ. Sci.* **2021**, *14* (5), 2883-2905.

228. Kang, Y.; Cretu, O.; Kikkawa, J.; Kimoto, K.; Nara, H.; Nugraha, A. S.; Kawamoto, H.; Eguchi, M.; Liao, T.; Sun, Z.; Asahi, T.; Yamauchi, Y. Mesoporous Multimetallic Nanospheres with Exposed Highly Entropic Alloy Sites. *Nat. Commun.* **2023**, *14* (1), 4182.

229. Atkins, T. M.; Thibert, A.; Larsen, D. S.; Dey, S.; Browning, N. D.; Kauzlarich, S. M. Femtosecond Ligand/Core Dynamics of Microwave-Assisted Synthesized Silicon Quantum Dots in Aqueous Solution. *J. Am. Chem. Soc.* **2011** *133* (51), 20664-20667.

230. Qiao, H.; Saray, M. T.; Wang, X.; Xu, S.; Chen, G.; Huang, Z.; Chen, C.; Zhong, G.; Dong, Q.; Hong, M.; Xie, H.; Shahbazian-Yassar, R.; Hu, L. Scalable Synthesis of High Entropy Alloy Nanoparticles by Microwave Heating. *ACS Nano* **2021**, *15* (9), 14928-14937.

231. Peng, L.; Peng, H.; Li, W.; Zhao, D. Monomicellar Assembly to Synthesize Structured and Functional Mesoporous Carbonaceous Nanomaterials. *Nat. Protoc.* **2023**, *18* (4), 1155-1178.

232. Fang, J.; Zhang, L.; Li, J.; Lu, L.; Ma, C.; Cheng, S.; Li, Z.; Xiong, Q.; You, H. A General Soft-Enveloping Strategy in the Templating Synthesis of Mesoporous Metal Nanostructures. *Nat. Commun.* **2018**, *9* (1), 521.

233. Soong, C.; Woo, P.; Hoyle, D. Contamination Cleaning of TEM/SEM Samples with the ZONE Cleaner. *Microsc. Today* **2012**, *20* (6), 44-48.

234. Kleitz, F.; Choi, S. H.; Ryoo, R. Cubic *Ia3d* Large Mesoporous Silica: Synthesis and Replication to Platinum Nanowires, Carbon Nanorods and Carbon Nanotubes. *Chem. Commun.* **2003**, (17), 2136-2137.

235. Wang, H.; Jeong, H. Y.; Imura, M.; Wang, L.; Radhakrishnan, L.; Fujita, N.; Castle, T.; Terasaki, O.; Yamauchi, Y. Shape- and Size-Controlled Synthesis in Hard Templates: Sophisticated Chemical Reduction for Mesoporous Monocrystalline Platinum Nanoparticles. *J. Am. Chem. Soc.* **2011**, *133* (37), 14526-14529.

236. Coley, C. W.; Thomas, D. A., 3rd; Lummiss, J. A. M.; Jaworski, J. N.; Breen, C. P.; Schultz, V.; Hart, T.; Fishman, J. S.; Rogers, L.; Gao, H.; Hicklin, R. W.; Plehiers, P. P.; Byington, J.; Piotti, J. S.; Green, W. H.; Hart, A. J.; Jamison, T. F.; Jensen, K. F. A Robotic Platform for Flow Synthesis of Organic Compounds Informed by AI Planning. *Science* **2019**, *365* (6453), eaax1566.

237. Slattery, A.; Wen, Z.; Tenblad, P.; Sanjose-Orduna, J.; Pintossi, D.; den Hartog, T.; Noel, T. Automated Self-Optimization, Intensification, and Scale-up of Photocatalysis in Flow. *Science* **2024**, *383* (6681), eadj1817.

238. Sun, S.; Hartono, N. T. P.; Ren, Z. D.; Oviedo, F.; Buscemi, A. M.; Layurova, M.; Chen, D. X.; Ogunfunmi, T.; Thapa, J.; Ramasamy, S.; Settens, C.; DeCost, B. L.; Kusne, A. G.; Liu, Z.; Tian, S. I. P.; Peters, I. M.; Correa-Baena, J.-P.; Buonassisi, T. Accelerated Development of Perovskite-Inspired Materials via High-Throughput Synthesis and Machine-Learning Diagnosis. *Joule* **2019**, *3* (6), 1437-1451.

239. Szymanski, N. J.; Rendy, B.; Fei, Y.; Kumar, R. E.; He, T.; Milsted, D.; McDermott, M. J.; Gallant, M.; Cubuk, E. D.; Merchant, A.; Kim, H.; Jain, A.; Bartel, C. J.; Persson, K.; Zeng, Y.; Ceder, G. An Autonomous Laboratory for the Accelerated Synthesis of Novel Materials. *Nature* **2023**, *624* (7990), 86-91.

240. Divilov, S.; Eckert, H.; Hicks, D.; Oses, C.; Toher, C.; Friedrich, R.; Esters, M.; Mehl, M. J.; Zettel, A. C.; Lederer, Y.; Zurek, E.; Maria, J. P.; Brenner, D. W.; Campilongo, X.; Filipovic, S.; Fahrenholtz, W. G.; Ryan, C. J.; DeSalle, C. M.; Crealese, R. J.; Wolfe, D. E.; Calzolari, A.; Curtarolo, S. Disordered Enthalpy-Entropy Descriptor for High-Entropy Ceramics discovery. *Nature* **2024**, *625* (7993), 66-73.